

UNIVERSITÀ DEGLI STUDI DI NAPOLI “FEDERICO II”
DIPARTIMENTO DI INGEGNERIA INDUSTRIALE



DOTTORATO DI RICERCA IN
“INGEGNERIA INDUSTRIALE”
XXXIV CICLO

**Optimization of biomass powered cogeneration systems based
on gasifiers and internal combustion engines**

PHD COORDINATOR:
Ch.mo Prof. Michele GRASSI

PHD CANDIDATE:
Ing. Gaia MARTORIELLO

PHD TUTOR :
Ch.mo Prof. Raffaele TUCCILLO
Dott. Ing. Michela COSTA – CNR STEMS

INDUSTRY TUTOR:
Ing. Domenico CIRILLO – CMD S.p.A.

Anno Accademico 2021/2022

The work performed in this Thesis was found within the Bilateral Agreement “Confindustria-National Research Council” and carried out in collaboration with the University of Naples “Federico II”, the National Research Council – Istituto di Scienze e Tecnologie per l'Energia e la Mobilità Sostenibili (CNR-STEMS) and the company Costruzioni Motori Diesel (CMD) SpA

Index

Nomenclature	13
Introduction	15
CHAPTER 1	21
The role of bioenergy in the current energy scenario	21
1.1. The resilience of renewables during Covid-19 outbreak	21
<i>1.1.1 European and Italian bioenergy scenario</i>	27
1.2. Biomass conversion energy processes	33
<i>1.2.1 Bio-chemical conversion processes</i>	35
<i>1.2.2 Thermochemical conversion processes</i>	36
1.3 Biomass gasification	36
<i>1.3.1 Upstream processing</i>	37
<i>1.3.2 Gasification reactions</i>	40
<i>1.3.3 Gasifier type</i>	44
<i>1.3.4 Syngas cleaning processes</i>	45
1.4 Cogeneration systems based on gasifier-ICE technology	46
References Chapter 1	53
CHAPTER 2	57
The case study: a micro-cogeneration system based on biomass gasification	57
2.1 The CMD ECO20x system	57
<i>2.1.1 Historical evolution of CMD ECO20x</i>	66
2.2 Experimental characterization of the CMD ECO20x operation under various feedstocks	67
<i>2.2.1 Experimental layout</i>	67
<i>2.2.2 Effect of feedstock composition on the performances of the gasifier and the internal combustion engine</i>	73
2.3 Energy efficiency evaluation of the CMD ECO20x plant	86

References Chapter 2	88
CHAPTER 3.....	91
Numerical modelling, optimization and experimental verification.....	91
3.1 Modelling of the micro-cogeneration system	93
3.1.1 <i>Thermoflex® model.....</i>	93
3.1.2 <i>GT-Power© model</i>	98
3.2. Numerical optimization.....	101
3.2.1. <i>Algorithms</i>	102
3.2.1.1 <i>Single-objective algorithm: gradient methods</i>	102
3.2.1.2 <i>Multi-objective algorithm (genetic methods)</i>	104
3.3 Optimization of the gasification section.....	108
3.4 Optimization of the internal combustion engine	112
3.4.2 <i>The CO emission trend.....</i>	118
3.4.3 <i>The NOx emission trend</i>	119
3.3.4 <i>The electrical output power trend</i>	119
3.5 Engine spark timing and misfire detection through an innovative ECU ...	120
3.5.1 <i>Ionization current and its interpretation.....</i>	122
3.5.2 <i>Modelling of Ion current</i>	126
3.5.3 <i>Fouling and misfiring detection</i>	129
3.5.4 <i>Implementation of spark timing optimization in an ECU</i>	132
3.6 Optimization of the waste heat recovery	133
3.6.1 <i>Effect of heat exchange surface.....</i>	134
3.6.2 <i>Effect of secondary circuit water mass flow rate</i>	135
3.6.3 <i>Biomass drying process.....</i>	136
References Chapter 3	140
CHAPTER 4.....	143

Validation of the improved CMD ECO20x unit in a real environment: the demo stage of the PROMETEO project	143
4.1 mCHP system as a green substitute in waste management and storage plant	144
4.1.1 <i>Engine sensibility analysis</i>	147
4.2 Air quality assessment analysis	156
4.2.1 <i>Location of the air pollution monitoring station.....</i>	158
4.2.2. <i>Air quality assessment analysis in the CMD ECO20x proximity.....</i>	160
4.3 Life cycle analysis	162
4.4 Economic analysis.....	165
CHAPTER 5.....	171
Biomass-powered micro-cogeneration plants as renewable systems in micro-grids	171
5.1 Micro-grid model development	177
5.1.1 <i>PV system model.....</i>	178
5.1.2 <i>CMD ECO20x model</i>	178
5.1.3 <i>Battery system model.....</i>	180
5.1.4 <i>H2 system model.....</i>	180
5.1.5 <i>Operational strategy and optimization module.....</i>	181
5.1.6 <i>Initialization for both scenarios</i>	183
5.2 Västerås case study	189
5.2.1 <i>Genetic algorithm optimization for Västerås case study</i>	197
5.3 Cilento case study	200
5.2.1 <i>Genetic algorithm optimization for Cilento case study.....</i>	208
References of Chapter 5.....	211
Conclusions	214
Acknowledgments.....	218

Figure Index

Figure 1. 1: Oil, natural gas and coal prices by region, 2010 – 2021	23
Figure 1. 2: Evolution of global GDP, total primary energy demand and energy related CO2 emissions, relative to 2019 (b) [12]	24
Figure 1. 3: Global emissions by scenario, 2000-2050 [12].....	25
Figure 1. 4: The rising share of low emissions fuels in the energy mix [12]	26
Figure 1. 5: EU member states installed renewable capacity in 2020 and scenario for 2030	27
Figure 1. 6: European gross electricity generation by source (a) and biofuels (b) [12] .	28
Figure 1. 7: Land use by type in EU27 in 2018 (%) [19].....	30
Figure 1. 8: Electricity Consumption in France, Germany, Italy, Spain, and Sweden [20].	30
Figure 1. 9: Natural gas prices for household (a) and non-household (b) consumers in the first half of 2021[25].	31
Figure 1. 10: Levelised cost of electricity for different renewable technologies compared with the range cost for fossil fuel technologies (€/MWh) [19].	32
Figure 1. 11: Biomass to energy conversion process [41].....	35
Figure 1. 12: C-H-O ternary diagram of biomass showing the gasification process[43].	38
Figure 1. 13: Effect of the air/fuel actual ratio (a) and gasification temperature (b) on the syngas composition (%vol)	43
Figure 1. 14: Gasification technologies classifications [48].....	44
Figure 1. 15: Cogeneration overall efficiency as compared to conventional methods [52]	47
Figure 1. 16: Distribution of CHP systems in Italy [72]	52
Figure 2. 1: CMD ECO20x m-CHP system (b) [1]	57
Figure 2. 2: CMD ECO 20x process workflow	58
Figure 2. 3:CMD ECO20x History [3].....	66
Figure 2. 4: List of installed sensors on the studied m-CHP plant.	68
Figure 2. 5: Experimental setup showing the ICE and sampling points for syngas analyses.	68

Figure 2. 6: Sensor Semtech Analyzer (a), probe for syngas sampling (b), three-way valve, Vario Luxx Analyzer (d)	70
Figure 2. 7: Installed volumetric flow meter (a), Continental UniNOx (b) and AVL smoke meter (c).....	71
Figure 2. 8: Experimental setup for the analysis of the tar concentration in the syngas	72
Figure 2. 9: AVL ZI45-F5D (a) and AVL LP12DA-05(b)	72
Figure 2. 10: Briquetting process for green waste HTC and olive pomace mixed with sawdust	74
Figure 2. 11: The Von Krevelen's diagram and here considered biomasses	77
Figure 2. 12: Parametric analysis of the calorific value of the syngas produced by the gasification of a mix of briquettes and mixed woodchips, depending on the %age of briquettes.	78
Figure 2. 13: Fragment of molten ash present in the reactor combustion area.....	79
Figure 2. 14: Comparison between temperatures (K) in relevant points of the m-CHP plant circuit (experimental analysis).	80
Figure 2. 15 Comparison between pressures (Pa) in relevant points of the m-CHP plant circuit (experimental analysis).	80
Figure 2. 16: Average pressure cycle for the considered samples (experimental analysis).	81
Figure 2. 17: Combustion development for the considered samples in terms of burned mass fraction as a function of the crank angle. Top dead center (TDC) is at 0°deg (experimental analysis).....	83
Figure 2. 18: Measured in-cylinder pressure during the intake phase for various feedstock (experimental analysis).....	84
Figure 2. 19: Emissions of CO, THC and NOx for sample a), b) and c) (experimental analysis).....	86
Figure 2. 20: Sankey diagram for sample a), b) and c) (Unit are expressed in kW).	88
Figure 3. 1: The CMD ECO20x system model (Thermoflex™ environment)	94
Figure 3. 2: Model results compared with experimental data for syngas composition (a), temperatures (b) and pressures (c) in various points of the plant.	97
Figure 3. 3: Engine model in GT-Suite®.	99

Figure 3. 4: Comparison between model results and experimental data relevant to the engine pressure cycle.....	101
Figure 3. 5: Flowchart of genetic algorithms.	106
Figure 3. 6: Stresses associated with an optimal solution for an optimization problem with two criteria [22]	107
Figure 3. 7: Bubble chart representing the value of the ICE brake power in the DOE space.	108
Figure 3. 8: Installation of ball valves on CMD ECO20x.	109
Figure 3. 9: Trend of the measured airflow at the reactor inlet and the temperature in the combustion zone (a) and pressure in the lower part of the reactor and power delivered by the engine (b).....	111
Figure 3. 10: SI engine combustion phase [13].	113
Figure 3. 11: Workflow of the optimization engine problem.....	113
Figure 3. 12: Numerical analysis of engine performance and pollutant emissions as obtained by varying the spark timing a), b), c), the air-to-fuel ratio d), e), f), and EGR ratio g), h), i).....	116
Figure 3. 13: Parallel chart of the optimization. Pareto optimal points are shown in bold blue.	117
Figure 3. 14: CO emissions at various EGR %ages: a) 0%, b) 10%, c) 15%.....	118
Figure 3. 15: NOx emission at various EGR %age: a) 0%, b) 10%, c) 15%	119
Figure 3. 16: Brake power at various EGR %age: a) 0%, b) 10%, c) 15%.....	120
Figure 3. 17: ECU prototype and related box field for actuations (a) and testing with signal simulators in the laboratory (b)	121
Figure 3. 18: ECU testing on the engine	122
Figure 3. 19: Ion current measurement system circuit (a) and oscilloscope (b).....	123
Figure 3. 20: Ion voltage acquired during engine working	124
Figure 3. 21: The measured signal (Spark advance= -20°CAD , $\lambda = 1.05$) compared with the two gaussian functions obtained from the model (a), and the peak pressure position with post flame phase ionization current obtained from the model (b).....	127
Figure 3. 22: Different examples of peak pressure position with post flame phase ionization current obtained from the model	128

Figure 3. 23: Correlation between the true peak pressure position and estimated peak position	129
Figure 3. 24: Ionization current of different spark plug states: normal (a) and fooled (b)	130
Figure 3. 25: Flow Chart for ECU engine management.....	133
Figure 3. 26: Direct drying process	136
Figure 3. 27: Energy flux for each of the analysed cases	138
Figure 3. 28: Parametric analysis made by varying the initial moisture (a) and β (b).	139
Figure 3. 29: Required biomass drying thermal power (a) and drying efficiency varying the exhaust bleeding ratio	140
Figure 4. 1: Installed CMD ECO20x from PROMETEO project	144
Figure 4. 2: IMEP, IMEP _{COV} , P _{max} , MFB50 and MFB10-90 for both biomasses (low load).....	148
Figure 4. 3: Combustion chamber pressure with (P _{cyl}) with spark advance =20° bTDC, $\lambda = 1.03$, low load, biomass 1.....	148
Figure 4. 4: MFB0-10, MFB10-50 e MFB50-90 for a spark =20°bTDC, $\lambda=1.03$, low load and biomass 1.	149
Figure 4. 5: IMEP, MFB10-90, MFB50, IMEP_COV,P _{max} and η_{therm} for both biomasses at medium load.....	150
Figure 4. 6: Pressure traces (P _{cyl}) of biomass 1, medium load and $\lambda=1.03$ for different SA.	152
Figure 4. 7: Ionization current peak for biomass 2 tests (a) and comparison between two ionization current peaks with $\lambda: 1.03$, SA: 20 deg bTDC(b).....	152
Figure 4. 8: Exhaust mass flow rate (a) and temperature (b) for both processed feedstocks.	153
Figure 4. 9: Emissions of CO (a), CO ₂ (b) and PM (c) for both biomasses	154
Figure 4. 10: Emissions of O ₂ (a) and NO _x (b) for both biomasses.....	155
Figure 4. 11: Installed ETL One in Mugnano, Napoli: external case (a) and sensors (b)	157
Figure 4. 12: Weather station	158
Figure 4. 13: Location of the CMD ECO20x (red circle) at the waste management and storage plant of the Municipality of Mugnano.	159

Figure 4. 14: Wind rose of the two test days	159
Figure 4. 15: Position of the ETL one during the two test days.	160
Figure 4. 16: External temperature (a) and humidity (b) for the two test days.	161
Figure 4. 17: 50km diameter with Mugnano (Napoli) as a centre [11].....	162
Figure 4. 18: Foreground system flow diagram	163
Figure 5. 1: Hierarchical architecture of a micro-grid [10]	172
Figure 5. 2 Typical time scale and size of energy storage systems [17].	174
Figure 5. 3: Comparison between different Li-Ion technologies [20].	176
Figure 5. 4: Schematic diagram of the proposed microgrid	177
Figure 5. 5: Fuel consumption map (g/s) vs speed (rpm) and torque (Nm) [27].	179
Figure 5. 6: Operational strategy flowchart for the micro-grid.	182
Figure 5. 7: Climatic data of Västerås, Sweden (a) and Cilento (b).....	184
Figure 5. 8: Proposed electric load (1 electric car recharge station).	186
Figure 5. 9: Required power to switch on CMD ECO20x	187
Figure 5. 10: Parametric analysis by varying the number of strings in a Li-Ion battery	188
Figure 5. 11: Simulation results for 2 selected months: January (up) and July (down) for the case a), b) and c) with CC operational strategy (Västerås case study).	192
Figure 5. 12: Simulation results for 2 selected months: January (up) and July (down) for the case a), b) and c) of LF operational strategy (Västerås case study).	195
Figure 5. 13: Hydrogen quantity over time for case b) and case c) for Västerås case study.	197
Figure 5. 14: Pareto front of the micro-grid located in Västerås.....	198
Figure 5. 15: Simulation results for 2 selected months: January (up) and July (down) for the case a), b) and c) with CC operational strategy (Cilento case study).	203
Figure 5. 16: Simulation results for 2 selected months: January (up) and July (down) for the case a), b) and c) of LF operational strategy (Cilento case study).	206
Figure 5. 17: Hydrogen quantity over time for case b) and case c) for Cilento case study.	208
Figure 5. 18: Pareto front of the micro-grid located in Cilento.....	209

Table Index

Table 1. 1 GBEP Sustainability Indicators Environmental Social Economic [34].	34
Table 1. 2: Natural syngas and biogas properties	39
Table 1. 3: Pyrolytic products in fast, intermediate and slow pyrolysis [43]	40
Table 1. 4: Reactions occurring in gasification [43], [46]	41
Table 1. 5: Characteristics of Fixed-Bed Gasifier [48]	45
Table 1. 6: efficiency of particulates and tar removals of syngas cleaning technologies. [50], [51]	46
Table 1. 7: Share of installed CHP system in Europe [53]	48
Table 1. 8: Main application of biomass CHP in Europe	51
Table 1. 9: Main application of biomass m-CHP in Italy	52
Table 2. 1: Biomass Classification based on UNI EN ISO 17225-4 [2]	59
Table 2. 2: Description of the main component of CMD ECO 20x	64
Table 2. 3: GM Vortec V-6 technical specifications	64
Table 2. 4: Limit emissions for CMD ECO20x [5]	71
Table 2. 5: Proximate and ultimate analysis results of the here used feedstock	76
Table 2. 6: Mean syngas composition (%vol) (DB) for each processed biomass	78
Table 2. 7: Comparison between engine parameters under different biomass powering modes	82
Table 2. 8: Combustion main angles	83
Table 2. 9: Standard deviation in /%vol on the syngas as online composition	85
Table 2. 10: Key performance indicators of the considered samples	88
Table 3. 1: Thermoflex™ components description	95
Table 3. 2: Comparison between laminar flame speed parameters used to evaluate laminar flame speed at different pressure and temperature for stoichiometric air/fuel mixture	100
Table 3. 3: Effect of opening and closing blue valve on some averaged quantities	110
Table 3. 4: Average values of some of the quantities measured before, during and after the partialization	111
Table 3. 5: Summary of the engine optimization	114
Table 3. 6: Citizens of Pareto Front with their weight	117
Table 3. 7: Matrix of the analyzed engine test points	126
Table 3. 8: Ion current peak of every acquisition with Fouling or Misfire presence	132
Table 3. 9: Specification for waste heat recovery in CMD ECO20x	133

Table 3. 10: Baseline conditions for waste heat recovery simulations.....	134
Table 3. 11: Effect of surface variation on thermal power (in blue baseline case)	134
Table 3. 12: Effect of secondary water mass flow rate on thermal power	135
Table 3. 13: Average values in baseline condition.....	139
Table 4. 1: Engine operating condition test matrix	145
Table 4. 2 Biomass proximate and ultimate analyses.....	146
Table 4. 3: Syngas compositions and lower heating values	146
Table 4. 4: ETL One technical specification [7]	156
Table 4. 5: Air quality assessment during the two test days and full-scale measurement.	161
Table 4. 6: LCA analysis of CMD ECO20x in comparison with a diesel generator to deliver 144 MWh to the user	165
Table 4. 7: Prices (€/MWh) for dedicated withdrawal in Italy in 2021[16].....	166
Table 4. 8: Data for the calculation of costs and revenues	167
Table 4. 9: Annual Savings, VAN, Gross %age profit and payback time obtained from the operation of the plant.	169
Table 5. 1: Main parameters of the micro-grid (pre-optimization).	184
Table 5. 2: Main supposed economic data [29].....	185
Table 5. 3: Max required power from each component of CMD ECO20x to switch on	187
Table 5. 4: Range of variation for the proposed simulation and summary optimization of the micro-grid.	188
Table 5. 5: Total LCC and reliability for each proposed case for Västerås case study	196
Table 5. 6: Main parameters of the pareto front points (case 3 LF - Västerås).....	200
Table 5. 7: Total LCC and reliability for each proposed case for Cilento case study..	207
Table 5. 8: Main parameters of the pareto front points (case 3 LF - Cilento).....	211

Nomenclature

Variables SI (unit)

- $\left(\frac{air}{fuel}\right)_{actual}$ Mass ratio of air to the gaseous fuel in the gasification process (kg/kg)
- ER Equivalence ratio of the gasifier (kg/kg)
- $HHV_{Milne,dry}$ Higher heating value of biomass calculated with Milne formula (kJ/kg)
- LHV_{dry} Lower heating value of biomass in dry basis (kJ/kg)
- LHV_{ar} Lower heating value of biomass as received (kJ/kg)
- LHV_{syn} Lower heating values of the syngas (kJ/Nm³)
- \dot{m}_{air} Air mass flow rate (kg/s)
- $\dot{m}_{biom,after\ drying\ process}$ Mass flow rate of the dried biomass (kg/s)
- M Molecular weight of the syngas (kg/kmol)
- M_i Molecular weight of the i-th syngas species (kg/kmol)
- $PC1$ Inlet pressure of the syngas before first cyclone (mbar)
- $P3$ Inlet pressure of the syngas before mixing with air (mbar)
- $P4$ Outlet pressure of the syngas exiting cooler (mbar)
- $P5$ Inlet pressure of the engine (mbar)
- $T_{F_{out}}$ Outlet temperature of the ICE exhaust gases into and from the shell and tube heat exchanger (°C)
- $T_{kA_{in}}$ Inlet temperature of water in the secondary circuit into and from the shell and tube heat exchanger (°C)
- $T_{kA_{out}}$ Outlet temperature of water in the secondary circuit into and from the shell and tube heat exchanger (°C)
- $T_{kRAD_{in}}$ Inlet temperature of water in the primary circuit into and from the radiator (°C)
- $T_{kRAD_{out}}$ Outlet temperature of water in the primary circuit into and from the radiator (°C)
- $T_{MOT_{in}}$ Inlet temperature of the engine cooling water in the primary circuit (°C)
- $T_{MOT_{out}}$ Outlet temperature of the engine cooling water in the primary circuit (°C)
- $T_{kC_{out}}$ Outlet temperature of the syngas into the cooler (°C)
- T_{RID} Temperature of the central part of the gasifier (°C)
- x_{mas} Mass fraction of i-th syngas species (kg/kg)
- x_{vol} Volumetric fraction of i-th syngas species (m³/m³)

Chemical formula

- C Carbon content in the fuel (–)
- CH_4 Methane content in the syngas (volume/volume)

CO₂ Carbon dioxide content in the syngas (volume/volume)
CO Carbon monoxide content in the syngas (volume/volume)
H Hydrogen content in the fuel (–)
H₂ Hydrogen content in the syngas (volume/volume)
H₂O Water content in the syngas (volume/volume)
N₂ Nitrogen content in the syngas (volume/volume)
NO_x Nitrogen oxides (volume/volume)

Acronyms/abbreviations

ATDC After Top Dead Center
BDF Backward Difference Formulae
BFGS Broyden Fletcher Goldfarb Shanno
BTDC Before Top Dead Center
CFD Computational Fluid Dynamics
CGE Cold gas efficiency
CHP Combined Heat and Power
CI Compression Ignition
CMD Costruzioni Motori Diesel
CNR Italian National Institute of Research
DOE Design Of Experiment
EL Electrolyzer
EN Referred to European Committee for Standardization
EU European Union
FC Fuel cell
GDI Gasoline Direct Injection
GHG Greenhouse gas
ICE Internal Combustion Engine
IMEP Indicated Mean Effective Pressure
m – CHP Micro-Combined Heat and Power
PID Proportional Integrative Derivative
RES Renewable Energy Source
SI Spark Ignition
UNI Referred to Italian National Unification

Introduction

Energy is a fundamental element of daily life and the main pillar of the modern economy. A secure and reliable energy supply is essential for development, as it is used for industrial processes as well as for public services such as lighting, heating, information, communication and today also, in an increasing trend, for mobility.

In the last years, the Intergovernmental Panel on Climate Change (IPCC) has unequivocally revealed the evidence of observations conducted on the increase in the average temperature on our planet, on the widespread melting of snow and ice and on the rise in the average sea level, definitely linking these phenomena to human activities and to the release of the so-called greenhouse gases (GHGs). The climate changes we are witnessing today have led to widespread impacts on human life and natural ecosystems on all continents and oceans. Recent climate-related phenomena, such as heat waves, droughts, floods, cyclones and fires, reveal a significant vulnerability and exposure of different geographical areas in particular of less developed countries.

Perspective worldwide scenarios show that the continued emission of GHGs will cause further warming, increasing the likelihood of serious, pervasive and irreversible impacts on people and ecosystems. Without further efforts to reduce emissions, the average temperature of the Earth surface would increase from 3.7 °C to 4.8 °C in 2100 compared to pre-industrial levels. As the conversion of fossil fuels is between main causes of GHGs release into the atmosphere, mitigation scenarios are unavoidable, that indeed imply the need for fast energy efficiency improvements and a tripling of the share of zero and/or low carbon energy. By the year 2050, energy from renewable sources, nuclear energy, fossil energy but with the capture and storage of carbon dioxide (CCS) and bioenergy with CCS (BECCS) have been indicated by the International Energy Agency (IEA) as the preferable mitigation measure to fight against climate changes. Achieving a complete energy transition requires investment and innovation, along with new business models and joint actions to be carried out on every segment of the market. Up to present, many actions have been taken both nationally and locally, but international cooperation in energy technology innovation is unavoidable, given the urgency to act.

Responding to the energy demand and at the same time complying with actions introduced to diminish the negative externalities of the conversion paths is a challenge that today is articulated mainly on three main measures:

1. electrification, in particular for mobility and light transport;
2. decentralization of energy production for the optimal exploitation of local resources, with the growing diffusion of distributed systems for energy storage, generation and management;
3. flexibility, through the digitalization of production and consumption.

As a result, biomass appears to be a perfect match for CO₂ neutrality, due to the diffused availability, especially in rural zones, and as the amount released by biomass conversion into energy is considerably offset by the absorbed quantity connected to plant development during their lives. Biomass may be easily produced, gathered, and directly processed locally on a micro-scale power level, allowing it to be used to lessen overall cradle to grave environmental effect. Sustainable biomass exploitation for combined heat and power (CHP) generation may therefore play a pivotal role in providing tangible solutions to contemporary concerns about climate change and energy supply security.

Among biomass conversion technologies, the gasification process is attractive because of its intrinsic environmental advantages, especially if non putrescible materials must be treated. It is a thermo-chemical process, originated in 1798 and developed during the World War II, that converts carbonaceous solid material into a gaseous fuel, the syngas, mainly composed of CO, H₂, CH₄, CO₂ and N₂. Dedicated energy crops, residuals from forest and agricultural activities, trash from the paper and food sectors, and even the humid portion of municipal solid waste can all be used as feedstock. In the future years, the market demand for micro-CHP powered by biomass is predicted to increase.

In this light, optimizing this technology is a fundamental task, as biomass gasification based micro-CHP is not a mature technology for a variety of reasons, including the syngas quality strong dependence upon the same biomass composition and the reactor operating conditions, as well as due to the difficulty of fully conditioning the syngas temperature at the gasifier exit for the highest volumetric efficiency of the involved thermal engine.

The present Ph.D. work, funded within the Bilateral Agreement Confindustria-National Research Council and carried out at the University of Naples “Federico II”, the National Research Council – Istituto di Scienze e Tecnologie per l'Energia e la Mobilità Sostenibili (CNR-STEMS) and the company Costruzioni Motori Diesel (CMD) SpA, has given a concrete contribution to improve the performance of a CHP plant of the micro scale of power, the CMD ECO20x, developed, manufactured and marketed by the Private

Company CMD. The work, as a long-term impact, may trigger an increase of the diffusion of energy valorisation of biomasses for heat and power generation, making for residual materials to become a resource able to provide energy at local level.

The performed work was both numerical and experimental. The involvement at CNR in a research group highly experienced in numerical simulation techniques and the joint collaboration with other research groups specialised in experimental activities, together with the technical and competent support of the CMD work team, allowed the thesis job to be highly multi-disciplinary. After an initial phase of documentation about the gasification technique and the actual state of art of biomass gasification for energy production, a full analysis of the real micro-scale CHP system consisting of a downdraft gasifier coupled with an internal combustion engine was carried out to characterize the energy flows and to highlight main inefficiencies of the system, with particular attention to the genset section for electricity production and heat recovery. From the experimental side, a mobile laboratory of CNR-STEMS was used to carry out the tests for the most at the CMD site in San Nicola La Strada. The chemical composition of the syngas and the exhaust gases were analysed, while the in-cylinder pressure cycles were fully acquired through in-cylinder AVL sensors. The main results of the experimental characterization of the plant under study were used to validate original numerical models able to simulate the whole biomass-to-energy conversion chain. The numerical results provided very useful information to optimize the considered energy system, both regarding the gasification section, the waste heat recovery and the engine power output and emissions at the exhaust. Numerical simulations allowed a considerable saving of time and costs if compared to the same analysis conducted through experimental measurements. Results were proven to be accurate and models were then included within multi-objective optimization problems to optimise the conversion process, namely, to get the highest electrical energy from the syngas powered engine, hence to identify the better calibration of the controlling parameters for syngas use. An appropriate experimental campaign was finally carried out to verify the results of the numerical optimization and to actually prove the technical feasibility of the improvements suggested by the performed calculations.

The matured know-how of the system and of the effect of main variables on the analysed process led to the identification of different technical solutions that overall led to important industrial improvement of the system, for enhanced performance, reduced

environmental impact and increased reliability. The management and automation of the engine were improved thanks to the use of an Electronic Control Unit capable of monitoring the state of the engine and managing the various phases of operation with closed-loop logics.

As an overall presentation of the thesis output, the work contributed to a decisive upgrade of the CMD ECO20x system. The engine was re-calibrated to optimize the electrical power and a three-way catalyst was installed to reduce the CO emissions. The engine cooling circuit was modified, by dividing it from the syngas cooling system to improve the latter capacity of separation of dusts and tars and a proper electronic control unit was developed to automatise the spark advance control as a function of the biomass, hence of the syngas quality.

A real operation demonstration of the improved biomass powered plant was in the end conducted within a waste management and storage plant, located in the Mugnano Municipality, in Southern Italy, by proving a decisive improvement of air quality in the real environment during real exercise.

In parallel, the biomass powered micro-CHP unit manufactured by CMD was numerically analysed as being a part of a renewable micro-grid, composed by a solar PV system, a battery energy storage and a hydrogen storage unit. Hydrogen was assumed as produced through an electrolyser. This last part of the work, made in cooperation with the Mälardalens University of Sweden, mainly consisted in the development of a numerical model of a renewable micro-grid. A simulation was performed to achieve the micro-grid correct sizing as serving a charging station for electric vehicles. The micro-grid was supposed to be located both in the South of Italy and in Västerås, Sweden. Each component sizing was found through optimization based on genetic algorithms, so to reach a high number of operative hours and a low total life cycle cost.

The thesis is, therefore, structured as follows:

- Chapter 1 presents the current world energy outlook and, specifically, the European and Italian energy contexts. It focuses the attention on bioenergy and the current Covid-19 situation, showing various types of future scenarios. Then, the potential of biomass as a fuel source and the main biomass conversion processes are highlighted. The characteristic parameters that influence this thermo-chemical conversion route are shown, to explain how they affect the

process performances. A particular relevance is given to the different technologies used for biomass gasification, showing, for each gasifier analysed, their advantages and disadvantages. Finally, the principles of the combined heat and power generation and the relevant technologies, such as the internal combustion engine, the micro gas turbines, the Stirling engines and the fuel cells, are explained.

- Chapter 2 shows into detail the main features of the considered micro-CHP plant fed by ligno-cellulosic biomasses, the CMD ECO20x, and reports the main results of a full experimental investigation under four main feedstocks. The whole system was equipped with measurement sensors to monitor pressure and temperature in all characteristic points of the plant. Specific accesses to allow the spillage of syngas and exhaust gases were set up to analyse both the composition of the fuel entering the engine and the exhaust gases released into the environment. In-cylinder sensors were used to characterize the syngas combustion process occurring within the engine cylinders. In the end, the analysis made with the four different feedstocks allowed to understand the systems sensitivity to feedstock composition.
- Chapter 3 describes the numerical activity and the relevant optimization of the system, as developed during the Ph.D. course. A description of the whole plant was achieved focussing on each component, their function and their features. Modelling of the plant was made within the Thermoflex® environment. Starting from the gasifier, each step of the model implementation was shown in order to justify the use of all components and to clarify the proximity of the model to the reality. Then, in the Chapter, the Thermoflex® model limits are highlighted to justify the need to resort to another software, the GT-Power®. The latter, indeed, helps to overcome the limits in the engine implementation in Thermoflex®, since a more reliable prediction of the air and gas flows and of the combustion development is ensured due to its intrinsic nature and scope. Optimization of each section is shown, achieved through genetic or gradient algorithm and then implemented on the CMD ECO20x. An Electronic Control Unit was specifically adapted for the engine equipping the system and different strategies for a closed loop control of the engine were explored. The main objective of the activities was

the reliability improvement and the fully automation, in a view of a greater diversification of usable biomasses.

- Chapter 4 illustrates the experience made in the Mugnano Municipality, where the system was installed for six months to be at service of a waste storage plant. A decisive improvement of air quality was pursued, proving in addition the lower impact of the whole supply chain of the energy source on a LCA basis.
- Chapter 5, finally, shows a numerical study on the here considered m-CHP system integration with photovoltaic (PV) solar energy and hydrogen storage. This part of the work allowed understanding the possibility of providing energy to charging stations for the electric mobility in the respect of constraints of compactness, high quality service and ultra-low environmental impact. These results are used as important information for the on-going Project “BORGO 4.0”, funded by POR CAMPANIA FESR 2014-2020, in the creation of a totally innovative and 100% renewable charging infrastructure.

The present thesis contributes to explore the biomass potentiality in the framework of renewable energy sources and the concrete possibility related to its exploitation in micro-cogeneration plants based on gasification and use of syngas in reciprocating engines. The described methodology could be easily applied to any commercial microcogeneration unit, as an example of tailored system calibration and optimization under syngas powering.

CHAPTER 1

The role of bioenergy in the current energy scenario

The strict link between climate change and energy generation is a matter of fact. Achieving a low-carbon future will be challenging and will require a comprehensive portfolio of technologies and policy measures. The world is facing a future where a sustainable use of resources is mandatory. Renewable and carbon-neutral energy sources have to be used to meet the increasing demands of power and heat. Nevertheless, it must be considered that any successful innovation is not only a matter of high-quality scientific research but should require favorable social and economic conditions.

According to the International Energy Agency (IEA), a major opportunity to reduce fossil CO₂ emissions is the transition to alternative sources of materials for energy production, including biomass from forests or agricultural crops [1].

The global renewable and sustainable energy scenario, which has burgeoned in the recent decades and enjoyed rapid growth, has encountered a serious challenge in these last 2 years.

In the following section, a sort of brief world energy outlook is given, with a focus on the resilience issue deriving from an increasing use of biomass and bioenergy.

1.1. The resilience of renewables during Covid-19 outbreak

In 2020, the Coronavirus disease 2019 (Covid-19) pandemic hit the world, driving nearly 100 countries, states and provinces – mainly in Europe, Asia and North America – from February through mid-May 2020 to implement full lockdown measures to contain the spread of the virus [2]. These safety regulations and mobility restrictions disrupted supply chains, reduced the energy consumption and, at the same time, temporarily delayed construction of renewable energy installations – especially onshore wind and solar photovoltaic (PV) systems – in key markets. In April 2020, thanks to these drastic measures, the spread of new infections slowed and plateaued globally, allowing renewables-based construction projects, equipment supplies, policy implementation

(permitting, licensing, auctions) and financing to return to a near-normal levels in many countries, by simultaneously adapting life to the on-going social-distancing rules [3].

Following the first peak, the number of Covid-19 cases reported globally began to increase rapidly again in June as more countries in Africa, Asia, Latin America, and the Middle East became severely affected and testing capacity expanded in North America, Europe, and the Russian Federation (“Russia”). By the end of summer, almost all European countries were recording a strong surge in cases [2]. Although enhanced quarantine rules applied to some workers in these areas, implications for renewable equipment manufacturing and renewable electricity construction activities were instead minimal, as facilities and sites were located mostly outside of heavily populated areas.

As an overall consequence, Covid-19 has impacted the whole world generating risks that actually disproportionately are affecting developing countries and whose effects will last in the months and years ahead. In these times of crisis, access to electric power plays a critical role in guaranteeing essential services to any population. The impact of the pandemic has compromised the noteworthy advances in the energy supply and serious dismissals and discontinuities in the sector were observed in various countries, especially among the poor ones, especially in Africa [4]. An analysis by the International energy agency (IEA) [5] showed that around 580 million people in sub-Saharan Africa lacked access to electricity in 2019 and that the number rose in 2020. 100 million people who had access to electricity, could not afford basic electrical services, forcing households to rely on more polluting and inefficient energy sources. The importance of distributed electricity generation, therefore, has risen even more than in the past. In many countries, however, there is still a gap between the spending required for smart, digital, and flexible energy networks and profits available to grid operators, posing to danger any investment. Specifically, the global economic crisis and the resulting drop in energy consumption had made it harder for many domestic customers and companies to pay for energy services.

Pandemic influenced deeply also personalities and social behavior. A survey of 1210 people revealed that out of the 53.8% who rated the psychological impact of the situation, 16.5% reported depressive symptoms, 28.8% reported moderate to severe anxiety symptoms and 8.1% reported stress levels between moderate and severe [6]. The absence of proper pandemic plans compromised the access to available social and health

resources. Public health has become the utmost priority, while the implications of Covid-19 in the environment is remaining largely underestimated. Covid-19 outbreak increased environmental house food wastage and plastic pollution, especially during lockdown measurements [7].

While, at first glance, in 2020 the epidemic seemed to be indirectly contributing towards the UN 2030 Sustainable Development Goals (SDGs) by increasing overall health and safety of cities by reducing the greenhouse gas emissions (GHG), outdoor air pollution, environmental noise level, it failed considering the poor indoor air quality, increased use-consumption patterns of single-use-plastics (including PPE) [8].

The swift but unequal economic rebound from Covid-induced recession of 2020 has imposed huge strains on elements of the energy system, causing natural gas, coal, and power prices to spike sharply, despite initial prevision which sustained the jeopardize of the long-term oil and gas contract [9] and a first oil price reduction in 2020 [10].

The renewed tightening of measures and the reintroduction of full and partial lockdowns in some European countries at the end of October 2020 had casted additional uncertainty over the expansion of renewable energy in the last quarter of 2020 and 2021 [3].

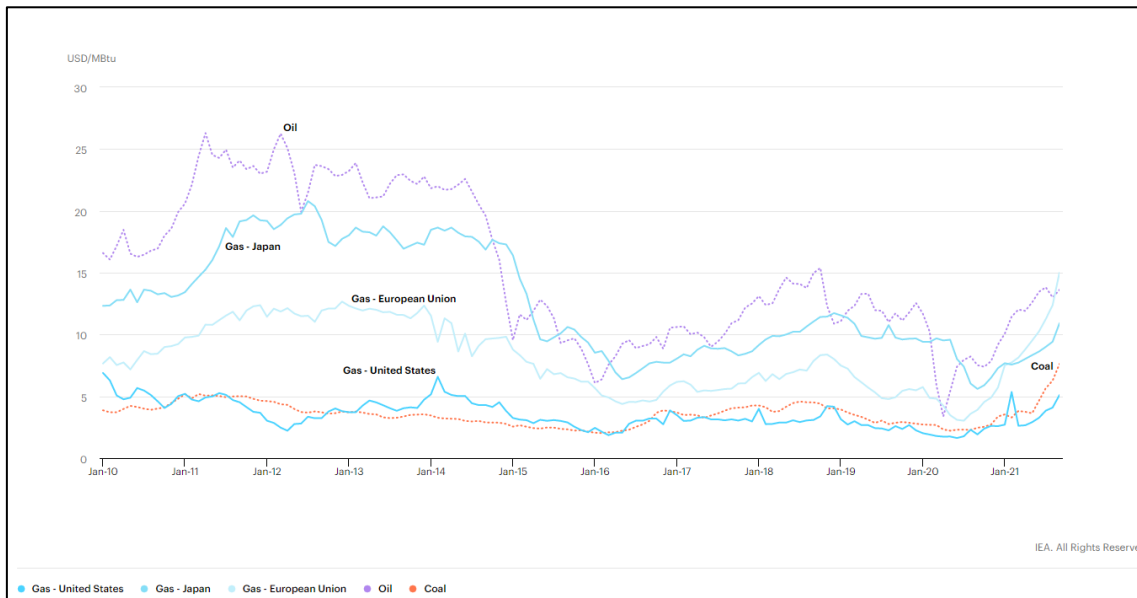


Figure 1. 1: Oil, natural gas and coal prices by region, 2010 – 2021

On 27th December 2020, the so-called “Vaccine day” [11], vaccination in Europe started; massive vaccination and the consequent relaxation on social distancing measures gave hope to the whole world for economic and energy recovers.

Despite all the progress achieved in renewable energy and electric mobility, 2021 was therefore a challenging year, with economies still dealing serious public health problem. As a main issue, there was a significant increase in the price of coal and oil (Figure 1. 2) [12]. Crude oil prices jumped from USD 20/barrel in the aftermath of the pandemic in mid-2020 to USD 70/barrel in mid-2021. Natural gas prices are steadily rising over the world, reaching their highest levels ever in Europe in the second half of 2021 – more than ten-times the record lows reached in June 2020.

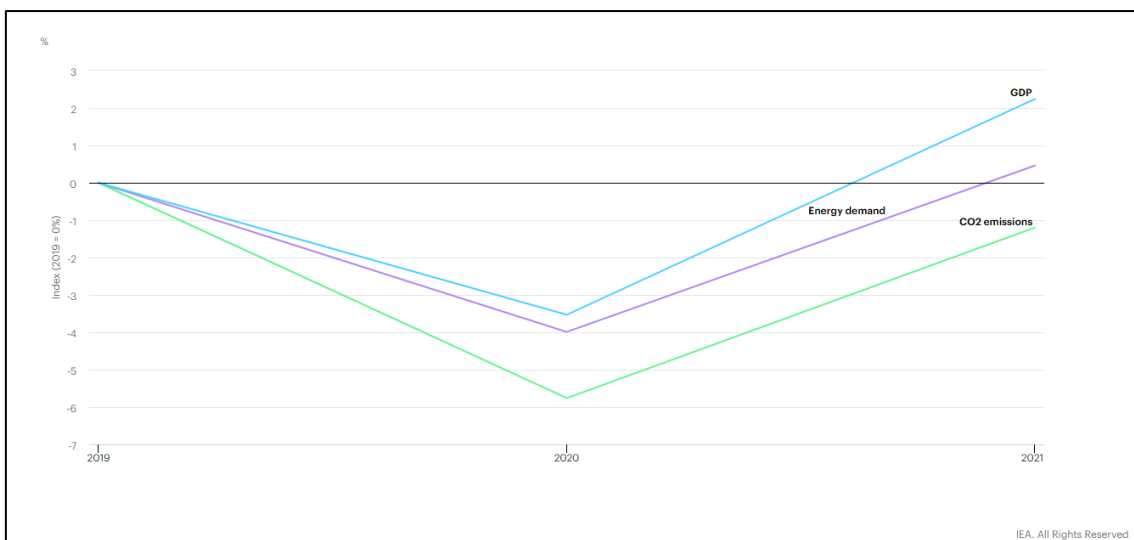


Figure 1. 2: Evolution of global GDP, total primary energy demand and energy related CO2 emissions, relative to 2019 (b) [12]

Coal prices also increased significantly in 2021. High natural gas and coal costs have led to higher power prices in many markets, especially when renewable energy supply was low.

In 2020, global energy demand had decreased by 4%, the biggest drop since World War II and the largest absolute drop ever. Based on quarterly statistics, predictions for 2021 show that once Covid limitations were eased and economies recovered, energy demand rebound by 4.6%, putting global energy use 0.5 % above pre-Covid19 levels in 2021(Figure 1. 2). Taking into account the uncertainty over the duration of the Covid-19 pandemic, its economic and social impacts, and the policy responses, the IEA World

Energy Outlook 2021 [12] identified four different energy case scenarios for the future and their impact over CO₂ emissions, hence on climate change. These are associated by different energy technology and policy pathways and open up a wide range of possible energy prospects (Figure 1. 3):

1. *Net Zero Emissions by 2050 Scenario* (NZE), which sets out a narrow but achievable pathway for the global energy sector to achieve net zero CO₂ emissions by 2050.
2. *Announced Pledges Scenario* (APS), which assumes that all climate commitments made by governments around the world, including Nationally Determined Contributions (NDCs) and longer-term net zero targets, will be met in full and on time.
3. *Stated Policies Scenario* (STEPS), which reflects current policy settings based on a sector-by-sector assessment of the specific policies that are in place, as well as those that have been announced by governments around the world.

According to the APS, clean energy investment and funding will double over the next decade, but this will not be enough to overcome the inertia of the current energy system. In particular, the actions in this scenario fall well short of the emissions reductions required to keep the door open to a Net Zero Emissions by 2050 trajectory in the important period from 2030 to 2050.

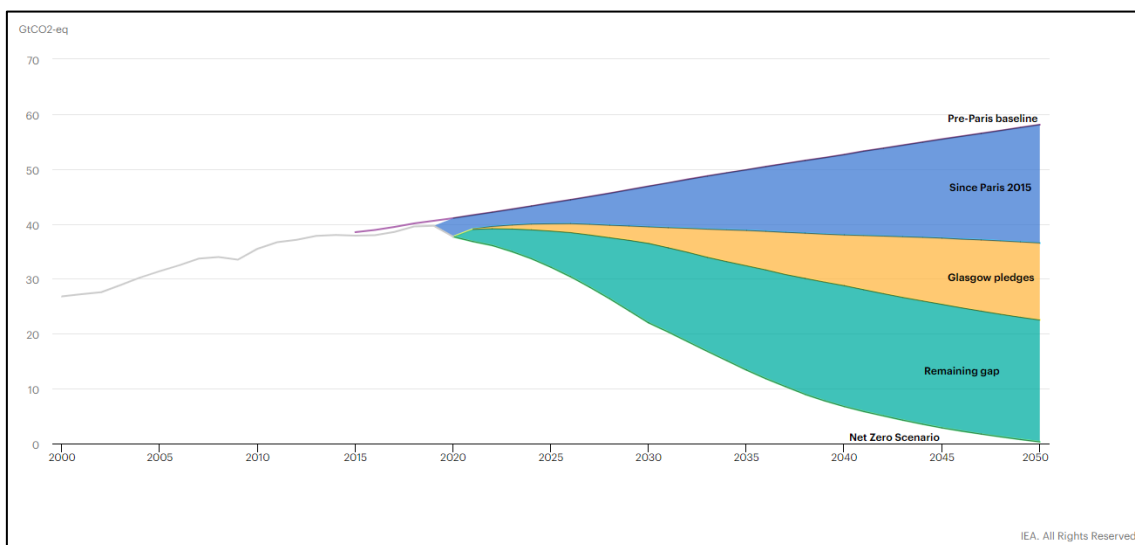


Figure 1. 3: Global emissions by scenario, 2000-2050 [12]

One of the main reasons for this shortfall is that climate pledges, as reflected in the APS, demonstrate significant differences in pledged energy transition speeds between countries. Figure 1. 4 shows the rising share of low emissions fuels in the energy mix. Alternative, low-emission fuels, such as modern bioenergy and hydrogen-based fuels, are becoming crucial in achieving net zero ambitions, particularly in sectors where direct electrification is the most difficult.



Figure 1. 4: The rising share of low emissions fuels in the energy mix [12]

Biofuels were used at just under 2 mb/d in 2020, but volumes doubled in the STEPS by 2030, increased by two-and-a-half times in the APS, and tripled in the NZE. Across all scenarios, the utilization of current forms of solid bioenergy rises by 30-70 % by 2030. Biogas provides clean cooking access to 400 million people in the NZE by 2030, with total biogas demand reaching 5.5 EJ.

To make the 2020s the decade of massive clean energy deployment, it is compulsory to follow the direction from 26th Conference of the Parties to the United Nations Framework Convention on Climate Change (COP26) [13].

COP26 ended on 12th November 2021 with the signing of the Glasgow Climate Pact (the "Glasgow Pact"), which listed the summit accomplishments, by all 197 participants. The Glasgow Pact confirms long-term global goals (including those in the Paris Agreement

of 2015) to keep global average temperature increases to 1.5°C. The pact claims and reinforce the necessity to a rapid, deep, and persistent reduction in global greenhouse gas emissions, including a 45 % decrease in global CO₂ by 2030 compared to 2010 and a net zero reduction in 2050 [14].

The way ahead is difficult and narrow, especially if investment continues to fall short of what is required, but the core message from the IEA World Energy Outlook 2021 [12] is nonetheless a hopeful one. A focus on driving clean electrification, improving efficiency and reducing carbon dioxide emissions accompanied by strategies to unlock capital flows in support of clean energy transitions and ensure reliability and affordability are the key for a sustainable and livable future.

1.1.1 European and Italian bioenergy scenario

The 2009/28/EC (Italian Legislation - Dlgs. 28 of March 3, 2011) gave Europe and, therefore, Italy two binding objectives in terms of exploitation of RES:

- *global objective*: to reach, by 2020, a share of gross final RES share of 20% (17% for Italy);
- *transport sector objective*: to reach, by 2020, a share of gross final consumption of energy in transport sector covered by RES equal to 10% in all European countries.

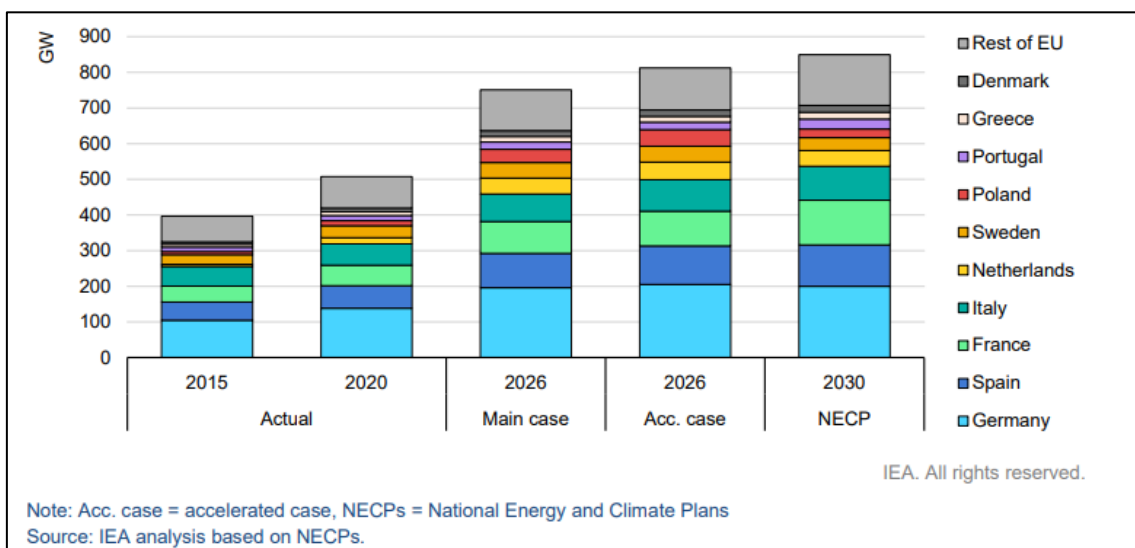
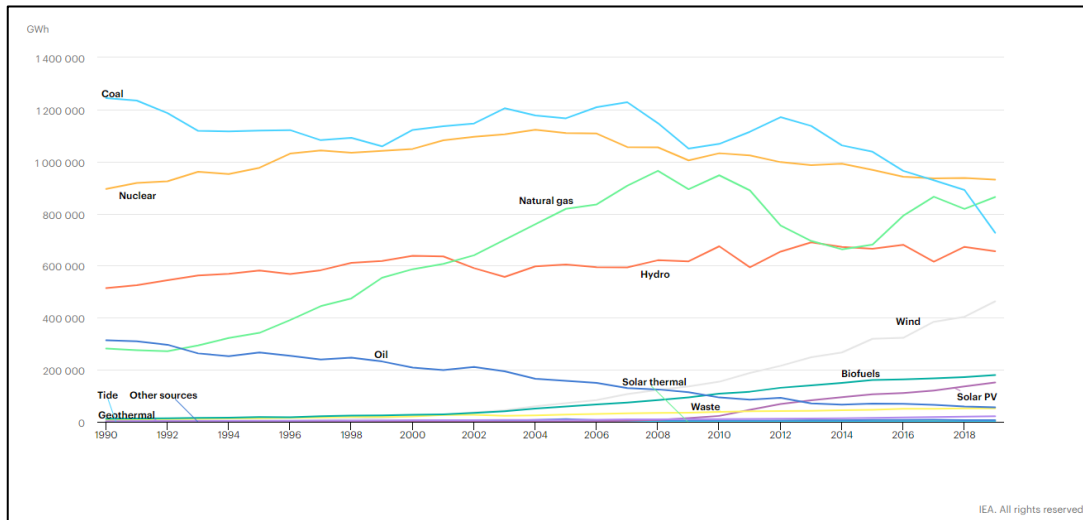


Figure 1. 5: EU member states installed renewable capacity in 2020 and scenario for 2030

In Italy, the National Action Plan [15] for renewable energy, identified the annual trajectories for achieving the two abovementioned objectives and introduced two new ones, more relating to the electrical and thermal sectors. The measures mainly concerned, in addition to the promotion of renewable sources, the simplifying of authorization procedures and the development of international projects.

Nowadays, the lengthy and complicated permitting procedure still remains the principal obstacle to more fast renewable energy development. During the permitting procedure, which can take up to six years, many projects are abandoned. Over 100 GW of renewable energy capacity stalled in the administrative process. A simplification decree was enacted in July 2021, with the goal of streamlining different administrative processes. The new policy impact, however, is still unknown [16].



a)

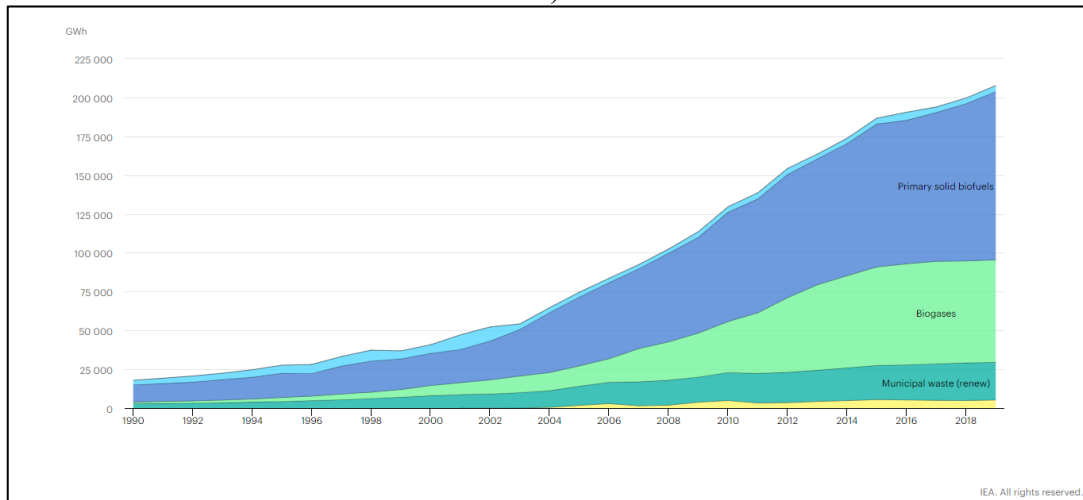


Figure 1. 6: European gross electricity generation by source (a) and biofuels (b) [12]

Fundamental will be the involvement and coordination between the various administrations, as well as dissemination operations.

For countries of the European Union, the 2030 renewable energy targets set out in the NECPs [16] remain a key policy underpinning renewable electricity capacity growth. These goals currently call for renewables to account for at least 32% of final energy consumption in the EU by 2030. Renewable energy capacity in the European Union is predicted to reach 750 GW by 2026, growing at a rate of 40 GW per year on average. In 2020, renewables stand for 500 GW, which are mainly led by Germany, Spain, France and Italy. The 2030 target is likely to be raised. However, EU commission plans of January 2022 to label gas and nuclear as green energy and the consequent discussion between EU states that are pro – France - and against – Italy and Germany – sets uncertainty over the EU taxonomy. EU taxonomy is a tool that investors can use when investing in projects and economic activities that will have a substantial positive impact on the climate and the environment [17], and consequently, on the EU energy mix in the 2022 – 2050 period. Indeed, in 2020, 13 EU Member States with nuclear electricity production generated 683 512 GWh of nuclear electricity, accounting for almost 25% of the EU's total electricity production [18], as shown in Figure 1. 6a.

However, bioenergy seems a viable alternative to the nuclear controversy and to the issue of limited land availability of solar PV and offshore wind. Starting from 2002, Europe saw an increase in bioenergy (liquid, gas and solid) from almost 25 GWh to less than 200 GWh in 2019, with solid biofuels and waste in the leading position (Figure 1. 6b).

Bioenergy accounted for almost 20 GWh of the electricity generation in Italy in 2020 and this number is expected to rise in 2021-2050 scenario, taking into consideration the unused and abandoned areas that could be used to grow energy crops or for afforestation. Forests represent, indeed, almost 15% of the total land use in Europe [19] (in Italy it is equal to almost 30%), which is significant amount that could lead the bioenergy to become more and more important in a net-zero emissions scenario.

In 2020, power demand in the EU decreased due to lower production volumes in the industry while, on the other hand, a rising share of renewable energy sources was registered in various countries [20].

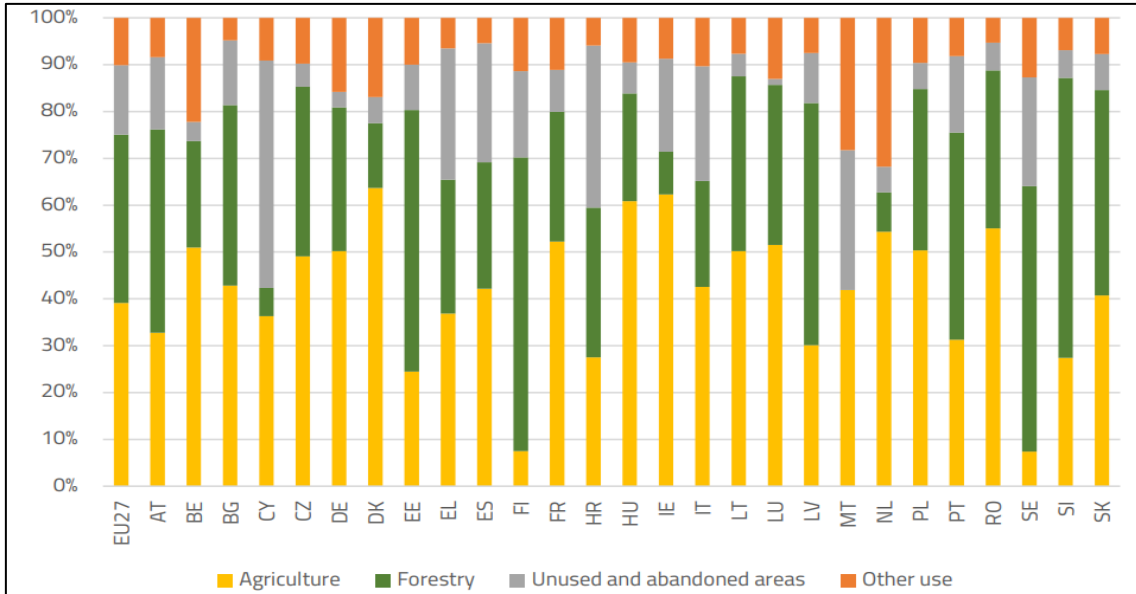


Figure 1. 7: Land use by type in EU27 in 2018 (%) [19]

Figure 1. 8 shows the impact of Covid-19 on electricity consumption in the first part of 2020 for various European countries, such as France, Germany, Italy, Spain and Sweden. This last is selected as it approached Covid-19 fight in a different way than the first ones, without imposing major restriction. Indeed, Sweden was the only country in which electricity consumption remained consistent with that of previous years.

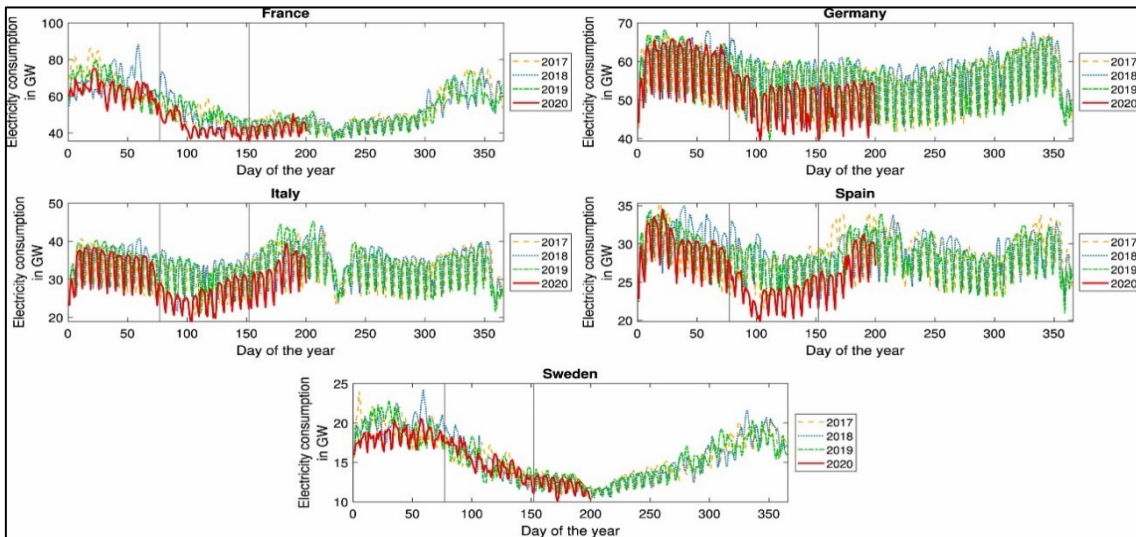
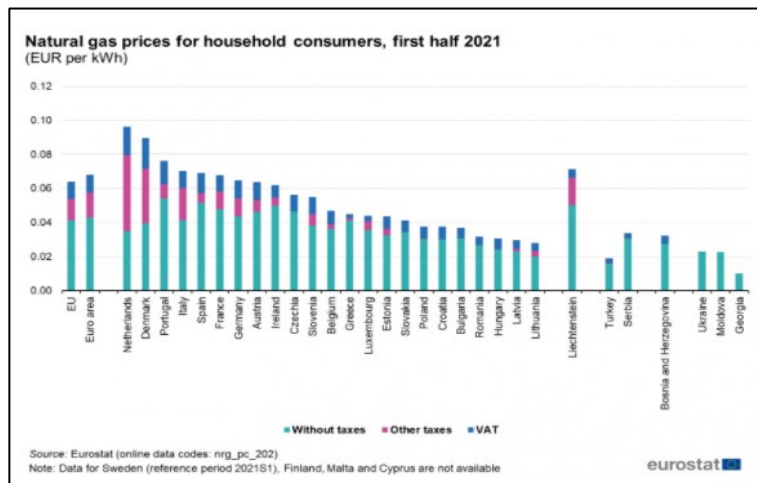


Figure 1. 8: Electricity Consumption in France, Germany, Italy, Spain, and Sweden [20].

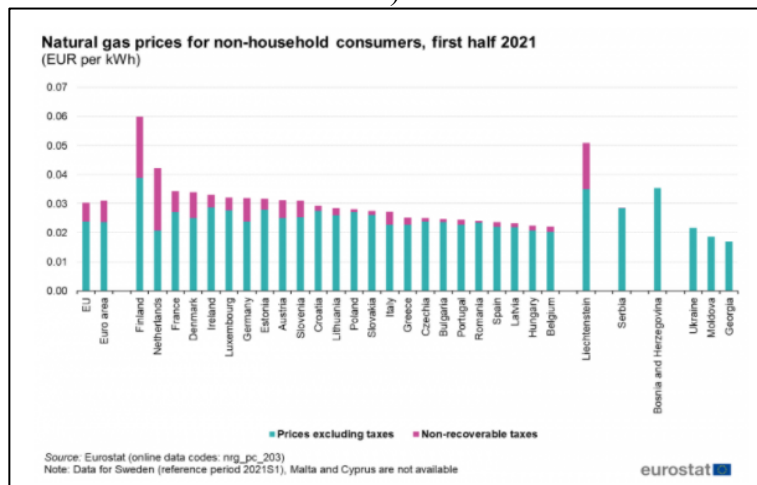
The reduction in the energy demand affected also the electricity prices and CO₂ emissions. In the 2010-2020 period, electricity prices for households in Italy increased

generally, rising from 19.65 eurocents per kilowatt-hour in 2010 to 22.26 eurocents in the first half of 2020 before significantly falling to 21.53 euro cents in the second half of 2020. In 2020, Italy paid some of the highest prices for electricity in the world [21].

This trend continued to increase also in the end of 2021, as shipments of natura gas from crucial Russian pipelines reduced. European gas prices, and therefore electricity, soared to new record highs, both for household and non-household consumers. Gas and electricity in Europe increased by, respectively, 14.4% and 29.8% more than 2020 [22], [23] (Figure 1. 9). These price increases should reduce later in 2022, as Russia announced that the Nord Stream 2 pipeline will start exporting [24].



a)



b)

Figure 1. 9: Natural gas prices for household (a) and non-household (b) consumers in the first half of 2021[25].

In this scenario, to fully recover from Covid-19 emergency and subsequent increased prices, a key factor is flexibility in order to successfully integrate renewable energy sources and maintain or even improve the resilience of future electricity (and, ultimately, energy) systems. The creation of sufficient flexibility has the dual benefit of satisfying energy and climate goals, as well as ensuring that the electricity system plays its part in securing long-term economic growth and contributing to the United Nations SDGs [26]. With massive rescue and economic recovery measures being planned and implemented, governments must act quickly to avoid losing time in the flexibility transition. Indeed, the NextGenerationEU [27], the European plan for recovery, will allow up to 800 billion euro in loans and grants to support European Member States reforms and investments. The goal is to mitigate the economic and social impact of the coronavirus pandemic and make the economies and societies of European countries more sustainable, resilient and prepared for the challenges and opportunities of the ecological and digital transition. Distributed energy source, such as micro-cogeneration and micro-grid will play a strategic role in the future, especially if coupled with RES.

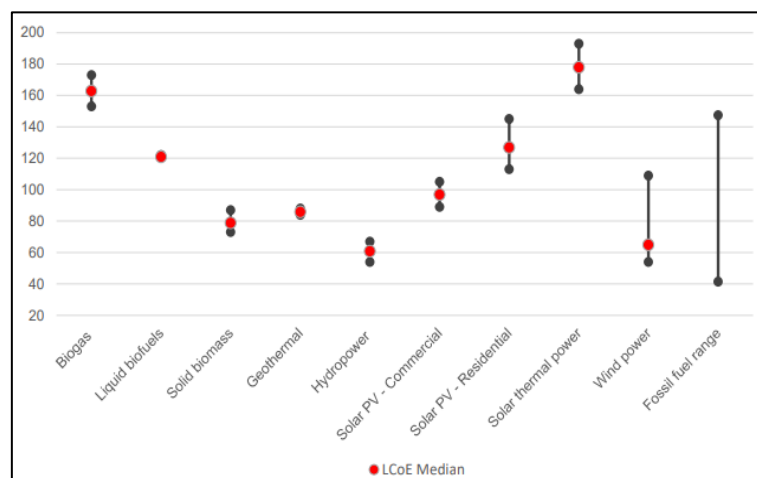


Figure 1. 10: Levelised cost of electricity for different renewable technologies compared with the range cost for fossil fuel technologies (€/MWh) [19].

Bioelectricity is becoming more competitive, as shown in Figure 1. 10. In general, the levelised costs of electricity (LCOE) of bioelectricity technologies are becoming comparable to those of fossil fuels, with the exception of biogas technologies, where cost reductions are expected in future years [19]. It should be emphasized that the cost range for biomass technologies can be rather wide depending on the technologies, feedstocks,

and geographical factors considered. The levelized cost of electricity ignores the potential value of heat in combined heat and power (CHP) plants, which might result in more favorable outcomes.

1.2. Biomass conversion energy processes

As aforementioned, modern bioenergy is currently the largest renewable energy source (RES), with a share in final energy consumption five times greater than wind and solar PV combined [28]. Bioenergy could be described as the energy derived from biomass feedstocks. Biomass definition is a complicated issue. Different legislations provide different definitions of renewable biomass [29]. The recognition of biomass as renewable means that biomass is considered by some to be an infinite feedstock that may be replenished in a short time frame. These, usually, include [30]–[33]:

- residues and co-products from agro-industries and the timber industry;
- crops grown for energy, including food crops such as corn, wheat, sugar and vegetable oils produced from palm, rapeseed and other raw materials;
- animal manure;
- non-food crops such as perennial lignocellulosic plants (e.g. grasses such as miscanthus and trees such as short-rotation willow and eucalyptus) and oil-bearing plants (such as jatropha and camelina).

In the IEA Technology Roadmap [34] the main GBEP Sustainability indicators are defined (Table 1. 1), representing 24 markers, divided into 3 categories, giving a clue on the major issues of biomass exploitation that need to be managed. This, along with the standard ISO 13065: 2015 Sustainability criteria for bioenergy [35], could be an aid for governments to define what is a sustainable biomass.

These indicators can draw attention to potential negative impacts from bioenergy, such as the land usage for energy purposes; however, they can also highlight positive bioenergy environmental, social and economic outcomes. Bioenergy may be integrated with waste management: biomass that was previously deemed waste could be indeed used to be economically profitable.

Over the last few years, the concept of biomass has expanded to include different non-traditional sources, such as algae [36], construction debris [37], municipal solid waste [38], yard waste [39], and food waste [40]. Bioenergy is employed for the stationary production of heat, electricity, as well as its application to the transportation field.

<i>Environmental</i>	<i>Social</i>	<i>Economic</i>
1. Life-cycle GHG emissions	9. Allocation and tenure of land for new bioenergy production	17. Productivity
2. Soil quality	10. Price and supply of a national food basket	18. Net energy balance
3. Harvest levels of wood resources	11. Change in income	19. Gross value added
4. Emissions of non-GHG air pollutants, including air toxics	12. Jobs in the bioenergy sector	20. Change in consumption of fossil fuels and traditional use of biomass
5. Water use and efficiency	13. Change in unpaid time spent by women and children collecting biomass	21. Training and re-qualification of the workforce
6. Water quality	14. Bioenergy used to expand access to modern energy services	22. Energy diversity
7. Biological diversity in the landscape	15. Change in mortality and burden of disease attributable to indoor smoke	23. Infrastructure and logistics for distribution of bioenergy
8. Land use and land use change related to bioenergy feedstock production	16. Incidence of occupational injury, illness and fatalities	24. Capacity and flexibility of use of bioenergy

Table 1. 1 GBEP Sustainability Indicators Environmental Social Economic [34].

For millennia, humans relied on burning gathered organic materials – biomass – to meet their energy demands. Many people in underdeveloped and emerging economies still rely on biomass for their primary energy source; however, this "traditional usage" of biomass is often unsustainable, with inefficient combustion resulting in toxic emissions with major health consequences. Modern technology can convert organic materials into solid, liquid, and gaseous forms, allowing for more efficient energy production. Some argue that biomass has had limited use as an energy source because it is not readily available as a year-round feedstock, is often located at dispersed sites, can be costly to transport, lacks long-term performance data, requires expensive technology to convert to energy, and may not meet quality specifications to reliably fuel electric generators. Because of its broad availability, woody biomass has gotten a lot of interest, but it's only been used for energy production in a few places so far, with the exception of sawmill waste.

Biomass-to-energy conversion technologies must deal with a feedstock that is highly variable in terms of mass and energy density, size, and moisture content. There are two main methods for converting biomass energy into biofuels or biopower: biochemical and thermochemical conversion processes (Figure 1. 11). The former refers to the decomposition of biomass into simple sugars and acids by microbes or enzymes, whereas the latter refers to the thermal degradation of biomass.

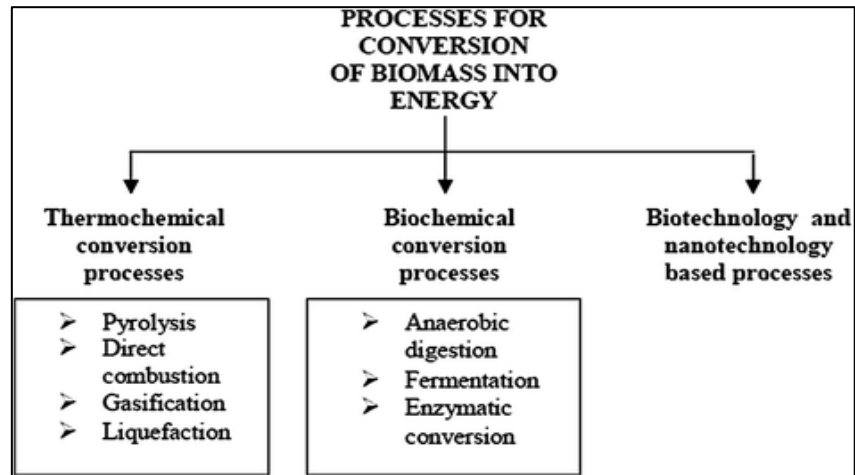


Figure 1. 11: Biomass to energy conversion process [41]

The water content (i.e. moisture) and carbon-nitrogen content ratio (C/N) of the biomass under consideration must be carefully evaluated when choosing between the two conversion methods. If the former is less than 30% but the latter is greater than 30%, thermochemical processes (in which heat exchanges are heavily involved) should be desirable; on the other hand, if moisture is greater than 30% and the C/N ratio is less than 30%, biochemical processes (in which biological species such as bacteria play a role) are the best options.

The following sections report an investigation on main biomass conversion process, with a particular emphasis on gasification processes

1.2.1 Bio-chemical conversion processes

Anaerobic and aerobic digestion are biological processes where organic matter is broken down by some pathogenic bacteria in oxygen-free environments (anaerobic) or in the presence of oxygen (aerobic) in order to produce a methane and carbon dioxide rich

biogas (anaerobic) and carbon dioxide, heat, and a solid digestate in case of aerobic digestion. Biogas can be used for combustion purposes with a lower heating value typically in the range $17 \div 29 \text{ MJ/Nm}^3$; digestate can be brought to landfill or used for soil regeneration in crops [41].

Fermentation is the process of turning sugar-rich biomass plants (such as sugarcane and corn) into alcohol with the use of bacteria, yeasts and enzymes. The same procedure is then extended to incorporate ethanol distillation (ethyl alcohol), that can be used as a fuel enhancer or as a green substitute for gasoline.

1.2.2 Thermochemical conversion processes

Thermochemical conversion methods convert the initial biomass feedstock into more convenient forms of energy carriers, such as syngas, oils, or methanol, under controlled temperature and oxygen conditions. These carriers are either more energy dense, lowering transportation costs, or they have more predictable and convenient combustion characteristics, making them suitable for use in internal combustion engines and gas turbines [41].

In comparison to biochemical conversion methods, the key benefits of thermochemical conversion technologies are that any type of biomass can be used as a feedstock for thermochemical conversion, and the product gases can be transformed into a variety of fuels (H_2 , Fischer-Tropsch diesels, synthetic gasoline) and chemicals (methanol, urea) to replace petroleum-based mixtures. The high cost of cleansing the produced gas from tar and other undesired pollutants such as alkali compounds is one of the key drawbacks. Inefficiencies stems from the high temperatures necessary and the use of products (syngas and bio-oil) as transportation fuels that has yet to be verified.

1.3 Biomass gasification

Biomass gasification is a thermochemical process which produces syngas, a mixture of carbon monoxide (CO), hydrogen (H_2), methane (CH_4), carbon dioxide (CO_2), nitrogen (N_2), and other hydrocarbons in a low-oxygen environment. Gasification is a complicated process that uses the pyrolysis mechanism to produce gaseous intermediates, which, in

the presence of reactive gases like oxygen or steam, transform the bulk of biomass into a gaseous fuel. As previously stated, the process evolves in a sub-stoichiometric amount of oxygen (pure or present in air or steam): the equivalence ratio, as also specified later on, namely the ratio of oxidant given to that necessary for full combustion, is typically in the range 0.27 – 0.4 [42]. Gasification requires the temperature to range from 800 up to 1000 °C. As a result, biomass is altered from one potential fuel source to another one. There are three main considerations for such a change:

- thorough cleaning sulfur and nitrogen contents are removed; syngas does not release their compounds into the atmosphere when burned;
- lower the carbon-to-hydrogen (C/H) mass ratio in the fuel so that it produces less greenhouse gases when combusted;
- syngas is a more versatile form of energy than the initial feedstock and it can be used in internal combustion engine and turbines.

Upstream processing, gasification, and downstream processing are the three primary processes in the gasification process, which are described in the following sections [43].

1.3.1 Upstream processing

Compaction, use of gasifying agents, drying, and pyrolysis are used as upstream processing to prepare biomass for gasification processes.

Size reduction

To be used in the gasifier, biomass feedstock must first be processed through a size reduction process to acquire adequate particle dimensions using mechanical processes (e.g., milling, cutting, and chipping). Furthermore, Tinaut et al. [44] suggest that smaller particles result in higher gas yields, gas energy content (LHV), and carbon conversion efficiency (C_{eff}).

Gasifying agents type

The gasification process mandates the use of gasifying agents such as steam, air, or oxygen; the amount of each of these components determines not only the composition but also the heating value of the producing gas.

Figure 1. 12 depicts the conversion routes of several products in a gasifier using a ternary diagram of carbon, hydrogen, and oxygen. The triangle corners represent pure carbon, oxygen, and hydrogen, i.e. 100% concentration.

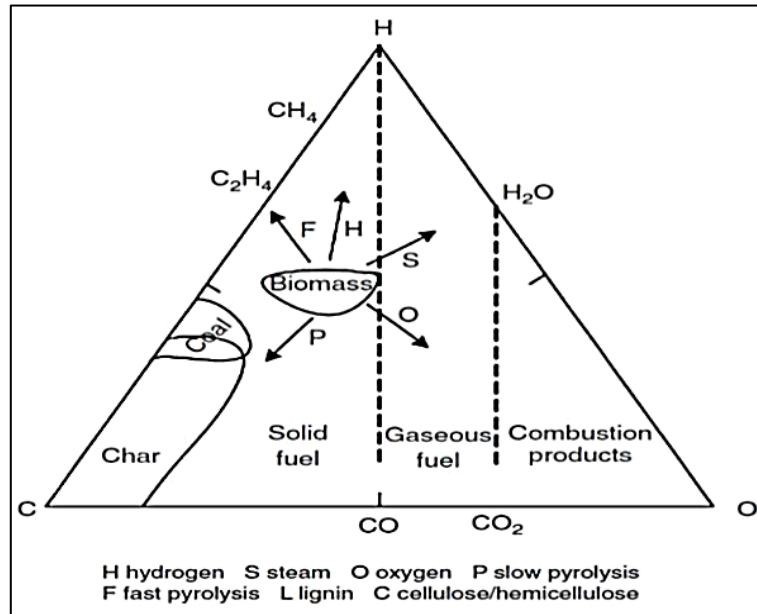


Figure 1. 12: C-H-O ternary diagram of biomass showing the gasification process[43].

If oxygen is used as gasifying agent, pure or diluted in air, the conversion path moves toward the oxygen corner. This shift leads to a reduction of the hydrogen content and an increase in carbon-based compounds such as CO and CO₂ in syngas. Conversely, if steam is used as the gasification agent, the path is towards the hydrogen corner. Thus, the gasification products contain more hydrogen per unit of carbon, resulting in a higher H/C ratio.

Oxygen gasification allows obtaining a syngas with the highest heating (12-28 MJ/Nm³) value followed by steam (10-18 MJ/Nm³) and air gasification (4-7 MJ/Nm³). On the other hand, using of pure oxygen imposes very expensive pre-treatments to extract it from air and for this reason it is not largely used.

Table 1. 2 reports typical syngas and biogas compositions compared to natural gas properties. Syngas derived from air gasification presents the lowest lower heating value, more than a tenth of natural gas one, with greater molar mass and air to fuel ratio. As compared to oxygen gasification, combustible compound of air gasification, sum of H₂, CO and CH₄ is much lower. Stoichiometric air to fuel ratio of biogases and syngas is similar.

Fuel Compos. (%. molar)	Nat. Gas (NG)	<i>BIOM_o</i> (Oxygen Gasification)	<i>BIOM_{AIR}</i> (Air Gasification)	<i>BIOM_{AD}</i> (Anaerobic Digestion)	<i>SW_P</i> (Solid Waste Pyrolysis)
CH ₄	92.00	18.00	0.20	65.00	7.00
C ₂ H ₆	3.70	2.00	--	--	7.00
C ₃ H ₈	1.00	2.00	--	--	7.00
C ₄ H ₁₀	0.25	2.00	--	--	--
N ₂	2.90	8.00	42.50	--	--
H ₂	--	25.00	20.00	--	18.00
CO	--	33.00	25.00	--	61.00
CO ₂	0.15	10.00	12.30	35.00	--
H ₂ O	--	--	--	--	--
Mol. Mass. g/mol	17.34	21.92	23.87	25.83	23.76
<i>LHV</i> . kJ/kg	47182	19198	4860	20183	21697
<i>f_{st}</i>	0.0620	0.1680	0.2057	0.145	0.1530
<i>a_{st}</i>	16.13	5.95	4.86	6.90	6.54
<i>T_{of}</i> . K	2220	2231	--	2126	2300

Table 1. 2: Natural syngas and biogas properties

Drying

Drying is an important step in obtaining syngas with a high heating value. Freshly cut wood has a moisture content of 30 to 60 %, and some biomass has a moisture content of more than 90 % [45]; however, for gasification purposes, a moisture level of 10-20% is required. Drying is a high-energy process: vaporizing one kilogram of moisture in biomass requires 2260 kJ of non-recoverable energy from the gasifier; if energy is not given by waste heat recovery circuit, this could reduce the gasification efficiency.

Pyrolysis

Pyrolysis is the first step of gasification and, as said, it is a thermal decomposition (400-800 °C) occurring in the absence of oxygen. This process causes devolatilization of some

compounds, namely the generation of a complex mixture of gases (CO, CO₂, CH₄, H₂O), condensable vapours and vegetable carbon.

Pyrolysis	Operating condition	Liquid	Char	Gas
Fast	Temperature: 500 °C Residence time: 1s	75%	12%	13%
Intermediate	Temperature: 500 °C Residence time: 10-20 s	50%	20%	30%
Slow	Temperature: 400 °C Residence time: very long	30%	35%	35%

Table 1. 3: Pyrolytic products in fast, intermediate and slow pyrolysis [43]

Depending on the thermal environment and the final temperature, pyrolysis will yield mainly biochar at low temperatures, less than 450 °C, and mainly gases at high temperatures, greater than 700 °C. The yield of pyrolytic products is influenced also by the velocity of the reaction involved, as seen in Table 1. 3.

1.3.2 Gasification reactions

The gasification, a quite complex process from a chemical perspective, is characterized by a significant number of reactions, which are summarized in Table 1. 4. When raw material particles are loaded into a gasifier, they begin to heat up and remove their moisture content, resulting in devolatilization. Three macro-products are produced as a result of this process: gas, tar, and char. CO, CO₂, H₂, CH₄, H₂O, and light hydrocarbons are commonly found in devolatilization gas. At the gasification temperature (more than 400 °C), tar refers to a wide spectrum of organic compounds that are in the vapour state at ambient temperature but liquid at gasification temperature. The solid residue is known as char. Both homogeneous and heterogeneous oxidation reactions occur when oxygen comes into contact with combustible volatile matter and char.

Through Table 1. 4 reactions *R7*, *R10*, *R12*, and *R13*, volatiles and tar combustion yield carbon dioxide and water. Through the heterogeneous reaction *R2*, char is oxidized. This produces both CO and CO₂, the proportions of which are determined by temperature, oxygen availability, and ash content. The combustion processes supply heat for the solid material's drying and devolatilization, as well as the other reactions in the process. Steam reforming of tar and CH₄ occurs in the gaseous phase (reactions *R8* and *R11* in Table 1.

4) and generates CO and H₂. Thermal cracking R₉ allows tar to breakdown at high temperatures, releasing lighter gases such as CO, CO₂, H₂, and CH₄. The water gas-shift reaction R₆ also has an impact on CO, water, carbon dioxide, and hydrogen concentrations. Due to heterogeneous interactions with carbon dioxide R₃, steam R₄, and hydrogen, char can be transformed through R₅ into a gas at high temperatures (greater than 600 °C) to CO, hydrogen, and CH₄ [43], [46].

<i>Physical process and chemical formula</i>	<i>Reaction</i>	<i>Chemical gasification process</i>
$\text{Biomass}_{\text{wet}} \rightarrow \text{Biomass}_{\text{dry}} + \text{H}_2\text{O}_{\text{vapour}}$	R _M	<i>Drying</i>
$\text{Biomass}_{\text{dry}} \rightarrow \text{Char} + \text{Volatiles (Gas + Tar)}$	R ₁	<i>Devolatilization</i>
$\text{C} + \phi\text{O}_{2(\text{g})} \rightarrow 2(1-\phi)\text{CO} + (2\phi-1)\text{CO}_2$	<i>(Oxidation) R₂</i>	<i>Heterogeneous Reactions</i>
$\text{C} + \text{CO}_{2(\text{g})} \rightarrow 2\text{CO}$	<i>(Boudard reaction) R₃</i>	
$\text{C} + \text{H}_2\text{O}_{(\text{g})} \rightarrow \text{CO} + \text{H}_2$	<i>(Water/gas heterogeneous reaction) R₄</i>	
$\text{C} + 2\text{H}_{2(\text{g})} \rightarrow \text{CH}_4$	<i>(Methane formation reaction) R₅</i>	
$\text{CO} + \text{H}_2\text{O}_{(\text{g})} \leftrightarrow \text{CO}_2 + \text{H}_2$	<i>(Water/gas shift reaction or Water/gas homogeneous reaction) R₆</i>	<i>Homogeneous Reactions</i>
$\text{TAR} + \text{O}_2 \rightarrow \text{CO} + \text{H}_2\text{O}$	R ₇	
$\text{TAR} + \text{H}_2\text{O} \rightarrow \text{CO} + \text{H}_2\text{O}$	<i>(Tar reforming) R₈</i>	
$\text{TAR} \rightarrow \text{CO} + \text{CO}_2 + \text{CH}_4 + \text{H}_2$	<i>(Tar cracking) R₉</i>	
$\text{CH}_4 + 1.5\text{O}_2 \rightarrow \text{CO} + 2\text{H}_2\text{O}$	R ₁₀	
$\text{CH}_4 + \text{H}_2\text{O} \leftrightarrow \text{CO} + 3\text{H}_2$	<i>(Methane reforming reaction) R₁₁</i>	
$\text{CO} + 0.5\text{O}_2 \rightarrow \text{CO}_2$	R ₁₂	
$\text{H}_2 + 0.5\text{O}_2 \rightarrow \text{H}_2\text{O}$	R ₁₃	

Table 1. 4: Reactions occurring in gasification [43], [46].

The gasification process is strongly influenced by the gasifying agent mass flow rate and by temperature: in the case of air, higher air mass flow rates result in higher temperatures, hence higher biomass conversion rates and higher quality of the fuel. An excess degree of combustion, however, results in a decreased energy content of the produced gas because a part of the biomass energy is spent during combustion. Besides, higher air mass flow rates shorten the residence time of the feedstock in the reactor which may decrease the extent of biomass conversion. An indirect measure of the air mass flow rate is done by the equivalence ratio (ER), calculated through the following equation (1.1):

$$ER = \frac{\frac{\dot{m}_{air}}{\dot{m}_{biom}}}{\left(\frac{\dot{m}_{air}}{\dot{m}_{biom}}\right)_{stochiom}} \quad (1.1)$$

If ER is equal to zero, there is no oxidant in the system, while ER equal to one represents stoichiometric combustion.

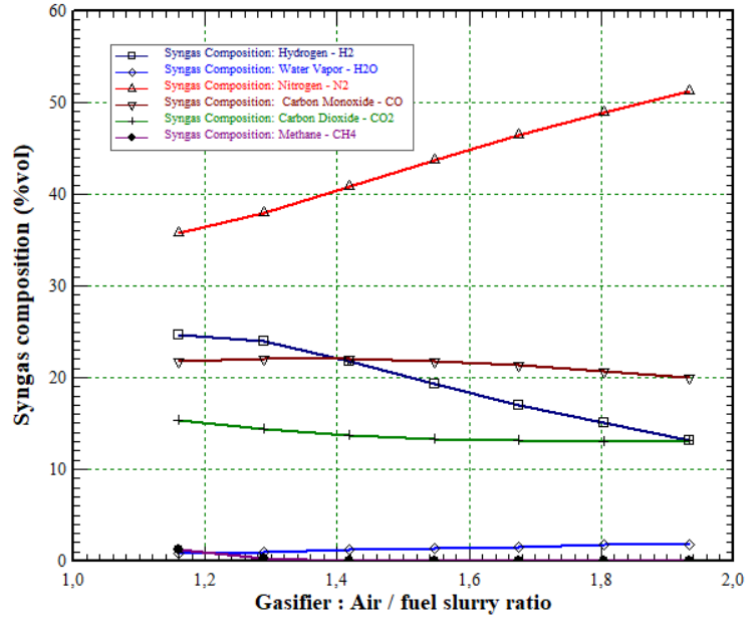
Typical ER values of gasification, as mentioned before, range between 0.27 and 0.4. Figure 1. 13a shows the effect of the numerator of equation (1.1) on syngas composition. The air-fuel ratio is related to the gasification of woodchip in which the air-fuel ratio ranges between 1.4 and 1.6.

For lower values of ER (<0.27) or an air-fuel ratio lower than 1.4, several problems occur, including incomplete gasification, excessive char formation and higher tar production. Moreover, for low amounts of the gasifying agent, the process could evolve as it was a pyrolysis process. Conversely, a too high ER (>0.4) or for an air-fuel ratio higher than 1.6 translates into an excessive formation of products of complete combustion, CO₂ and H₂O, and of N₂, reducing consequently the syngas calorific value [42]. An ER value between 0.3 and 0.4 [42], [47], which corresponds to an air-fuel ratio of about 1.5 for chipped ligneous biomass represents the right compromise solution between an acceptable calorific value of the syngas and a not excessive formation of tar and other heavy hydrocarbons.

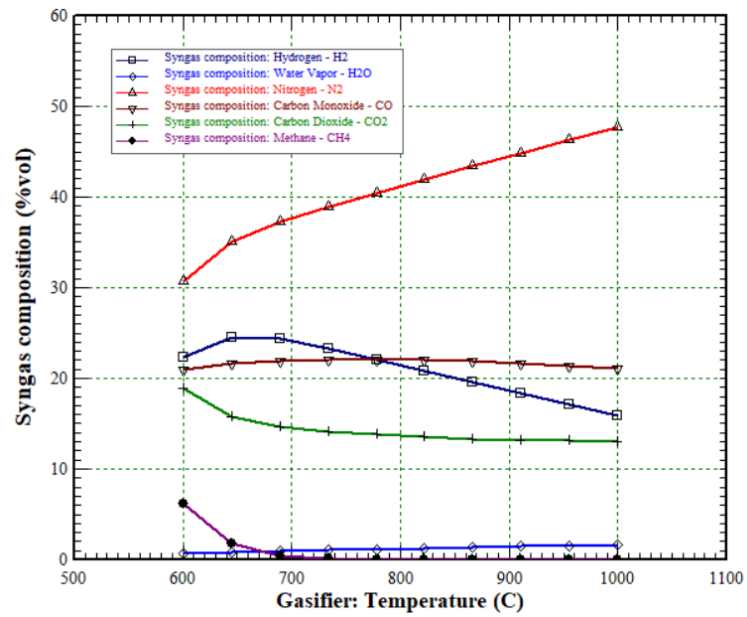
The same happens when increasing the gasification temperature (Figure 1. 13b). A high gasification temperature (>900 °C) translates into a high yield of CO₂ and N₂ compounds, as reaction shift to complete combustion; low temperature (<700 °C) has the effect of shifting the reaction to pyrolysis resulting into a high H₂ yield.

The amounts and proportions of H₂, CO, CO₂, and CH₄ in syngas are determined by temperature and partial pressures of reactants because the reactions from *R3* to *R6* of Table 1. 4 run simultaneously. The endothermic nature of the H₂ generation reactions (*R6* and *R11*) leads to an increase in H₂ content and a decrease in CH₄ concentration when the temperature rises above 750–800 °C. Both steam reforming *R11* and the Boudouard *R3* reactions dominate at temperatures over 850 – 900 °C, resulting in a CO content rise. A

high temperature also encourages destruction and reforming of tar decreasing tar content in syngas.



a)



b)

Figure 1. 13: Effect of the air/fuel actual ratio (a) and gasification temperature (b) on the syngas composition (%vol)

1.3.3 Gasifier type

A crucial impact on the syngas conversion efficiency is made by the gasifier shape and geometrical characteristics. Gasifiers are classified primarily by the manner of gas–solid contact [48], as shown in the Figure 1. 14: fixed or moving bed, fluidized bed and entrained flow.

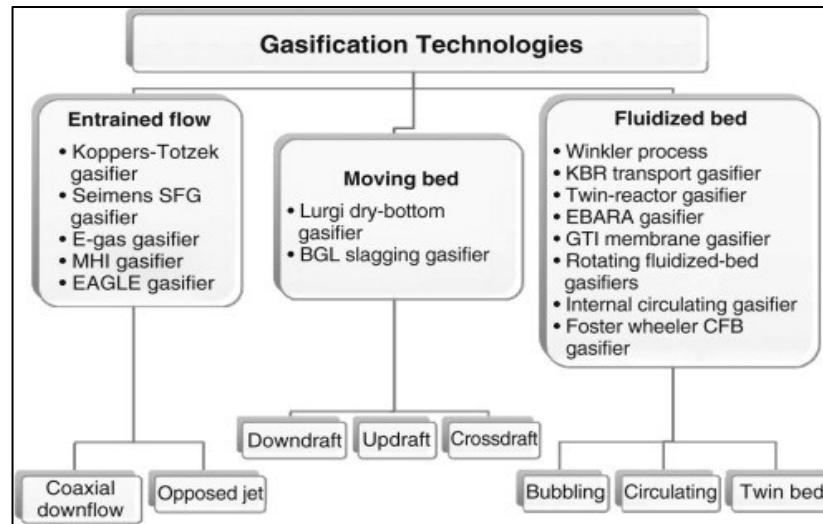


Figure 1. 14: Gasification technologies classifications [48]

In this thesis, the focus is set only on Fixed-Bed/Moving-Bed Gasifiers. In these types of gasifiers, fuel is supported on a grate (hence its name) and because the fuel travels down in the gasifier like a plug, this type is also known as moving bed. One of the main advantages of fixed bed gasifiers is that they can be built cheaply and even in small sizes. As a result, several small-scale moving-bed biomass gasifiers are in use all over the world.

Within the moving (stationary) bed, both mixing and heat transfer are poor, making impossible a uniform distribution of fuel, temperature, and gas composition across the cross-section of the gasifier. As a result, fuels that are prone to agglomeration may form agglomerates during the gasification process. Therefore, fixed-bed gasifiers are not very effective for biomass fuels or coal with a high caking index in large-capacity units.

There are three main types of fixed- or moving-bed gasifier: updraft, downdraft and crossdraft, whose characteristics and main differences are reported in Table 1. 5.

Fuel (wood)	Updraft	Downdraft	Crossdraft
Gas/solid interaction	Countercurrent	Co-current	Co-current
Point of Release of syngas	Top	Bottom	Side
Moisture wet basis (%)	60 max	25 max	10-20
Dry-ash basis (%)	25 max	6 max	0.5-1.0
Ash melting temperature (°C)	>1000	>1250	-
Size (mm)	5-100	20-100	5-20
Application range (MW)	2-30	1-2	-
Gas exit temperature (°C)	200-400	700	1250
Tar (g/Nm ³)	30-150	0.015-3.0	0.01-0.1
Gas LHV (MJ/Nm ³)	5-6	4.5-5.0	4.0-4.5
Hot-gas efficiency (%)	90-95	85-90	75-90

Table 1. 5: Characteristics of Fixed-Bed Gasifier [48]

1.3.4 Syngas cleaning processes

The produced gas derived from biomass gasification of solid fuels normally contains CO₂, H₂, CO, CH₄, H₂O, N₂ and in addition to the main components organic and inorganic impurities as well as solid matter.

Into detail, the following components can be found:

- Tar (a complex mixture of condensable hydrocarbons).
- Sulfide compounds (mainly H₂S and COS, if the biomass used includes sulfur).
- Nitrogen compounds (NH₃, HCN, NO_x, generated from the N contained in the biomass).
- Halogen compounds (ex. HCl).
- Particulate matter.
- Alkali and metallic compounds.

Syngas contains these pollutants in a variety of quantities. As a result, it must be adequately cooled and cleaned for productive and reliable engine operations as well as biofuel generation. Tar is the most difficult contaminant to separate, and its removal is one of the most complex technical issues awaiting the commercialization of gasification technology. The tar condenses on the walls of downstream equipment such as heat exchangers, combustion engines, reactors, and fuel cells if it is not removed [49]. The goal of cooling syngas is to reduce its temperature (from 500-800 °C to 600-100 °C) so that dry particle filtration can be done with *ceramic* or *cloth filters*.

Gas coolers or *water coolers* can accomplish this task; the first is fairly straightforward because the cooler uses natural or forced circulation to reduce the temperature without requiring any additional energy. Water coolers, on the other hand, are more efficient but more difficult to be operated: *scrubbers* and *heat exchangers* are two types of water coolers in which the condensed tar contents come into direct touch with the circulated water.

Typically, the gas cleaning session is designed and manufactured to meet the specific needs of the following energy production system.

To summarize, the most prevalent technologies for smaller applications (below 20 kW) for removing various contaminants are listed in Table 1. 6.

Syngas cleaning technology	Operating Temperature (°C)	Particulate matter reduction (%)	Tar reduction (%)
Sand bed filter	10-20	70-99	50-97
Wash Tower	50-60	60-98	10-25
Venturi scrubber	n.a	n.a	50-90
Rotational atomizer	<100	95 ± 99	n.a
Wet electrostatic precipitator	40-50	>99	0-60
Fabric Filter	130	70-95	0-50
Rotational particle separator	130	85-90	30-70
Fixed bed tar adsorber	80	n.d.	50
Catalytic tar cracker	900	n.d.	>95

Table 1. 6: efficiency of particulates and tar removals of syngas cleaning technologies. [50], [51]

1.4 Cogeneration systems based on gasifier-ICE technology

Cogeneration or CHP generation is defined as the simultaneous generation of two different forms of useful energy (usually electricity and heat) from a single primary source; this leads to great improvements of global efficiency with respect to the separate production of electricity and heat, as shown in Figure 1. 15.

By no means, cogeneration offers the following benefits, compared to conventional methods [53]:

- increased global efficiency of energy conversion;

- lower emissions to the environment, in particular of CO₂;
- large cost savings, offering additional competitiveness for industrial and commercial users and affordable heat for domestic users;
- an opportunity to move towards more decentralized forms of electricity generation, where the plant is designed to meet the needs of local consumers, lowering transmission and transportation losses;
- improved local and general security of supply; local generation reduce the risk of consumers left without electricity and/or heating supplies.

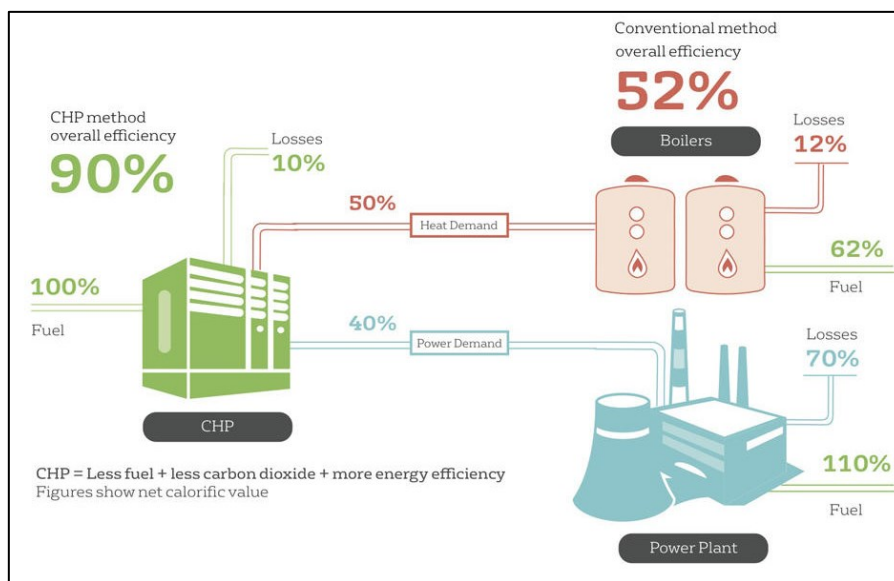


Figure 1. 15: Cogeneration overall efficiency as compared to conventional methods [52]

Calculated on a European scale, cogeneration in 2020 still accounted for only a fraction of installed capacity, roughly 12 %, according to COGEN Europe [53] (Table 1. 7). The structure of the electricity sector in key markets like Germany and France, where centralized nuclear and coal-fired power units are the common, is, of course, a major factor.

The EU Commission has however strongly recognized the benefits of cogeneration, which already in 2013 was highlighted as the single largest measure to decrease greenhouse gas emissions in the EU.

	CHP electricity generation, TWh	Share of CHP in total gross electricity generation	total CHP Electrical capacity, GW	total CHP Heat capacity, GW	Primary energy savings (PJ)
European Union 27 countries (from 2020)	344,55	11,7%	133,60	280,48	1.264,56
European Union 28 countries (2013-2020)	366,86	11,2%	138,31	288,22	1.344,42

Table 1. 7: Share of installed CHP system in Europe [53]

The European Commission (EC) published on 28th September 2021 its Recommendation and Guidelines on Energy Efficiency First (EE1st) [54] that will give an important tool for Member States to follow an integrated approach to energy systems with the goal of facilitating and fostering the implementation of the Clean Energy Package. CHP is mentioned as a key facilitator of the EE1st goals as it should be considered as a valuable alternative in cost-benefit analyses. However, medium- and large-scale CHP presents still some substantial barriers to their development, such as the large up front capital investment and running costs, the requirement of space for the CHP "energy center" and the high heat losses to the ground.

According to the Energy Efficiency Directive micro-CHP definition [55], micro-CHP can be used to fulfill a variety of heat needs in individual homes, public buildings, and commercial structures. Key benefits of micro-CHP are:

1. *More power to the consumer.* Micro-CHP has the potential to turn European consumers into energy prosumers, placing them at the center of the future energy system and providing them more influence over their energy expenditures.
2. *Renewable energy balance.* Micro-CHP helps to balance renewables, which can be intermittent and variable, by generating power close to where it is needed.
3. *Reduction of carbon emissions.* Micro-CHP is a highly efficient method of generating heat and electricity from gas. Because of the use of renewable fuels and/or biogas injection into gas networks, it saves carbon dioxide now and can save much more in the future.
4. *Energy stability.* Micro-CHP helps to sustain the power system by reducing the amount of total primary energy required.

5. *Creating and preserving jobs.*

Reduced primary energy consumption reduces greenhouse gas (GHG) emissions, and the micro-CHP unit operation allows for grid integration of fluctuating renewables. The COGEN Europe report about micro-CHP technology [55] stated that the European policy should inspire confidence in key market players to team up in the spirit of technological leadership and commercial innovation and develop a range of offerings to consumers and installers alike, empowering energy prosumers and creating green jobs. Micro-CHP systems are adjustable solutions that can generate power during peak load hours (or anytime the grid requires it), replacing the existent diesel generators with a low-efficiency, high-CO₂-intensity electricity mix.

The above reasonings can also be applied to biomass powered systems, especially by exploiting energy production through thermochemical process.

Technologies for CHP production based on biomass gasification have been intensively developed in recent years, according to the mentioned opportunity to transition towards more decentralized and flexible power system. It is a matter of fact that the conventional energy system is under a sharp pressure for a substantial change in its configuration, namely for an upgrade of its infrastructures and the development of more flexible management strategies. Electrical generation employing syngas technologies can be used in both the developed and developing countries to reduce greenhouse gas emissions and to provide electricity in rural locations where biomass is normally available.

In terms of CHP plant architecture, different are the available technologies that could be coupled with gasification to obtain heat and power: spark ignition (SI) and compression ignition (diesel) internal combustion engines (ICEs), gas turbines, Stirling engines and fuel cells. In particular, the following general considerations can be made with reference to the above mentioned technologies for energy conversion:

- *Internal combustion engine:* CHPs powered by wood chips or other biomass fuels have electrical efficiencies of 13 % to 25 % and overall efficiencies of 60 % to 74 % in micro-scale plants. The electrical efficiency, which is 12.5-28 %, and the total efficiency, which can reach 96 %, are slightly greater at the small-scale level. Electrical efficiencies in large-scale facilities range from 25 to 30 %, with total efficiencies hovering around 81 %.

- *Stirling engines*: electrical efficiencies for micro-CHP Stirling-based units are 9.2-33 %, with total efficiencies ranging from 65 to 92 %. At small-scale, Stirling engines obtain 12 - 35 % of electrical efficiency and 85÷90 % of total efficiency. Stirling engines do not have large-scale data because they are only appropriate for micro and small-scale applications.
- *Steam and gas turbine*: electrical efficiencies in micro-scale systems decrease to 68%; on the large-scale, electrical efficiencies can be as low as 15%, rising to 44% as output power rises, although total efficiencies are always around 60%.
- *Fuel cell*: wide range of applications with high electrical efficiency (50÷65%) at all ranges.

Among these, the conventional ICE is a mature and flexible technology, with an efficiency that is higher than other prime movers and especially with a short start-up time. Moreover, syngas can be used in ICEs that were designed to run on gasoline or diesel fuels to decrease or eliminate the need for petroleum-based fuels. Because of the gap in stoichiometric air-fuel ratios of producer gas – typically 1.4-1.6 [42] – and gasoline or diesel fuel, correspondingly to 14.7 and 14.5, engine power derating when operating with syngas is expected. Normally it is of the order of 15 to 40%, which is less than the difference in energy contents between producer gas and petroleum fuel would indicate. Indeed, biomass based syngas has on average a lower heating value of 4 – 6 MJ/kg, a tenth of gasoline energy contents [56], so making this fuel viable for ICEs application.

The capacity to run on syngas fuel alone rather than on dual fuel mode required in Compression Ignition (CI) engines operating with syngas, thereby eliminating the requirement for any petroleum fuel, is a significant advantage of syngas use in SI engines as opposed to or diesel engines [57].

Higher compression ratios are feasible with syngas-fueled SI engines due to the high antiknock characteristics (low flame speed) of CO and CH₄ as well as diluents N₂ and CO₂ in syngas compared to those possible with gasoline-fueled SI engines [58].

The following classification in terms of technologies and size from bioenergy CHP systems based on gasifiers coupled with ICEs is assumed [59]:

- *micro-scale plants* (5÷50kWel) and *small-scale plants* (50kWel÷1MWel) – downdraft, updraft and fluidized bed gasifiers coupled with ICE;
- *medium-scale plants* (1MWel÷2MWel) – only downdraft and fluidized bed gasifiers coupled with ICE;
- *large-scale plants* (>2MWel) – pressurized fluidized bed gasification coupled with ICE.

The IEA Bioenergy Task 33 status report on thermal gasification of biomass and waste [60] monitors each 3 years the status of thermal gasification worldwide. For small scale applications, there are nowadays more than 1500 thermal gasification facilities worldwide.

In Europe, most operational facilities are located mainly in Germany and Austria, manufactured by Burkhardt GmbH, Spanner Re² GmbH, Urbas Maschinenfabrik GmbH, Syncraft, Lipro, Volter and Glock Ökoenergie GmbH, which are reported in Table 1. 8. Cogeneration in the Northern Part of Europe, such as Norway, Netherlands and Sweden, usually involves the co-firing with coal. The majority of European companies reported in Table 1. 8 employ a fixed bed reactor coupled with a reciprocating engine. Cogeneration units in Europe are usually in the range of micro-scale plants: only Spanner Re² allows the possibility to upscale its gasifier + ICE technology into the range of large-scale plants with an electrical power of 4 MWe. In this last case, co-firing is required.

Company Name	Countries	Technology	Biomass	Pel [kW]	Pth [kW]	Ref.
Burkhardt	Germany	Patented reactor + ICE	Wood pellets	50 to 210	100 to 310	[61]
Spanner Re ²	Germany	Fixed bed gasifier + ICE	Woodchips	30 to 4000	79.5 to 1200	[62]
Urbas	Austria	Fixed bed gasifier+ ICE	Woodchips	150	310	[63]
Syncraft	Austria	Floating bed reactor + ICE	Woodchips	200 to 1000	328 to 1404	[64]
Lipro	Germany	Fixed bed reactor + ICE	Woodchips	30 to 50	60 to 100	[65]
Volter	Switzerland	Downdraft reactor + ICE	Dry clean Woodchips	40	100	[66]
Glock Ökoenergie GmbH	Austria	Imbert gasifier + ICE	Woodchips	18 to 50	44 to 110	[67]

Table 1. 8: Main application of biomass CHP in Europe

The spread of biomass cogeneration plants in Italy is noteworthy, even if not evenly throughout the nation, as shown in Figure 1. 16. The majority of these systems are small and medium scale CHP, based on commercial fixed bed gasifier technology, particularly downdraft configurations.

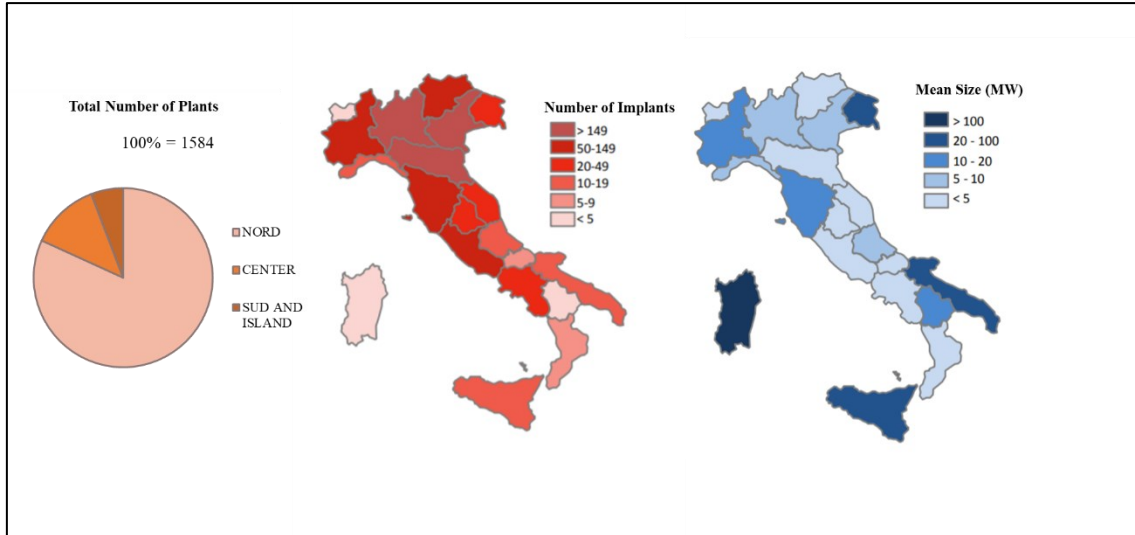


Figure 1. 16: Distribution of CHP systems in Italy [72]

Worth mentioning as example for Italian m-CHP system based on biomass gasification – ICE syngas combustion are SyngaSmart 35 [68], BioSyn 50 [69], CHiP 50 [70] (50kWe) and the CMD ECO20x [71] (20 kWe), whose main characteristics are reported in Table 1. 9. The CMD ECO20x unit is the system considered within the present thesis work.

Name	Company	Technology	Biomass	Pel [kW]	Pth [kW]	Ref.
SyngaSmart 35	RESET	Downdraft + ICE	Woodchips and briquettes from wood	35	66	[68]
BioSyn 50	BioSyn	Double Fire + ICE	Woodchips	49	150	[69]
CHiP50	ESPE	Downdraft + ICE	Woodchips	49	110	[70]
ECO20x	CMD	Downdraft + ICE	Woodchips and briquettes from wood	20	40	[71]

Table 1. 9: Main application of biomass m-CHP in Italy

References Chapter 1

- [1] F. Kraxner, E. Nordström, P. Havlik, M. Gusti, A. Mosnier, S. Frank, H. Valin and S. Fritz, “Global bioenergy scenarios – Future forest development, land-use implications, and trade-offs,” *Biomass Bioenergy*, vol. 57, pp. 86–96, Oct. 2013, doi: 10.1016/j.biombioe.2013.02.003.
- [2] AJMC Staff, “A Timeline of COVID-19 Developments in 2020,” Jan. 01, 2021. <https://www.ajmc.com/view/a-timeline-of-covid19-developments-in-2020>. (Accessed: Jan. 12, 2022).
- [3] “Renewables 2020 - Analysis and forecast to 2025,” p. 172, 2020.
- [4] H. Eroğlu, “Effects of Covid-19 outbreak on environment and renewable energy sector,” *Environ. Dev. Sustain.*, vol. 23, no. 4, pp. 4782–4790, Apr. 2021, doi: 10.1007/s10668-020-00837-4.
- [5] “World Energy Outlook 2020 – Analysis,” *IEA*. <https://www.iea.org/reports/world-energy-outlook-2020> (accessed Sep. 29, 2021).
- [6] M. A. Bhuiyan, J. An, A. Mikhaylov, N. Moiseev, and M. S. S. Danish, “Renewable energy deployment and covid-19 measures for sustainable development,” *Sustainability*, vol. 13, no. 8, p. 4418, 2021, <https://doi.org/10.3390/su13084418>.
- [7] S. Jribi, H. Ben Ismail, D. Doggui, and H. Debbabi, “COVID-19 virus outbreak lockdown: What impacts on household food wastage?,” *Environ. Dev. Sustain.*, vol. 22, no. 5, pp. 3939–3955, Jun. 2020, doi: 10.1007/s10668-020-00740-y.
- [8] Silva, A. L. P., Prata, J. C., Walker, T. R., Duarte, A. C., Ouyang, W., Barcelò, D., & Rocha-Santos, T., Increased plastic pollution due to COVID-19 pandemic: Challenges and recommendations. *Chemical Engineering Journal*, vol. 405, 126683, 2021, doi: <https://doi.org/10.1016/j.cej.2020.126683>.
- [9] S. E. Hosseini, “An outlook on the global development of renewable and sustainable energy at the time of COVID-19,” *Energy Res. Soc. Sci.*, vol. 68, p. 101633, Oct. 2020, doi: 10.1016/j.erss.2020.101633.
- [10] “Crude Oil Price Forecast: 2021, 2022 and Long Term to 2050 - knoema.com,” *Knoema*. <https://knoema.com//infographics/yxtpab/crude-oil-price-forecast-2021-2022-and-long-term-to-2050> (accessed Sep. 27, 2021).
- [11] EpiCentro, “Piano nazionale di vaccinazione COVID-19.” <https://www.epicentro.iss.it/vaccini/covid-19-piano-vaccinazione> (accessed Jan. 11, 2022).
- [12] “World Energy Outlook 2021 – Analysis,” *IEA*. <https://www.iea.org/reports/world-energy-outlook-2021> (accessed Jan. 11, 2022).
- [13] “COP26 Outcomes,” *UN Climate Change Conference (COP26) at the SEC – Glasgow 2021*. <https://ukcop26.org/the-conference/cop26-outcomes/> (accessed Jan. 11, 2022).
- [14] “The Results of COP26,” *The National Law Review*. <https://www.natlawreview.com/article/results-cop26> (accessed Jan. 11, 2022).
- [15] PAN, “PAN DETTAGLIO.pdf.”, https://www.gse.it/Dati-e-Scenari_site/monitoraggiofer_site/area-documentale_site/Documenti%20Piano%20di%20Azione%20Nazionale/PAN%20DETTAGLIO.pdf. (Accessed: Oct. 05, 2021)
- [16] “Renewables 2021 - Analysis and forecast to 2026,” p. 175, 2021.
- [17] EU Taxonomy, “EU Taxonomy: Commission begins expert consultations,” *European Commission - European Commission*. https://ec.europa.eu/commission/presscorner/detail/en/IP_22_2 (accessed Jan. 11, 2022).
- [18] “25% of EU electricity production from nuclear sources - Products Eurostat News - Eurostat.” <https://ec.europa.eu/eurostat/web/products-eurostat-news/-/ddn-20220111-1> (accessed Jan. 11, 2022).
- [20] Bioenergy Europe, “Statistical Report 2021.” <https://bioenergyeurope.org/article.html/303> (accessed Jan. 11, 2022).

- [20] S. Halbrügge, P. Schott, M. Weibelzahl, H. U. Buhl, G. Fridgen, and M. Schöpf, “How did the German and other European electricity systems react to the COVID-19 pandemic?,” *Appl. Energy*, vol. 285, p. 116370, Mar. 2021, doi: 10.1016/j.apenergy.2020.116370.
- [22] Statista, “Italy: household electricity prices 2020,” *Statista*. <https://www.statista.com/statistics/418092/electricity-prices-for-households-in-italy/> (accessed Oct. 05, 2021).
- [23] T. Wilson and N. Hume, “European gas prices shoot to new high as energy crunch worsens,” *Financial Times*, Dec. 21, 2021. <https://www.ft.com/content/a0bc7996-ab5d-465b-aab4-90472e088af7> (Accessed: Jan. 11, 2022).
- [23] M. Ballarin, “Rincaro bollette, tra geopolitica, interventi governativi e sprechi,” *Il Sole 24 ORE*, Jan. 06, 2022. <https://www.ilssole24ore.com/art/rincaro-bollette-geopolitica-interventi-governativi-e-sprechi-AE6jNd6> (accessed Jan. 11, 2022).
- [24] iPolitics P. on Jan 4 and 2022 11:36am, “Net Zero: EU proposes classifying gas and nuclear power as green,” *iPolitics*, Jan. 04, 2022. <https://ipolitics.ca/2022/01/04/net-zero-eu-proposes-classifying-gas-and-nuclear-power-as-green/> (accessed Jan. 11, 2022).
- [26] Eurostat, “Data - Energy - Eurostat.” <https://ec.europa.eu/eurostat/web/energy/data> (accessed Oct. 12, 2021).
- [26] R. J. Heffron, M.-F. Körner, M. Schöpf, J. Wagner, and M. Weibelzahl, “The role of flexibility in the light of the COVID-19 pandemic and beyond: Contributing to a sustainable and resilient energy future in Europe,” *Renew. Sustain. Energy Rev.*, vol. 140, p. 110743, Apr. 2021, doi: 10.1016/j.rser.2021.110743.
- [27] “Piano per la ripresa dell’Europa,” *Commissione europea - European Commission*. https://ec.europa.eu/info/strategy/recovery-plan-europe_it (accessed Oct. 05, 2021).
- [29] P. Frankl, “IEA Technology Roadmap: The need to scale up sustainable bioenergy,” p. 13, 2017, https://ec.europa.eu/energy/sites/default/files/documents/5_paolo_frankl.pdf. (Accessed: Sept. 14, 2021)
- [30] K. Braemort, “Biomass: Comparison of Definitions in Legislation,” p. 20. <https://sgp.fas.org/crs/misc/R40529.pdf> (Accessed: Sept. 30, 2021)
- [30] N. G. Society, “biomass energy,” *National Geographic Society*, Nov. 19, 2012. <http://www.nationalgeographic.org/encyclopedia/biomass-energy/> (accessed Sep. 27, 2021).
- [31] D. O. Hall, “Biomass energy,” *Energy Policy*, vol. 19, no. 8, pp. 711–737, Oct. 1991, doi: 10.1016/0301-4215(91)90042-M.
- [32] P. Lauri, P. Havlík, G. Kindermann, N. Forsell, H. Böttcher, and M. Obersteiner, “Woody biomass energy potential in 2050,” *Energy Policy*, vol. 66, pp. 19–31, Mar. 2014, doi: 10.1016/j.enpol.2013.11.033.
- [33] N. S. Bentsen, C. Felby, and B. J. Thorsen, “Agricultural residue production and potentials for energy and materials services,” *Prog. Energy Combust. Sci.*, vol. 40, pp. 59–73, Feb. 2014, doi: 10.1016/j.pecs.2013.09.003.
- [35] “Technology Roadmap: Delivering Sustainable Bioenergy,” p. 94, 2017. <https://www.ieabioenergy.com/blog/publications/technology-roadmap-delivering-sustainable-bioenergy/> (Accessed: Sept. 30, 2021)
- [36] A. Demirbas, “Use of algae as biofuel sources,” *Energy Convers. Manag.*, vol. 51, no. 12, pp. 2738–2749, Dec. 2010, doi: 10.1016/j.enconman.2010.06.010.
- [37] S. Akhtari, K. T. Malladi, T. Sowlati, and F. Mirza, “Incorporating risk in multi-criteria decision making: The case study of biofuel production from construction and demolition wood waste,” *Resour. Conserv. Recycl.*, vol. 167, p. 105233, Apr. 2021, doi: 10.1016/j.resconrec.2020.105233.
- [38] A. Z. Shi, L. P. Koh, and H. T. W. Tan, “The biofuel potential of municipal solid waste,” *GCB Bioenergy*, vol. 1, no. 5, pp. 317–320, 2009, doi: 10.1111/j.1757-1707.2009.01024.x.

- [39] Y. Shi, Y. Ge, J. Chang, H. Shao, and Y. Tang, “Garden waste biomass for renewable and sustainable energy production in China: Potential, challenges and development,” *Renew. Sustain. Energy Rev.*, vol. 22, pp. 432–437, Jun. 2013, doi: 10.1016/j.rser.2013.02.003.
- [40] H. M. Breunig, L. Jin, A. Robinson, and C. D. Scown, “Bioenergy Potential from Food Waste in California,” *Environ. Sci. Technol.*, vol. 51, no. 3, pp. 1120–1128, Feb. 2017, doi: 10.1021/acs.est.6b04591.
- [41] M. Pande and A. N. Bhaskarwar, “Biomass Conversion to Energy,” in *Biomass Conversion: The Interface of Biotechnology, Chemistry and Materials Science*, C. Baskar, S. Baskar, and R. S. Dhillon, Eds. Berlin, Heidelberg: Springer, 2012, pp. 1–90. doi: 10.1007/978-3-642-28418-2_1.
- [42] M. Costa, V. Rocco, C. Caputo, D. Cirillo, G. Di Blasio, M. La Villetta, G. Martoriello and R. Tuccillo, “Model based optimization of the control strategy of a gasifier coupled with a spark ignition engine in a biomass powered cogeneration system”, *Appl. Therm. Eng.*, vol. 160, p. 114083, Sep. 2019, doi: 10.1016/j.applthermaleng.2019.114083.
- [43] G. Martoriello, *Modelling and optimization of an integrated micro-cogeneration system based on biomass gasification*. University of Naples “Federico II”: Master’s Thesis, 2018.
- [44] F. V. Tinaut, A. Melgar, J. F. Pérez, and A. Horrillo, “Effect of biomass particle size and air superficial velocity on the gasification process in a downdraft fixed bed gasifier. An experimental and modelling study,” *Fuel Process. Technol.*, vol. 89, no. 11, pp. 1076–1089, Nov. 2008, doi: 10.1016/j.fuproc.2008.04.010.
- [45] M. La Villetta, “Biomass-to-Energy systems: techno-economic aspects and modelling approaches for characterization and improvement of performance,” 2017. doi: 10.13140/RG.2.2.23662.77120/1.
- [46] C. Higman and M. van der Burgt, “Chapter 5 - Gasification Processes,” in *Gasification (Second Edition)*, C. Higman and M. van der Burgt, Eds. Burlington: Gulf Professional Publishing, 2008, pp. 91–191. doi: 10.1016/B978-0-7506-8528-3.00005-5.
- [47] C. Caputo, *Modelling approach and technical solutions for characterization and performance improvement of real biomass powered m-CHP system*, PhD Thesis. University of Rome “Tor Vergata,” 2020.
- [48] P. Basu, “Chapter 6 - Design of Biomass Gasifiers,” in *Biomass Gasification and Pyrolysis*, P. Basu, Ed. Boston: Academic Press, 2010, pp. 167–228. doi: 10.1016/B978-0-12-374988-8.00006-4.
- [49] Harb Rita, Rivera-Tinoco Rodrigo, Nemer Maroun, Zeghondy Barbar, and Bouallou Chakib, “Process Simulation of Tar Removal from Gasification Producer Gas,” *Chem. Eng. Trans.*, vol. 81, pp. 931–936, Aug. 2020, doi: 10.3303/CET2081156.
- [50] S. Anis and Z. A. Zainal, “Tar reduction in biomass producer gas via mechanical, catalytic and thermal methods: A review,” *Renew. Sustain. Energy Rev.*, vol. 15, no. 5, pp. 2355–2377, Jun. 2011, doi: 10.1016/j.rser.2011.02.018.
- [51] S. D. Sharma *et al.*, “A critical review of syngas cleaning technologies — fundamental limitations and practical problems,” *Powder Technol.*, vol. 180, no. 1, pp. 115–121, Jan. 2008, doi: 10.1016/j.powtec.2007.03.023.
- [52] “How does cogeneration work?,” *Veolia CHP*. <https://www.veolia.co.uk/combined-heat-power/learn-about-chp/how-does-cogeneration-work> (accessed Oct. 12, 2021).
- [53] “Cogeneration - COGEN Europe - The European Association for the Promotion of Cogeneration.” <https://www.cogeneurope.eu/> (accessed Oct. 12, 2021).
- [54] “Recommendation and guidelines on Energy Efficiency First: from principles to practice,” *European Commission - European Commission*. https://ec.europa.eu/info/events/recommendation-energy-efficiency-first-principles-practice-2021-sep-28_en (accessed Oct. 12, 2021).
- [55] “micro-CHP study_merged.pdf,” http://www.cogeneurope.eu/medialibrary/2015/05/19/d6648069/micro-CHP%20study_merged.pdf (Accessed Oct. 20, 2021)

- [56] M. Costa, G. Di Blasio, M. V. Prati, M. A. Costagliola, D. Cirillo, M. La Villetta, C. Caputo and G. Martoriello, "Multi-objective optimization of a syngas powered reciprocating engine equipping a combined heat and power unit," *Appl. Energy*, vol. 275, p. 115418, Oct. 2020, doi: 10.1016/j.apenergy.2020.115418.
- [57] R. Bates and K. Dölle, "Syngas Use in Internal Combustion Engines - A Review," *Adv. Res.*, vol. 10, no. 1, pp. 1–8, Jan. 2017, doi: 10.9734/AIR/2017/32896.
- [58] J. D. Martínez, K. Mahkamov, R. V. Andrade, and E. E. S. Lora, "Syngas production in downdraft biomass gasifiers and its application using internal combustion engines," *Renew. Energy*, vol. 38, no. 1, pp. 1–9, 2012, <https://doi.org/10.1016/j.renene.2011.07.035>.
- [59] T. Warren, R. Poulter, and R. Parfitt, "Converting biomass to electricity on a farm-sized scale using downdraft gasification and a spark-ignition engine," *Bioresour. Technol.*, vol. 52, no. 1, pp. 95–98, 1995, [https://doi.org/10.1016/0960-8524\(95\)00022-7](https://doi.org/10.1016/0960-8524(95)00022-7).
- [60] IEA Bioenergy Task 33, "Status report on thermal gasification of biomass and waste | Bioenergy." <https://www.ieabioenergy.com/blog/publications/new-publication-2019-status-report-on-thermal-gasification-of-biomass-and-waste/> (accessed Jan. 17, 2022).
- [61] "Burkhardt biomass power plants – CHP with wood pellets | Burkhardt Energy." <https://burkhardt-gruppe.de/en/power-engineering/heat-and-power-from-wood/> (accessed Jan. 17, 2022).
- [62] S. Seidel, "Spanner Re² - Biomass power plant - overview," *Spanner Re²*. <https://www.holz-kraft.com/en/products/biomass-chp.html> (accessed Jan. 17, 2022).
- [64] Urbas, "URBAS Energietechnik und Stahlbau," *URBAS*. <https://www.urbas.at/> (accessed Jan. 17, 2022).
- [65] Syncraft, "SYNCRAFT® - Das Holzkraftwerk," *Syncraft*. <https://www.syncraft.at/> (accessed Jan. 17, 2022).
- [66] Lipro, "LiPRO Energy - renewable decentral regional," *LiPRO Energy*. <https://lipro-energy.de/en/> (accessed Jan. 17, 2022).
- [67] "Volter - Power from wood," *Volter*. <https://volter.fi/technology/> (accessed Jan. 17, 2022).
- [68] Glock, "Glock ecoenergy." <https://www.glock-ecoenergy.com/en/technology> (accessed Jan. 17, 2022).
- [69] SyngaSmart, "SyngaSmart - Containerized biomass CHP," *SYNGASMART*. <https://www.syngasmart.com/syngasmart/> (accessed Nov. 05, 2021).
- [70] Biosyn, "TECNOLOGIA - BIOSYN." <http://www.biosyn.it/tecnologia-.html> (accessed Nov. 05, 2021).
- [71] Espe, "espe_1024_folder_biomassa_web.pdf." Accessed: Nov. 05, 2021. [Online]. Available: http://www.rinnovaenergia.eu/uploads/files/espe_1024_folder_biomassa_web.pdf
- [72] CMD, "ECO20X - Pirogassificatore | CMD Engine - a Loncin Company - Costruzioni Motori Diesel - Progettazione e realizzazione di motori e parti meccaniche per l'industria automobilistica, la nautica, l'aviazione, sistemi di microgenerazione - Produzione motori marini diesel, elettrici e ibridi, general aviation, aerei ultraleggeri, pirogassificatore CHP - FNM, Avio, ECO20X - Basilicata, Atella, Campania, Caserta." <http://www.cmdengine.com/eco20-pirogassificatore/> (accessed Nov. 05, 2021).
- [73] MISE, "IT-RELAZIONE-ANNUALE-COGENERAZIONE-2018.pdf.", <https://www.mise.gov.it/images/stories/documenti/IT-RELAZIONE-ANNUALE-COGENERAZIONE-2018.pdf> (Accessed: Nov. 05, 2021).

CHAPTER 2

The case study: a micro-cogeneration system based on biomass gasification

2.1 The CMD ECO20x system

The here considered biomass powered cogeneration unit is the CMD ECO20x, a system of the micro-scale of power for biomass-powered combined heat and power generation designed by the Italian company Costruzioni Motori Diesel S.p.A. (CMD), whose headquarter is in San Nicola La Strada (Caserta, Italy).

A downdraft gasifier, syngas cleaning systems, a spark ignition internal combustion engine (ICE), an electric generator, and a waste heat recovery system are the main components of the system. The CMD ECO20x m-CHP unit complies with European Conformity (CE) and it is certified according to UNI EN ISO 9001/2017 - ISO 14001 - ISO 9100: 2009 - ISO / TS 16949: 2002 [1].

Figure 2. 1 shows the CMD ECO20x with its characteristic container, while Figure 2. 2 shows its process workflow.



¹Courtesy of Stefano Esposito, Senior Designer at CMD S.p.A., R&D Energy Dpt.

Figure 2. 1: CMD ECO20x m-CHP system (b) [1]

The CMD ECO20x produces electrical and thermal energy by thermo-chemically converting organic material (biomass) at high temperatures in a low amount of oxygen and then burning the produced syngas in a reciprocating engine. Before secondary

conversion into a 4.3L GM Vortec V-6 engine, gasification creates an exceptionally clean syngas, which is further purified through a process of cleaning, chilling, and filtration. The alternator MeccAlte, mod. ECP 028, is linked to the engine crankshaft and can produce up to 20 kW_e of electric power. Proper heat exchangers along the engine cooling circuit and the exhaust gases line are used to recover waste heat for up to 40 kW_{th}.

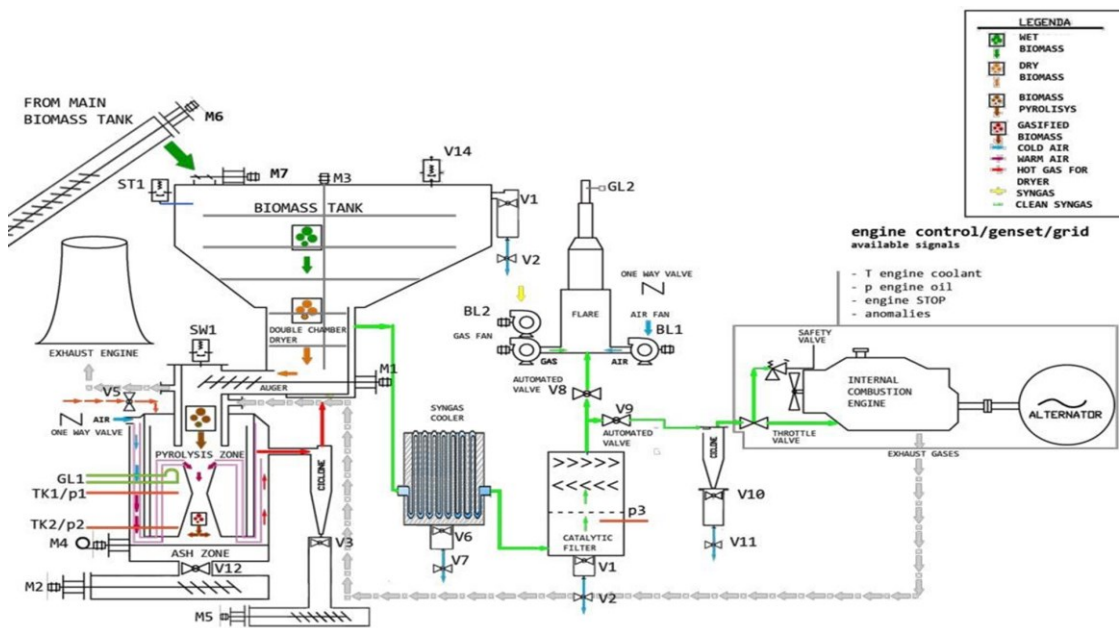


Figure 2. 2: CMD ECO 20x process workflow

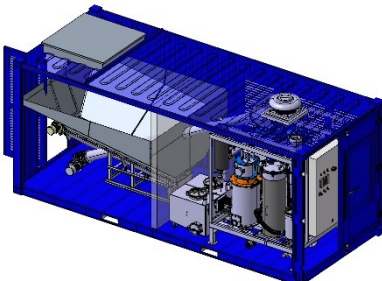
The CMD ECO20x was designed to process wooden biomass of G30 size (30mm) with 20% humidity, classified A1+ or A1 according to UNI EN ISO 17225-4 [2]. Indeed, UNI EN ISO 17225-4 [2] classifies biomass in 4 classes (A1+, A1, A2, B1) based on source, moisture content (M), ash content (A), Lower heating value (LHV) Bulkness (B). Table 2. 1 reports the biomass classification according to the mentioned legislation.

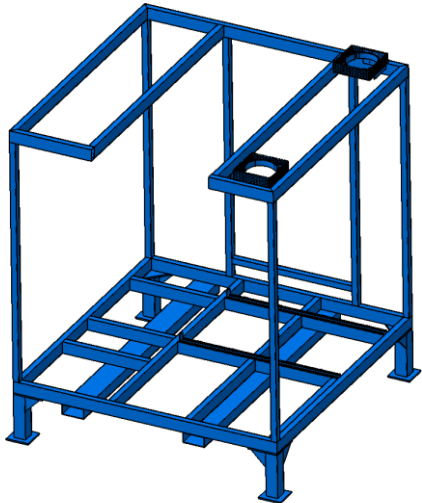
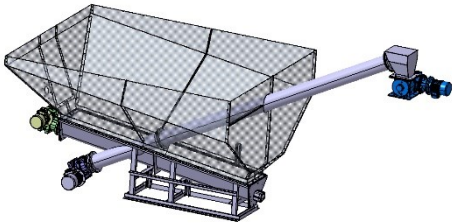
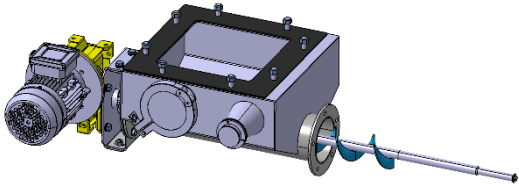
The cogeneration system is fully automated: from the downloading of the biomass into the hopper, the start-up and operation of the gasification reaction, the starting of the generator up to either the realization of the connection with the electric national grid or the direct energy use on site. The control system manages the ash discharge, the condensed matter, the biochar and can act with suitable strategies (until the system shuts down) in the case of possible failures, thanks to the presence of proper sensors and automatic safety alarms.

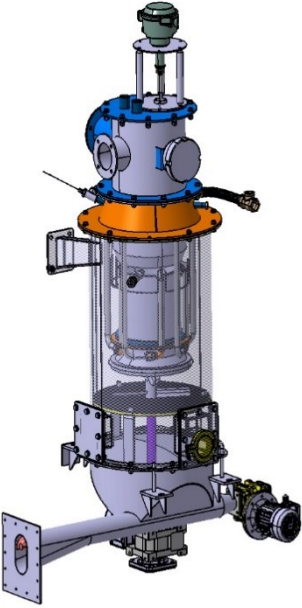
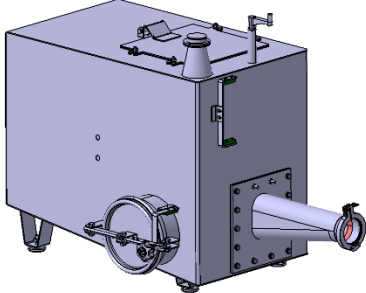
	A1+	A1	A2	B1
Source	Whole trees without roots Logs Forestry Residues Untreated Wood residues	Whole trees without roots Logs Forestry Residues Untreated Wood residues	Whole trees without roots Logs Forestry Residues Untreated Wood residues	Virgin biomass Untreated Wood residues
M (% on weight)	< 10	<25	<35	-
A (% on weight)	<1.0	<1.0	<1.5	<3.0
LHV (MJ/kg)	>16	-	-	-
B (kg/ m³)	>150	>150	>150	-

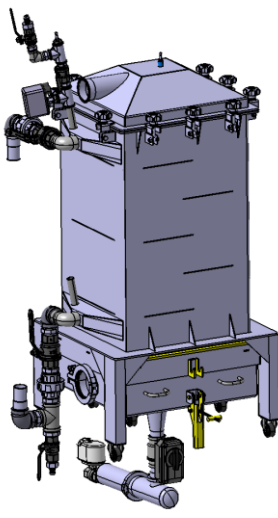
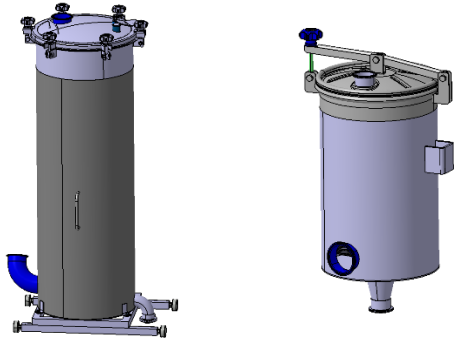
Table 2. 1: Biomass Classification based on UNI EN ISO 17225-4 [2]

The CMD ECO20x unit is equipped with a web service interface that allows analysis of the stored data, monitoring of the device parameters, and system management via a simple internet connection, without the need of an operator present in the operative environment. The most important components of CMD ECO 20x are briefly described in Table 2. 2, while Table 2. 3 reports the engine technical features.

Name	Figures	Description
External Container¹		<p>The container is an equipment used for transport, 9 meters long. Could be soundproofed.</p>

<p><i>Chassis</i>¹</p>		<p>The chassis consists of a box built with galvanized welded profiles, through a continuous wire arc welding and reinforced steel, able to support the static and dynamic loads during the system operation</p>
<p><i>Hopper</i>¹</p>		<p>The hopper is made with high resistance stainless steel, with a maximum capacity of 0.5 m³ and has the shape of an inverted truncated cone. It allows biomass to be delivered in the plenum chamber placed below.</p>
<p><i>Plenum Chamber</i>¹</p>		<p>The plenum chamber is characterized by a double sealed chamber, is built with high resistance stainless steel AISI 316L thickness 3 mm placed below the hopper.</p>

<p><i>Gasifier¹</i></p>		<p>The gasifier is a vertical type of structure in a downdraft configuration, equipped with an internal agitator to decompose and remove ashes.</p>
<p><i>Ash Tank¹</i></p>		<p>A storage tank is made of high resistance stainless steel, and it is able to store ashes up to 7 days.</p>
<p><i>Cyclone for dust¹</i></p>		<p>The cyclone, placed immediately after the gasifier, is used to separate the finest dust from the gas flow that can cross the reactor grid</p>

<p><i>Cooler¹</i></p>		<p>The cooler is a water/gas exchanger that reduces the gas temperature up to 50 ± 70 ° C. In this way, the steam and tar condense and, thanks to an automatic discharge system, can be drained towards the outside.</p>
<p><i>Biological Filters¹</i></p>		<p>Two filters, filled with woodchips, are used to retain dust, humidity and residual tar, separating it from the gas flow.</p>
<p><i>Cyclone for air humidity¹</i></p>		<p>This cyclone, different from the first one, is located downstream of the mixing of syngas with air</p>

<p><i>GM Vortec 4.3L V-6</i></p>		<p>Main Technical features will be described in Table 2. 3</p>
<p><i>Mecc Alte ECO-ECP</i></p>		<p>The alternator series Mecc Alte ECO-ECP self-regulated P/N ECP 28-VL/4A, brushless 4 poles, 50 Hz frequency, voltage output 400V, is equipped with a SR7/2-G protection, (protection of low speed whose threshold is adjustable via a trimmer).</p>
<p><i>Control system</i></p>		<p>The first panel (on the left in Figure) is called Main Supervisor and controls and manages the gasification operations and the entire system alarms, data logging and web access service.</p> <p>The second panel (on the right) controls the engine operation and manages the synchronization and the direct input of electricity in the national grid</p>

<p><i>Plate Heat Exchanger</i></p>		<p>A plate heat exchanger for the heat recovery from the engine cooling system</p>
<p><i>Shell and Tube Heat Exchanger</i></p>		<p>A shell and tube heat exchanger is used to recover heat from exhaust gases line.</p>

¹ Courtesy of Stefano Esposito, Senior Designer at CMD S.p.A., R&D Energy Dpt.

Table 2. 2: Description of the main component of CMD ECO 20x

<i>Cylinder</i>	N°	6
<i>Total displacement</i>	l	4.30
<i>Bore</i>	mm	101.6
<i>Stroke</i>	mm	91.4
<i>Compression ratio</i>	-	10.5:1
<i>Aspiration</i>	-	Natural
<i>Regulator</i>	-	Electronic
<i>Cup oil capacity (without oil filter)</i>	l	3.8
<i>Input fuel required pressure</i>	mbar	18÷38

Table 2. 3: GM Vortec V-6 technical specifications

Two throttle valves control the air mass flow rate and the air/syngas mixture composition:

- the first throttle body opens in response to the signal from the lambda probe, which detects the oxygen content in the exhaust gases;
- the second throttle body controls the engine rotational speed and power output.

Attention must be dedicated to the engine start-up period. This is managed by both the throttle bodies and it can be divided into four sequences:

- the cranking phase;
- the phase of minimum stabilization;
- the parallel phase with the network;
- the phase of power release towards the network.

The *cranking phase*, which lasts 20 seconds and is powered by an electric starter motor, begins with the air valve gradually opening until the maximum set point is achieved; in the meantime, the air/syngas valve manages its opening degree as a function of the engine rotational speed. The oscillating action of the air/syngas throttle body is in phase opposition with the engine rotational speed during the *minimal stabilization phase*; consequently, as the engine rotational speed increases, the throttle body reduces the opening degree and vice versa. Once the engine rotation speed reaches 1500 rpm, the oscillating action is completed and stabilized. If this occurrence is not reached within the first 30 seconds after the cranking phase, the system goes in a 5 second pause and then the test is repeated for a maximum of three times before reporting an anomaly in the engine start-up phase.

If the 1500 rpm regime is achieved within 30 seconds, the control unit begins the *parallel phase* with the 50 Hz network; the throttle bodies, in turn, forecast a configuration in which the air valve follows the stoichiometry within the engine combustion chamber and the air/syngas valve acts to maintain the 1500 rpm rotational speed. In order to achieve the right synchronism, the system also adjusts the net and generator sinusoids. The system shuts the parallel with the network and shifts to the *phase of power release* to the network after synchronism is established.

Power is delivered in this phase, and the throttle body reaches its maximum opening degree as a function of the imposed power, as measured by a unit value of the lambda sensor, which is determined by the engine aspirated syngas quality.

2.1.1 Historical evolution of CMD ECO20x

The micro-CHP system has quite a recent history (Figure 2. 3). The idea came up in 2014 to intelligently dispose several tons of ligneous material, primarily made of boxes and pallets that did not meet the European regulation, which accompanied foreign shipments. The considerable amount of 27 tons of wood waste per month, equating to around 450 MJ of primary energy, constituted a disposal cost that could not only be avoided, but could also be used as a source of energy for the manufacturing plant.

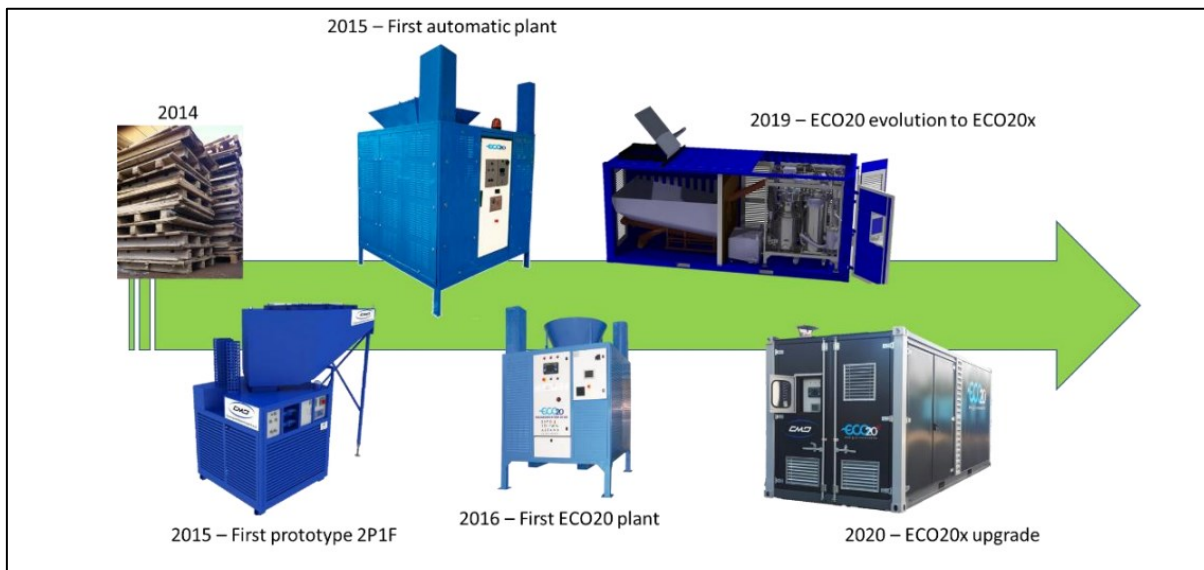


Figure 2. 3:CMD ECO20x History [3]

In 2015, the first prototype 2P1F was realized, which was progressively developed into the 2016 first version of CMD ECO20. This first version had a smaller engine (GM Vortec I-4 3.0L) and a downdraft gasifier with Imbert which allowed, however, to gasify only woodchips. CMD ECO20 was upgraded in the CMD ECO20x thanks to funding of two MISE (Italian Ministry of Economic Development) projects:

- *INNOVARE* (Impianti iNNOVAtivi per poligenerazione distribuita da biomasse REsiduali) – Fondo per la Crescita Sostenibile, Horizon 2020 - PON Imprese e Competitività 2014-2020;
- *PROMETEO* (PROduzione di energia elettrica, terMica e frigorifEra con micro-cogeneraTore alimEntato a biOmassa residuale) – Grandi progetti R&S – PON Imprese e Competitività 2014-2020.

In addition to the modifications made to the engine, others important updates were done to improve the automation and reliability of the system. It is worth mentioning some of the most important:

- the cover of the system was removed, and the chassis was adapted to fit into a standard container, in order to be more preserved from atmospheric agents and easily transportable;
- the hopper placed on the head of the chassis was removed and it was obtained in the rear part of the container, by increasing the carrying capacity from 0.5 m³ to 12 m³. In this way, no external loading system is needed anymore, since the plant is able to manage the biomass loaded by itself;
- the loading system was totally revised, to avoid blockages along the loading line that would affect the operation of the whole CHP;
- the control logic of the system of ash discharge was modified to avoid cap formation or bridge formation of the biomass in the reactor;
- the engine cooling circuit was modified, by dividing it from the syngas cooling system. In this way, the separate management of the syngas cooling system made it possible to improve its capacity of separation of dust and tar from the syngas flow.

The new version guarantees the gasification of briquettes ligneous biomass with the same efficiency of woodchips.

2.2 Experimental characterization of the CMD ECO20x operation under various feedstoks

2.2.1 Experimental layout

The here described experimental activity was possible thanks to the joint work between CNR – Istituto di Scienze e Tecnologie per l'Energia e la Mobilità Sostenibili (CNR-STEMS) and CMD during the afore mentioned PROMETEO project.

The whole system was appropriately equipped with low-frequency pressure sensors and k-type thermocouples along the entire gas circuit and with high-frequency instrumented sparks on the reciprocating engine for the detection of the in-cylinder pressure trace. Two

mass flow rate sensors were also installed to measure both the inlet air at the gasifier and at the ICE. Figure 2. 4 reports a schematization of the measurement chain with main variables named according to the labels used hereafter, while Figure 2. 5 shows the characteristic points along the gas line where the said fluid properties were measured.

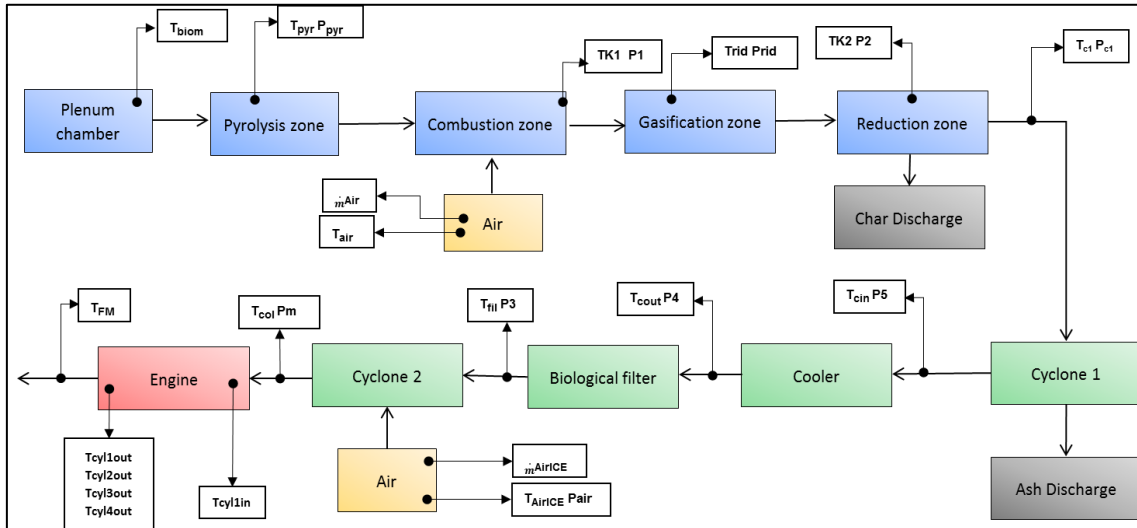


Figure 2. 4: List of installed sensors on the studied m-CHP plant.

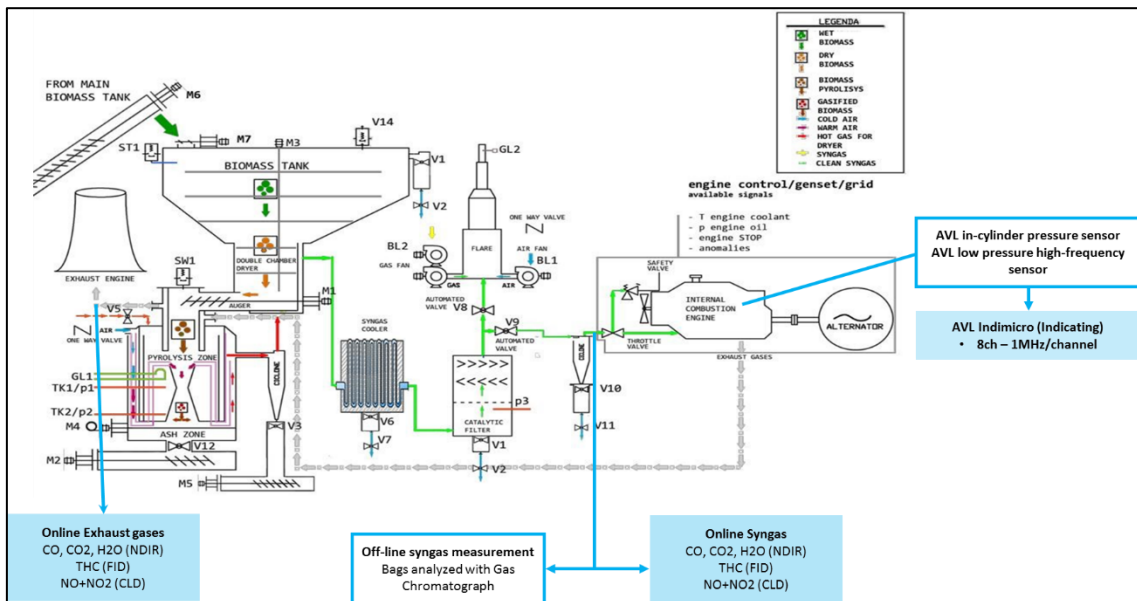


Figure 2. 5: Experimental setup showing the ICE and sampling points for syngas analyses.

The experimental characterization of syngas and exhaust gases composition was carried out by using a mobile laboratory owned by CNR-STEMS, online through a direct measurement with Sensors Semtech analyzer (Figure 2. 6a). The system is equipped with

a NDIR infrared absorption analyzer for the measurement of CO, CO₂, a UV absorption detector (NDUV) for NO_x and an electrochemical sensor for O₂. All these species are measured on a dry basis. The syngas sampling was performed with a probe heated to 463K, positioned on the syngas supply duct to the engine, as shown in Figure 2. 6b. A 3-way valve was mounted, shown in Figure 2. 6c, to operate alternatively the sampling of the gas at the engine exhaust or in the syngas stream.

Since the Semtech flame ionization analyzer (FID) for the determination of THC requires low temperature from a chiller (at 277-279K) to be operative, it was usually coupled with another online measurement by Vario Luxx analyzer (Figure 2. 6d) and an off-line sampling in Tedlar bags, the content of which was subsequently analyzed through a gas chromatograph. The chromatographic gas method uses the SUPELCO-Carboxen 1006 PLOT column (30 m x 0.53 mm x 0.2 um), helium as carrier gas and reference gas, injector temperature at 470K and TCD temperature at 500 K. The programmed temperature used for the oven is: 300 K C for 5 min, 323 K / min up to 493 K, 493 K for 40 min. The analytical method used for these tests did not allow to separate the N₂ from the O₂ possibly present in the syngas sample.

As mentioned before, exhaust gases concentrations were analyzed with the Semtech analyzer as well. A volumetric flow meter (0-4.96 m³/min) was also installed, operating using the Pitot principle and forming part of the Semtech system. The meter was installed downstream of the silencer. The exhaust gas temperature was measured near the exhaust gas flow measurement section (Figure 2. 7a). An NO_x/O₂ sensor (Continental UniNO_x in Figure 2. 7b) was also mounted, in order to obtain a verification of the measured data with an additional system. An AVL smoke meter (Figure 2. 7c) was mounted on the engine exhaust to measure the soot concentration (PM, expressed in FSN and subsequently converted into mg/m³).

The sampling line from the sampling point to the smoke meter is as well heated to a temperature of 463K. The oxygen measurement was used to correct the values of polluting emissions, according to the following formula provided for by DlgS 152/2006 - Part V [4]:

$$E = \frac{21 - O_{2ref}}{21 - O_2} * E_m \quad (2.1)$$

where:

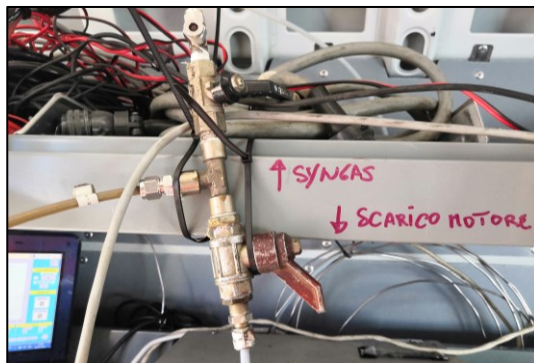
- O_{2ref} is the reference oxygen content in %;
- O_2 is the measured oxygen content in %;
- E_m is the emissions measured value;
- E is the emissions corrected value.



a)



b)



c)



d)

Figure 2. 6: Sensor Semtech Analyzer (a), probe for syngas sampling (b), three-way valve, Vario Luxx Analyzer (d)

In the Dlgs 15 November 2017, n. 183 [5], CMD ECO20x falls into "Fixed Engines part of m-CHP plants fueled by biogas or synthesis gas derived by biomass gasification of less than 1 MW installed since December 19, 2017", whose Table 2. 4 reports the emission limits. In this case the values of exhaust gases compositions must refer to an oxygen content in the gaseous effluent of 15%, to be considered in formula 2.1.

To the purpose of tar quantity evaluation in the syngas, the collected samples were forced to pass through a quartz fiber filter, to restrain any solid particles. Then, the syngas flow

was sent to a double condensation stage: the first happens at room temperature, to condense the highest molecular weights, while the temperature of the second stage was kept constantly below 273 K through a refrigeration unit to collect the lightest tars.



a)



b)



c)

Figure 2. 7: Installed volumetric flow meter (a), Continental UniNOx (b) and AVL smoke meter (c)

<i>Nominal Power (MW)</i>	≤ 0.3 MW
<i>NO_x</i>	190 mg/Nm ³
<i>SO_x</i>	60 mg/Nm ³
<i>CO</i>	300 mg/Nm ³
<i>COT</i>	40 mg/Nm ³
<i>NH₃</i>	2 mg/Nm ³
<i>HCl</i>	2 mg/Nm ³

Table 2. 4: Limit emissions for CMD ECO20x [5]

The experimental setup used for the analysis of the tar concentration is shown in Figure 2. 8.



Figure 2. 8: Experimental setup for the analysis of the tar concentration in the syngas

In order to measure the ICE indicated pressure cycle, as afore said, the engine was equipped with properly defined and/or designed sensors, specialized for non-traditional gaseous fuels, shown in Figure 2. 9:

- a spark plug sensor, type AVL ZI45-F5D (Figure 2. 9a), for the high frequency measurement of the indicated pressure cycle, placed in the spark-plug seat, based on the piezo-quartz principle, very precise and robust;
- a low-pressure sensor, type AVL LP12DA-05 (Figure 2. 9b), for the high frequency measurement of the dynamic pressure in the intake duct, necessary for referencing, using the pegging technique, the signal coming from the instrumented spark plug, based on the piezo-resistive principle. It was placed in a proper realized threatened hole in the intake runner.



a)



b)

Figure 2. 9: AVL ZI45-F5D (a) and AVL LP12DA-05(b)

2.2.2 Effect of feedstock composition on the performances of the gasifier and the internal combustion engine

The afore described setup allowed the generation of a useful database for the characterization of the system and gave the possibility to acquire, monitor and save for the subsequent analyses an interesting set of data.

In particular, the experimental set-up allowed highlighting the effect of powering the CMD ECO20X with different biomasses, as specified in the following. For the correct analysis of the engine performance, from 256 to 512 consecutive chamber pressure cycles were acquired. A baseline condition was set at spark ignition of 34° BTDC (Before Top Dead Center) and stoichiometric air/fuel ratio.

The gasifier equivalence ratio was indeed kept at 0.3 but various biomasses were tested. The system behaviour with two kinds of woodchip, a mix of olive pomace and sawdust and green waste treated by HTC is here discussed.

While woodchip has the consistence and size suitable of direct gasification, preliminary briquetting process was needed for the other two biomasses. The green waste HTC came indeed in the form of a powder provided by the company Ingelia and derived from their processing plant located in Spain, in the Valencia region [6].

An appropriate previous study on the compactness of the briquettes [7] was necessary to determine the %age of sawdust able to ensure the tolerance to the mechanical stresses of the handling and loading devices.

While the briquette made of 100% green waste HTC was found sufficiently compact to resist tangential stresses without crumbling, a mix with 30% in weight of sawdust was necessary for olive pomace in order to guarantee the good compactness of the briquette.

Figure 2. 10 shows some images of the mechanical pretreatment needed to make the biomass suitable for gasification.

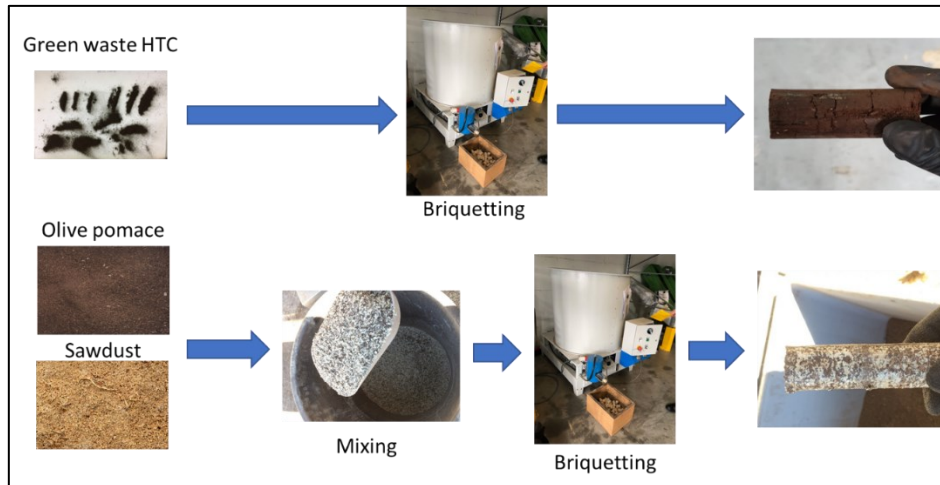


Figure 2. 10: Briquetting process for green waste HTC and olive pomace mixed with sawdust

Main methods for physical-chemical characterization of the biomass are proximate and ultimate (or elemental) analyses.

The first one measures gross components such as moisture, volatile matter, ash and fixed carbon, while the second one measures contents of carbon, hydrogen, nitrogen and sulfur[8].

Ash and moisture particularly affect the gasification process since ash fusion could create agglomerations inhibiting the flow of the gasifier agent, while moisture reduces the energy content.

The following bases for ultimate analysis are usually used:

- AR (as received) basis: all components of the biomass are considered;
- DB (dry basis): water presence is ignored;
- DAF (dry and ash-free basis): both water and ash presence is ignored.

When the biomass chemical composition is known, it is possible to determinate the high and lower heating value (HHV and LHV) of the initial biomass.

Two different approaches are mostly used in the literature, using Basu's formulas:

$$\text{HHV}_{\text{Basu dry}} = 0.3491 C_{\text{dry}} + 1.1783 H_{\text{dry}} - 0.1034 O_{\text{dry}} - 0.0151 N_{\text{dry}} + 0.1005 S_{\text{dry}} - 0.0211 A_{\text{dry}} \quad (2.2) \quad [9]$$

$$\text{HHV}_{\text{Basu ar}} = \text{HHV}_{\text{Basu dry}} * \left(1 - \frac{\text{Moisture}}{100}\right) \quad (2.3) \quad [9]$$

$$\text{LHV}_{\text{Basu}_{\text{ar}}} = \text{HHV}_{\text{Basu}}(\text{ar}) - 2.260 \cdot \left\{ 9 \cdot \left[\frac{\text{H}_{\text{ar}}}{100} \right] - \left(\frac{\text{Moisture}}{100} \right) \right\} \quad (2.4) \quad [9]$$

For the present experimental study, as said before, four different initial ligneous feedstocks were taken into account:

- a) woodchip from mixed wood type;
- b) poplar woodchip classified A+ by Italian Legislation (UNI EN ISO 17225[2]);
- c) briquettes of olive pomace and sawdust (80-20% weight ratio);
- d) green waste after a process of HydroThermal Carbonization (HTC);

whose analyses, made according to reference standards ASTM D 5142 for proximate analysis and ASTM D 5373 for ultimate one, are listed down in Table 2. 5. Typically, it is convenient to normalize the molar fraction of hydrogen and oxygen with respect to carbon, by applying the equations listed in (2.5).

Type of Analysis	Physical or Chemical Property	Sample a)	Sample b)	Sample c)	Sample d)
Proximate Analysis	Moisture (%)	21.0	11.2	8.3	12.4
	Fixed Carbon (%)	14.1	14.8	19.6	20.6
	Volatiles (%)	63.2	73.6	68.7	51.8
	Ash (%)	1.7	0.5	3.4	15.2

Type of Analysis	Physical or Chemical Property	AR			
		Sample a)	Sample b)	Sample c)	Sample d)
Ultimate Analysis	Carbon (%)	42.5	40.2	43.9	47.2
	Hydrogen (%)	5.1	5.0	5.2	4.6
	Oxygen (%)	29.1	50.1	37.8	19.7
	Nitrogen (%)	0.6	0.0	1.3	0.9
-	LHV (MJ/kg)	16.1	15.8	15.8	18.1

Type of Analysis	Physical or Chemical Property	DAF			
		Sample a)	Sample b)	Sample c)	Sample d)
Ultimate Analysis	Carbon (%)	55.0	45.5	49.8	65.2
	Hydrogen (%)	6.6	5.6	5.9	6.3
	Oxygen (%)	37.6	48.9	42.8	27.2
	Nitrogen (%)	0.7	0.0	1.5	1.3

Type of Analysis	Physical or Chemical Property	DB			
		Sample a)	Sample b)	Sample c)	Sample d)
Ultimate Analysis	Carbon (%)	53.8	45.2	48.0	53.9
	Hydrogen (%)	6.5	5.6	5.7	5.9
	Oxygen (%)	36.8	48.7	41.1	22.5
	Nitrogen (%)	0.7	0.0	1.4	1.1
-	LHV (MJ/kg)	21.0	15.8	17.4	22.2
Chemical Formula	-	CH _{1.44} O _{0.51}	CH _{1.47} O _{0.8}	CH _{1.41} O _{0.64}	CH _{1.3} O _{0.3}

Table 2. 5: Proximate and ultimate analysis results of the here used feedstock.

Known the number of atoms of the equivalent molecule, it is possible to calculate the following atomic ratios (2.6) and (2.7).

$$x = \frac{C M_C}{C M_C}, \quad y = \frac{H M_C}{C M_H}, \quad z = \frac{O M_C}{C M_O}, \quad (2.5)$$

$$\frac{H}{C} = \frac{y}{x} \quad (2.6)$$

$$\frac{O}{C} = \frac{z}{x} \quad (2.7)$$

The Von Krevelen's diagram, shown in Figure 2. 11, characterizes the organic matter on a plot of atomic O/C vs atomic H/C coming from proximate analysis (on dry basis) [10]. The LHV is closely correlated with the O/C and H/C ratios. LHV is reduced when the O/C ratio increases. Similarly, when the H/C ratio increases, the upper calorific value of the biomass is reduced [11]. The here considered biomasses are represented in dots of different colors in the diagram.

The lower heating value for the samples used in the experimental tests was calculated using the aforementioned correlations and confirmed by using a PARR 6200 system with a calorimetric bomb of Mahler.

According to the tables, sample a) has moisture above the 20%, while, for sample b) it is lower. This is an important factor for gasification as less energy required for complete drying. The calorific value is comparable for the two types of woodchip and olive pomace, while it is higher for green waste HTC because of the higher amount of carbon

and hydrogen and the lower oxygen content. The fraction of ash is higher for sample d) and it can lead to a higher %age of slag [12].

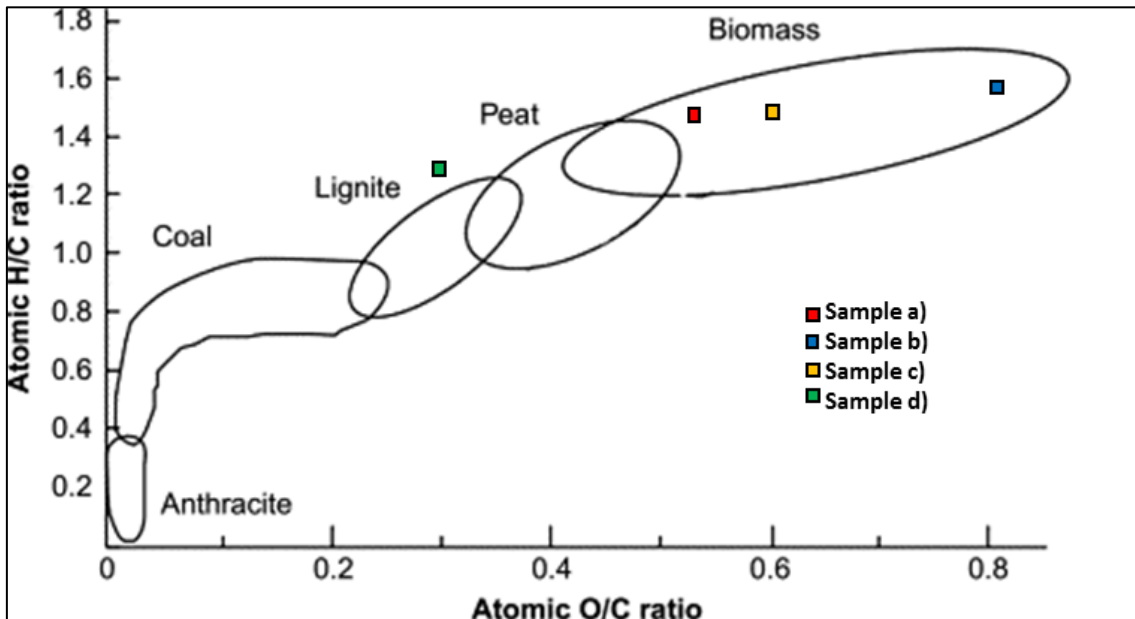


Figure 2. 11: The Von Krevelen's diagram and here considered biomasses

Table 2. 6 collects the results of the analysis on dry basis (DB) of the syngas resulting from gasification, as made on the collected bags when the afore-described feedstocks are used in the considered CMD ECO20X cogeneration unit, always measured under the same previously introduced baseline operating condition of the ICE.

The higher %age of carbon content for sample a) leads to a syngas with higher carbon content; a higher H₂ content in the syngas from this feedstock is due to the higher %age of hydrogen in the ultimate analysis. The higher N₂ content in the syngas derived from sample d) is due to the initial higher %age of nitrogen in the elemental analysis. Sample b) and sample d) convert into the syngas exhibiting the lowest CO₂ %age. In the end, it can be said that stoichiometric air-to-fuel ratios (α) are lower for sample d) due to the lower CH₄ amount.

By considering the above-made considerations, and as expected, it can be assumed that poplar woodchip (sample a) has the best characteristics when it is gasified.

%vol (DB)	Sample a)	Sample b)	Sample c)	Sample d)
CO	18.45	18.44	19.0	17.2
CO ₂	12.28	8.74	16.7	9.2
CH ₄	1.89	1.83	2.0	1.6
H ₂	20.47	15.54	17.0	10.3
N ₂	46.91	55.45	45.3	61.3*
LHV (MJ/Nm ³)	5.2	4.2	4.95	3.92
Stoichiometric α	1.24	1.21	1.46	1.09

*N₂+O₂

Table 2. 6: Mean syngas composition (%vol) (DB) for each processed biomass.

The experimental tests with ligneous biomass were conducted as a first step and no particular problem arose. Conversely, for olive pomace and green waste HTC, the experimental campaign highlighted some inefficiency. The oleaginous matrix of the exhausted olive pomace, if this material was used without mixing with other elements, resulted in an excessive tar production (>5g/Nm³), hence in a critical operation. The low temperature (<1070K) and the excessive tar production led to an excessive fouling of the whole plant up to its stop. These results suggested the possibility of a dilution of the pomace with wooden biomass to reduce the aforementioned problems.

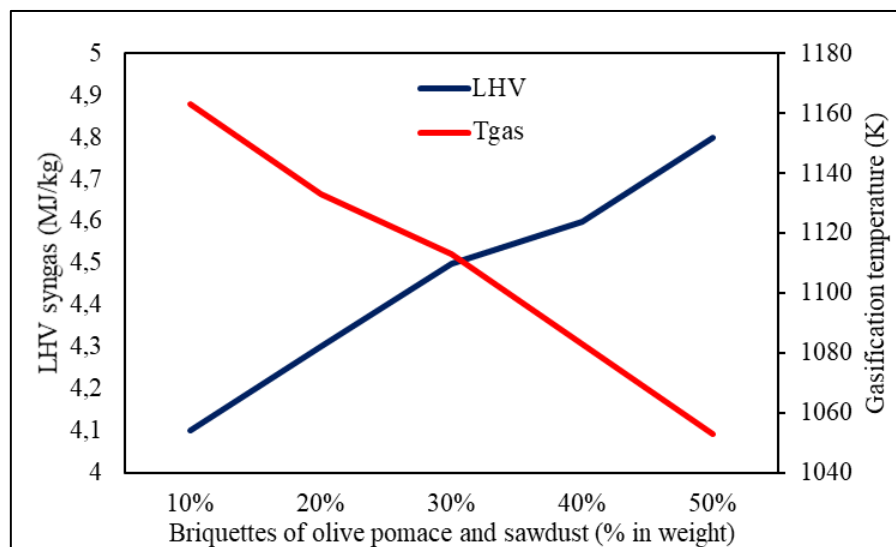


Figure 2. 12: Parametric analysis of the calorific value of the syngas produced by the gasification of a mix of briquettes and mixed woodchips, depending on the %age of briquettes.

In order to establish the best blend of olive pomace and sawdust a preliminary numerical analysis was performed by using a properly developed “digital twin” of the CMD

ECO20X system. This was assessed by authors in ref. [13] by coupling a gasification and a syngas combustion model.

The calorific value of the produced syngas was found to increase with the %age of mass of pomace, while the gasification temperature having on opposite trend (Figure 2. 12).

The right compromise solution that guaranteed an acceptable syngas calorific value, hence good conversion rate of tar (> 1073 K), was found to be the 30% by mass of olive pomace (Figure 2. 12). In this case, tar production reduced to 4.7 g/Nm³.

For the green waste HTC, the moisture and the ash contents in the feedstock were found to play a decisive role. The last, in particular, strongly affected the thermal process as ash fusion created agglomerations that did not allow a smooth flow of the gasifier agent. The formation of agglomerates, some of which shown Figure 2. 13, reduced the overall efficiency of the plant until its blockage was reached.



Figure 2. 13: Fragment of molten ash present in the reactor combustion area.

Some values of temperature along the gas circuit are shown in Figure 2. 14, while Figure 2. 15 represents values of pressure. No particular differences are found between the cases relevant to the two woodchips. Just it is worth nothing that the value of temperature before the section of syngas mixing with air (T_{fil}) is lower for sample b). Sample d) shows the lowest temperature in the reduction zone due to the presence of molten ash inhibiting the air passage. A temperature lower than 970 K is index of a poor-quality gasification [9] This presence is also confirmed by the high gasifier temperature drop, namely the difference between TK1 and TK2, that is higher than 720 K, while for the other samples it stays below 670 K.

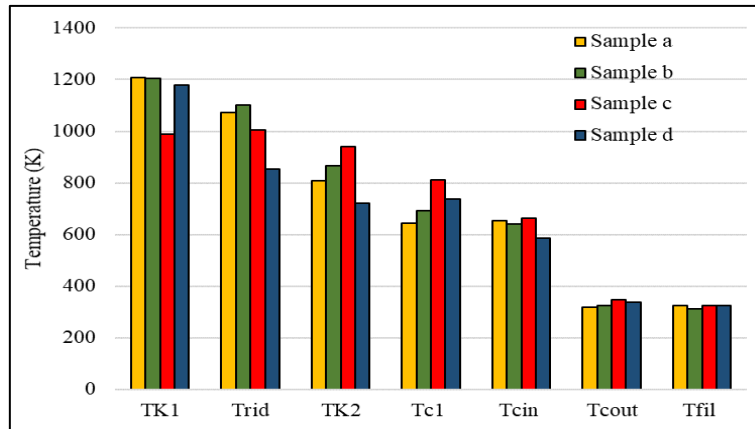


Figure 2. 14: Comparison between temperatures (K) in relevant points of the m-CHP plant circuit (experimental analysis).

The pressure drop in the cleaning circuit, visible in Figure 2. 15, is higher for sample a) and sample d). It follows that inlet pressure of the syngas-air mixture at the internal combustion engine is lower.

Volumetric efficiency is in fact badly affected by pressure losses along the intake circuit and by higher mixture temperatures. This is due to the high amount of ash in the initial feedstock, causing a higher pressure drop. The lower temperature and higher pressure of sample b) result in a higher volumetric efficiency. Indeed, the indicated mean effective pressure (IMEP) is the highest in this case as visible from Figure 2. 16 that shows the averaged in-cylinder pressure cycle under the different feedstock feeding modes.

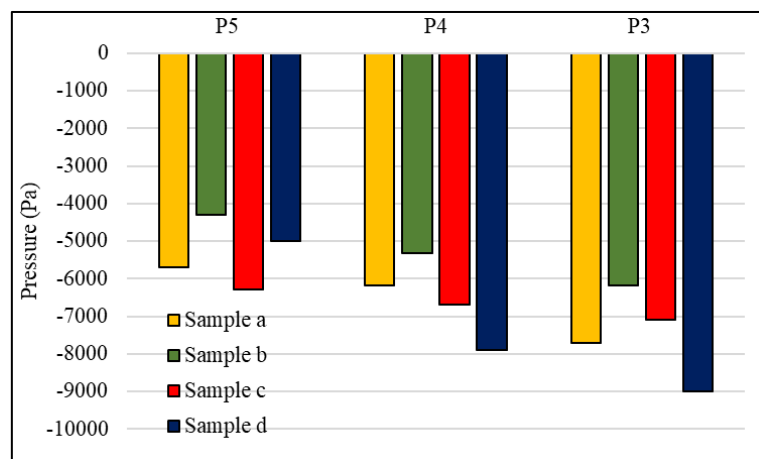


Figure 2. 15 Comparison between pressures (Pa) in relevant points of the m-CHP plant circuit (experimental analysis).

Table 2. 7 summarizes the main engine parameters for the considered samples. Stoichiometric engine combustion is always achieved as a lambda sensor is mounted on

the exhaust gas line that acts as a feedback controller to adjust the air mass flow rate entering the engine intake manifold through a properly controlled throttle valve.

It is well known that for SI engine, the profile of the burned mass fraction as a function of the crank angle follows a S-shape curve that is described by the Wiebe function (equation 2.8) [14]:

$$x_b = 1 - \exp \left[-a \left(\frac{\theta - \theta_0}{\Delta\theta} \right)^{m+1} \right] \quad 2.8$$

where θ is the crank angle, θ_0 is the start of combustion, $\Delta\theta$ is defined as the angular difference between MBF90 and MBF10, these last defined as in the following, and a and m are adjustable parameters usually equal to 5 and 2, respectively.

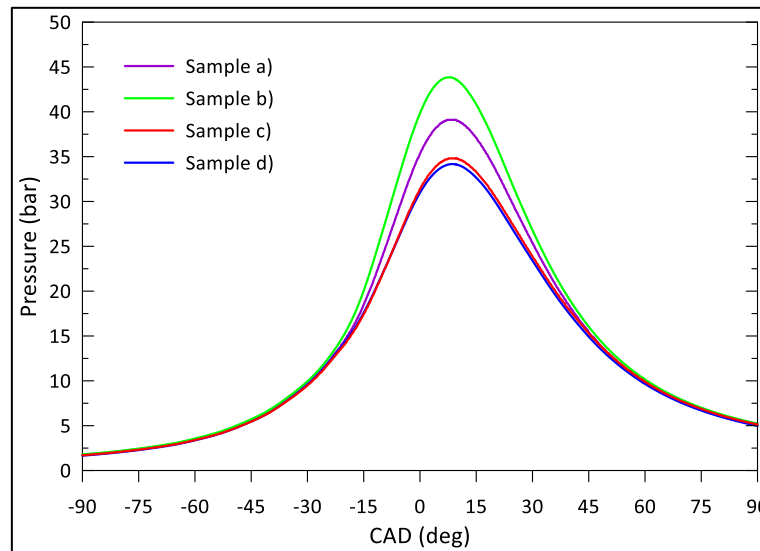


Figure 2. 16: Average pressure cycle for the considered samples (experimental analysis).

The flame development process is highly influenced by the fuel composition and the combustion condition. Three stages can be identified for the characterization of the combustion process in a SI engine:

1. *flame-development phase*: the crank angle interval between the spark discharge and the time when the 10% of the mixture fraction has burned (MBF10 - Flame initiation angle);

2. *rapid-burning phase*: the crank angle interval between the end of the flame-development stage and the end of the flame-propagation process, where 90% of the fraction has burned (MBF90 – Flame development);
3. *final stage*, where the remainder of the charge burns up to completion.

An important parameter to be considered for the thermodynamic analysis of the indicated combustion cycle is the burning of 50% of the fuel feed (MBF50) that is referred to the angle of the center of combustion and allows an effective comparative determination of the combustion phase with respect to MBF10 and MBF90.

The evolution of the burned mass fraction with respect to the engine crank angle was calculated by the measured pressure traces in the hypothesis of a complete combustion process. Although this last assumption is not strictly true, as %ages of CO are found in the exhaust flow, this study is anyhow meaningful to make a comparison between the various syngas conversion efficiency in the combustion chamber relevant to the various processed biomasses.

Engine Parameter	Sample a)	Sample b)	Sample c)	Sample d)
Spark Ignition (°BTDC)	34	34	34	34
P _{MAX} (MPa)	3.91	4.38	3.48	3.47
IMEP (MPa)	0.554	0.588	0.534	0.516
L _{IND} (J)	411	436	396	382
MBF50 (grad)	3.3	-0.3	8	8.24
COV _{IMEP} (%)	0.71	0.64	2.09	2.46
COV _{P_{MAX}} (%)	5.56	4.88	6.59	7.01
P intake manifold (MPa)	0.091	0.094	0.085	0.081
T _{CYL IN} (K)	312	309	310	309
Fuel burning rate FBR (mm/s)	0.27	0.28	0.23	0.23

Table 2. 7: Comparison between engine parameters under different biomass powering modes.

As shown in Figure 2. 17, the burning duration, namely the difference between MBF90 and MBF10, is the lowest for sample b), possibly due to lower content of CO₂ in the mixed fuel [15], while it is the highest for sample d) due to the low H₂/CO ratio, that

results in a slower laminar speed of the syngas-air mixture in the combustion chamber [16]. The combustion phase is similar and slower for sample c) and d) and takes place later in the cycle [15]–[17]. The higher indicated mean effective pressure (IMEP) of sample b) (+6% than sample a), +9% than sample c) and +12% than sample d)) is due to the fact that the in-chamber conditions at inlet valve closing are more favorable, due to the lower pressure drop and temperature conditions for the volumetric efficiency.

A summary of the values of MBF10, MBF50, MBF90 and relevant angular differences is also reported in Table 2. 8.

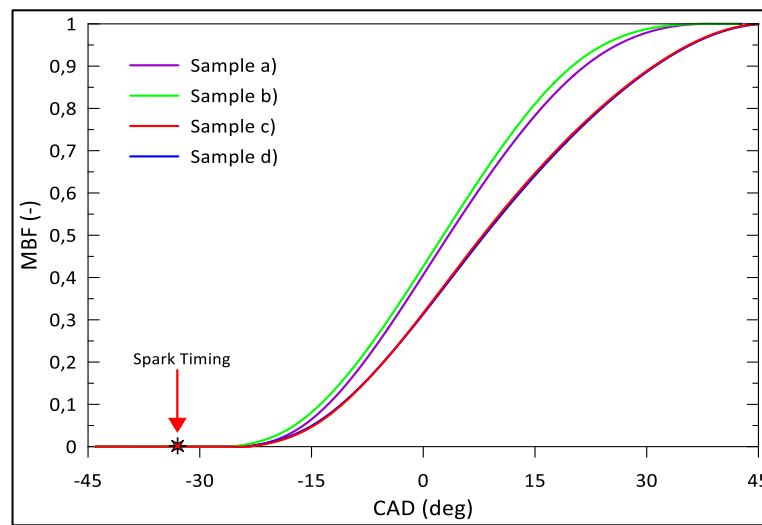


Figure 2. 17: Combustion development for the considered samples in terms of burned mass fraction as a function of the crank angle. Top dead center (TDC) is at 0°deg (experimental analysis).

Sample name	MBF10	MBF50	MBF90	$\Delta\theta_{10}=\text{MBF10}-\text{Start of spark}$	$\Delta\theta_{90-10}=\text{MBF90}-\text{MBF10}$
Woodchip from mixed wood type	-17.7	3.3	20	16.3	37.7
Poplar woodchip classified A+	-18.3	-0.3	15.8	15.7	34.1
briquettes of olive pomace and sawdust	-14.68	8	30.92	19.32	45.6
green waste after HTC	-14.93	8.24	31.1	19.07	46.03

Table 2. 8: Combustion main angles

The four in-cylinder pressure cycles of Figure 2. 16 show a similar trend for what regards the open valve phases, while the compression phases show some discrepancies, in

particular between the two woodchips and olive pomace or green waste HTC. Indeed, differences in the pressure traces along the intake lines are better visible in Figure 2. 18.

The whole gasifier to ICE line is placed below the atmospheric pressure with the ICE that draws the whole process. Each pressure drop that happens in the gasifier along the cleaning circuit has a strong effect on the in-cylinder trapped mass, as it is almost entirely determined by the pressure level in the inlet port.

The ash melting process that happened when the system was fuelled with a biomass like green waste HTC increased the pressure drop both in the gasifier and along cleaning circuit, thus resulting in a lower pressure level in the inlet port (Figure 2. 18).

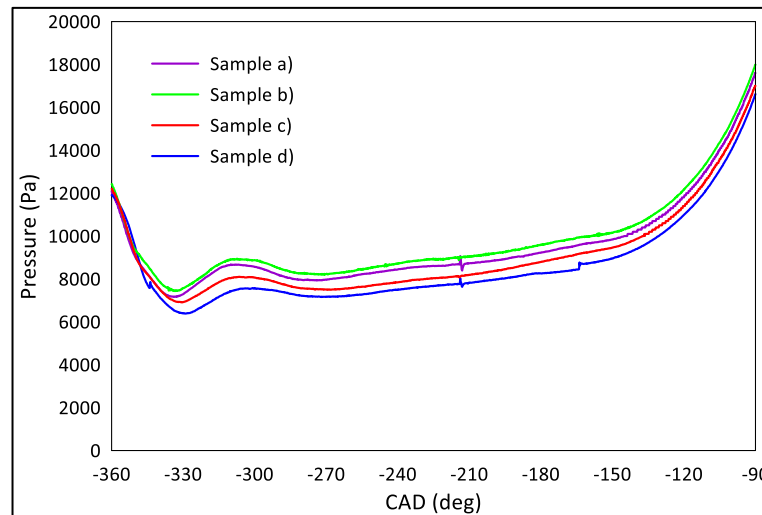


Figure 2. 18: Measured in-cylinder pressure during the intake phase for various feedstock (experimental analysis).

A consideration between the two kinds of woodchip has to be made. In spite of the high LHV_{syn} of sample b), this last exhibited a higher %age of ash and moisture, increasing pressure drop and decreasing the ICE volumetric efficiency, with a consequent lower efficiency despite the faster combustion development in Figure 2. 17. Again, with reference to Table 2. 8, it can be seen that for both woodchips, the cycle-to-cycle variation is similar with a coefficient of variation (COV) on the IMEP that is almost the same, due to the correlation between COV and equivalence ratio explained by Cho et al. [18].

COV on the IMEP is an index of the ICE combustion stability: if slow burn, partial burn or misfire cycles occur with frequency, the value of COV_{IMEP} increases up to the

maximum value of 10%, where the engine stable operating condition is no longer possible [14].

Sample	CO ₂	CO	THC
a)	0.3	0.2	0.1
b)	0.3	0.0	0.1
c)	0.8	0.8	0.3
d)	0.2	0.3	0.4

Table 2. 9: Standard deviation in /%vol on the syngas as online composition

For olive pomace and green waste HTC, it is higher than for the two woodchips, due to the extreme variability in the syngas composition happening when a sample that is not standard woodchip is gasified (Table 2. 9). The same trend could be seen for the COV on the peak pressure that is high for all samples, with sample d) exhibiting a slightly higher value.

As regards the engine exhaust emissions, main results are shown in Figure 2. 19. For sample d) the acquisition was not possible due to the presence of the aforementioned agglomerations in the gasifier that actually blocked the whole plant.

Nitrogen oxides (NO_x) and total unburned hydrocarbons (THC) have opposite trends: NO_x is lower for sample c) and, instead, THC is highest. This is explained in relationship with the peak pressure and the maximum in-cylinder temperature achieved during combustion [19]. Indeed, since most of the fuel burns after the TDC, due to the higher value of MBF50, the peak pressure, and, therefore, the peak charge temperature both reduce [16], [17]. Moreover, syngas deriving from sample b) contains high %age of N₂, resulting in higher NO_x emissions.

The CO emissions are quite similar, because of the carbon monoxide dependence upon the operating condition and air-fuel ratio, as explained by Koç et al. [20] and due to the CO %ages in the syngas and the not complete combustion observed through a 3D CFD numerical simulation of the considered engine performed in ref. [13].

Emissions of particulate matter are found negligible in all the analyzed situations, thanks to the excellent cleaning and filtering circuit mounted on the m-CHP plant.

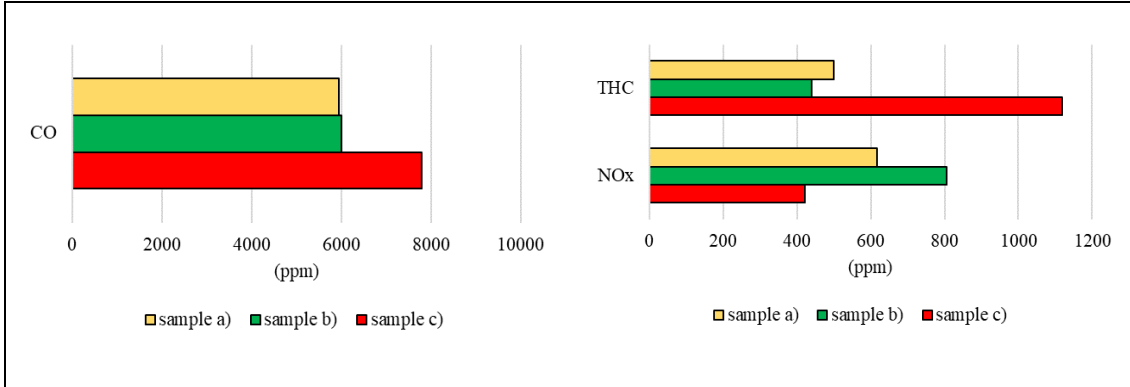


Figure 2. 19: Emissions of CO, THC and NOx for sample a), b) and c) (experimental analysis).

2.3 Energy efficiency evaluation of the CMD ECO20x plant

Thanks to the measurement performed during the mentioned experimental activity, it was possible to characterize the energy fluxes.

Figure 2. 20 shows Sankey diagrams, that help visualizing the main energy flows, for the two types of woodchip and the olive pomace sample. The energy content of biomass is converted in the gasifier, minus gasification inefficiency, into energy stored in the produced gas, the syngas. Likewise, the syngas energy content is converted in the engine into electrical and thermal energies; the last one through the waste heat circuit.

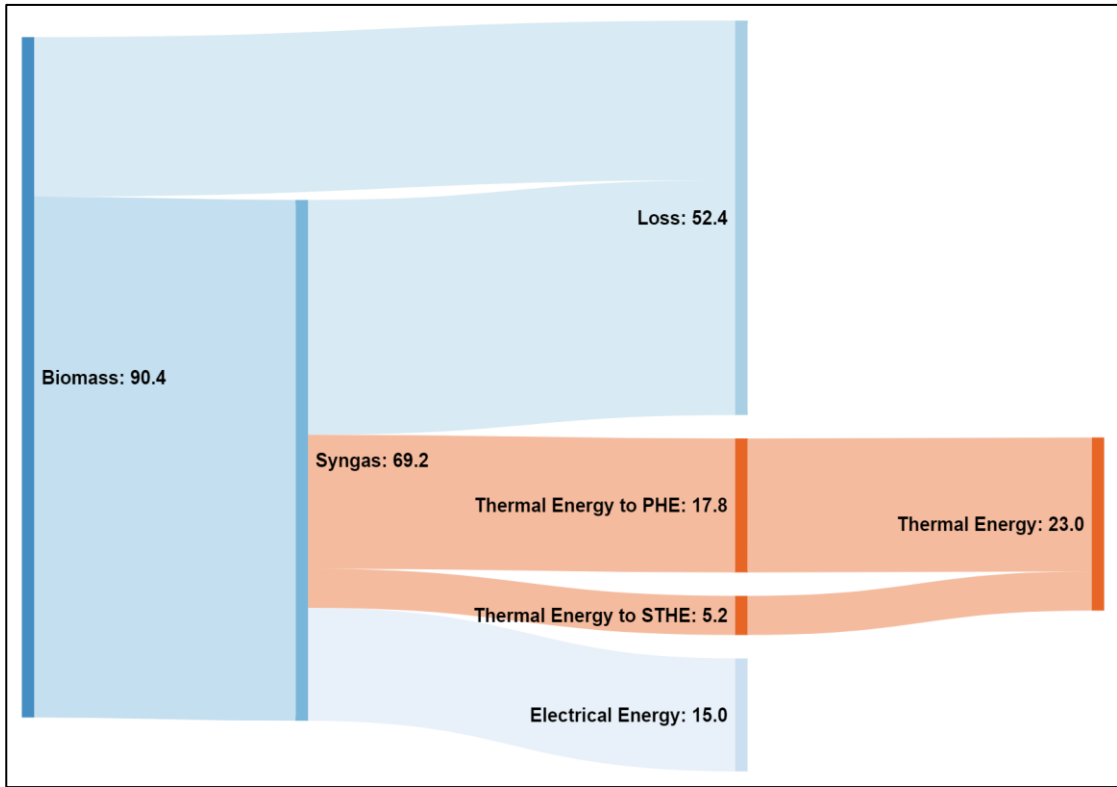
As expected, sample a) has the highest biomass energy content, resulting in a syngas with the highest energy content. Sample b) and c) both produced 17 kW of electrical power, +13.3.% compared to sample a). Sample b) total waste heat recovery is the highest, +11.5% and +5%, respectively, compared to sample a) and c). Total loss of sample a) is almost 2 times sample b) losses and 1.7 times sample c) losses.

Finally, Table 2. 10 summarizes three key performance indicators, i.e. cold gas efficiency and engine electrical and thermal efficiencies, calculated through equations 2.9 to 2.11.

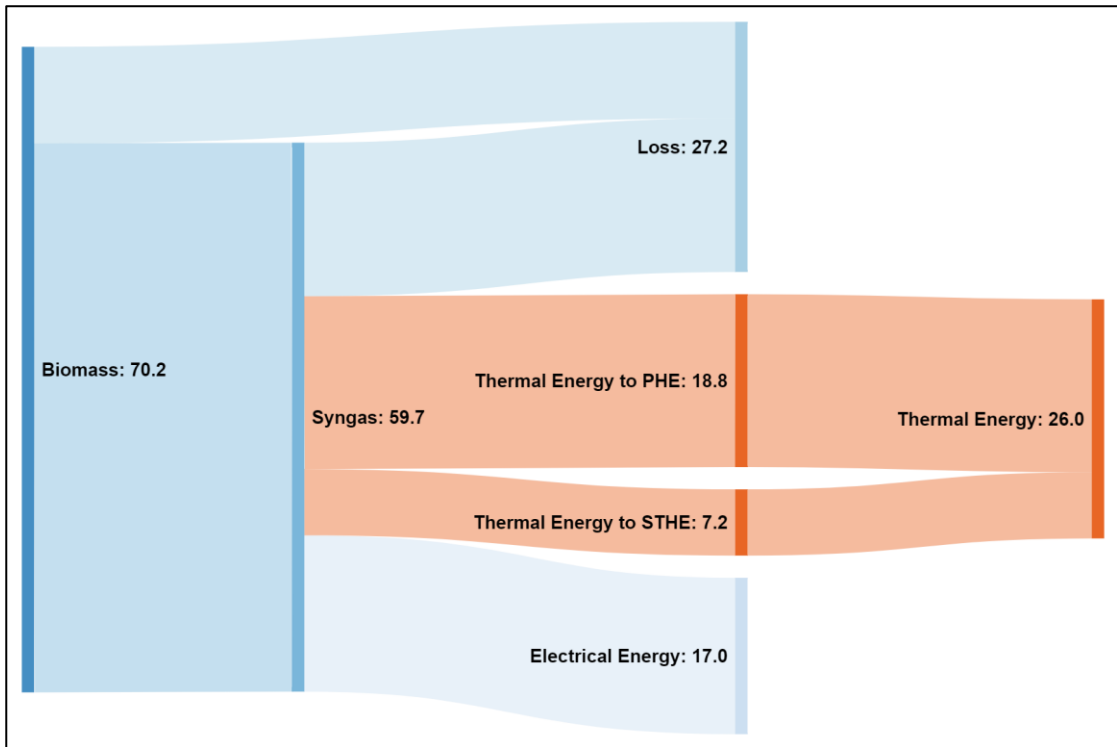
$$\text{Cold Gas Efficiency} = \frac{\text{Biomass energy content}}{\text{Syngas energy content}} \quad (2.9)$$

$$\text{Electrical efficiency} = \frac{\text{Electrical Energy}}{\text{Syngas energy content}} \quad (2.10)$$

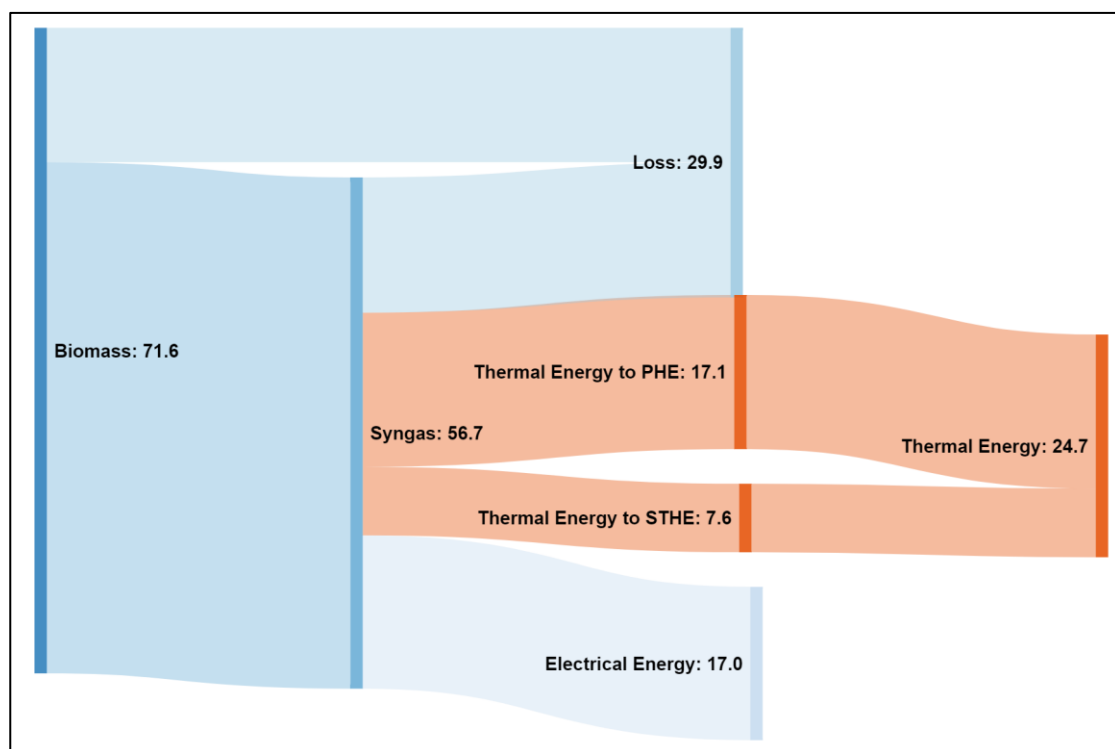
$$\text{Thermal efficiency} = \frac{\text{Thermal energy}}{\text{Syngas energy content}} \quad (2.11)$$



Sample a



Sample b



Sample c

Figure 2. 20: Sankey diagram for sample a), b) and c) (Unit are expressed in kW).

Sample	Sample a)	Sample b)	Sample c)
Cold gas efficiency	0.76	0.85	0.79
Electrical efficiency	0.22	0.28	0.30
Thermal efficiency	0.33	0.43	0.44
Overall efficiency	0.55	0.71	0.74

Table 2. 10: Key performance indicators of the considered samples.

Sample c) presented the highest efficiencies, reaching an overall efficiency of around 75%, a value close to those found in ref. [21]. In all cases, a value higher than 70% is expected, with electrical efficiency approximately falling in the range 20%-25% [21]. Nonetheless, for sample a), the overall efficiency was around 55%, due to the lower ICE filling efficiency that resulted in a lower heat recovery through the shell and tube heat exchanger and a lower electrical output.

References Chapter 2

- [1] CMD, “ECO20X - Pirogassificatore | CMD Engine - a Loncin Company - Costruzioni Motori Diesel - Progettazione e realizzazione di motori e parti meccaniche per l’industria automobilistica, la nautica, l’aviazione, sistemi di

- microgenerazione - Produzione motori marini diesel, elettrici e ibridi, general aviation, aerei ultraleggeri, pirogassificatore CHP - FNM, Avio, ECO20X - Basilicata, Atella, Campania, Caserta.” <http://www.cmdengine.com/eco20-pirogassificatore/> (accessed Nov. 05, 2021).
- [2] UNI, “UNI EN ISO 17225-1:2014.” <http://store.uni.com/catalogo/uni-en-iso-17225-1-2014> (accessed Nov. 11, 2021).
- [3] C. Caputo, Modelling approach and technical solutions for characterization and performance improvement of real biomass powered m-CHP system, *PhD Thesis. University of Rome “Tor Vergata,”* 2020.
- [4] D.lgs., “D.lgs. n. 152/2006 (T.U. ambiente).” https://www.bosettiegatti.eu/info/norme/statali/2006_0152.htm (accessed Nov. 12, 2021).
- [5] D.lgs., “D.lgs. n. 183, 15 novembre 2017, - Normattiva.” <https://www.normattiva.it/uri-res/N2Ls?urn:nir:stato:decreto.legislativo:2017-11-15;183> (accessed Nov. 12, 2021).
- [6] Ingelia, “INGELIA HTC process.” <http://www.ingelia.it/la-tecnologia-htc/> (Accessed, Nov. 21, 2021).
- [7] M. Costa, N. Massarotti, A. Stasi, D. Cirillo, M. La Villetta, G. Blasio, M.V. Prati, M.A. Costagliola, A. Mauro, L. Vanoli, A. Macaluso, A. Carotenuto, M. Migliaccio, A. Buono, V. Mulone, V. Rocco, C. Caputo, and G. Martoriello, “Innovative plants for distributed poly-generation by residual biomass”, *Energies*, 13(15), 4020, 2020, pp. 834–848. <https://doi.org/10.3390/en13154020>.
- [8] M. Costa, G.Di Blasio, M.V.Prati, M.A.Costagliola, D.Cirillo, M.La Villetta, C.Caputo and G.Martoriello, “Multi-objective optimization of a syngas powered reciprocating engine equipping a combined heat and power unit,” *Appl. Energy*, vol. 275, p. 115418, Oct. 2020, doi: 10.1016/j.apenergy.2020.115418.
- [9] P. Basu, Biomass gasification, pyrolysis and torrefaction: practical design and theory. *Academic press*, 2018.
- [10] K. Peters, X. Xia, A. Pomerantz, and O. Mullins, “Geochemistry applied to evaluation of unconventional resources,” *Unconventional oil and gas resources handbook, Elsevier*, 2016, pp. 71–126. <https://doi.org/10.1016/B978-0-12-802238-2.00003-1>.
- [11] M. J. Prins, K. J. Ptasiński, and F. J. Janssen, “From coal to biomass gasification: Comparison of thermodynamic efficiency,” *Energy*, vol. 32, no. 7, pp. 1248–1259, 2007. <https://doi.org/10.1016/j.energy.2006.07.017>.
- [12] R. Jayathilake and S. Rudra, “Numerical and experimental investigation of Equivalence Ratio (ER) and feedstock particle size on birchwood gasification” *Energies*, vol. 10, no. 8, p. 1232, 2017. <https://doi.org/10.3390/en10081232>.
- [13] C. Caputo, D. Cirillo, M. Costa, G. Di Blasio, M. Di Palma, D. Piazzullo and M.Vujanović, “Multi-Level Modeling of Real Syngas Combustion in a Spark Ignition Engine and Experimental Validation”, *SAE Technical Paper*, 0148–7191, 2019. <https://doi.org/10.4271/2019-24-0012>.
- [14] J. B. Heywood, Internal combustion engine fundamentals. *McGraw-Hill Education*, 2018.
- [15] J. Natarajan, S. Nandula, T. Lieuwen, and J. Seitzman, “Laminar flame speeds of synthetic gas fuel mixtures”, 2005, vol. 4725, pp. 677–686. Presented at *Turboexpo 2005*, doi: 10.1115/GT2005-68917.

- [16] C. Dong, Q. Zhou, Q. Zhao, Y. Zhang, T. Xu, and S. Hui, “Experimental study on the laminar flame speed of hydrogen/carbon monoxide/air mixtures”, *Fuel*, vol. 88, no. 10, pp. 1858–1863, 2009. <https://doi.org/10.1016/j.fuel.2009.04.024>.
- [17] S. Leonhardt, N. Muller, and R. Isermann, “Methods for engine supervision and control based on cylinder pressure information”, *IEEEASME Trans. Mechatron.*, vol. 4, no. 3, pp. 235–245, 1999. doi: 10.1109/3516.789682.
- [18] H. M. Cho and B.-Q. He, “Spark ignition natural gas engines—A review”, *Energy Convers. Manag.*, vol. 48, no. 2, pp. 608–618, 2007. <https://doi.org/10.1016/j.enconman.2006.05.023>.
- [19] D. Agarwal, S. Sinha, and A. K. Agarwal, “Experimental investigation of control of NOx emissions in biodiesel-fueled compression ignition engine”, *Renew. Energy*, vol. 31, no. 14, pp. 2356–2369, 2006. <https://doi.org/10.1016/j.renene.2005.12.003>.
- [20] M. Koç, Y. Sekmen, T. Topgül, and H. S. Yücesu, “The effects of ethanol–unleaded gasoline blends on engine performance and exhaust emissions in a spark-ignition engine”, *Renew. Energy*, vol. 34, no. 10, pp. 2101–2106, 2009. <https://doi.org/10.1016/j.renene.2009.01.018>.
- [21] F. Patuzzi, D. Prando, S. Vakalis, A.M.Rizzo, D. Chiaramonti, W. Tirlir, T. Mimmo, A. Gasparella and M. Baratieria, “Small-scale biomass gasification CHP systems: Comparative performance assessment and monitoring experiences in South Tyrol (Italy),” *Energy*, vol. 112, pp. 285–293, 2016. <https://doi.org/10.1016/j.energy.2016.06.077>.

CHAPTER 3

Numerical modelling, optimization and experimental verification

Chapter 3 focuses on the numerical modelling of the CMD ECO20x system, realized to deeply understand the gasification reaction occurring in the reactor, the engine combustion process and the waste heat recovery. The developed model is used for optimization purposes, in order to achieve the best operating conditions, whose are then verified by experimental characterization to find solutions that are industrially implementable and increase the actual plant competitiveness on the market.

In the last years, numerical simulation has become an indispensable tool for the design and development of engineering systems. Initially, it was limited to high-tech engineering areas such as aerospace engineering; nowadays, with the progresses made in the development of numerical methods and in computer power, it has become an extensively employed instrument to characterize processes and components, hence to solve technological problems in a wide range of applications.

First numerical analyses of a flow inside an engine were carried out in the 1950s. Haller[1] (1945) and Jenny[2] (1950) should be mentioned as important pioneers in the development of numerical methods. Their codes were developed within a one-dimensional (1D) schematization of the computational domain. Today, 1D modelling is still a good approach to assist the development process of energy systems, primarily due to their very low computational effort and satisfying accurateness.

Regarding the numerical modelling of a biomass powered micro-CHP unit that includes a gasifier and an ICE, it can be considered a valid and cost-effective method to optimize both of them by keeping low the time to get relevant results from proper simulations.

For biomass gasification systems, different numerical models have been developed both to estimate reactor performances and to identify variables having the greatest impact on the conversion process. Most of the work presented in the literature proposes thermal-equilibrium models, because of their simplicity and high velocity of convergence [3]. Just to make some examples, Jarungthammachote et al.[4] and Mendiburu et al. [5] developed a thermodynamic equilibrium model based on the evaluation of the equilibrium constants to predict the composition of the producer gas as derived from a downdraft gasifier. The

first uses the Gibbs free energy minimization method, while the latter employs the stoichiometric method. Another numerical analysis based on the Gibbs free energy minimization method of the gasification section was developed by Cirillo et al. [6], using the commercial software Aspen Plus®, and by Costa et al. [3], using the commercial software Thermoflex™. Both pointed out the basic assumptions of a thermodynamic equilibrium model:

- steady-state and isothermal model;
- zero-dimensional and kinetic-free model;
- all the gases involved in the reactions are considered ideal gases;
- the char contains only carbon;
- S and N reactions are not considered;
- tar formation has been neglected;
- instantaneous devolatilization of the biomass is considered;
- considered volatile products are H₂, CO, CO₂, CH₄ and water (H₂O);
- the chemical reactions in the gasifier are in an equilibrium state.

Mehrpooyaa et al. [7] and Yan et al. [8] proposed a comparison between a thermal equilibrium model and a 3-D model, showing that the first one guarantees a maximum error of 10%. Sharma [9] used both thermal equilibrium and kinetic models to simulate a gasifier with good agreement with experimental data and rapid convergence. As an overall consideration, thermal equilibrium models, even without entering in the geometric details of the reactor design, can allow quite simply studying the gasification process and highlighting how syngas quality is influenced by the gasifier operating conditions and, in particular, by the ratio between the biomass and the gasifying agent. This last can be air, pure oxygen or water vapour.

Concerning ICEs numerical simulation, a largely implemented software for 0-1D modelling is GT-Suite® [10]. This includes sub-models of gas exchange, with mixing and combustion calculated using empirical or semi-empirical sub-models. The use of 0-1D models requires detailed design information of the simulated engine and the fuel combustion properties and setting-up empirical relations and coefficients to be assessed in a relatively labor-intensive verification with respect to experimental data.

The here considered engine is a spark ignition (SI) one. Several aspects influence the performance of an engine of this kind, the most essential and straightforward of which is

just spark timing advance. In SI ICEs fueled by traditional fuels, optimization based on spark timing is commonly utilized for calibration of the engine electronic control unit, while there is no similar work in the literature for syngas applications due to the extreme variability of its composition, which is itself dependent upon the initial biomass and gasifier operating conditions. For this reason, identifying the optimal spark timing advance that maximizes the performance of the here analyzed SI engine for different syngas compositions is a remarkable task, as the gained electrical output is responsible for making the plant more competitive in the industrial market. On the other hand, it must be said that, once the initial biomass and the design of the gasifier are set, what most influences the composition of the producer gas is the equivalence ratio (ER) within the reactor, namely the actual air-to-feedstock mass ratio divided for the air-to-feedstock mass ratio needed for complete combustion.

In this thesis, two software tools were used to create an optimization tool that can forecast m-CHP system performance under a variety of gasifier and engine operating scenarios (i.e. equivalence ratio at the gasifier, biomass composition and ICE spark advance timing). Thermoflex™ is used to model the syngas production, cooling, and cleaning section, while the GT-Suite® environment is used to model the engine, as an increased detail can be achieved. The following models are described in detail in the following sections.

3.1 Modelling of the micro-cogeneration system

3.1.1 Thermoflex® model

Thermoflow Inc.'s Thermoflex™[12] software is one of the numerous commercial thermal engineering tools for the modelling and development of power and cogeneration plants. It uses the first thermodynamic principle method, namely mass and energy balance, to analyze energy conversion systems and their components in steady state condition. Unlike other tools, Thermoflex™ is a more generic, fully flexible software that can be used to model a wide range of thermal systems, including gas turbines, steam cycles, gasification, photovoltaic systems, etc..

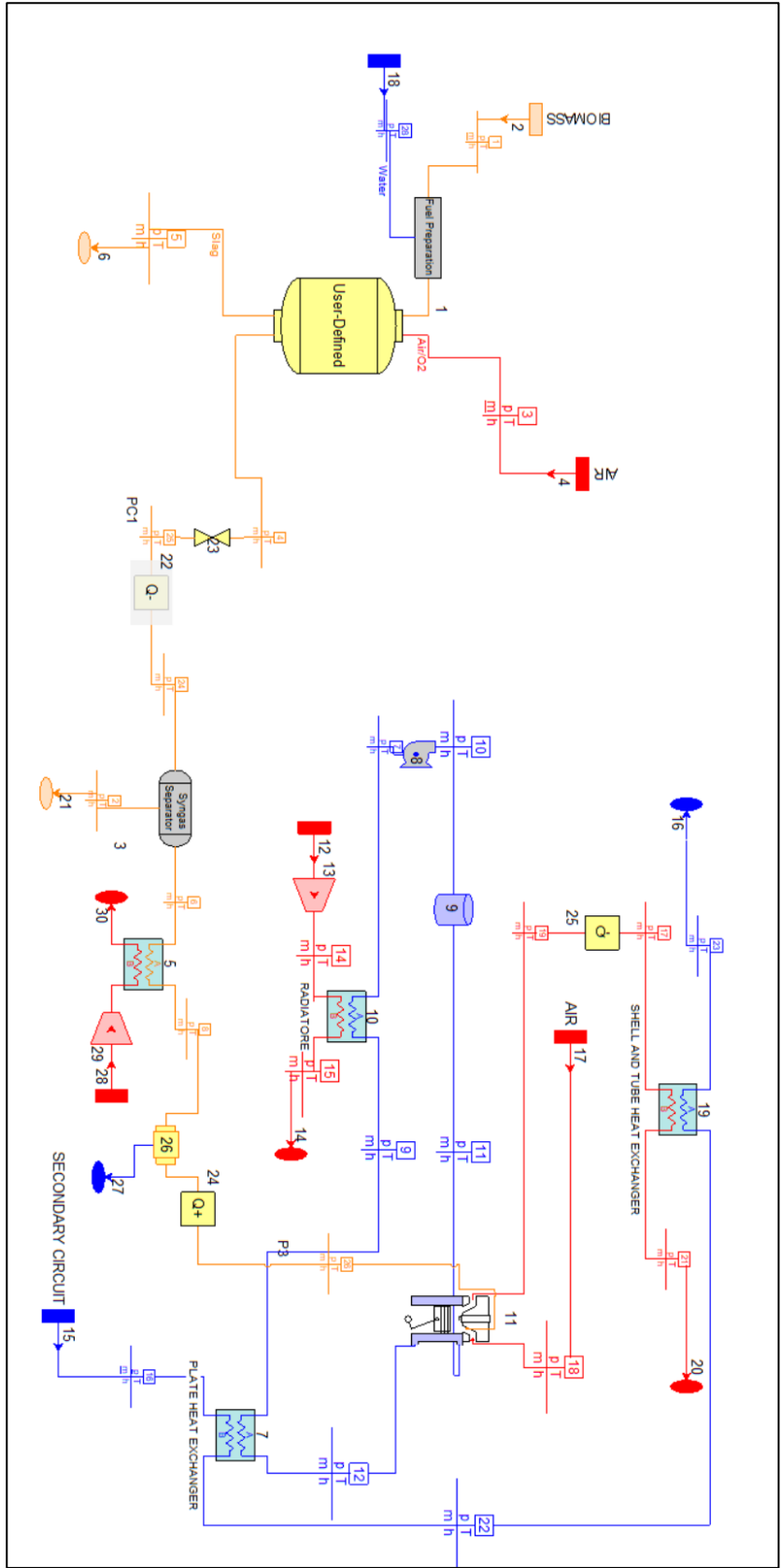


Figure 3. 1: The CMD ECO20x system model (Thermoflex™ environment)

#	Component	Input	Output
1	Gasifier	p_{syn} , Conversion efficiency	CO_{syn} , CH_{4syn} , N_{2syn} , CO_{2syn} , H_{2syn} , H_2O_{syn}
2	Biomass Entrance	T_{bio} , p_{bio} , \dot{m}_{bio} and biomass proximate and ultimate analysis	-
3	Syngas separator	Moisture separator efficiency	$CO_{syn,dry}$, $CH_{4syn,dry}$, $N_{2syn,dry}$, $CO_{2syn,dry}$, $H_{2syn,dry}$
4	Air entrance	T_{air} , p_{air} , \dot{m}_{air}	-
5	Cooler	Thermal efficiency	T_{syn} , p_{syn}
6	Ash exit	-	\dot{m}
7	Plate Heat exchanger	Size, Thermal efficiency	T_{syn} , p_{syn}
8	Pump	Efficiency	T_{H_2O} , p_{H_2O}
9	Tank	Capacity	-
10	Radiator	Thermal efficiency	T_{H_2O} , p_{H_2O}
11	ICE	Power output, fuel primary energy	T_{exh} , p_{exh} , \dot{m}_{exh}
12	Air entrance	T_{air} , p_{air} , \dot{m}_{air}	-
13	Pump	Efficiency	-
14	Air exit	-	T_{air} , p_{air}
15	Secondary circuit entrance	T_{H_2O} , p_{H_2O} , \dot{m}_{H_2O}	-
16	Secondary circuit exit	-	T_{H_2O} , p_{H_2O}
17	Air entrance	T_{air} , p_{air} , \dot{m}_{air}	-
18	Water input (disabled)	-	-
19	Shell and tube heat exchanger	Size, Thermal efficiency	T_{H_2O} , p_{H_2O}
20	Exhaust gases exit	-	T_{exh} , p_{exh}
21	Moisture exit1	-	T_{H_2O} , p_{H_2O}
22	Temperature control	-	T_{syn}
23	Valve	Pressure drop	p_{syn}
24	Temperature control	-	T_{syn}
25	Temperature control	-	T_{exh}
26	Moisture separator	Efficiency	T_{H_2O} , p_{H_2O}
27	Moisture exit2	-	T_{H_2O} , p_{H_2O}
28	Air entrance	T_{air} , p_{air} , \dot{m}_{air}	-
29	Air exit	-	T_{air} , p_{air}

Table 3. 1: Thermoflex™ components description

For a good view of the specific scheme, each component presents a specific color based on the treated fluid:

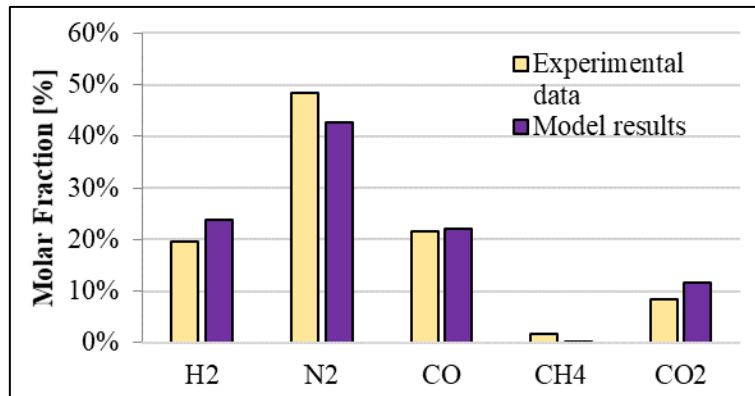
- red: gas (including combustion products);
- blue: water (in any phase);
- orange: fuel;
- purple: refrigerant (or however high molecular weight fluid);
- pink: thermal oil.

Each component has an options menu where the user can configure all design settings (i.e. efficiencies, head or heat losses, desired pressure and temperature, etc.). Once the plant layout of interest is defined, proper boundary conditions are set and simulation can then begin. After convergence is achieved, results are displayed. It should be noted that the results are based on full-load steady-state conditions, and the transient phase is not included. Off-design and part-load simulations, on the other hand, can be achieved after the design computation is accomplished.

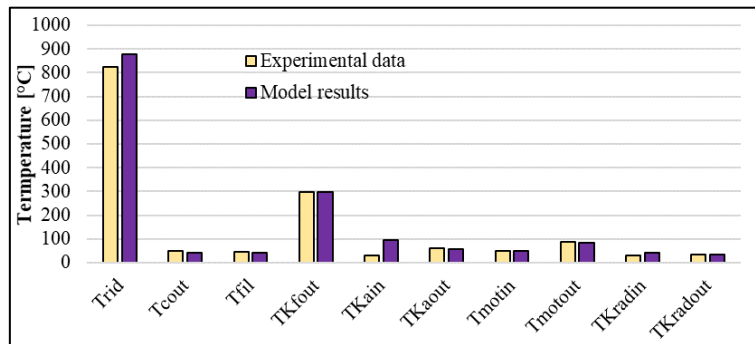
A schematization of the CMD ECO20 system is shown in Figure 3. 1 while Table 3. 1 reports the name and requested input/output for each component. T, \dot{m} and p stands for temperature, mass flow and pressure.

The fundamental advantage of this gasifier model, over others that are always based on the concept of thermal equilibrium, is that it allows entirely duplicating the system as it is, by accounting for the influence of the temperature of the engine exhaust gases on the operation of the gasifier, as well as for the influence of the presence of cleaning devices affecting the final syngas composition. However, as seen in Table 3. 1, the ICE model requires the mechanical (or electrical) power and the fuel primary energy, which cannot be known a priori, due to the coupling between the gasifier and the engine, hence to the influence of the biomass composition on the ICE performance. These are therefore evaluated through a proper model developed within GT-Power® environment.

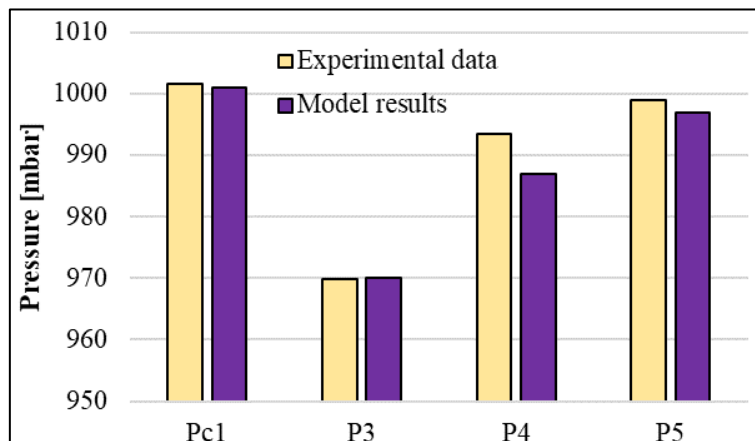
Figure 3. 2 shows the results of the numerical model as compared to the experimental data. The proposed model shows a very good agreement with experimental data.



a)



b)



c)

Figure 3. 2: Model results compared with experimental data for syngas composition (a), temperatures (b) and pressures (c) in various points of the plant [3].

3.1.2 GT-Power® model

GT-Power® [10] is the market-leading engine simulation software, thanks to its state of the art Navier-Stokes pressure wave solver, detailed thermodynamics, and advanced combustion models. GT-ISE® is the primary interface for creating models, defining simulation settings, and running simulations (both single and batch). An option menu is associated with each component. Results are shown in GT-post®, a graphical interface that enables viewing and manipulating of the data collected from the simulation. In a GT-Power® model, the Euler equations are solved in one dimension. In other words, the RANS equations do not account for viscosity effects.

The system is modelled as separate sections such as pipes, pipe bends, flow splits, and other components such as the engine cylinders, cylinder valves to replicate all engine components.

The flow properties through the more complex parts of the engine, such as the intake and exhaust valves, the flow through the compressor and turbine, and the combustion process in the cylinder, are modelled without accounting for the actual geometrical features and rely on empirical relations and measured input data, while the flow properties through the pipe components are modelled with the assumption of one-dimensional flow.

Pressure, temperature, density, internal energy, enthalpy, and species concentrations in each volume are considered to be uniform.

When simulating any kind of engine, spark or compression ignited, it is important to apply the correct and appropriate combustion model.

For a non-traditional fuel such as syngas, the widely-used Wiebe approach, defined by equation (3.1) [13], is not preferable, since it requires information about the turbulence intensity and length scale, which are not available for syngas, and it does not account for any changes in fuel composition.

$$x_b(\theta) = 1 - \exp\left(-a \frac{\theta - \theta_0}{\Delta\theta}\right)^{m+1} \quad (3.1)$$

where $x_b(\theta)$ is the mass fraction burned, θ is the crank angle, θ_0 is the crank angle at the start of combustion, $\Delta\theta$ is the combustion duration defined as the difference between the start of combustion and the end of combustion, m is the form factor because it determines

the shape of the combustion process curve, and α is the efficiency parameter because it controls the duration of the combustion process.

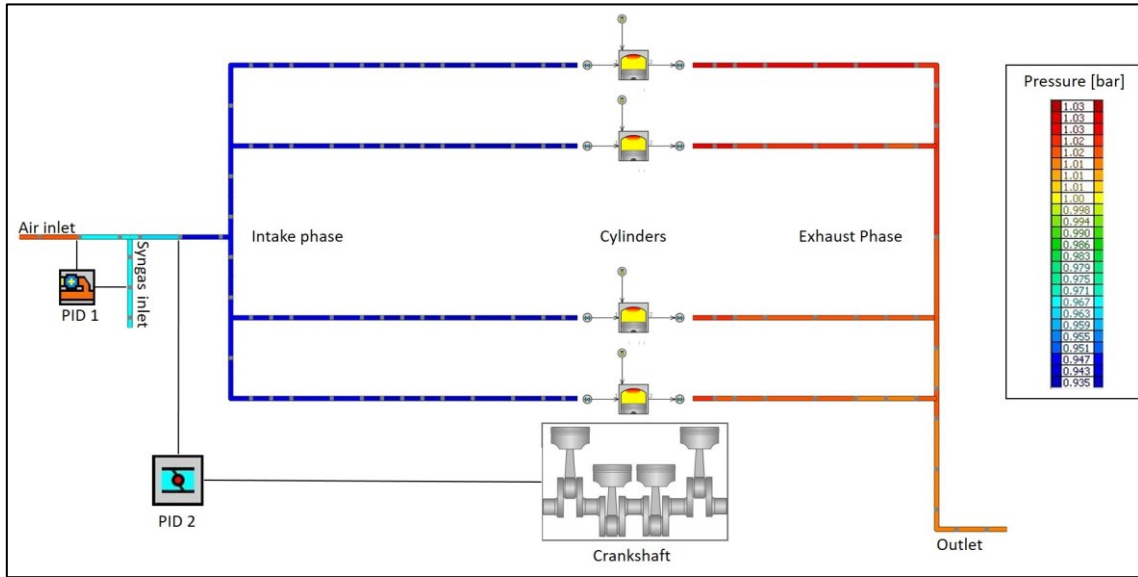


Figure 3. 3: Engine model in GT-Suite®.

A preferable approach is the one based on adjusting parameters regulating combustion reported in equation (3.2):

$$S_L = [B_{max} + B_{\varphi}(\varphi - \varphi_{max})^2] \left(\frac{T_u}{T_{ref}} \right)^{\alpha} \left(\frac{p}{p_{ref}} \right)^{\beta} \quad (3.2)$$

where B_{max} is the maximum laminar flame speed [m/s] at 300 K and 1 bar; B_{φ} indicates the dependence of the laminar flame speed upon the equivalence ratio; φ is the equivalence ratio; φ_{max} is the equivalence ratio at maximum laminar flame speed; T_u is the unburned gases temperature; p is the operative pressure; α is a parameter indicating the growth of the laminar flame speed with temperature; β is a parameter indicating the decrease of the laminar flame speed with pressure.

Considering the absence of any kind of information about this fuel in the GT-Power library, there was the need to perform a specific study of the characteristics of this fuel in a different way. For this reason, a CHEMKIN calculation was performed by using a detailed kinetic scheme of reaction, namely the GRI-mech 3.0 kinetic scheme for methane, as this includes in the reaction path and between the participating components, all the reactions and species, respectively, involved in the syngas combustion [14]. Table

3. 2 shows the comparison between the main parameters of equation (3.2) for syngas, gasoline and diesel fuels.

Laminar flame speed parameters	Syngas from Woodchip A1+ [15]	Gasoline	Natural Gas
$B\phi$ [m/s]	-0.679	-0.549	-1.649
φ_m	1.2	1.1	1.06
α	2.20	2.129	1.58
β	-0.45	-0.217	-0.39

Table 3. 2: Comparison between laminar flame speed parameters used to evaluate laminar flame speed at different pressure and temperature for stoichiometric air/fuel mixture.

The here considered 1D ICE model, to account for the gasifier-engine coupling, is fuelled by two reservoirs: one for air and one for syngas. The Thermoflex™ gasifier and cooling system model are used to calculate pressure and temperature of both fluids as well as the syngas composition. The air mass flow rate is controlled by a PID controller (PID 1 in Figure 3. 3) that acts on the throttle valve opening, hence on the stoichiometry of the mixture. Another PID controller (PID 2 in Figure 3. 3) is set to regulate the mixture to achieve an imposed desired power, as happens in the real system through the panel control.

Figure 3. 4 shows the comparison between the average pressure cycle measured in the first cylinder of the engine at the maximum load and the pressure cycle calculated with the 0D-1D model. The obtained agreement is possible thanks to the original implementation of the aforementioned combustion model.

The main found difference is on the peak pressure, with an error of 5.6%, that is acceptable for a 0-1D model.

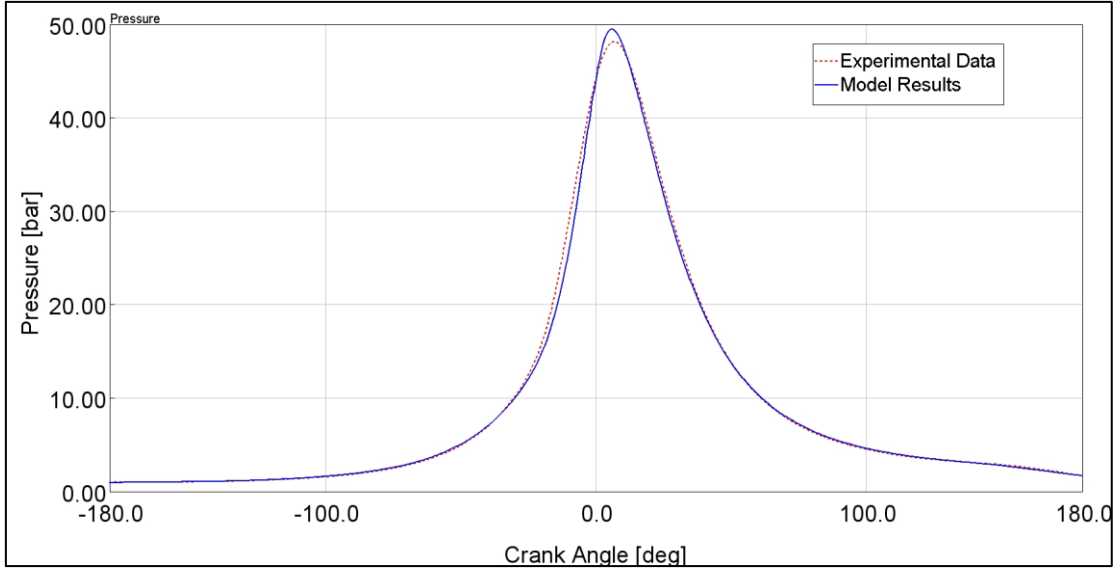


Figure 3. 4: Comparison between model results and experimental data relevant to the engine pressure cycle [3].

3.2. Numerical optimization

Numerical optimization may assist in finding the best way to deal with a complex system by looking for the best control logic to achieve some defined objectives. Coupling a numerical model of a given engineering system with an algorithm for decision-making has been proved an effective and cost-saving option to achieve the desired results even without resorting to real counterparts and spending time in heavy experimental tests.

Multi-target optimization could have contrasting objectives, in which a reduction for one target makes for an increment in another one.

The primary objective of single and multi-objective optimization is to numerically model the choices made by the user or designer. A problem that needs to be optimized [3], [16] can be written as :

$$\begin{cases} \max\{F_i(x_1, \dots, x_n)\} & i = 1, \dots, m \\ G_k(x_1, \dots, x_n) \leq 0 & k = 1, \dots, l \end{cases} \quad (3.3)$$

$$G_k(X_{1...nv}) > 0 \quad (3.3)$$

$$G'_n(X_{1...nv}) < 0 \quad (3.4)$$

$$G''_m(X_{1...nv}) = 0 \quad (3.5)$$

with x as the variable vector, F the objective vector and G the constraint vector. The values of n -input variables of x_j have to be found in such a way that respect the G_k

constraints and that m -objective functions F_i are maximized. When $i > 1$ and objectives are conflicting, the problem is called multi-objective.

As not always $F_i(x)$ and $G_k(X)$ are known, it is compulsory to investigate space solutions completely and effectively. This space solution is called a Design of Experiments (D.O.E.). D.O.E. enables users to:

- reduce the size of the project and the number of experiments to be run;
- get relevant information;
- test the solutions robustness, i.e. capacity to remain unaffected by tiny changes in design variables;
- understand the objective functions behavior;
- understand the relationship between objectives and constraints – sensibility analysis.

The D.O.E. size depends upon the number of variables, intervals within each variable are divided and constrains.

3.2.1. Algorithms

An initial family of solutions is formed once the D.O.E. is chosen, however, to fully investigate the space solution, an optimized method must be chosen.

A successful algorithm uses to exploit the previous results to determine the next family, so to explore deeply the D.O.E. and find absolute maximum or minimum points.

It is characterized by:

- *robustness*, the ability to tolerate perturbations that might affect the system functionality;
- *accuracy*, degree of closeness measurement;
- *velocity of convergence*, speed to get a solution;

The next sections describe single-objective and multi-objective algorithms.

3.2.1.1 Single-objective algorithm: gradient methods

Single-objective algorithms usually involve gradient methods. A gradient method is a generic and straightforward optimization technique that iteratively changes a parameter

to increase (or decrease in the case of minimization) the gradient of the objective function, defined by expression (3.6). A gradient ascending solution is guaranteed to be locally optimal, which corresponds to a local mountain peak, and the objective value cannot be enhanced by any local parameter update under a moderate assumption [17].

$$\vec{\nabla}f(x_o) = \begin{cases} \frac{\partial f}{\partial x_1} \\ \vdots \\ \frac{\partial f}{\partial x_n} \end{cases} \quad (3.6)$$

The basic structure of the iteration is outlined in the following steps.

Given an initial starting vector \overline{X}^0 , an estimate of the Lagrange multiplier λ^0 , a set of active constraints, penalty parameters π_c^0, π_d^0 , and an upper bound M for the number of unconstrained minimizations to be performed, set:

1. *Outer loop* begins: $k \leftarrow 0$;
2. *Convergence test*: check the optimality condition and terminate with X^k as solution or exit if $k > M$.
3. Begin *optimization cycle*: $\overline{X}^0 = \overline{X}^k$ being the starting point, let $\overline{X}^{k+1} = \overline{X}_{p+1}$ be the best approximation after p+1 inner iterations of the optimization problem.
4. Update the *Lagrange multiplier*: modify, if necessary, the specification of the active constraints set and compute a new estimate of the Lagrange multiplier according to the recursive formula:

$$\lambda^{k+1} = \lambda^k - \pi_c^k * C(\overline{X}^{k+1}) \quad (3.7)$$

5. *Penalty update*: increase the penalty parameters if the constraints violations at X^{k+1} have not been reduced sufficiently. The π_d, π_c increase is operated by:

$$\pi^{k+1} = \frac{\lambda^{k+1}}{\varepsilon^k} \quad (3.8)$$

The error term, ε^k , is progressively decreased at each new cycle.

6. *Outer loop update*: set for the new cycle and return to step 2.

Step 3 is carried out with a Newton-type method whose search directions are computed as:

$$\min[F(\bar{X})] \rightarrow \bar{X}_{l+1} - \bar{X}_l = -\nabla F(\bar{X}_l) * \bar{H}^{-1} * [F(\bar{X}_l)] \quad l = 0, p \quad (3.9)$$

The computational cost of the method is therefore mainly due to the estimate of the Hessian matrix, \bar{H} , and of the gradient. In addition, the algorithm implies the positive definiteness of \bar{H} , in which case quadratic convergence is attained if the initial vector guess, \bar{X}^0 , is sufficiently close to the final solution. When \bar{H} is indefinite, the Newton method is replaced by a simpler steepest descent method or quasi-Newton method of the following type.

Quasi-Newton method or Broyden Fletcher Goldfarb Shanno (BFGS) [18] employs a pseudo-Hessian matrix to maintain a high velocity of convergence.

$$\lim_{i \rightarrow \infty} [H_i] = [J]^{-1} \quad (3.10)$$

Given a starting point x_0 that belong to the initial D.O.E., it estimates H^{-1} (method varies) and calculates changes in x using the following equation:

$$x^{k+1} = x^k - [H^{-1}]_k * \vec{\nabla} f(x_k) \quad (3.11)$$

The main pros of gradient methods are the quadratic velocity of convergence and high accuracy, even if this method presents low robustness and do not well handle constraints.

3.2.1.2 Multi-objective algorithm (genetic methods)

The term genetic algorithm (GA) refers to a family of models or abstractions of biological evolution based on Charles Darwin's theory of natural selection, introduced by John Holland and his collaborators in the 1960s and 1970s [19]. They are a class of numerical and combinatorial optimizers that are especially useful for solving complex nonlinear and nonconvex problems. Every point of a n-variable space is like an individual and has a given genetic code. Points are grouped in generation and the first generation is D.O.E. itself. The operative structure of the algorithm follows a series of fundamental steps summarized by Goldberg in 1989 [20], even though Holland in 1975 was the first to use crossover and recombination, mutation, and selection in the study of adaptive and artificial systems. GA follows 6 fundamental steps, depicted in Figure 3. 5:

- 1) A *random generation* of an initial population of individuals.

- 2) A *mating-pool* phase that matches the best individuals for the following reproduction step. The choice criteria are the roulette-wheel one, which assigns a higher probability level to those individuals who are characterized by the best values in the objective function.
- 3) A *cross-over* process that allows a gene exchange between the individuals mated and therefore the generation of new individuals, to achieve a species evolution in the impeller population.
- 4) *Genetic Mutations* in the best individuals, according to random (± 1) changes in a single gene within their genetic string.
- 5) *Selection* of individuals who either will survive or must be killed.
- 6) The cycle of genetic search is repeated from step (1), but the random generation is allowed for a reduced number of new individuals, to take into account those who survived after the selection at step (5).

The process is considered to be concluded if the same optimal genetic code has been found after five consecutive cycles.

Each point of the n-variable space is like an individual, with a certain given genetic code [16]. Each individual is characterized by a unique set of variables (genes) that form a string or chromosomes (solution). Through the use of a fitness function, each individual is associated with a score (rank) that represents its ability to compete with other solutions. Individuals are grouped into generations, whose first one is the DOE space set by the user itself.

As regard selection, an individual with a good value of an objective function or low rank has a good probability to be selected to transmit their genetic heritage to the next generations. In the mating process, two solutions with low rank, i.e. parents, are selected to originate a new generation. For each pair of parents, a crossover point is chosen randomly and some individuals are generated by exchanging genes of their parents until the crossover point is reached. Finally, some individuals are generated through the mutation of a gene in the chromosome string to bring absolute's research to unexplored zones. Best genes are transmitted untouched to the next generation (elitism). The next generation is selected as follows:

1. solution with low rank are selected;
2. if the rank is the same, solutions with larger crowding distances are selected.

A combination of these operators creates:

- following generation with a better mean behavior;
- solutions completely new;
- better individual than their fathers.

With respect to single-objective optimization, in which the optimal solution is univocally determined, problems with multiple objectives give rise to a set of optimal solutions, that is known as Pareto-optimal solutions (or simply Pareto front). These last, in the absence of any further information, are all valid as relevant to the set objectives. In other words, the Pareto front is the element in a GA that allows dealing with conflicting goals, none of which is dominating one on each other [21].

Genetic algorithm, differently from gradient descent ones, has better robustness but lower accuracy and velocity.

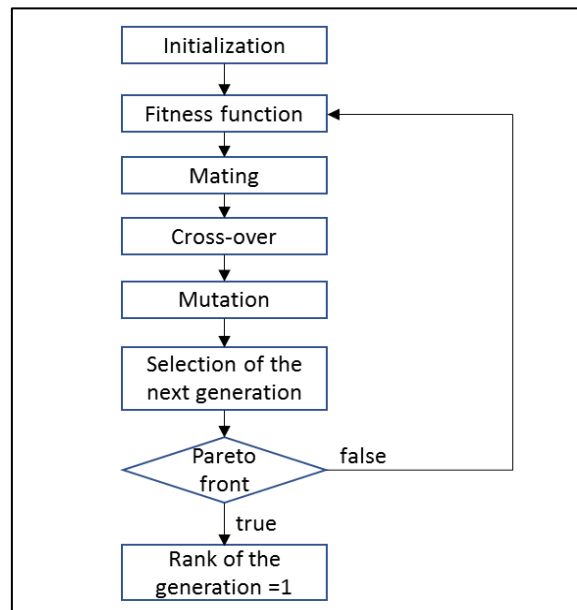


Figure 3. 5: Flowchart of genetic algorithms.

To choose a citizen from the Pareto front a Decision Maker (DM) could be applied. A weighted stress function is here used for optimization as it can integrate the user's preferences [22]. The main principle is based on the idea that the best solution must:

1. belong to the Pareto Frontier;
2. satisfy the best weighted distance between criteria i and the i -th component of the ideal objective vector (Figure 3. 6) – i.e. the vector maximizing each one of the objective functions.

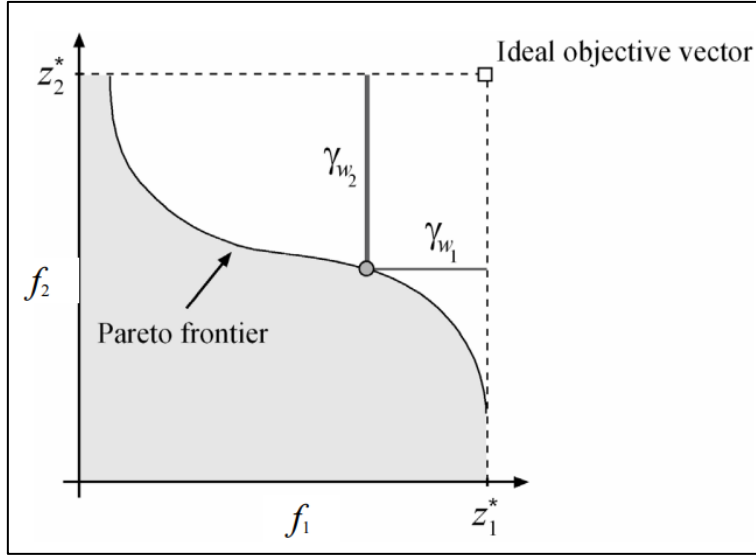


Figure 3. 6: Stresses associated with an optimal solution for an optimization problem with two criteria [22]

For each solution belonging to the Pareto frontier, two stresses, γ_{w1} and γ_{w2} , are defined, each one associated with the corresponding criteria, f_1 and f_2 . The stress γ_{w1} is not sufficient for searching solutions with the best values, due to the conflicting nature of criteria.

The weighted distance is calculated, directly by the optimizer by following the equation (3.12):

$$\gamma_{w_i}(x) = \begin{cases} \frac{(w_i)}{2} \tan\left(-\frac{\pi}{\Psi(w_i)}(x - w_i)\right) + \xi(w_i), & x < w_i \\ -\frac{\xi(w_i)}{\tan\left(\frac{\pi}{\varphi(w_i)}(w_i - 1)\right)} \tan\left(\frac{\pi}{\varphi(w_i)}(x - w_i)\right) + \xi(w_i), & x > w_i \end{cases} \quad (3.12)$$

$$\varphi(w_i) = \frac{3}{4}(1 - w_i)^2 + 2(1 - w_i) + \delta_1 \quad (3.13)$$

$$\Psi(w_i) = \varphi(w_i) + 4w_i - 2 \quad (3.14)$$

$$\xi(w_i) = \frac{1}{\tan\left(-\frac{\pi}{2 + 2\delta_2}\right)} \tan\left(\frac{\pi}{1 + 2\delta_2}\left(w_i - \frac{1}{2}\right)\right) + 1 \quad (3.15)$$

3.3 Optimization of the gasification section

As mentioned in Chapter 1, in a gasification process, the ratio between the biomass and air mass flow rate and the gasification temperature deeply influence the resulting syngas composition. In the present study it must be considered that these variables heavily affect the performance of the whole CMD ECO20x unit. An ER value between 0.3 and 0.4 [3], [23] represents the right compromise solution between an acceptable calorific value of the syngas and a not excessive formation of tar and other heavy hydrocarbons [3].

An optimization to increase the CMD ECO20x engine electrical output was made by using the afore described models, by varying the gasifier equivalence ratio (ER) and the engine start of spark (SA). The single-objective optimization was resolved using a BFGS algorithm, as explained in the previous paragraph.

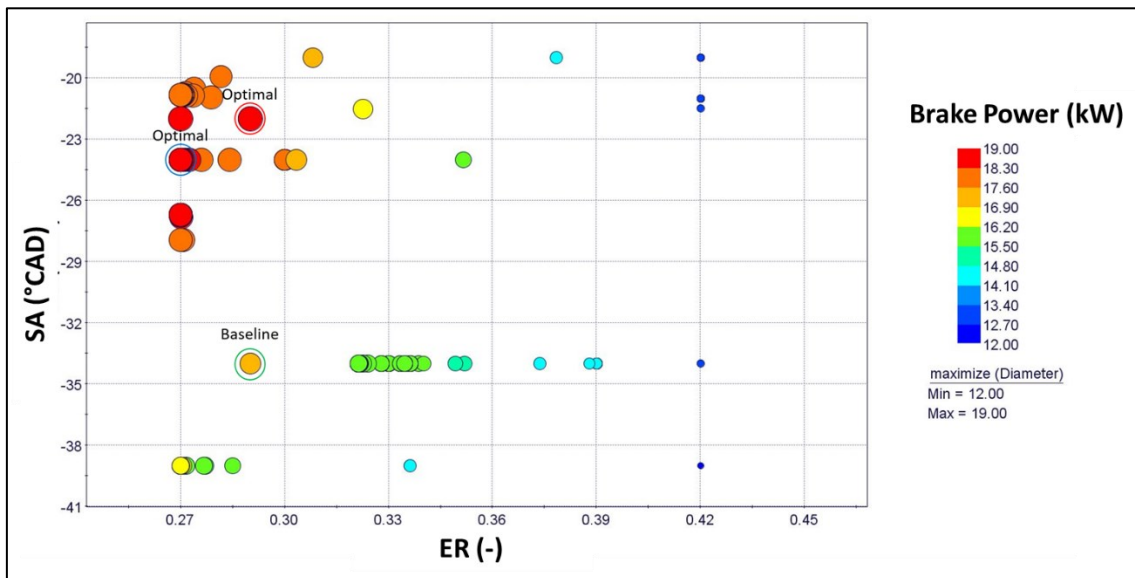


Figure 3. 7: Bubble chart representing the value of the ICE brake power in the DOE space.

Figure 3. 7 reports the bubble chart of the proposed optimization. Compared with the case of 0.29 ER of the baseline condition, the dependence of engine output power (Brake Power) upon this parameter shows the necessity of improving the blending between air and biomass to reach a lower equivalence ratio. This, coupled with a delayed spark timing, brings an improvement of almost 20% on the brake power.

CMD ECO20x did not have an ER regulation. To overcome this condition, manual ball valves were therefore set up in two points of the system. The first placed at the air inlet,

highlighted in red in Figure 3. 8, the second inserted in the place of the gasifier ignition plug, highlighted in blue in Figure 3. 8.



Figure 3. 8: Installation of ball valves on CMD ECO20x.

The red valve has the effect of choking the air entering the reactor; the blue one, if opened, adds new air in the inlet ducts, increasing the gasifying agent mass flow rate. The two valves were opened and closed, independently one from each other, to evaluate which of the two airflow control modes was the most effective.

An air mass flow sensor was positioned on the main air circuit and not after valves, due to the proximity to the reactor high temperature, which could destroy the sensor or invalidate the measurement.

It was found that with the opening of the blue valve, therefore adding air to the gasifier directly into the combustion area, the production of combustible gas stopped. The lack of syngas production, due to complete combustion in the gasifier, resulted in the instant shutdown of the engine.

The opening of the blue valve decreases the main inlet mass flow rate. This effect can be explained by assuming that the system adapts itself to the addition of new airflow in the ducts and, therefore, the increase of the airflow rate by balancing with the reduction of the main conduct air flow rate.

This solution does not allow to change the gasifier ER, even though it has a minor benefit on the pressure drop on the cleaning circuit.

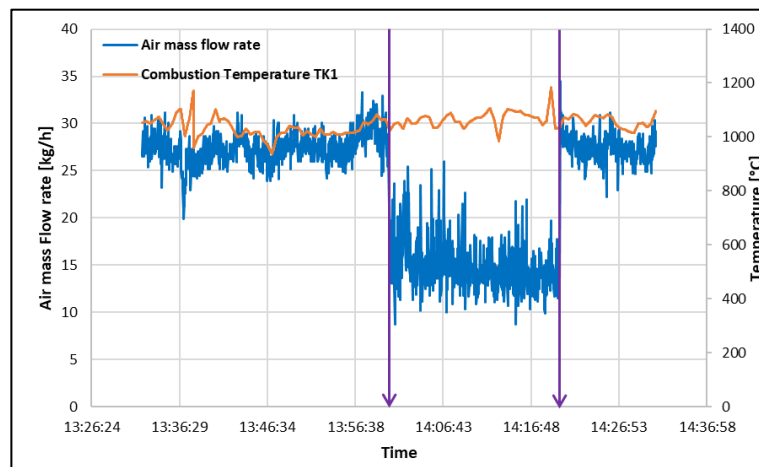
Table 3. 3 reports the airflow rate and the relative pressures before and after the valve opening.

	Blue valve closed	Blue valve opened
Main conduct air mass flow rate (kg/h)	46.8	32.3
Relative pressure in the gasifier (bar)	-13	-7
Relative pressure after cyclone (bar)	-15	-8
Relative pressure after cooler (bar)	-46	-41

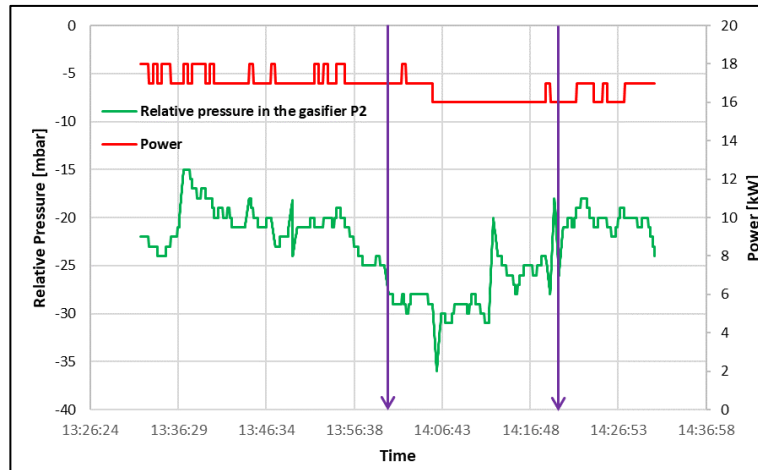
Table 3. 3: Effect of opening and closing blue valve on some averaged quantities.

By closing the red valve, thus decreasing the amount of air to the gasifier, the system continued to operate, allowing to acquire useful data for the characterization of the syngas.

Figure 3. 9 shows some quantities measured in this last case, at the gasifier and the corresponding power of the entire plant. In particular, the flow of air entering the gasifier, the combustion temperature in the area where the air is mixed with the biomass, the pressure in the lower part of the reactor and the power delivered by the engine were measured. In the graphs, the beginning and end of the trial period are indicated with two purple arrows.



a)



b)

Figure 3. 9: Trend of the measured airflow at the reactor inlet and the temperature in the combustion zone (a) and pressure in the lower part of the reactor and power delivered by the engine (b).

The following Table 3. 4 shows the values of the aforesaid quantities averaged over an interval of time equal to that of the reduction immediately before, during and immediately after this. From the images, it is evident that the decrease in the flow rate did not affect the combustion temperature in the reactor, the trend of which remained almost stable around an average value. Conversely, the effect on the pressure and power delivered by the system is clearly more substantial.

	Red valve opened	Red valve closed
Air mass flow rate [kg/h]	27,30	14,92
Relative pressure in the gasifier [mbar]	-21,02	-28,55
Combustion temperature [°C]	1032,33	1066,40
Power [kW]	17,28	16,30
Syngas composition (%vol)		
H₂	19,80%	20,65%
N₂	45,70%	44,76%
CO	23,60%	24,11%
CH₄	1,80%	1,73%
CO₂	9,10%	8,75%
LHV	5.75 MJ/Nm ³	5.88 MJ/Nm ³

Table 3. 4: Average values of some of the quantities measured before, during and after the partialization.

Indeed, following the reduction of the air entering the reactor, the pressure drops inside it increased (the pressure P2 shown in green in Figure 3. 9b is the pressure in the lower part of the reactor), resulting in less filling of the reciprocating engine and less power fed into the grid by the system.

During the tests, two syngas bags were acquired for the analysis of their composition. The averaged results as obtained from the gas chromatograph are shown in Table 3. 4.

The decrease in airflow did not cause major variations on the biomass gasification process and the composition of the syngas, but it mainly reverberated on the increase in pressure drops which, in turn, led to a lower power fed to the national grid. This effect can be explained by assuming that the system adapts its operation to the lower airflow by processing the same amount of biomass but over longer times, with the result of decreasing the instantaneous biomass flow in the considered range. Since the reactor works as a batch reactor and it is not possible to release the biomass inlet from the measurement of its filling level, what happens is that the modification of the airflow determines an automatic modification of the hopper load and therefore the biomass flow rate, for an equivalence ratio which remains therefore unchanged. In other words, from the analysis carried out, it emerged that at present there is a technological difficulty in varying the equivalence ratio to the reactor because, to a variation of the incoming air, the process adapts itself to maintain its operation and ER.

The coupling between the two main elements of the cogeneration system, gasifier and engine and the consequent difficulty in separating the gas production section from the unit of use (because the engine is the organ that sucks in the air so that it reacts with biomass to form syngas) led to the abandonment of this solution.

3.4 Optimization of the internal combustion engine

Spark advance angle affects deeply the engine power output, by influencing the compression phase [21]. Finding the best value of this variable depends on speed and load. A bell-shaped curve (Figure 3. 10) is a classical behaviour of the engine torque as a function of the spark advance. As shown in the previous paragraph, the necessity to delay the spark advance has been highlighted when the single objective optimization was

performed. However, the NOx and CO emission should be considered when optimizing the engine section.

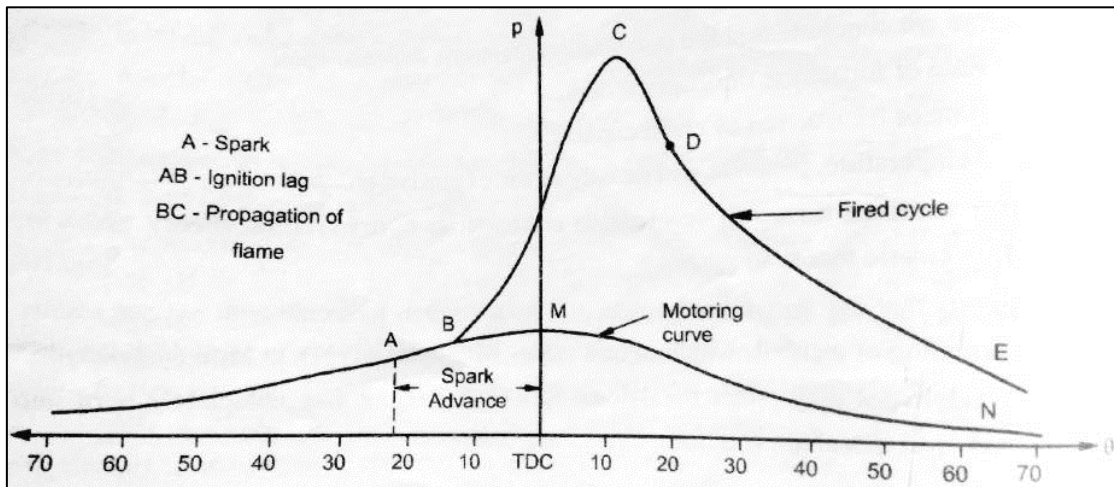


Figure 3. 10: SI engine combustion phase [13].

Changing the air-to-fuel ratio also affects the combustion development and the amount of pollutants released at the exhaust, whereas increasing the EGR fraction creates an inert part of gases in the combustion chamber, thus reducing the free space for the fresh mixture, practically so realizing a virtual reduction of the real displacement.

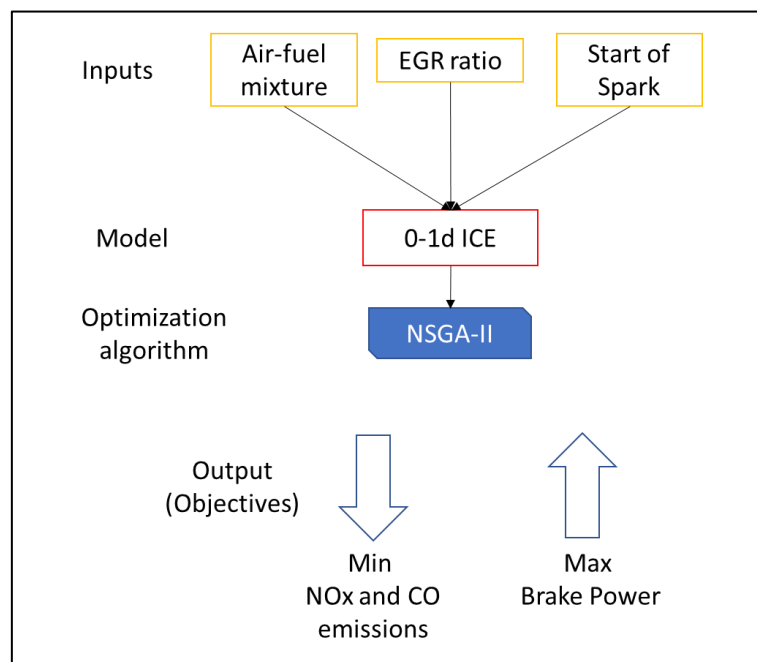


Figure 3. 11: Workflow of the optimization engine problem.

The afore-described 0-1D engine model was embedded to perform a multi-objective optimization, with a Non-dominated Sorting Genetic Algorithm II (NSGA-II) of the chosen controlling parameters. The set workflow is shown in Figure 3. 11. Like all GAs, the main parameter to be considered for the chosen algorithm, the NSGA-II, is the number of generations, as well as the cross-over and mutation probability (Table 3. 5). A high value of mutation probability reduces premature convergence, brings casualty and allows a better exploration of the D.O.E.. However, in order to reduce the calculation time, a proper number of generations could not be high, as highlighted by D'Errico et al. [24].

The baseline working condition of the considered SI engine is with a mixture at the stoichiometric ratio, EGR fraction equal to zero and spark ignition of 34° BTDC. Therefore, the D.O.E. (Table 3. 5) is set around these values. High amplitude variations are not feasible for an efficient combustion process. The first generation is built using a quasi-random algorithm, namely based on a random number generation.

Parameters	-
Number of generations	9
Cross-over probability	0.9
Mutation probability	1.0
Variables	Ranges
Spark Timing (°BTDC)	19-36
EGR rate (%)	0-15
Lambda	0.9-1.1
Objectives	Max or Min
NO _x emission	Min
CO emission	Min
Brake Power	Max

Table 3. 5: Summary of the engine optimization.

Three objectives, the minimisation of NO_x and CO emissions and the maximisation of ICE brake power, are selected to let the population evolve up to the Pareto front. Constant engine rotational speed, load, inlet pressure and temperature are taken as for the baseline case. The computational efficiency is improved by excluding unfeasible and unreal solutions.

In order to preliminarily characterize the syngas-powered powerplant, a parametric analysis was performed, in which each variable of interest was changed separately while

the other two were left unchanged. Figure 3. 12 depicts the outcomes of each individual variation. By appropriately managing parameters, significant improvements can be achieved.

Figure 3. 12a to Figure 3. 12c shows the net reduction of NO emissions obtained by lowering the start of the spark to 19° BTDC, with an obvious increase in CO content in the exhaust flow and a low IMEP, or the reduction of both the IMEP and NO as a result of increasing the EGR ratio, as shown in Figure 3. 12g to Figure 3. 12h.

The NSGA-II applied to the set problem converges after 50 generations of individuals. Each generation produces a further generation up to the optimal configuration constituting the Pareto front at convergence.

Table 3. 6 reports the citizens of the Pareto front and their worsening/improvement concerning the baseline case (34°BTDC – Stoichiometric ratio – EGR =0%).

The citizens of the Pareto front include both the optimum point of each individual variable, as one target remains constant while the others change, as well as solutions that are the best balance for reducing emissions without severely reducing brake power. The trade-off between emissions and the ICE power is quickly confirmed: fewer NO_x and CO emissions result in reduced brake pressure.

The analysis shows a wider range of possible operating conditions of the SI engine of the CMD ECO20 system and highlights the necessity of increasing the air mass flow rate and work with slightly leaner mixtures. In these cases, higher reductions of NO_x and CO are possible, even though with a slight reduction of brake power. A stoichiometric mixture and a delayed spark timing led both to an increase of brake power and a reduction of NO_x emission, while CO emission increases.

A solution with high emission reduction without penalizing too much power is the preferred one (in green in Table 3. 6).

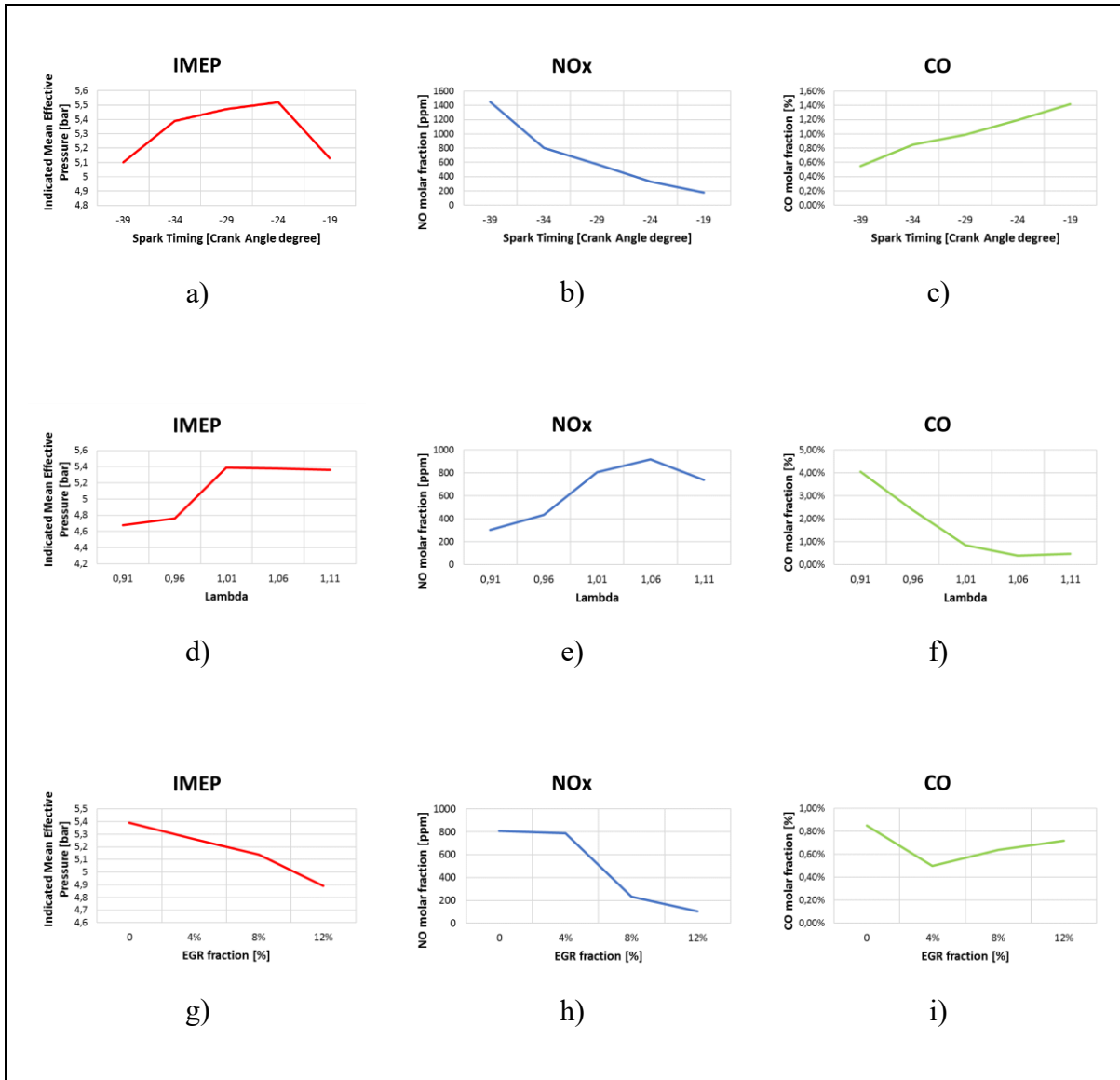


Figure 3. 12: Numerical analysis of engine performance and pollutant emissions as obtained by varying the spark timing a), b), c), the air-to-fuel ratio d), e), f), and EGR ratio g), h), i).

Spark Timing (°CAD)	EGR rate (%)	Lambda (-)	Δ CO (%)	Δ NO _x (%)	Δ Power (%)	Weight
-24	2	1.1	-34	-69	-3	100
-24	3	1.1	-32	-72	-5	99
-24	4	1.1	-15	-79	-8	86
-29	3	1.1	-57	-47	-1	101
-19	3	1.1	7	-86	-12	67
-24	0	1.1	-36	-66	-1	103
-24	3	1.1	-31	-74	-5	100
-24	4	1.1	-25	-76	-7	94
-24	2	1	-39	-61	1	101
-24	1	1	15	-75	6	66

Table 3. 6: Citizens of Pareto Front with their weight

Figure 3. 13 shows the parallel chart of the proposed optimization. The Pareto front is reported in bold blue for better visualization of the compromise between emissions and brake power.

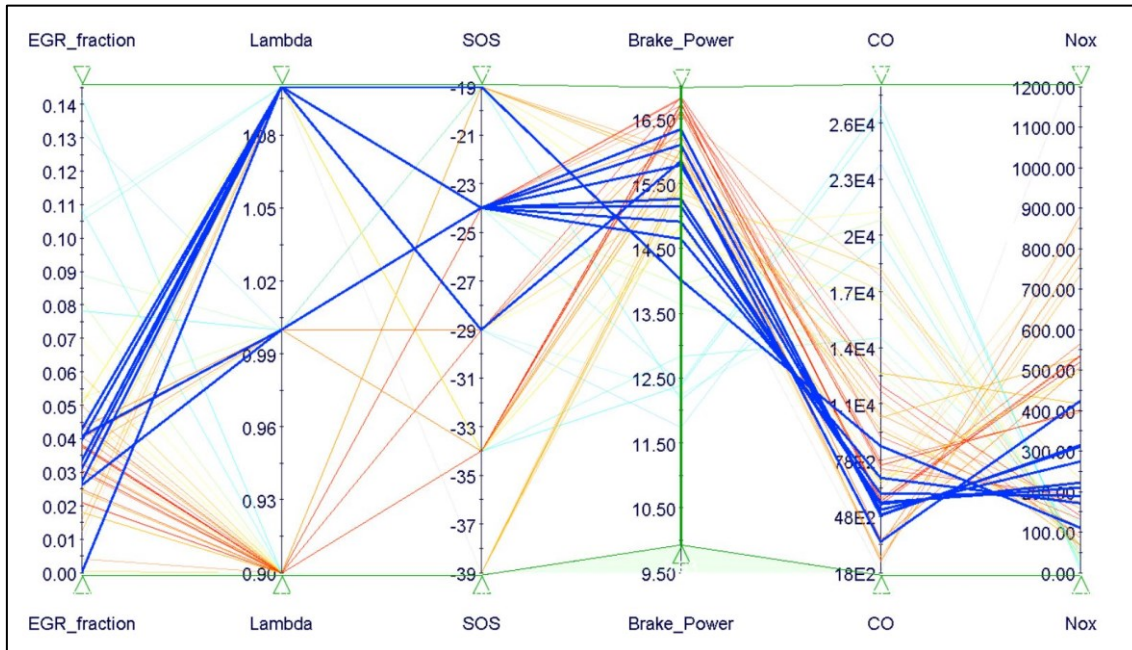


Figure 3. 13: Parallel chart of the optimization. Pareto optimal points are shown in bold blue.

The investigation reveals significant deviations from the usual behavior of the same engine running on traditional fuels. With a tiny proportion of EGR, high NO_x reductions are possible. An excessive rise in this %age, on the other hand, results in a modest decrease in emissions and a significant reduction in brake power. Spark timing can be adjusted to have a favorable influence on NO_x production and brake power at the same time.

The effect of the controlling variables on emissions and electrical output is described in detail in the next paragraphs, to get useful information to properly calibrate the ICE.

3.4.2 The CO emission trend

Figure 3. 14 shows the results of the optimization of the CO emissions before the three-way catalyst. CO emissions are highly influenced by the spark timing and air-fuel mixture. Because the temperature of combustion rises with a rich mixture, it has a favorable influence on CO emissions [25]. However, as the proportion of EGR is increased over 10%, the combustion quality deteriorates, and CO emissions climb rapidly, as expected from literature data [26]. The advance of combustion negatively affects the CO emissions, as a lower efficiency of combustion occurs with less CO converted to CO₂.

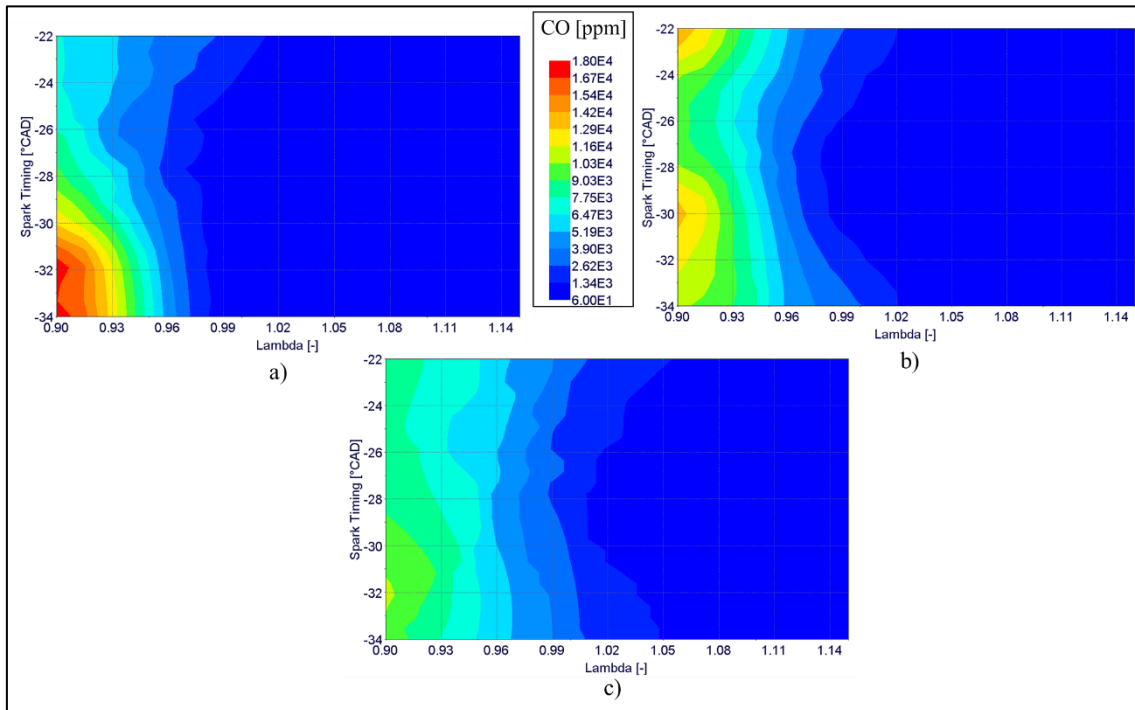


Figure 3. 14: CO emissions at various EGR %ages: a) 0%, b) 10%, c) 15%.

3.4.3 The NO_x emission trend

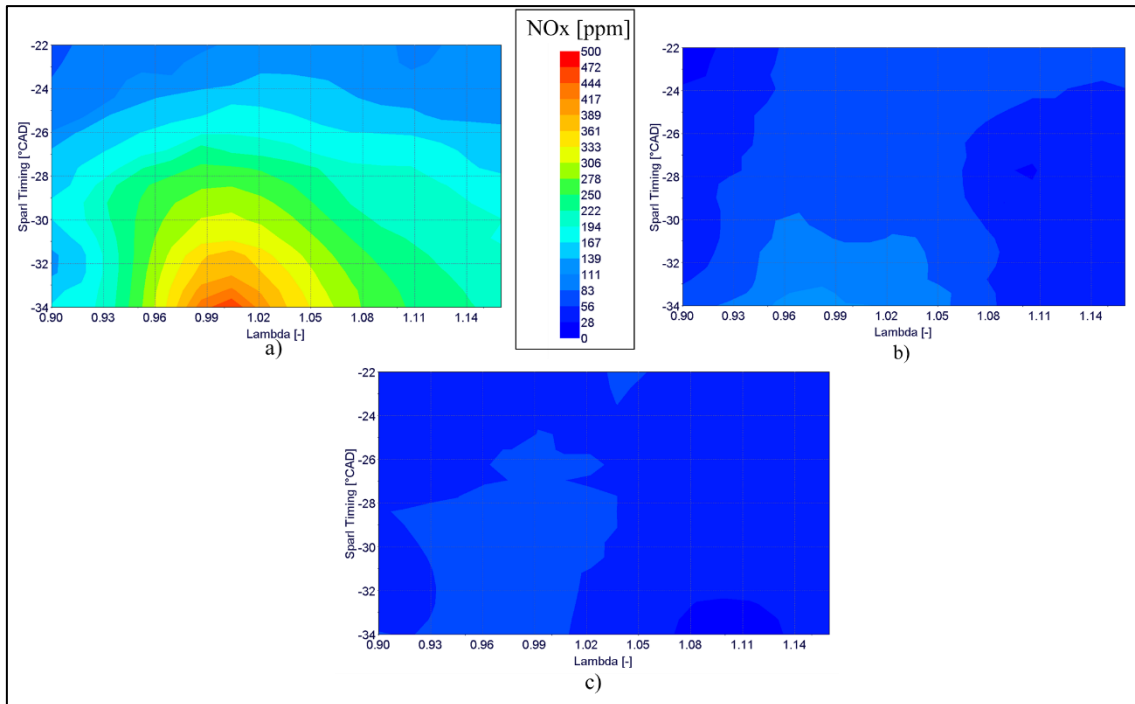


Figure 3. 15: NO_x emission at various EGR %age: a) 0%, b) 10%, c) 15%

NO_x emissions are influenced by the spark timing advance, as shown in Figure 3. 15. By increasing the EGR mass fraction, a positive effect can be noticed, with low NO_x emissions already achieved with a %age of 10% of EGR. Delaying the combustion process has a positive effect on NO_x emissions since the reduction of the peak pressure and temperature in the combustion chamber reduces the formation of such species. By enriching the mixture, the NO_x emissions are reduced drastically.

3.3.4 The electrical output power trend

Figure 3. 16 highlights the effect on the brake power of each operating parameter. A stoichiometric blend is desirable without EGR, although a delayed spark timing and a poor mixture are favoured as the EGR rate increases. Excessive EGR has a negative impact on engine efficiency since reduces the fresh air-fuel mixture in the cylinder. [25]. Indeed, the maximum brake power for EGR higher than 10% reaches 16.5 kW while for EGR=0% the maximum brake power is 17.5 kW.

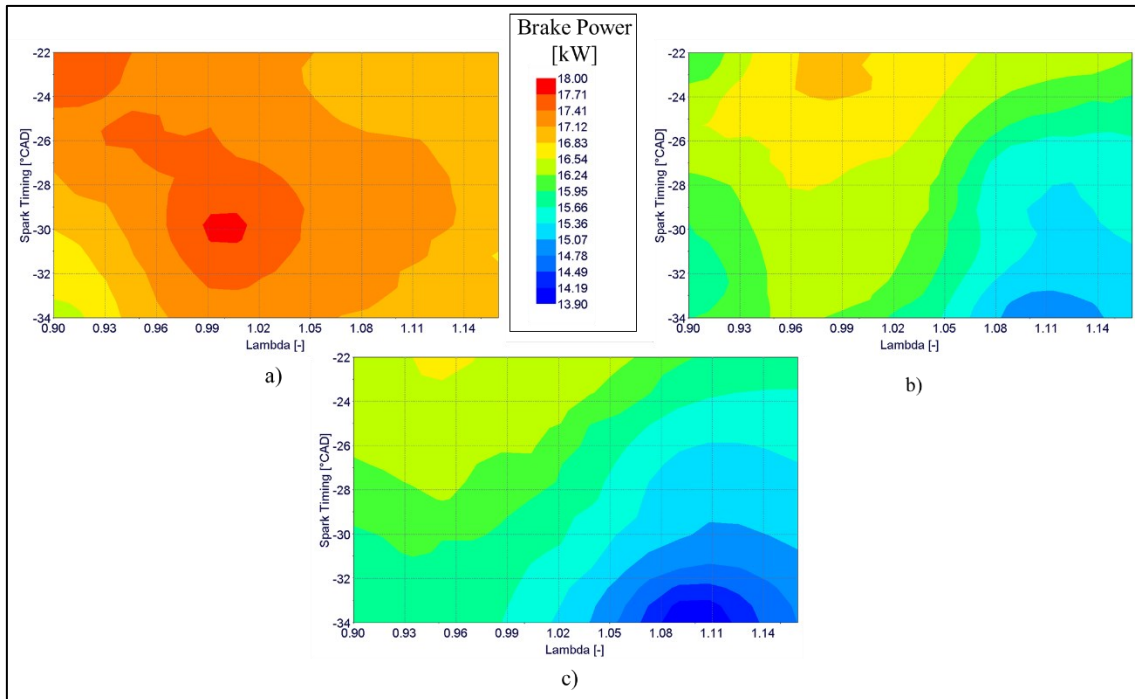


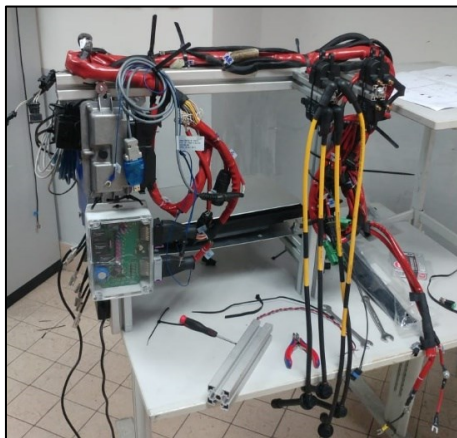
Figure 3. 16: Brake power at various EGR %age: a) 0%, b) 10%, c) 15%

3.5 Engine spark timing and misfire detection through an innovative ECU

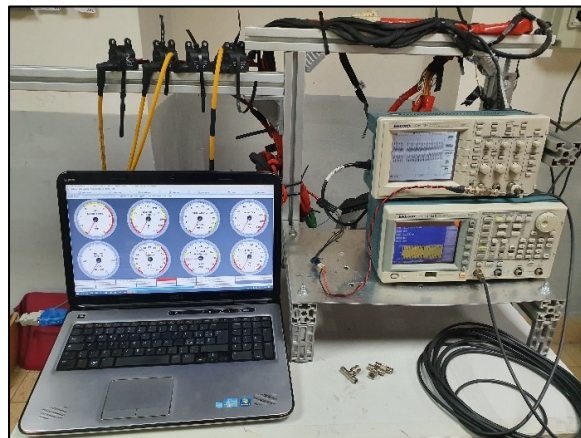
Since the CMD ECO20x engine was developed and utilized for stationary and single-fuel applications, it was equipped with a manual-style spark timing control system. The classic distributor, which is keyed to the crankshaft and can transfer the sparking energy to the individual spark plugs according to the desired ignition order, was the element that handled the spark sequence. It was a conventional and relatively simple mechanical device allowing the spark advance to be changed but not dynamically adjusted. In other words, for every working condition of the engine, the chosen value stayed constant. However, different spark advance timing could be considered in the light of the previously described optimization. For this reason, a more advanced ignition management system was developed within the PROMETEO project, to better implement combustion management logics, according to different operating conditions or compositions of the used gaseous fuel.

The chosen starting hardware and software were an open access product from MS controller [27], suitably adapted for the operation with the engine in question. The inputs and outputs required for the control unit operation were established and set, and a customized field box was built to actuate the control unit signals. The hardware setup of

the rpm sensor needs special consideration. Because the engine generally has a phonic wheel with two consecutive missing teeth, a hall sensor was utilized to detect the presence of each tooth as well as the throat caused to the teeth absence. Because the wheel rotates at the same speed as the crankshaft, the angular velocity of the crankshaft may be calculated by measuring the time between two consecutive teeth and knowing the total number of them. The throat was used to identify the angular position of the piston of the first cylinder of the ignition sequence, in this case, the first one, due to the missing teeth. This knowledge was utilized to set up the Electronic Control Unit (ECU), and the prototype was tested in CNR-STEMS electronic laboratory to ensure that it worked properly. Figure 3. 17a depicts the ECU prototype, whereas Figure 3. 17b depicts the testing phase, which was carried out by using two signal emulators that could simulate the real engine operation.



a)



b)

Figure 3. 17: ECU prototype and related box field for actuations (a) and testing with signal simulators in the laboratory (b)

After demonstrating the system effectiveness in a series of laboratory tests, the full system was installed on the CMD ECO20x engine. The control was made as based on rpm and motor phase, with a varied ignition advance value managed depending on whether the engine was cranking, idle, or under full load. The ECU placed on the real engine is shown in Figure 3. 18. A strobe gun, commonly used for spark timing checks on automobile engines, was utilized to verify the value of the spark in real-time for each phase.



Figure 3. 18: ECU testing on the engine

To set the required spark advance table rpm vs load, the ionization current intensity as sensing variable was measured, as described in the following. The ionization current signal can be utilized to extract information about the peak pressure location in the engine cycle, which can then be employed in a feedback loop control for spark advance choice and optimization.

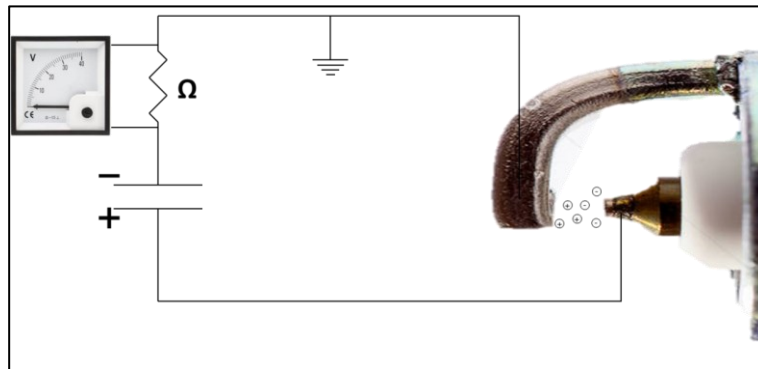
3.5.1 Ionization current and its interpretation

The ionization current, which is measured in the combustion chamber by using a spark plug as a sensor, is a non-intrusive direct measurement already used under traditional fuel powering in SI engines. No application indeed exists for biomass powered cogeneration units. In order to establish an electric field between the two electrodes, the sensing technique applies a DC bias to the spark plug. As the flame front propagates, the electrical field controls the ions that are generated in the combustion chamber. If the electric current is measured, useful data on the pressure trace could be achieved.

Even though it is not used in commercial applications, ionization current measurement devices have been extensively investigated in the past for monitoring knocking [28], misfire [29], spark plug fouling [30], and ignition control [31] in ICEs.

In the here studied case, information about fouling could be useful when using different biomasses that determine a big amount of dust and tar in the produced syngas, whose accumulation could even cause misfire.

A DC bias of 240 V was introduced to the spark plug for the electrical field production and ions detections. A coil for a double spark engine was utilized, with one termination generally attached to the spark plug and the other used to disclose the ion current. Figure 3. 19a depicts a simplified idealized scheme of the measurement system, while Figure 3. 19b reports the photography of the oscilloscope monitor for ion determination. Thanks to this system, the typical signal from ionization current was acquired, measuring the potential drop across a 10 k Ω resistance.



a)



b)

Figure 3. 19: Ion current measurement system circuit (a) and oscilloscope (b)

According to Eriksson and Nielsen [31], the shape of an ion current signal (Figure 3. 20) can be divided into three different phases:

1. *Ignition phase*: The ignition phase starts with the charging of the ignition coil and ends with the coil ringing after the spark. Ionization current is very high;
2. *Flame front phase*: The high level of ions produces one peak in the flame-front phase. The ions generated by the flame have different recombination rates. Some ions recombine very quickly to become more-stable molecules, while others have longer residual times;
3. *Post-flame phase*: in the post-flame phase, the most stable ions remain, generating a signal that follows the cylinder pressure due to its effect on the molecule concentration. A second peak is referred to as the peak pressure. The high temperature gives a contribution to the ionization current for the relatively low ionization energy of nitric oxide [32].

Different models have been created for the interpretation of the ion current generating process occurring within the combustion chamber of spark-ignition engines. Reinmann's model [32] gives an interpretation of the post-flame phase, useful for the determination of the peak pressure position. It is assumed that the gas in the spark plug gap is entirely combusted and in thermodynamic equilibrium. An expression for ion current is obtained as follows:

$$I = U \frac{\pi r^2}{d} \frac{e^2}{\sigma m_e \sqrt{\frac{8kT}{\pi m_e}}} \sqrt{\varphi_s} \sqrt{\frac{2 \left(\frac{2\pi m_e kT}{h^2} \right)^{\frac{3}{2}} \frac{B_1}{B_0} \exp \left[-\frac{E_1}{kT} \right]}{n_{tot}}} \quad (3.16)$$

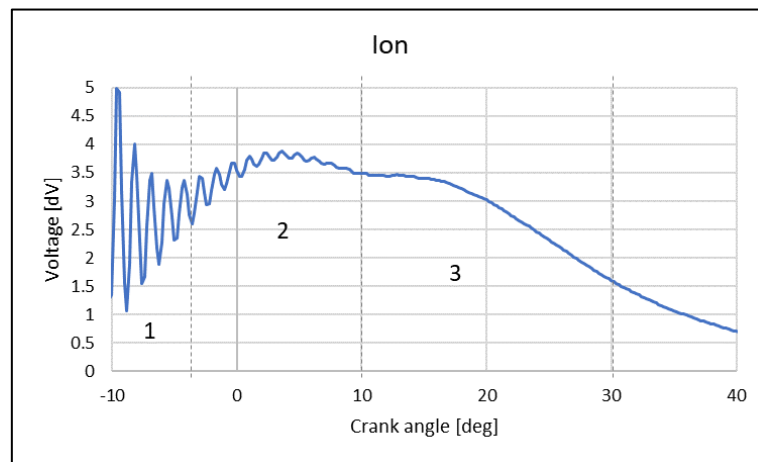


Figure 3. 20: Ion voltage acquired during engine working

Since the temperature is dependent upon pressure, equation (3.16) can be rewritten by comparing the relative current with the relative pressure, as the model suggests, thus obtaining for a known pressure trace, the following equation:

$$\frac{I}{I_{max}} = \frac{1}{\left(\frac{p}{p_{max}}\right)^{\frac{1}{2} \frac{3\gamma-1}{4\gamma}}} \exp \left[-\frac{E_i}{2kT_{max}} \left(\left(\frac{1}{\left(\frac{p}{p_{max}}\right)^{\frac{\gamma-1}{\gamma}}} \right) - 1 \right) \right], \quad (3.17)$$

where:

- I : Ionization current;
- I_{max} : Ionization Current maximum;
- p : Cylinder pressure;
- p_{max} : Cylinder pressure maximum;
- T_{max} : Maximum temperature;
- γ : Specific heat ratio;
- k : Boltzmann's constant;
- E_i : Ionization energy.

Using the function and the measured cylinder pressure, the component of the ionization current related to the cylinder pressure has a shape close to a Gaussian function. Larss Eriksson [31] proposed a simple and effective method to obtain this shape from the ionization current signal. The ionization current can be modelled as the sum of two Gaussian curves, one representative of the flame-front phase and the second one for the post-flame phase. The following expression holds:

$$I(\theta) = \alpha_1 e^{-\frac{1}{\alpha_2}(\theta-\alpha_3)^2} + \beta_1 e^{-\frac{1}{\beta_2}(\theta-\beta_3)^2} \quad (3.18)$$

where each parameter can be interpreted as height, width and position of the Gaussian representative of the flame front and the Gaussian representative of the post-flame phase. With this parametrization, the interpretation of the peak pressure position is simple, since the position of the second Gaussian signal, β_3 , corresponds to the peak pressure position.

3.5.2 Modelling of Ion current

A model of the interpretation of Ion current was implemented in the Matlab® environment. The model reads the experimental ionization current and determine the set of parameters $(\bar{\alpha}, \bar{\beta})$ best fitting the model to the measured signal, by using the least squares method. The best set is chosen if the six parameters minimize the sum:

$$\sum_{i=1}^n (I(\theta_i) - I_{meas}(i))^2 \quad (3.19)$$

where:

- i is the sample number referred to crank angle;
- n is the total number of samples;
- θ_i is the crank angle at sample i ;
- $I(\theta_i)$ the calculated value of Ion with the proposed model at crank angle θ_i ;
- $I_{meas}(i)$ the measured Ion.

For different scenarios, the stated approach was used to validate the position of the pressure peak using the ion current derived signal, which was characterized simultaneously with an AVL spark plug sensor for measuring the pressure in the combustion chamber directly. The various situations were created by altering the start of spark (SOS) and Lambda values. A matrix of the operating point studied for two different types of biomasses is shown in Table 3. 7.

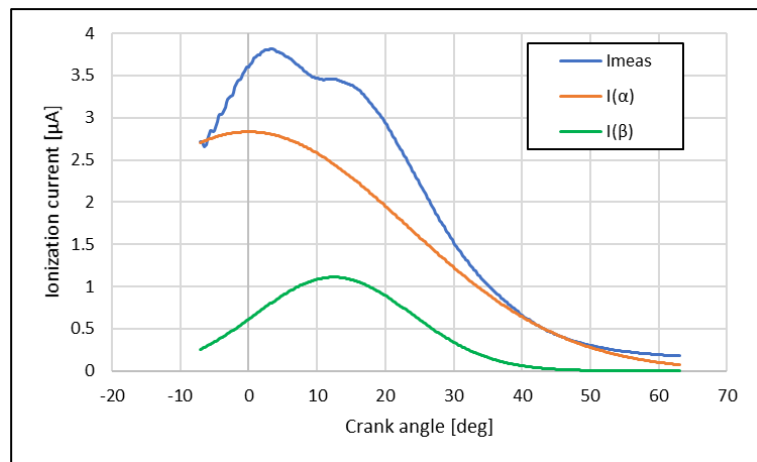
	$\lambda=1.001$	$\lambda=1.025$	$\lambda=1.050$
SOS [BTDC]		15	
	20	20	20
	25	25	25
	30	30	30
		35	

Table 3. 7: Matrix of the analyzed engine test points

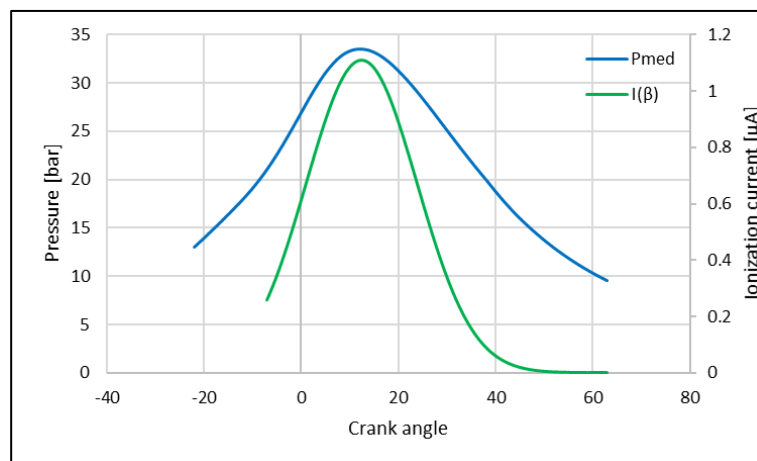
The ion current signal was averaged to smooth the effects of the ringing coil and the first phase related to ignition was considered to not affect the calculation. Since the ringing time is defined in the ECU setup and the engine speed is constant, the crank angle duration

of the ignition is constant and can be filtered by deleting the first 8° CAD after spark ignition [31].

Figure 3. 21a shows the two gaussian obtained with a generalized gradient search method. The sum of the curves best fits the ionization current. Figure 3. 21b shows the pressure trace acquired in the combustion chamber (spark advance value = -20 °CAD and $\lambda = 1.05$) with the gaussian related to the post-flame phase, calculated from the spark plug signal. The biomass feedstock was woodchip. The measured position of the peak pressure was 12.1 °CAD; the value of the β_3 , index of the position of the peak of the second gaussian, was 12.4 °CAD, thus revealing a certain prediction capability of the measured ion current signal.



a)



b)

Figure 3. 21: The measured signal (Spark advance = -20 °CAD, $\lambda = 1.05$) compared with the two gaussian functions obtained from the model (a), and the peak pressure position with post flame phase ionization current obtained from the model (b).

Both the pressure trace and ion signal were acquired for different working points of the engine by varying the SOS from 15° before the top dead centre (BTDC) to 35° BTDC. Figure 3. 22 shows some further examples of the obtained curves relevant to the post flame phase by ion measurements as correlated with the relative pressure signals acquired within the combustion chamber through the AVL sensor described in Chapter 2.

Figure 3. 23 shows the distribution of the estimated peak pressure and the real peak pressure for all the tested conditions. The spots closest to the red line suggest a more accurate pressure peak estimate. The effect of spark plug fouling causes the model to slightly overestimate the position of the pressure peak. The presence of a carbon deposit on the spark plug electrodes helps the ion current to travel across the spark gap, making the current peak less defined. In any case, the estimated position of the pressure peak can be regarded as more than satisfactory.

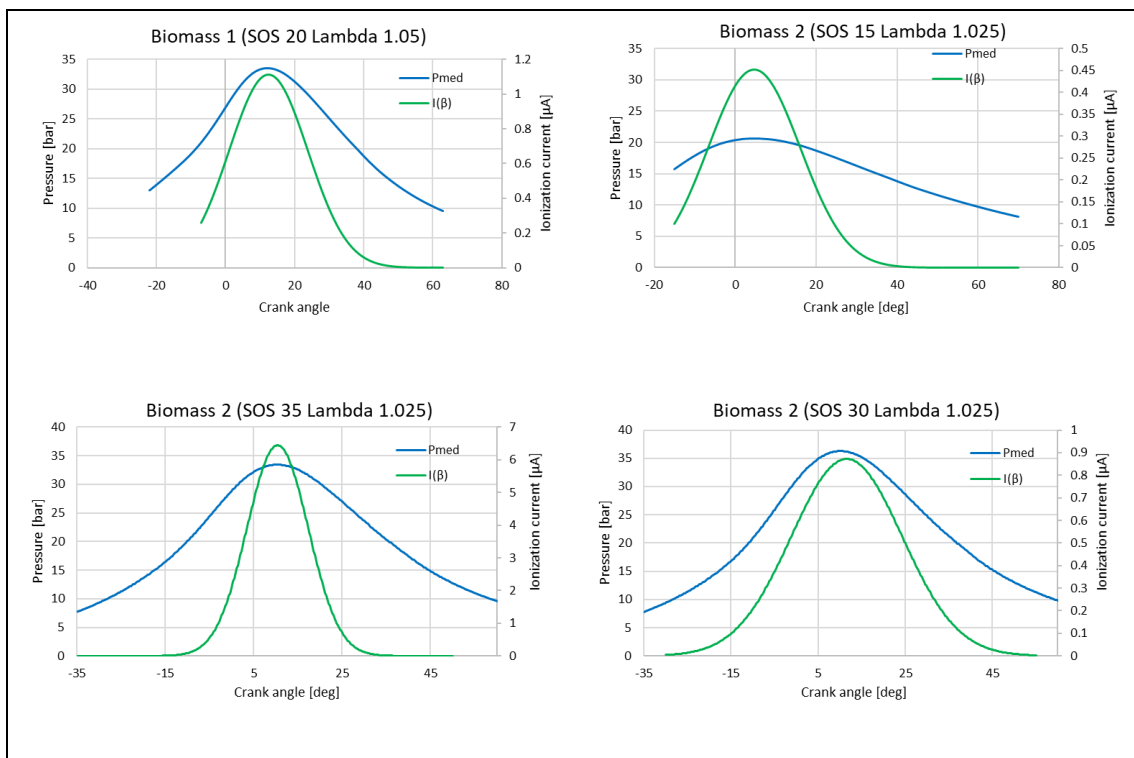


Figure 3. 22: Different examples of peak pressure position with post flame phase ionization current obtained from the model

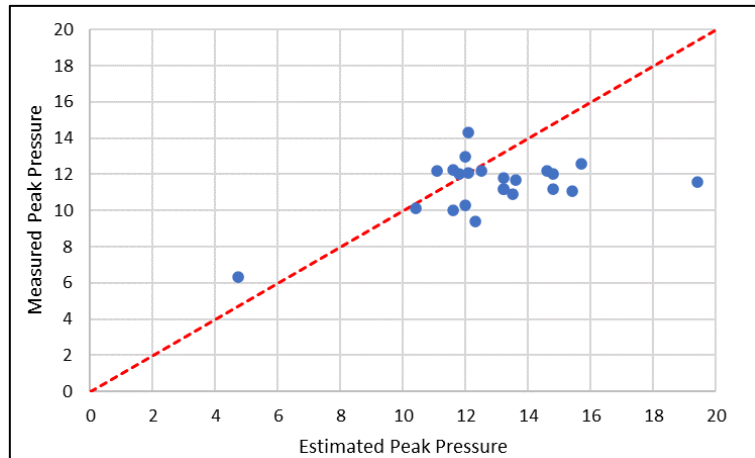


Figure 3. 23: Correlation between the true peak pressure position and estimated peak position

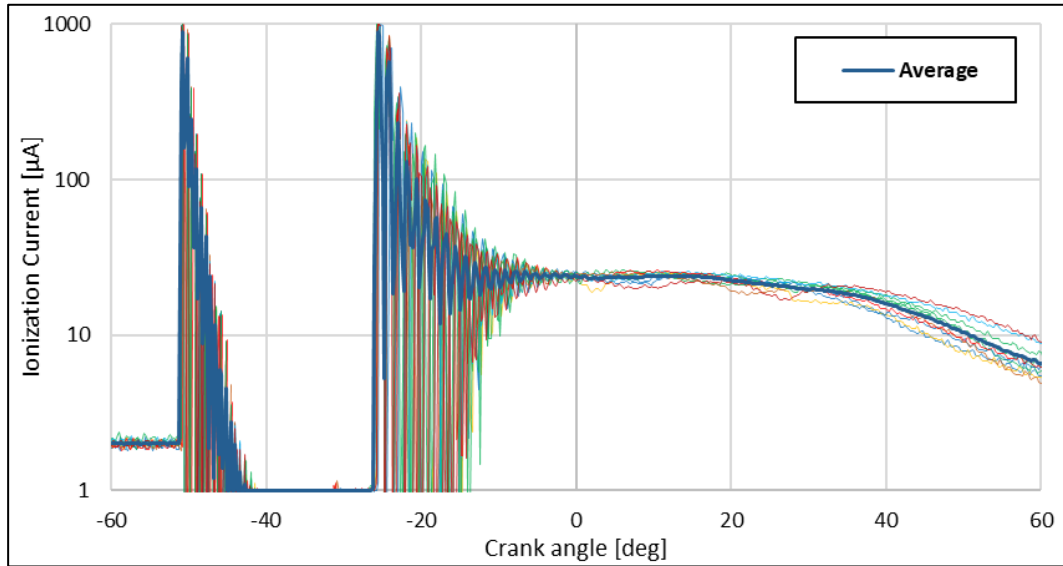
3.5.3 Fouling and misfiring detection

The ion current signal proves to be beneficial in detecting plug fouling. This can lead to perceive the production of carbonaceous material on the spark plug electrodes by monitoring the ion energy before, during, and after the ignition and combustion phases. This substance is an electrical conductor, and when it is deposited on the electrodes, it reduces the distance between them, resulting in a considerable rise in the observed ionization current [29]. The accumulation of these carbon residues can even completely cancel the gap between electrodes, resulting in a short circuit between the positive electrode and the ground, with no spark occurrence – i.e. misfire. The persistence of this phenomenon must be avoided because it causes strong vibration that can stress the entire engine block. If the spark plug detects fouling more than once, the engine stops itself and cannot restart until the spark plugs are cleaned or replaced, thus reducing the reliability and extending the maintenance times of the whole plant.

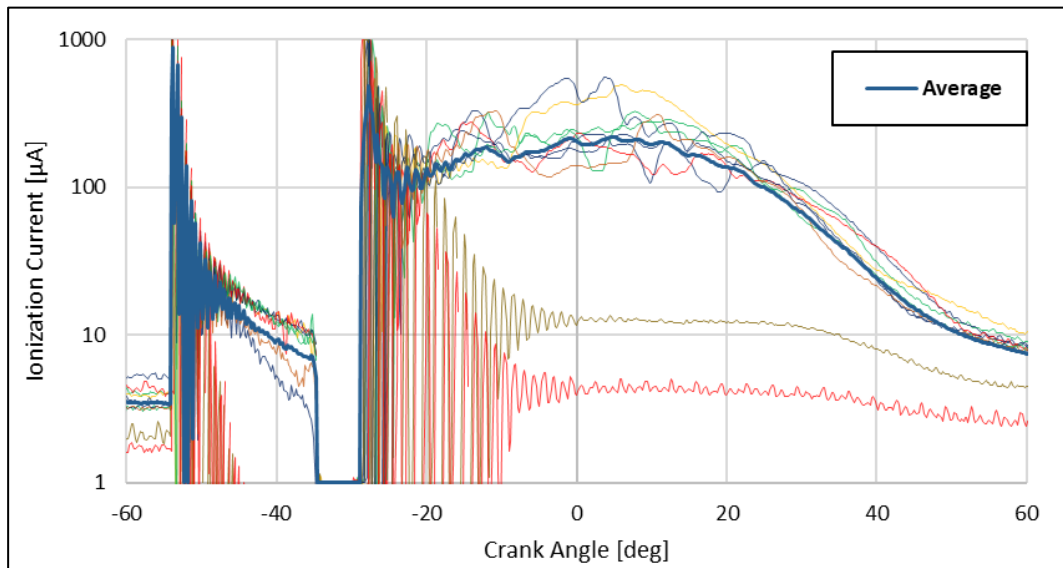
Figure 3. 24 shows two samples of the 10 consecutive ion current traces, was measured for a clean spark plug (a) and a dirty one (b).

Figure 3. 24 shows the discrepancies between the two graphs; a dirty spark ion signal includes a larger value of the ionization current peak observed during the combustion phase and a fake ion current measured before the spark initiation. A misfiring principle may be seen in Figure 3. 24b, with two of the ten cycles failing to burn and yielding no ion signal.

Data collection enabled the determination of a threshold value for distinguishing fouling on spark plugs. Instead of using a typical mechanic system with a distributor, an ECU for smart spark timing allows for spark cleaning methods or shutting down the engine to avoid prolonged running under misfire conditions.



a)



b)

Figure 3. 24: Ionization current of different spark plug states: normal (a) and fouled (b)

Table 3. 8 resumes the average peak value of ionization currents measured for 38 different acquisitions made by varying the engine operating conditions. Each data was averaged over 250 consecutive cycles.

Fouling could be defined as a condition in which at least 5% of the total number of cycles has values of ionization current greater than zero in the pre-ignition phase due to the presence of carbon deposits. Because the presence of these deposits tends to increase the value of the measured current peak, a threshold value for the average peak to detect fouling can be set at 70 μA . When the measured current is larger than 200 μA , the fouling is so strong that it prevents the spark from firing and the engine starts vibrating violently, revealing a significant cylinder imbalance.

N.	Measured Ion Current Peak [μA]	Fouling	Misfire
1	36.19	No	No
2	40.04	No	No
3	49.25	No	No
4	39.82	No	No
5	46.87	No	No
6	38.27	No	No
7	41.40	No	No
8	58.64	No	No
9	54.76	No	No
10	45.80	No	No
11	42.00	No	No
12	37.90	No	No
13	38.05	No	No
14	69.31	No	No
15	60.53	No	No
16	89.13	Yes	No
17	57.74	No	No
18	36.49	No	No
19	43.08	No	No
20	295.82	Yes	Yes
21	54.78	No	No
22	61.08	No	No
23	75.02	Yes	No
24	29.86	No	No
25	46.23	No	No
26	38.74	No	No
27	43.74	No	No
28	53.80	No	No
29	81.55	Yes	No
30	58.76	No	No
31	47.71	No	No
32	31.02	No	No
33	47.91	No	No

N.	Measured Ion Current Peak [μA]	Fouling	Misfire
34	267.70	Yes	Yes
35	241.66	Yes	Yes
36	48.18	No	No
37	49.66	No	No
38	73.56	Yes	No

Table 3. 8: Ion current peak of every acquisition with Fouling or Misfire presence

3.5.4 Implementation of spark timing optimization in an ECU

Some examples of managing strategies in engines are available in the literature [33]–[35], but no one of them was designed and tested for use with an engine powered by syngas deriving from biomass gasification.

The logic control of the ECU provides a correction of the spark timing calculating it from the estimated Peak Pressure Position (PPP) of the model developed in Matlab® environment. Since the model calculates the position of the peak pressure, the correction for the spark timing can be evaluated by using the following equation:

$$\begin{aligned}
 C &= PPP_{TARG} - PPP_{CALC} \\
 \begin{cases}
 SOS_{new} = SOS_{old} + 1^\circ, & C > 0 \\
 SOS_{new} = SOS_{old} - 1^\circ, & C < 0 \\
 SOS_{new} = SOS_{old} & , \quad C = 0
 \end{cases}
 \end{aligned} \tag{3.20}$$

where:

- SOS_{new} is the correction to actuate on the actual spark timing (SOS_{old});
- PPP_{TARG} represents the target position of the peak pressure;
- PPP_{CALC} is the actual position of the peak pressure calculated from the ion signal.

Contextually to the spark timing correction, a check on the spark fouling is made on the same signal acquired from the ion current. The right side of the flow chart of Figure 3. 25 checks the value of the peak of the ion current measured, comparing it with the threshold value found from the experimentation. To blast away the carbonaceous deposits and clear the gap, an appropriate approach for removing deposits from the spark plug electrodes gives a doubling of the spark energy.

In addition, a second threshold value was added with a value of 200 μA . When the current reaches this value, there is a good chance that the cleaning strategy has not worked, and the engine is stopped as a precaution before catastrophic damaging. The presence of an

HMI (Human Machine Interface) on the plant can be useful to this case, and the ECU can communicate the cylinder failure to the operator, who can easily clean or replace the spark plug.

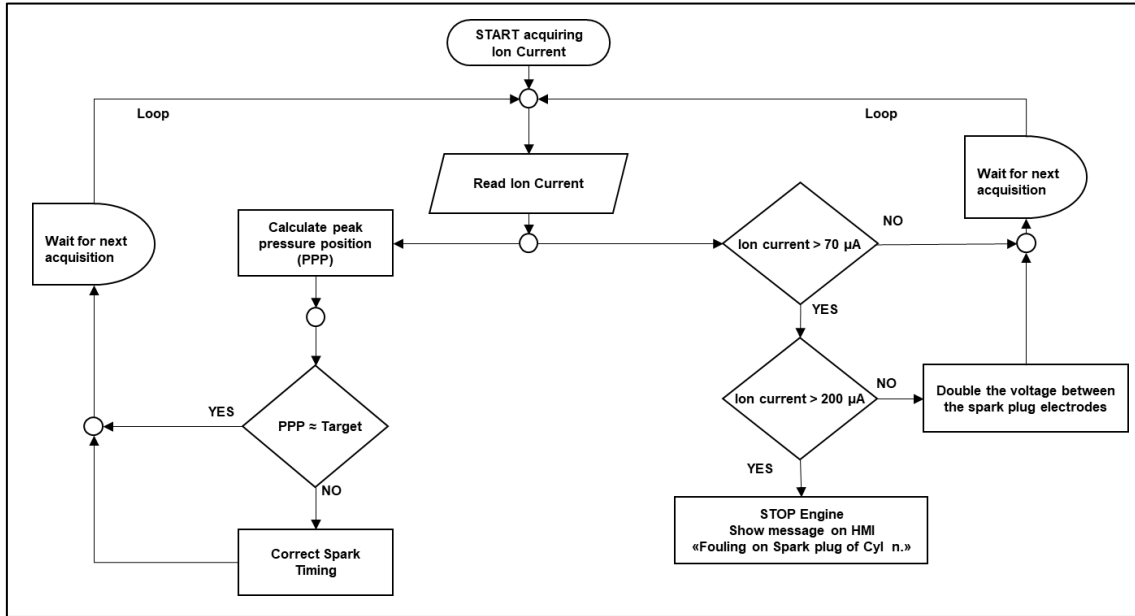


Figure 3. 25: Flow Chart for ECU engine management

3.6 Optimization of the waste heat recovery

As said in Chapter 2, waste heat recovery in CMD ECO 20x is made thanks to two heat exchangers, whose specifications are reported in Table 3. 9.

	Plate heat exchanger (PHE)	Shell and tube heat exchanger (SHTE)
Heat exchange surface A (m^2)	1.06	0.8
Geometry	40 plate counter-current	24 pipes ($D_i = 12$ mm, $s = 1$ mm)
External size	130x320x120 mm	850x90 mm
Thermal transmittance U (kW/m^2K)	0.98	0.07
Thermal conductance UA (kW/K)*	1,04	0,056

*Thermoflex™

Table 3. 9: Specification for waste heat recovery in CMD ECO20x

In order to evaluate the effects of the variation of some exchanger characteristics on the heat recovery performance, some parametric analyses were carried out by using the plant model developed within the Thermoflex™ environment.

Baseline conditions were set in Table 3. 10.

Secondary circuit	-
A (m ²)	1.06
T _{in} (°C)	65.18
\dot{m} (l/min)	22.35
Primary circuit	-
A (m ²)	0.8
T _{in} (°C)	85
\dot{m} (l/min)	7.5

Table 3. 10: Baseline conditions for waste heat recovery simulations

3.6.1 Effect of heat exchange surface

The effect of heat exchange surface on thermal power was evaluated for three different cases: surface variation of both exchangers (1); surface variation of the plate heat exchanger (PHE) (2); surface variation of the shell and tube heat exchanger (STHE) (3).

A _{PHE} (m ²)	A _{STHE} (m ²)	Q _{TOT} (kW)	ΔQ _{TOT} (%)
0.53	0.8	13.41	-7.9
0.795	0.8	14.16	-2.8
1.06	0.8	14.57	
1.325	0.8	14.82	+1.7
1.6	0.8	15.02	+3.0
1.06	0.4	12.29	-15.6
1.06	0.6	13.65	-6.3
1.06	1	15.22	+4.4
1.06	1.2	15.67	+7.5
0.53	0.4	11.12	-23.6
0.795	0.6	13.23	-9.1
1.325	1	15.46	+6.1
1.6	1.2	16.11	+10.5

Table 3. 11: Effect of surface variation on thermal power (in blue baseline case)

Table 3. 11 shows a summary of the values of quantities for each numerical test performed. The variations in waste heat recovery power are small. The variation of the STHE surface has a greater weight on the thermal output (Q_{TOT}) than a variation of the PHE surface.

These improvements, however, are too low to be considered for an investment in an application in the CMD ECO20x.

3.6.2 Effect of secondary circuit water mass flow rate

This paragraph considers the effect of the change in the water flow rate of the secondary circuit on the exchanged thermal power.

Five different operating conditions were analyzed in which the system processes a secondary water mass flow rate equal to 10, 30, 50, 70 and 100% more than in the baseline case, with the same inlet temperature. The following Table 3. 12 reports a summary of the effect of the water mass flow rate on the recovered thermal power.

A 5% increase in thermal power exchanged in the PHE was possible with a 100% increase of the water flow rate compared to the baseline case at the intake of the secondary circuit. The benefits of increasing the secondary circuit mass flow rate were, however, more noticeable in the thermal power recovered in the STHE, where an increase of 100% allowed for a 10% improvement.

m_{STHE} (kg/s)	ΔQ_{PHE} (%)	ΔQ_{STHE} (%)	Q_{TOT} (kW)	ΔQ_{TOT} (%)
0.3725			14.57	
0.4097	+1.0	+1.5	14.76	+1.3
0.4842	+2.0	+4.0	15.12	+3.7
0.5587	+3.0	+6.0	15.26	+4.7
0.6332	+3.8	+7.0	15.43	+5.9
0.745	+4.5	+10.0	15.62	+7.2

Table 3. 12: Effect of secondary water mass flow rate on thermal power

The increase of 100% of the secondary circuit mass flow rate was considered for future application in the CMD ECO20x since no investment or modification in geometry and displacement are required in this case.

3.6.3 Biomass drying process

The direct drying process can be summarized according to an open system approach, as shown in Figure 3. 26. Wet biomass enters the system in section 0 and is hit by a flow of exhaust gases coming from section 1 and exiting through section 2, and totally or partially dried biomass exits from section 3.

The input data required for the aforementioned Thermoflex™ model, in which a direct dryer was added, are the temperature T^0 and the mass flow rate \dot{m}^0 of biomass, temperature T^1 and the mass flow rate \dot{m}^1 of exhaust gases, proximate and ultimate analysis of biomass y_k^0 and composition of exhaust gases y_k^1 . Thermoflex™ gives as output the drying efficiency, the biomass final temperature (T^3) and the thermal power transferred.

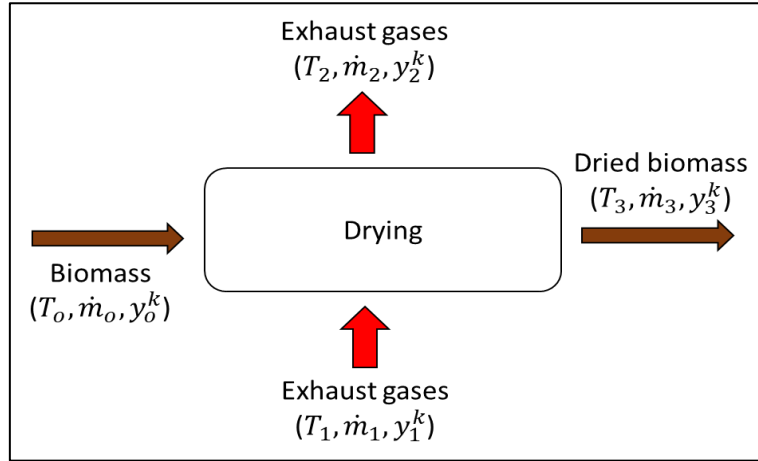


Figure 3. 26: Direct drying process

Since biomass is supposed to be chemically inert, the biomass organic fraction and biomass organic and inorganic mass flow rate, remain unvaried from section 0 to section 3 [36]:

$$y_k^{OM,3} = y_k^{OM,0} \quad k = C, H, O, N, S, Cl \quad (3.19)$$

$$\dot{m}^0 y_{INO}^0 = \dot{m}^3 y_{INO}^3 \quad (3.20)$$

$$\dot{m}^0 y_{OM}^0 = \dot{m}^3 y_{OM}^3 \quad (3.21)$$

The fraction of vapor leaving the drying section is equal to its saturation value at the temperature calculated at the exit of this section $y_{H_2O}^{sat,2}$, that depends on the saturation pressure ($p_{H_2O}^{sat}(T^2)$).

If $y_{H_2O}^{dry,2} < y_{H_2O}^{sat,2}$, biomass is completely dried, it is possible to suppose:

$$\begin{aligned} y_{H_2O}^2 &= y_{H_2O}^{dry,2} \\ y_{H_2O}^3 &= 0 \end{aligned} \quad (3.22)$$

If $y_{H_2O}^{dry,2} > y_{H_2O}^{sat,2}$, however, the drying process is incomplete, so:

$$\begin{aligned} y_{H_2O}^2 &= y_{H_2O}^{sat,2} \\ y_{H_2O}^3 &= \frac{\dot{m}^0 y_{H_2O}^0 + \dot{m}^1 y_{H_2O}^1 - \dot{m}^2 y_{H_2O}^2}{\dot{m}^3} \end{aligned} \quad 3.23)$$

The ratio β is defined as the ratio between \dot{m}^1 and \dot{m}^0 .

A parametric analysis is made by evaluating how the heat recovery is influenced by the mass flow rate of the exhaust gases.

Three cases are analyzed, as schematized in Figure 3. 27:

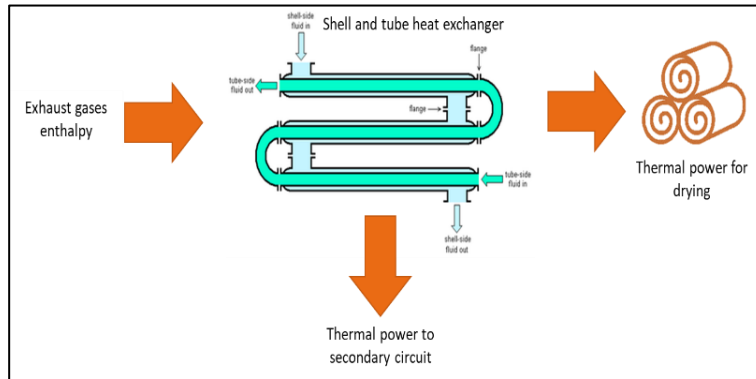
- a) The entire mass flow rate of the exhaust gases, downstream of the shell and tube exchanger, is used to dry the biomass;
- b) a small portion of exhaust gases is taken upstream the shell and tube exchanger and used to dry the biomass.
- c) a small portion of exhaust gases upstream the shell and tube exchanger is mixed with the remaining flow downstream the shell and tube exchanger and used to dry the biomass.

For case b) and case c), an exhaust bleeding ratio is defined as the ratio between the exhaust gases mass flow ratio bleed and the total exhaust gases mass flow ratio. Baseline conditions are reported in Table 3. 13.

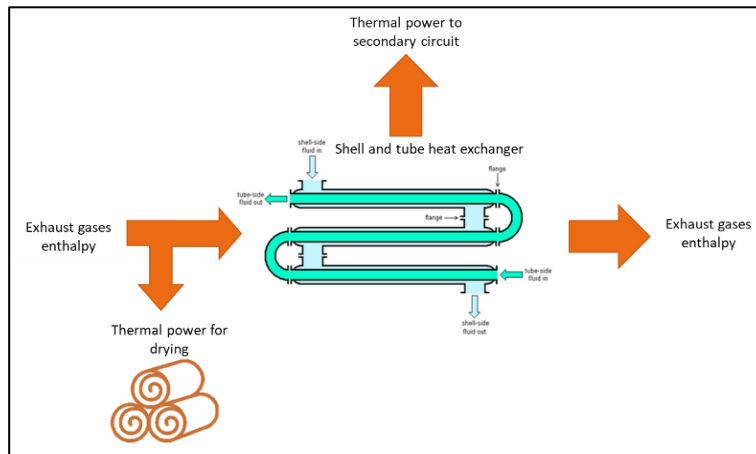
For each of the three cases, an initial moisture of 30% of the biomass is considered. The thermal power transferred to the biomass $\dot{Q}_{B,DRYING}$, sum of the latent and sensible ones, is calculated, as well as the drying efficiency, the residual %age of moisture and the effective thermal power transferred to the secondary circuit $\dot{Q}_{F,SH}$, as reported in Table 3. 13..

Case a) has a higher thermal power transferred to the secondary circuit (+40%) than the case b) and case c), even though the thermal power for drying is lower than case c) by 14.4%. Case c) is the best solution to maximize the thermal power for drying.

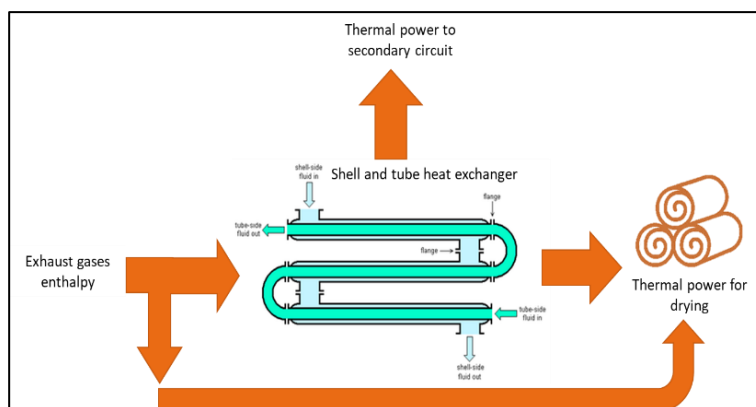
Two parametric analyses are carried out for the case a) by varying the %age of moisture in the used feedstock and the value of β , in order to evaluate the exhaust gas drying efficiency and biomass final temperature.



case a)



case b)



case c)

Figure 3. 27: Energy flux for each of the analysed cases

With a biomass initial moisture of 17.5%, the drying efficiency (Figure 3. 28a) reaches its maximum and the final temperature of biomass starts to increase.

Quantities	Case a)	Case b)	Case c)
T^0 (°C)	23.46	23.46	23.46
\dot{m}^0 (kg/s)	0.005	0.005	0.005
Exhaust Bleeding Ratio	0	0.1	0.1
$\dot{m}_{F,SH}$ (kg/s)	0.03	0.027	0.027
\dot{m}^1 (kg/s)	0.03	0.003	0.03
T^1 (°C)	119	316	139.3
T^3 (°C)	48.26	55.39	49.4
$\dot{Q}_{B,LATENT}$ (kW)	2.08	0.45	2.45
$\dot{Q}_{B,SENSIBLE}$ (kW)	0.29	0.36	0.30
$\dot{Q}_{B,DRYING}$ (kW)	2.37	0.82	2.75
Drying efficiency (%)	56.5	12.5	66.5
Final moisture of biomass (%)	15.7	27.27	12.55
$\dot{Q}_{F,SH}$ (kW)	8.80	5.63	5.63

Table 3. 13: Average values in baseline condition

By looking at Figure 3. 28b, instead, it can be noted that for $\beta < 1$ the drying efficiency is very low, then it increases for $\beta > 1$ until it reaches the maximum value at $\beta = 4.31$, or for a flow rate of exhaust gases equal to 0.022 kg/s. The evaporation process takes place at almost constant biomass temperature. When the flow rate of the drying agent determines an evaporation ideally higher than the 100%, the remaining thermal power is spent to increase the biomass enthalpy, and therefore its temperature.

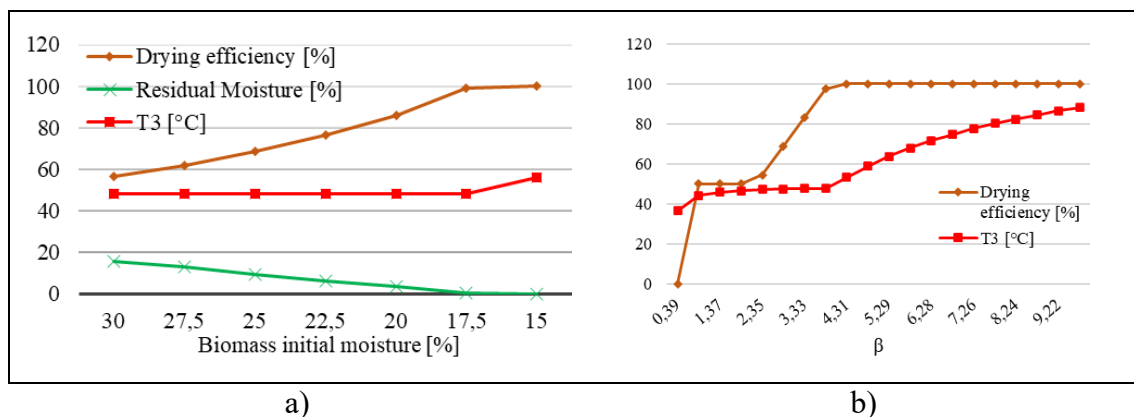


Figure 3. 28: Parametric analysis made by varying the initial moisture (a) and β (b).

A third parametric analysis is made for case b) and case c) by varying the exhaust bleeding ratio up to 0.4. The parametric analysis, shown in Figure 3. 29, shows the thermal power transferred to the secondary circuit and the thermal power transferred to the biomass, in order to search for the best exhaust bleeding ratio.

In both the cases, if the Exhaust Bleeding Ratio increases, the thermal power to the secondary circuit reduces drastically, while the thermal power transferred to the biomass and the drying efficiency increases. In Figure 3. 29b, it can be seen that for all Exhaust Bleeding Ratios, case c) has a higher drying efficiency with respect to case b).

The best solution to maximize the drying potential is to take a small portion (10%) of exhaust gases upstream of the shell and tube exchanger and mix it with the remaining flow downstream the shell and tube exchanger (case c).

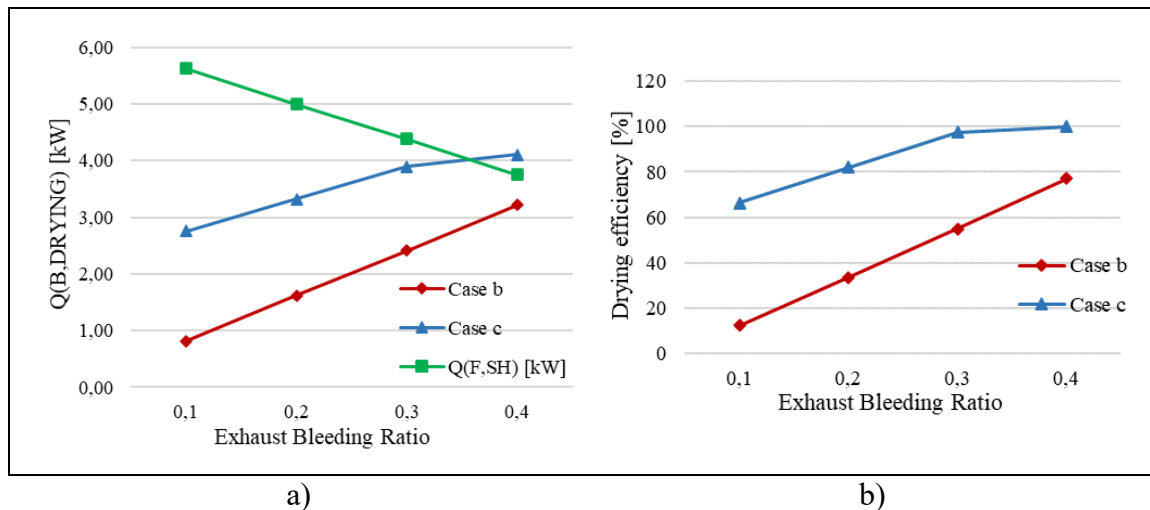


Figure 3. 29: Required biomass drying thermal power (a) and drying efficiency varying the exhaust bleeding ratio

References Chapter 3

- [1] P. Haller, "DE: Über eine graphische Methode in der Gasdynamik," *Tech. Rundsch. Sulzer*, vol. 1, 1945.
- [2] E. Jenny, "Unidimensional Transient Flow with Consideration of Friction, Heat Transfer, and Area Change of Section," *Brown Boveri Rev.*, pp. 447–461, 1950.
- [3] M. Costa, V.Rocco, C.Caputo, D.Cirillo, G.Di Blasio, M.La Villetta, G.Martoriello and R.Tuccillo, "Model based optimization of the control strategy of a gasifier coupled with a spark ignition engine in a biomass powered cogeneration system," *Appl. Therm. Eng.*, vol. 160, p. 114083, Sep. 2019, doi: 10.1016/j.applthermaleng.2019.114083.
- [4] S. Jarungthammachote and A. Dutta, "Equilibrium modeling of gasification: Gibbs free energy minimization approach and its application to spouted bed and spout-

- fluid bed gasifiers,” *Energy Convers. Manag.*, vol. 49, no. 6, pp. 1345–1356, 2008. <https://doi.org/10.1016/j.enconman.2008.01.006>.
- [5] A. Z. Mendiburu, J. A. Carvalho Jr, and C. J. Coronado, “Thermochemical equilibrium modeling of biomass downdraft gasifier: Stoichiometric models,” *Energy*, vol. 66, pp. 189–201, 2014. <https://doi.org/10.1016/j.energy.2013.11.022>.
- [6] D. Cirillo, M. Di Palma, M. La Villetta, A. Macaluso, A. Mauro, and L. Vanoli, “A novel biomass gasification micro-cogeneration plant: Experimental and numerical analysis,” *Energy Convers. Manag.*, vol. 243, p. 114349, Sep. 2021, doi: 10.1016/j.enconman.2021.114349.
- [7] M. Mehrpooya, M. Khalili, and M. M. M. Sharifzadeh, “Model development and energy and exergy analysis of the biomass gasification process (Based on the various biomass sources),” *Renew. Sustain. Energy Rev.*, vol. 91, pp. 869–887, Aug. 2018, doi: 10.1016/j.rser.2018.04.076.
- [8] W.-C. Yan *et al.*, “Model-based downdraft biomass gasifier operation and design for synthetic gas production,” *J. Clean. Prod.*, vol. 178, pp. 476–493, Mar. 2018, doi: 10.1016/j.jclepro.2018.01.009.
- [9] A. Kr. Sharma, “Modeling and simulation of a downdraft biomass gasifier 1. Model development and validation,” *Energy Convers. Manag.*, vol. 52, no. 2, pp. 1386–1396, Feb. 2011, doi: 10.1016/j.enconman.2010.10.001.
- [10] GT-Suite, “GT-SUITE Overview | Gamma Technologies.” <https://www.gtisoft.com/gt-suite/gt-suite-overview/> (accessed Dec. 14, 2021).
- [11] AVL, “AVL CRUISE™ M - avl.com.” <https://www.avl.com/cruise-m> (accessed Dec. 14, 2021).
- [12] Thermoflow, “THERMOFLEX - General Purpose Program - Heat Balance Software.” https://www.thermoflow.com/products_generalpurpose.html (accessed Dec. 17, 2021).
- [13] J. B. Heywood, *Internal Combustion Engine Fundamentals*. McGraw-Hill Education, 2018. <https://www.accessengineeringlibrary.com/content/book/9781260116106> (Accessed: Dec. 20, 2021).
- [14] GRI-Mech 3.0, “GRI-Mech 3.0.” <http://combustion.berkeley.edu/gri-mech/version30/text30.html> (accessed Dec. 22, 2021).
- [15] UNI, “UNI EN ISO 17225-1:2014.” <http://store.uni.com/catalogo/uni-en-iso-17225-1-2014> (accessed Nov. 11, 2021).
- [16] R. Tuccillo and A. Senatore, “Genetic Algorithm Based Strategies for Radial Flow Impeller Design,” presented at the *ASME 1998 International Gas Turbine and Aeroengine Congress and Exhibition*, Dec. 2014. doi: 10.1115/98-GT-427.
- [17] Gradient Method, “Gradient Method - an overview | ScienceDirect Topics.” <https://www.sciencedirect.com/topics/computer-science/gradient-method> (accessed Dec. 27, 2021).
- [18] Y.X. Yuan, “A Modified BFGS Algorithm for Unconstrained Optimization,” *IMA J. Numer. Anal.*, vol. 11, no. 3, pp. 325–332, Jul. 1991, doi: 10.1093/imanum/11.3.325.
- [19] Genetic Algorithm, “Genetic Algorithm - an overview | ScienceDirect Topics.” <https://www.sciencedirect.com/topics/engineering/genetic-algorithm> (accessed Dec. 27, 2021).

- [20] Goldberg, “Goldberg_Genetic_Algorithms_in_Search.pdf”, http://www2.fiit.stuba.sk/~kvasnicka/Free%20books/Goldberg_Genetic_Algorithms_in_Search.pdf (Accessed: Dec. 27, 2021).
- [21] M. Costa, G.Di Blasio, M.V.Prati, M.A.Costagliola, D.Cirillo, M.La Villetta, C.Caputo and G.Martoriello, “Multi-objective optimization of a syngas powered reciprocating engine equipping a combined heat and power unit,” *Appl. Energy*, vol. 275, p. 115418, Oct. 2020, doi: 10.1016/j.apenergy.2020.115418.
- [22] J. Ferreira, C. Fonseca, and A. Gaspar-Cunha, “Methodology to select solutions from the pareto-optimal set: A comparative study,” Presented at the *GECCO '07: 9th annual conference on Genetic and evolutionary computation*, Jan. 2007, pp. 789–796. doi: 10.1145/1276958.1277117.
- [23] C. Caputo, Modelling approach and technical solutions for characterization and performance improvement of real biomass powered m-CHP system, *PhD Thesis. University of Rome “Tor Vergata,”* 2020.
- [24] G. D’Errico, T. Cerri, G. Pertusi, “Multi-objective optimization of internal combustion engine by means of 1D fluid-dynamic models”, *Applied Energy*, vol. 88 (3), pp.767-777, 2011. <https://doi.org/10.1016/j.apenergy.2010.09.001>
- [25] M. Abdelaal and A. Hegab, “Combustion and emission characteristics of a natural gas-fueled diesel engine with EGR,” *Energy Convers. Manag.*, vol. 64, pp. 301–312, 2012. <https://doi.org/10.1016/j.enconman.2012.05.021>.
- [26] X. Gu, Z. Huang, J. Cai, J. Gong, X. Wu, and C. Lee, “Emission characteristics of a spark-ignition engine fuelled with gasoline-n-butanol blends in combination with EGR,” *Fuel*, vol. 93, pp. 611–617, 2012. <https://doi.org/10.1016/j.fuel.2011.11.040>.
- [27] MegaSquirt, “Products | MegaSquirt.” <https://megasquirt.info/products/> (accessed Jan. 03, 2022).
- [28] J. Auzins, H. Johansson, and J. Nytomt, “Ion-gap sense in misfire detection, knock and engine control,” *SAE Trans.*, pp. 1–8, 1995. <https://doi.org/10.4271/950004>.
- [29] N. Collings, S. Dinsdale, and T. Hands, “Plug fouling investigations on a running engine-an application of a novel multi-purpose diagnostic system based on the spark plug,” *SAE Trans.*, pp. 681–686, 1991. <https://doi.org/10.4271/912318>.
- [30] L. Eriksson, A Real-time Platform for Closed-loop Spark-advance Control. *Univ.*, 1997.
- [31] L. Eriksson and L. Nielsen, “Ionization current interpretation for ignition control in internal combustion engines,” *Control Eng. Pract.*, vol. 5, no. 8, pp. 1107–1113, 1997. [https://doi.org/10.1016/S0967-0661\(97\)00103-2](https://doi.org/10.1016/S0967-0661(97)00103-2).
- [32] A. Saitzkoff, R. Reinmann, T. Berglind, and M. Glavmo, “An Ionization Equilibrium Analysis of the Spark Plug as an Ionization Sensor,” SAE International, Warrendale, PA, *SAE Technical Paper* 960337, Feb. 1996. doi: 10.4271/960337.
- [33] C. P. Glugla, D. L. Meyer, M. J. Cullen, G. J. Huberts, M. D. Czekala, and B. A. Strayer, “Ignition energy management with ion current feedback to correct spark plug fouling,” Mar. 2012, *US Patent* n. US8132556B2
- [34] R. Greenshields, “Spark-Plug Fouling Studies,” *SAE Trans.*, pp. 3–13, 1953.
- [35] R. Senior and N. W. Morrow, “Spark plug fouling detection,” 2012, *US Patent* n. US20160138553A1.
- [36] M. Costa, D. Cirillo, V. Rocco, R. Tuccillo, M. La Villetta, C. Caputo, G. Martoriello, Characterization and optimization of heat recovery in a combined heat and power generation unit, vol. 63. *TECNICA ITALIANA-Italian Journal of Engineering Science*, 2019. <https://doi.org/10.18280/ti-ijes.632-448>.

CHAPTER 4

Validation of the improved CMD ECO20x unit in a real environment: the demo stage of the PROMETEO project

The previous numerical analyses and experimental studies allowed strong improvement in the biomass-powered micro-CHP plant.

The CMD ECO20x in the wake of the results deriving from the research project “PROMETEO (PROduzione di energia elettrica, terMica e frigorifEra con micro-cogeneraTore alimEntato a biOmassa residuale)” was installed in a waste management and storage plant in the Municipality of Mugnano, Naples, in the south of Italy (Figure 4. 1). The electrical output was meant to power the plant machines for the operations of waste storage. The project PROMETEO, in a joint collaboration between CNR – STEMS, EPM S.r.l., University of Naples “Parthenope”, Ingelia Italia and CMD, pursued concrete objectives that can be considered perfectly in line with the current social challenges of the European Union and the SDGs to:

- reduce the impact of human activities on the climate, or a decrease in gas emissions greenhouse on the entire cycle of transformation of raw material into energy (SDG 7 and 13);
- create a biomass-energy chains capable of creating jobs, reducing management costs from Municipal (SDG 10 and 11).

The project was focused on a detailed analysis and an energy and environmental optimization of the whole plant for energy production and aimed at concretely verifying the sustainability of whole biomass-to-energy chains. The following paragraph presents an energy, economic and environmental analysis to evaluate the possibility for mCHP system to be a green substitute in waste management and storage plant.



Figure 4. 1: Installed CMD ECO20x from PROMETEO project

4.1 mCHP system as a green substitute in waste management and storage plant

The CMD ECO20x was moved to the chosen site for demonstration and connected to the grid. Experimental measurements were carried out during two days at the end of July 2021, by feeding the plant with sawdust (hereafter called Biomass 1) and straw (Biomass 2), as they are the main waste of the storage plant, and by applying the following techniques:

- Biomasses were dried out to acceptable values and briquetted in order to be used in the plant.
- CMD ECO20x was located near to National grid medium tension plug (220V);

- An ad hoc spark advance parametric analysis was done to determine the optimal spark advance for each biomasses.
- Two different loads were simulated. A low load with only the waste management plant connected, which draws a maximum of 6 kW_e; a medium load of 15 kW_e was achieved by adding an electric heater.
- Characterization of syngas and exhaust composition, as well as engine pressure cycles and ionization current, were achieved by following the same investigation as reported in Chapter 2.
- An evaluation of pollutant emissions was done to estimate the environmental impact of CMD ECO20x.

Table 4. 1 reports the engine operating condition test matrix adopted for both biomasses. It should be noted that the table shows a range of load, low or medium, due to the variability of load required by plant machines for the operations of waste storage during the execution of the experimental tests.

Load	Spark Advance	λ
(kW _e)	(°CAD)	(-)
L: 4-6	-20	1.03
M: 14-15	-15	1.03
	-20	
	-25	
	-30	

Table 4. 1: Engine operating condition test matrix

Table 4. 2 reports the proximate and ultimate analysis of the used feedstocks, while Table 4. 3 shows the mediated syngas compositions, analysed through gas chromatography.

It is important to notice the high presence of ash and moisture in the straw composition, which is slightly over CMD ECO20x limits. This is what probably cause the difference in the tar %age in the cleaning circuit (Table 4. 3); indeed, straw gasification results in a three times higher tar concentration. Despite that, the cleaning circuit ran well, as no plant stop is noticed during both days.

Regarding the ultimate analysis, compositions are similar to each other, except for the greater nitrogen composition in sawdust analysis. Syngas compositions do not differ much; lower heating values and stoichiometric ratios are comparable.

	Sawdust (Biomass 1)	Straw (Biomass 2)
Proximate Analysis (%)		
Moisture	7.2	23.9
Ash	2.5	5.1
Fixed Carbon	18.0	14.1
Volatile matter	72.3	57.0
Ultimate Analysis (%) ash and moisture free		
C	48.1	46.7
N	4.5	0.2
O	41.4	46.7
H	6.0	6.3

Table 4. 2 Biomass proximate and ultimate analyses

	Biomass 1	Biomass 2
O ₂ (%vol)	1.64	1.26
CO ₂ (%vol)	11.48	12.02
CO (%vol)	18.77	18.35
H ₂ S (ppm)	9.65	12.82
CH ₄ (%vol)	2.05	1.82
H ₂ (%vol)	16.74	16.94
N ₂ (%vol)	49.32	49.61
LHV (MJ/kg)	4.21	4.13
α_{st}	1.45	1.42
Tar concentration (g/m ³)	2.13	8.57

Table 4. 3: Syngas compositions and lower heating values

Next paragraph reports the engine sensibility analysis and exhaust emissions for each test point.

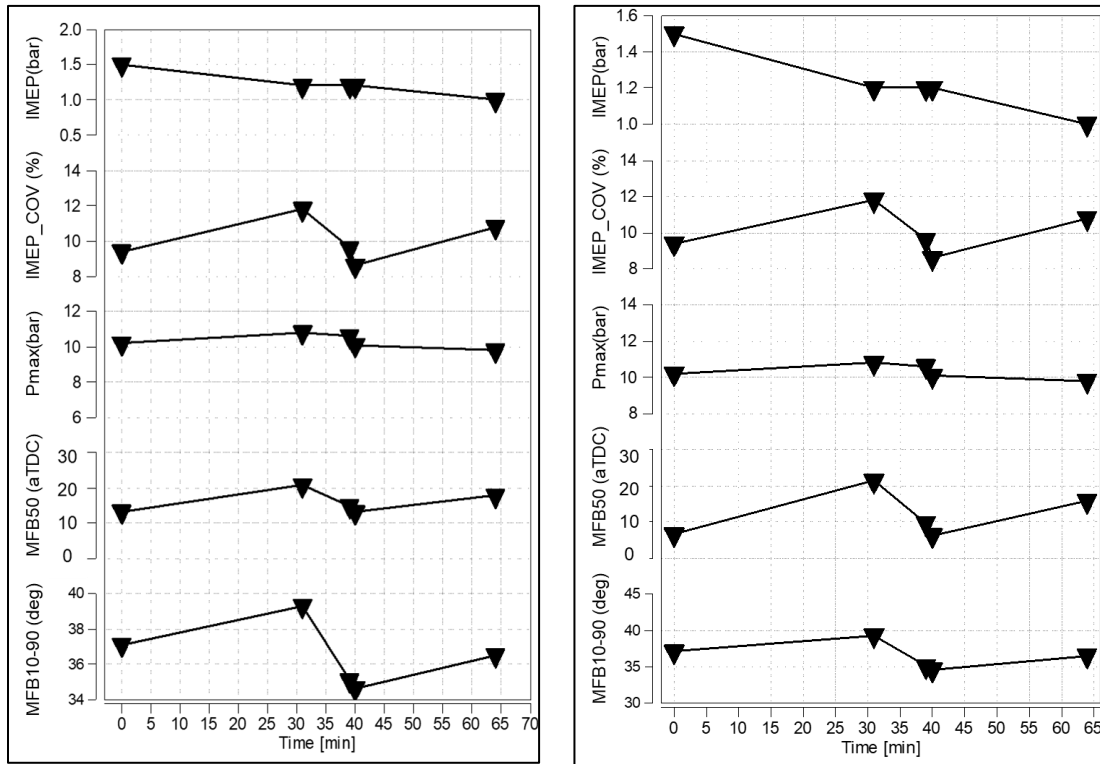
4.1.1 Engine sensibility analysis

The following analysis is made to show the engine sensibility when fuelled by two biomasses to different loads and spark advances.

Figure 4. 2 shows the trend of the main engine parameters indicated as the Mean Indicated Pressure (IMEP), covariance of the IMEP ($IMEP_{COV}$), the maximum pressure (P_{max}), the combustion centre of gravity (MFB50), and the combustion duration (MFB10-90) deriving from the measured pressure curve in the combustion chamber by means of the pressure transducer, explained in Chapter 2. In particular, to remark, MFB50 is defined as the corresponding angle in which 50% of the fuel, adducted for each work cycle, is burned. MFB10-90, on the other hand, is the angular range between 10% and 90% of the burned mass.

The temporal trends of these variables are intended to highlight the variations of these parameters as a function of the external load that is required by the users of the waste management and operation plant, to validate the system's ability to adapt to such load, which varies between 4-6 kWhe. In Figure 4. 2, the data refers to the performance of the mCHP engine, fed with syngas deriving from wood sawdust briquettes (left) and straw briquettes (right). Operating conditions for both test are spark advance set at 20 deg bTDC and lambda value (λ) of 1.03. These values, of relative optimum in terms of efficiency and emissions, derived from Chapter 3 engine analysis.

The IMEP values fluctuate in the range 1-1.5 bar with a maximum pressure value of about 10 bar. As regards the covariance, as well as the centre of gravity and the duration of combustion, an important variability is highlighted, due to the non-constant syngas composition. Indeed, the covariance, which is indicative of the combustion stability, oscillates between 8-12% for biomass 1 and 10-13% for biomass 2, much higher values compared to automotive or natural gases applications, whose maximum values set about 5% [3]. Evidently, this instability is partially transferred to MFB10-90 and MFB50 values. To underline this consideration, Figure 4. 3 shows the pressure cycle traces for biomass 1. It reveals all the 256 consecutive cycles acquired by the system, where the traces characterized by the minimum and maximum value of P_{max} are highlighted in red. The average value is shown in blue.



Biomass 1

Biomass 2

Figure 4. 2: IMEP, IMEP_{COV}, P_{max}, MFB50 and MFB10-90 for both biomasses (low load).

With biomass 1, it is important to emphasise that, despite having low load values and a significant variability in the combustion process, no misfiring phenomena (cycles with no IMEP) occurs, demonstrating the robustness of operation guaranteed by the quality of the syngas and by the efficiency of the engine.

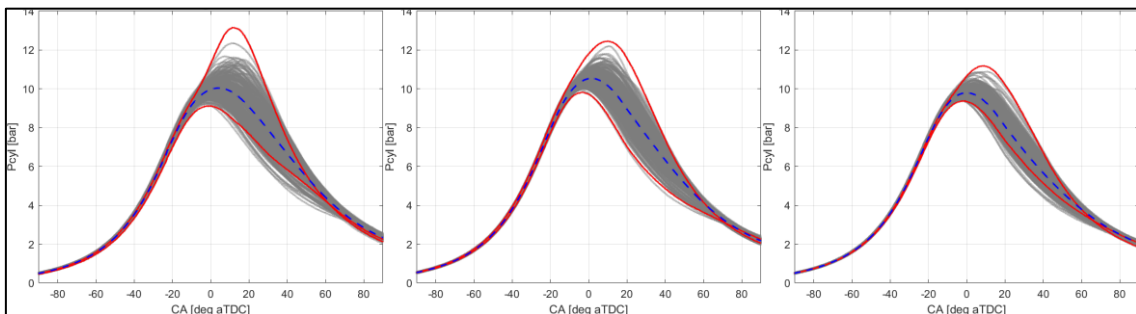


Figure 4. 3: Combustion chamber pressure with (P_{cyl}) with spark advance = 20° bTDC, $\lambda = 1.03$, low load, biomass 1.

The effect of the syngas inhomogeneity on combustion could be notice in Figure 4. 4 in the MFB0-10 (angular interval between the set value of advance at ignition with respect

to MFB10), MFB10-50 and MFB50-90. The inhomogeneity has a predominant effect on the MFB0-10 parameter, which varies between 36-43 °CAD even though the IMEP remains the same (about 1.2 bar).

For a more accurate analysis, the thermodynamic efficiency (η_T) of the spark ignition engine is also calculated on the basis of the averaged values using the following relations:

$$P_{ind} = \frac{IMEP * V * n}{\varepsilon} \quad (4.1)$$

$$\dot{m}_{syng} = \frac{\dot{m}_{exh}}{(1 + \lambda * \alpha_{stochiom})} \quad (4.2)$$

$$\eta_T = \frac{P_{ICE}}{\dot{m}_{syng} * LHV_{syng}} \quad (4.3)$$

Where P_{ind} is the indicated power calculated starting from the IMEP taking into consideration the engine displacement V , the number of engine revolutions n and ε parameter which is equal to 2 in 4-stroke engines; \dot{m}_{syng} is the mass flow rate of syngas calculated from the measured exhaust gas flow rate (\dot{m}_{exh}) and LHV_{syng} is the measured syngas lower heating value.

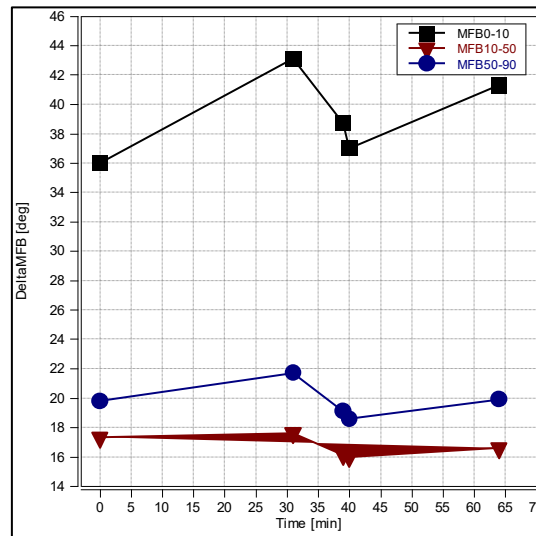


Figure 4. 4: MFB0-10, MFB10-50 e MFB50-90 for a spark =20°bTDC, $\lambda=1.03$, low load and biomass 1.

In load condition (SA = 20° bTDC, $\lambda=1.03$, 4-6kWe) the engine thermodynamic efficiency is 0.22 for biomass 1, while for biomass 2, on the other hand, is 0.14, hence 36% less.

Following Table 4. 1, the system is also characterized at higher load, about 70% of the maximum electrical load, which is equivalent to about 14-15 kWhe.

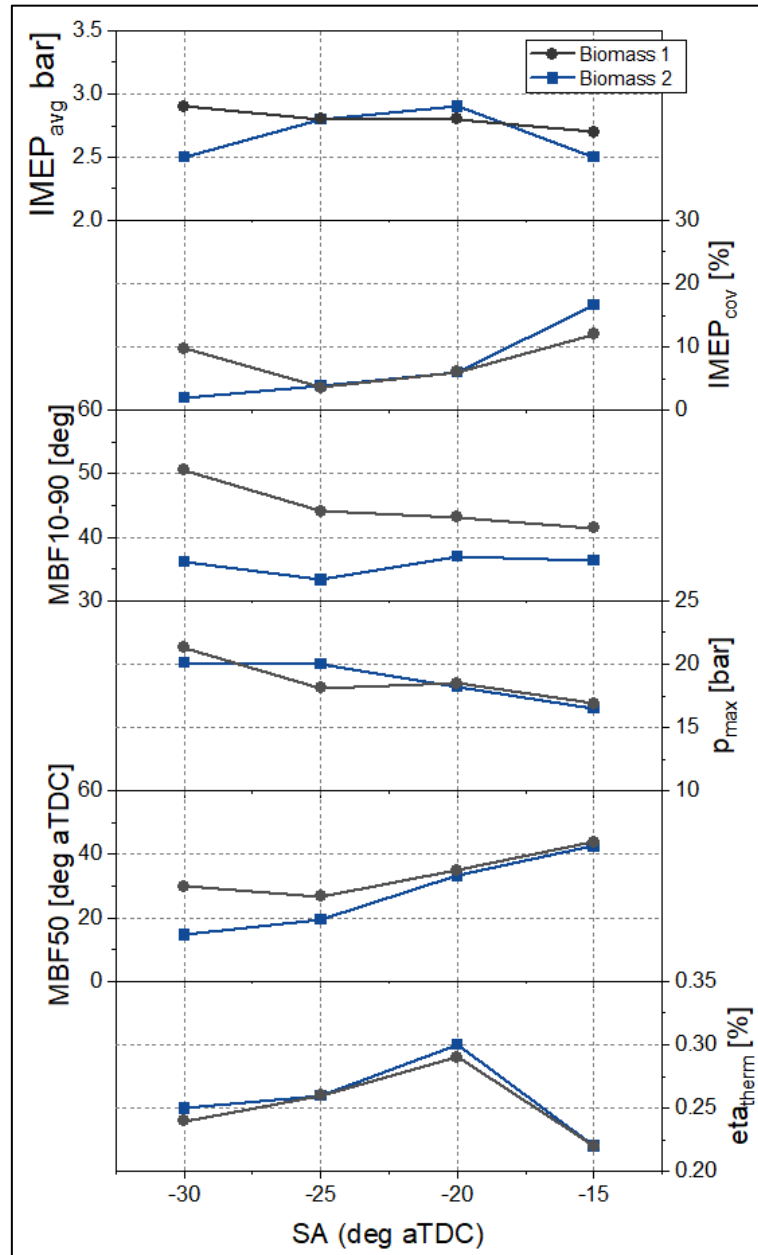


Figure 4. 5: IMEP, MFB10-90, MFB50, IMEP_COV, Pmax and η_{therm} for both biomasses at medium load.

For the medium load condition, the thermodynamic efficiency trends and the combustion main parameters at different start of spark are shown in Figure 4. 5. There are no radical differences between the two fuels; the thermodynamic efficiency are in line with those present in the literature [4]–[6].

Thermodynamic efficiency is sensitive to the ignition advance variation and has an optimal value for both biomasses for an ignition advance equal to 20° bTDC. This demonstrates the optimal calibration obtained from both numerical models and experimental measurement.

The IMEP values for biomass 2 are less sensitive to the variation of the spark advance. Indeed, a rather flat trend is observed. Combustion stability, on the other hand, is markedly sensitive to early ignitions, with values almost in line with the previous case (sawdust), except for the most anticipated case. Regarding the maximum peak pressure, values and trends between the two fuels are aligned. MFB50 is in line with the low load cases. Syngas deriving from biomass 1 presents a higher burn duration than biomass 1 for all spark advances.

To confirm what has already been illustrated, the pressure trends for each test of biomass 1 are shown below in Figure 4. 6. With a start of spark equal to -30 °CAD, an important variability of about 10 bar is observed on the peak pressure value, but with an almost constant angular position (AP_{max}). With greater delay of the advance (SA, Spark Advance), there is a reduction in this interval resulting from a general worsening of combustion and indicative of greater process instability. Similarly, the performance of the engine fed with syngas produced by the gasification of straw briquettes is analysed below with the acquisition of the ionization currents by means of the appropriate electronic device explained in Chapter 3.

A characterization of the fouling of the spark plug was also carried out by reading the ionization currents. Figure 4. 7a, under low load conditions, shows an almost constant trend of the average current value (Peak Ion_{mean}) with maximum values close to about 60 μA, without showing any fouling or misfiring. Starting from Test # 4, a slight increase (70-80 μA) in variability begins to appear, attributable to a slight fouling of the spark plug electrodes.

For medium load, an important increase in the Ion peak value is visible, up to about 630 μA), which can be justified by the temporary misfiring of the electrodes due to the temporary presence of carbon residues that could derive from the release temporary on the part of the supply system of carbon deposits that come off due to the sudden movement of the throttle valve.

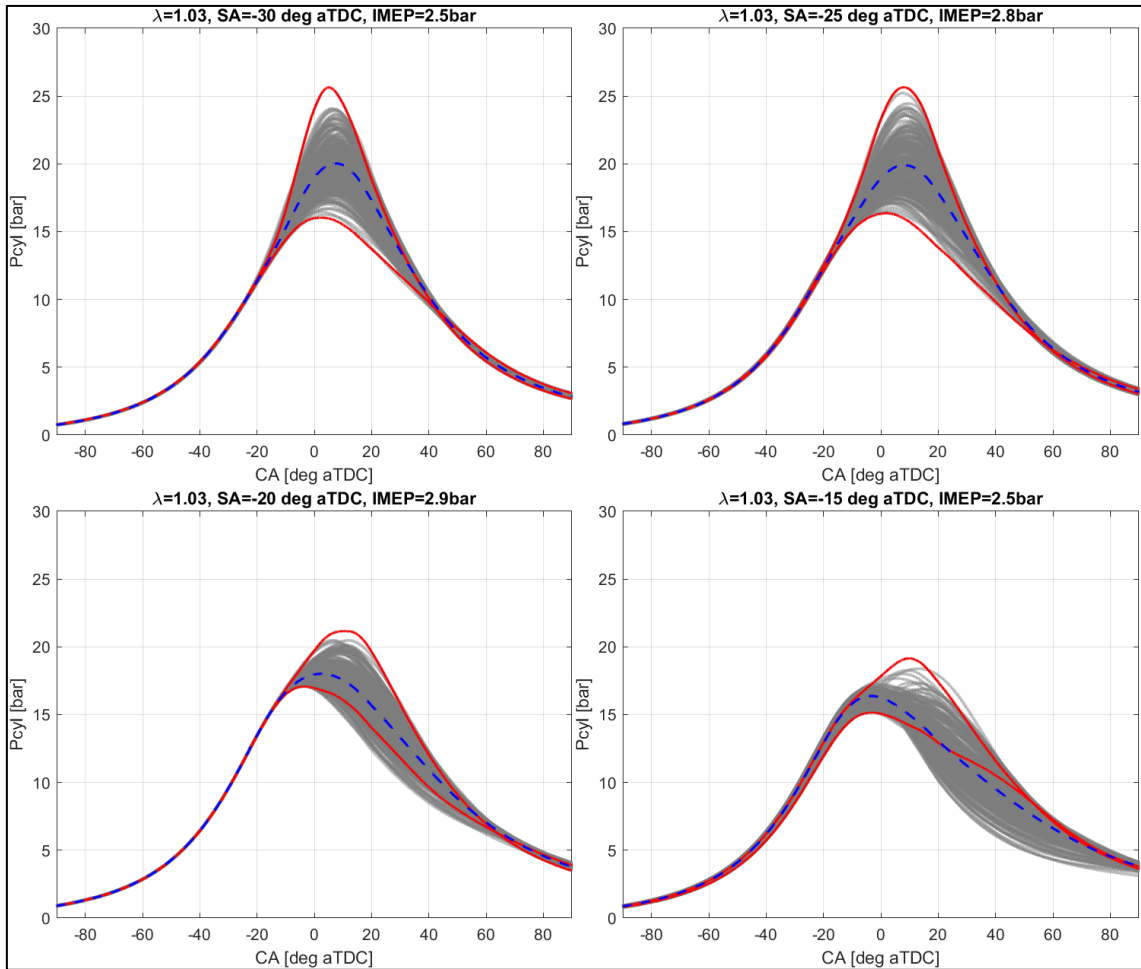


Figure 4. 6: Pressure traces (P_{cyl}) of biomass 1, medium load and $\lambda=1.03$ for different SA.

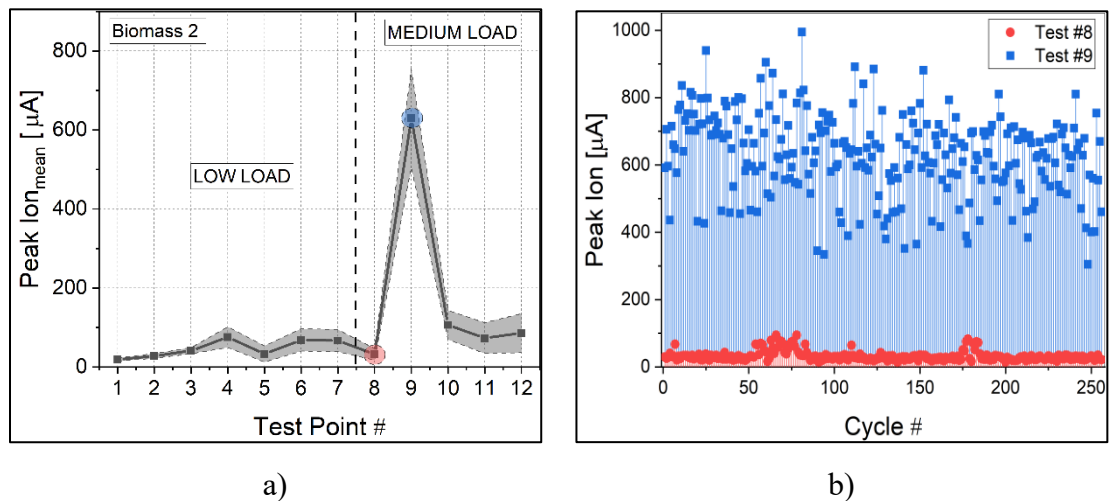


Figure 4. 7: Ionization current peak for biomass 2 tests (a) and comparison between two ionization current peaks with $\lambda: 1.03$, SA: 20 deg bTDC(b).

A zoom of the ionization current peak of the 256 consecutive acquired pressure cycle of test #8 and test#9 is shown in Figure 4. 7b. Test #8 presents ionization peak in the non-fouling range (40-70 μA), with some cycles that overtake the 70 μA limit, which shows the start of a slightly electrodes fouling. Test #9 presents high ionization peaks (400-1000 μA), which shows the misfiring taking place. In the following test #10 (Figure 4. 7a), the current Peak Ion_{mean} value returns to acceptable values (100 μA), significantly lower than the previous condition. This value shows a carbonaceous leftover on the electrodes. No misfiring is noticed in subsequent tests. The ECU for reading the ionization currents is confirmed to be suitable for an "on-board" and real-time control of the combustion and/or of the syngas quality, capable of providing information on the degree of fouling of the spark plug. This last allows to understand the operating status of the engine and highlights the need for maintenance interventions.

Figure 4. 8 shows the exhaust mass flow (a) and temperature (b) of both feedstocks. No difference between sawdust and straw arises for exhaust mass flow ratio, which appears to not be influenced by the initial feedstock.

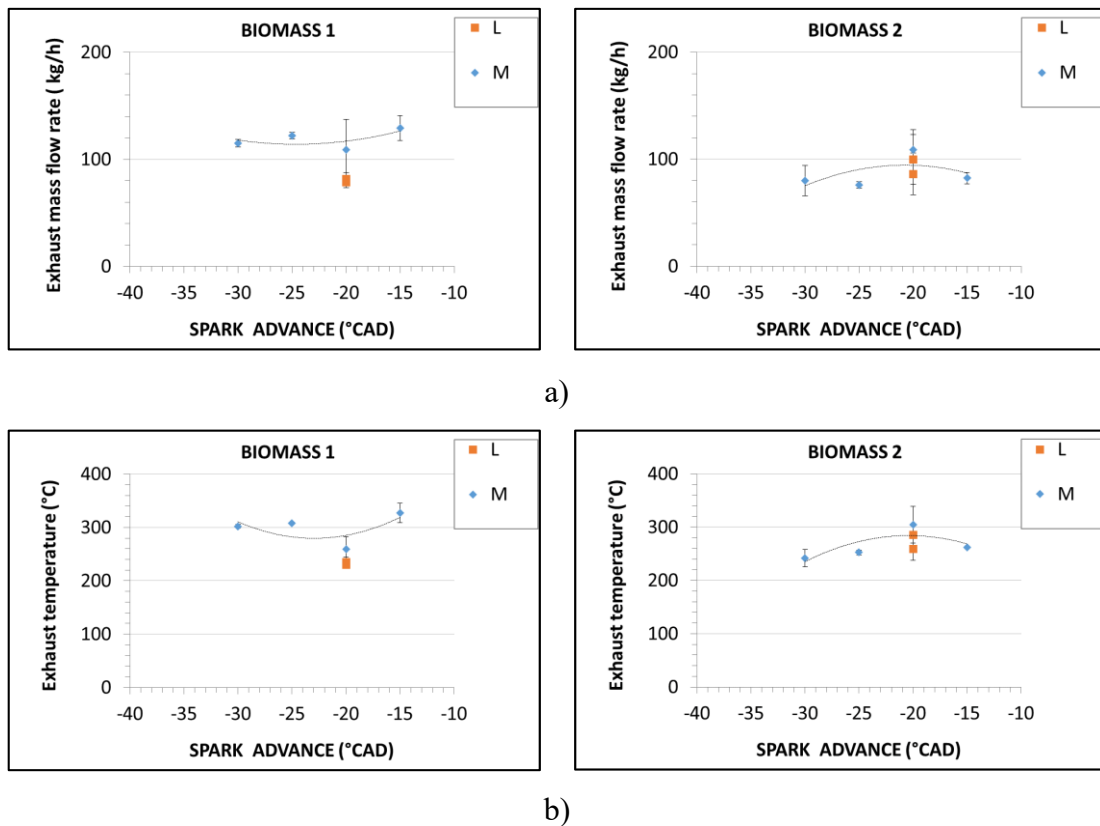


Figure 4. 8: Exhaust mass flow rate (a) and temperature (b) for both processed feedstocks.

Biomass 2 presents a slightly higher exhaust temperature than biomass 1 for medium load and a spark advance of -20° CAD. However, these values remain in the range of effective exhaust temperature for the reduction of CO emissions, as it is not higher than 650°C . An extreme exhaust temperatures, indeed, can destroy the catalytic converter [1].

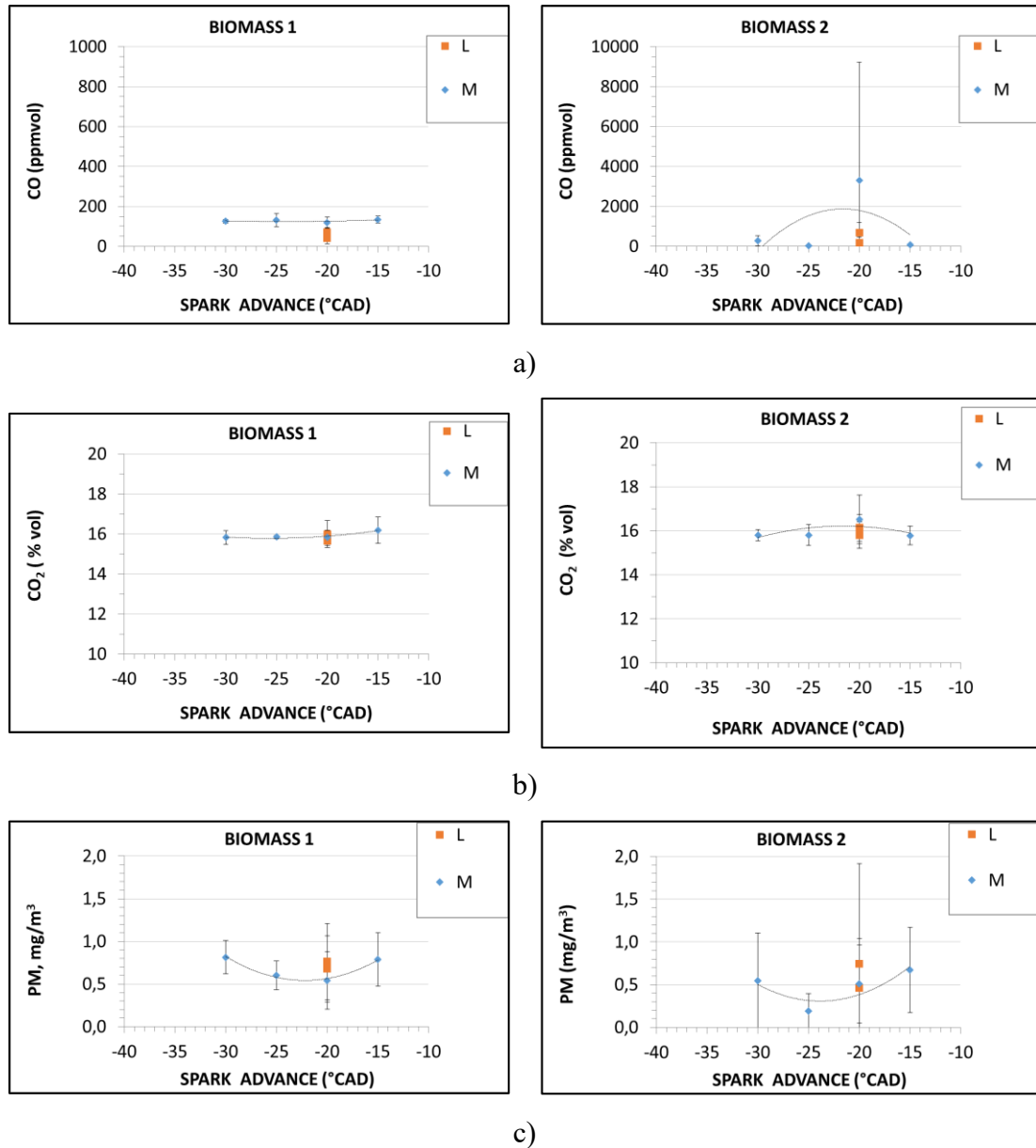


Figure 4. 9: Emissions of CO (a), CO₂ (b) and PM (c) for both biomasses

The measured emission species are summarized in Figure 4. 9 and Figure 4. 10. Since the Semtech analyser measures components on a dry basis, those have been recalculated on a wet basis as required by the Italian legislation Dlgs. 11/15/2017, no. 183 [2].

In the M load condition and -15 °CAD spark advance, a high variability is found in the determination of CO and CO₂ due to a sudden and fast load variation, so the data were recalculated only in the times with a fairly constant load condition. The concentrations of CO and NO_x are not particularly variable with the ignition advance. PM is always lower than 2 mg / m³.

Taking into account the measured oxygen concentrations in the exhaust gases, the polluting emissions of CO, NO_x and PM are corrected according to formulas reported in Chapter 2. The corrected data are used to calculate the emissions in mg/m³ (under normal conditions of temperature and pressure equal to 273.15 K and 101.3 kPa), to make a comparison with the legal limits set by Italian legislation.

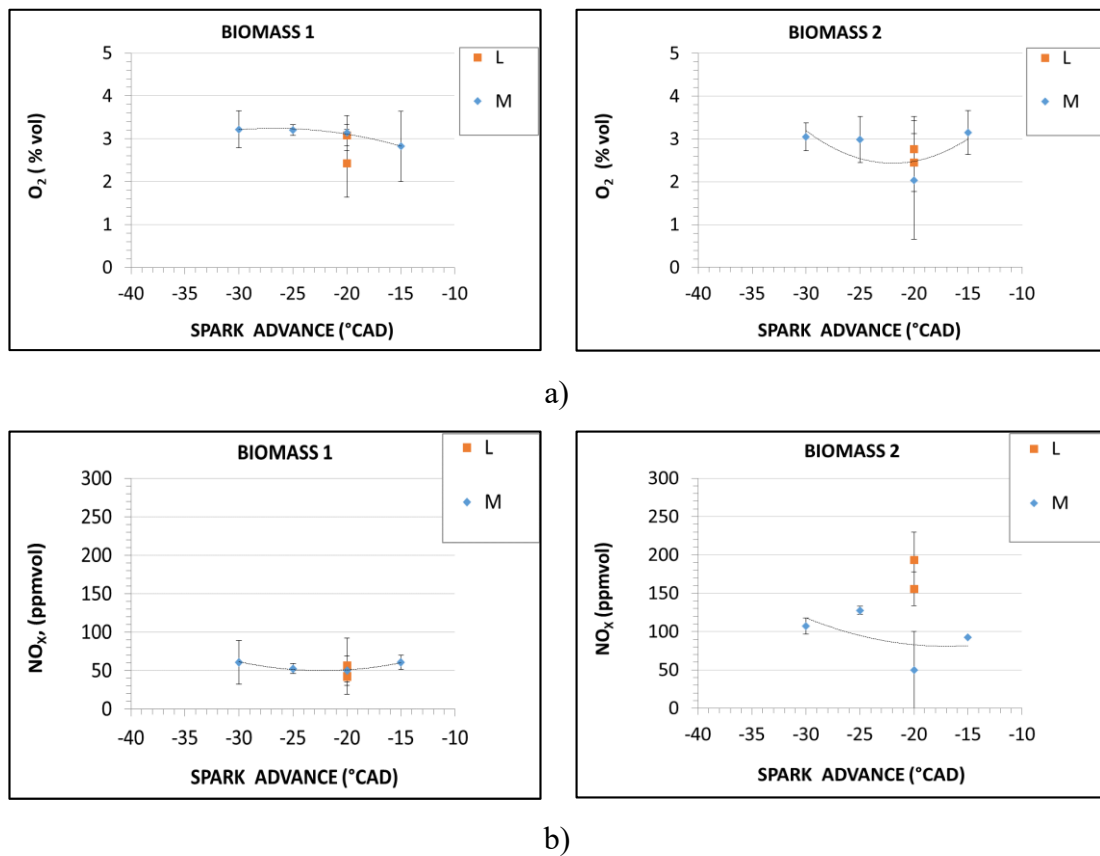


Figure 4. 10: Emissions of O₂ (a) and NO_x (b) for both biomasses

For biomass 1 (sawdust) CO and NO_x emissions are below the limits in all tested conditions (70 mg/m³). Even in the most critical condition for CO, which occurred at M load and advance -15 ° with a sudden load variation, the CO remains below 600 mg/m³ limit.

It should be noted that on the biomass 2 test day there was a concurrence with a small fire in a close area (south) which influenced the air quality assessment (in terms of CO and PM) and, therefore, also the air sucked by the system itself. Furthermore, there were problems on the lambda control which in some conditions dropped to 0.9. In the conducted analyses, it is not always possible to filter the data to eliminate these effects. This is highlighted in the Biomass 2 CO emission that presents high variability and, in some cases, also overtakes Italian limits. The same problem is also visible for CO₂ and O₂. NOx analysis for biomass 2 were always below limits.

For both biomasses, PM emissions are confirmed not to represent a criticality for the internal combustion engine of the plant in question.

4.2 Air quality assessment analysis

The ETL-One station [7] was hired from the Orion company for air quality assessment analysis during CMD ECO20x installation in the waste management and storage plant of Mugnano, Napoli.

ETL ONE				
	PARAMETERS	RANGE	PRECISION	RESOLUTION
SENS-IT (TF-MOS – Thick Film Metal Oxide Semiconductor)	CO	0.1-80 ppm	0.2 ppm	0.1 ppm
	NO ₂	10-250 ppb	10 ppb	1 ppb
	O ₃	10-250 ppb	10 ppb	1 ppb
	C _x H _x	0.1-30 ppb	0.2 ppb	0.1 ppb
	CH ₄	1-1,500 ppm	5 ppm	1 ppm
SENS-IT (EC - Electrochemical Technology)	NH ₃	7-100 ppm	0.3 ppm	0.1 ppm
	SO ₂	5-10,000 ppb	20 ppb	1 ppb
	H ₂ S	2-3,000 ppb	15 ppb	1 ppb
	VOC	0.6-25 ppm	0.1 ppm	0.1 ppm
SENS-IT (IR - Infrared Technology)	CO ₂	10-5,000 ppm	50 ppm	1 ppm
DUST MODULE (Orthogonal Light Scattering)	PM10 or PM2.5 or PM1	1-400 µg/m ³	< 2% f.s.	1 µg/m ³
DUST MODULE (OPC)	PM10 and PM2.5 and PM1	1-6,000 µg/m ³	< 1% f.s.	1 µg/m ³

Table 4. 4: ETL One technical specification [7]

The ETL One is a multiparametric station with Unitec SENS-IT technology for continuous gas and dust monitoring with high accuracy and precision, as well as ease of use and low ownership costs. The IP55 casing allows for simple and direct outdoor installation without the need for cooling or air treatment systems. 4

The Unitec SENS-IT gas sensors can constantly monitor gas pollution with exceptional sensitivity and selectivity (even at ppb levels) and requiring no frequent maintenance or calibration. Each SENS-IT sensor is dedicated to a single gas and is connected to the datalogger through a plug-in connector, allowing for quick in-field replacement.

A completely integrated dust monitoring module based on orthogonal light scattering technology is included with the ETL One for real-time particulate monitoring (PM10).

Principal technical specifications are reported in Table 4. 4, while Figure 4. 11 shows the external case and the selected gas and PM sensors.

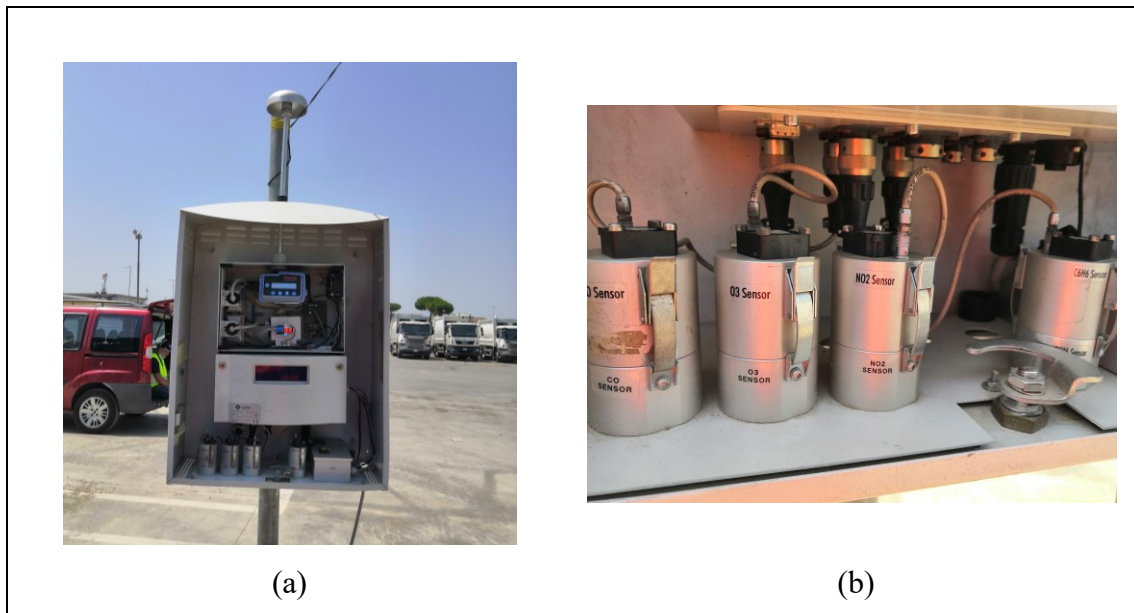


Figure 4. 11: Installed ETL One in Mugnano, Napoli: external case (a) and sensors (b)

Together with the ETL-One station, a weather station (Figure 4. 12) was also hired to obtain information on wind speed and direction, external temperature and humidity at the measurement site.

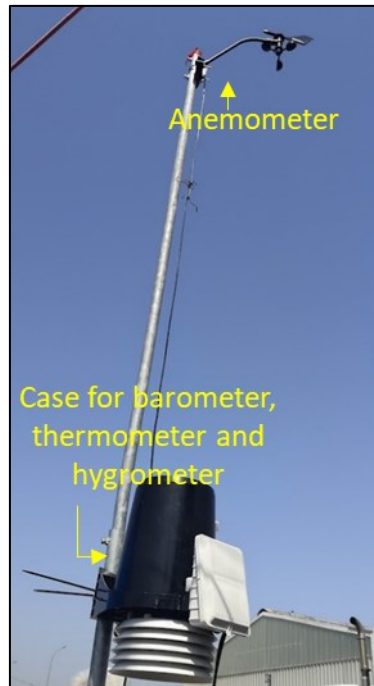


Figure 4. 12: Weather station

The selected weather stations have the following instruments:

- *Thermometer* for measuring air and sea surface temperature;
- *Barometer* for measuring atmospheric pressure;
- *Hygrometer* for measuring humidity;
- *Anemometer* for measuring wind speed and direction.

4.2.1 Location of the air pollution monitoring station

Figure 4. 13 shows a photo from above of the waste management and storage plant of the Mugnano Municipality (NA) and the position of the CMD ECO 20x is highlighted in the red circle. A compass is useful to specify its orientation.

To define the best location for the ETL-One monitoring station, in a zone characterized by the maximum falling of pollutants, the prevailing wind direction was previously assessed.



Figure 4. 13: Location of the CMD ECO20x (red circle) at the waste management and storage plant of the Municipality of Mugnano.

Figure 4. 14 shows the wind rose with the prevailing direction and the average speed on both test days. For both days, the prevailing wind is a wind that blows from the SOUTH-WEST with an angle of around 220 ° and an average intensity of around 2-4 m/s for biomass 1 test day and 1-5m/s for biomass 2 test day.

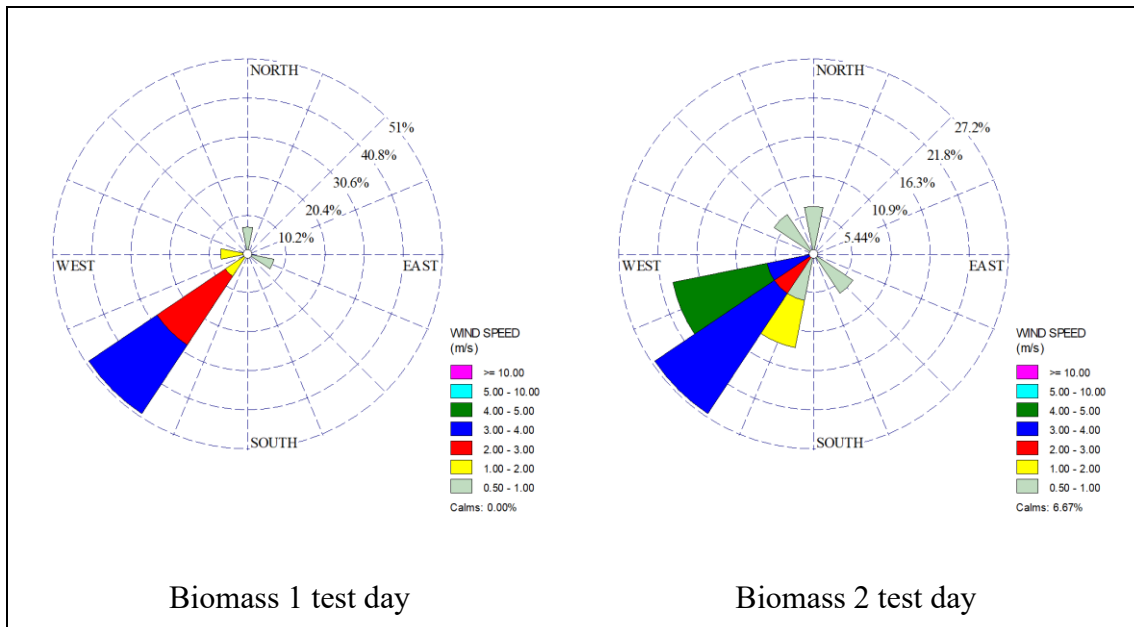


Figure 4. 14: Wind rose of the two test days

Therefore, the monitoring station is located in a NORTH, NORTH-EAST position related to the position of the mCHP plant in order to be downwind of the polluting emissions (Figure 4. 15).



Figure 4. 15: Position of the ETL one during the two test days.

4.2.2. Air quality assessment analysis in the CMD ECO20x proximity.

The air quality assessment analysis is carried out for both test days. ETL-One is left overnight, with the system shut off, to have the full-scale measurement. This measure will help understand the effect of the installation of CMD ECO20x in the area.

The hourly average concentrations of carbon monoxide (CO), nitrogen dioxide (NO₂), benzene (C₆H₆), ozone (O₃) and dust (PM10) are obtained for both test days.

The ambient temperature in both days of the experimental activity varied in the range of 23-37 °C with relative humidity of the air between 21-57% (Figure 4. 16). During the two measurement sessions the ambient temperature exceeded 35°C.

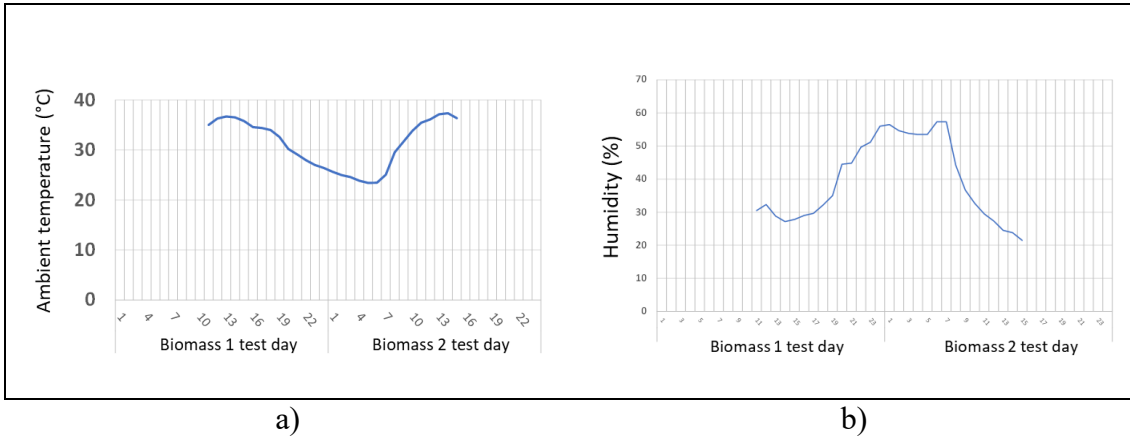


Figure 4. 16: External temperature (a) and humidity (b) for the two test days.

The following Table 4. 5 shows the hourly average measured concentrations measured in $\mu\text{g}/\text{m}^3$. The measurements taken with the CMD ECO20x system switched on (i.e. with the engine running) show average values that fall between the values measured as full-scale.

A conclusion that can be drawn in relation to the environmental impact of the CMD ECO20x mCHP system does not influence the air quality assessment. The measured values are below the daily and hourly limits set by D.lgs. n°155 [8].

	CO ($\mu\text{g}/\text{m}^3$)	NO ₂ ($\mu\text{g}/\text{m}^3$)	C ₆ H ₆ ($\mu\text{g}/\text{m}^3$)	O ₃ ($\mu\text{g}/\text{m}^3$)	PM10 ($\mu\text{g}/\text{m}^3$)
Biomass 1 test day	350	44,2	0,50	97,6	15,30
Biomass 2 test day	1150	67,0	0,60	26,4	1,5
Full-scale	300÷1700	37÷100	0,3÷2,9	6÷95	0,6÷22
Limit [8] (Sampling time)	10000 (8 h moving average)	200 (1h)	5 (1year)	-	50 (24h)

Table 4. 5: Air quality assessment during the two test days and full-scale measurement.

4.3 Life cycle analysis

The principles, framework, and requirements of life cycle analysis (LCA) are outlined by Guinee et al. [9] and Guest et al. [10]. LCA is a widely used tool in the examination of renewable energy systems for environmental implications.

The LCA is used to analyze the environmental impacts of the CMD ECO20x m-CHP plant fuelled by forest residues in a radius of 25 km from the municipality of Mugnano (NA) (Figure 4. 17). This allows the collection of biomasses from countryside in a rather vast area that could even comprehend Vesuvio National Park and Caserta countryside.

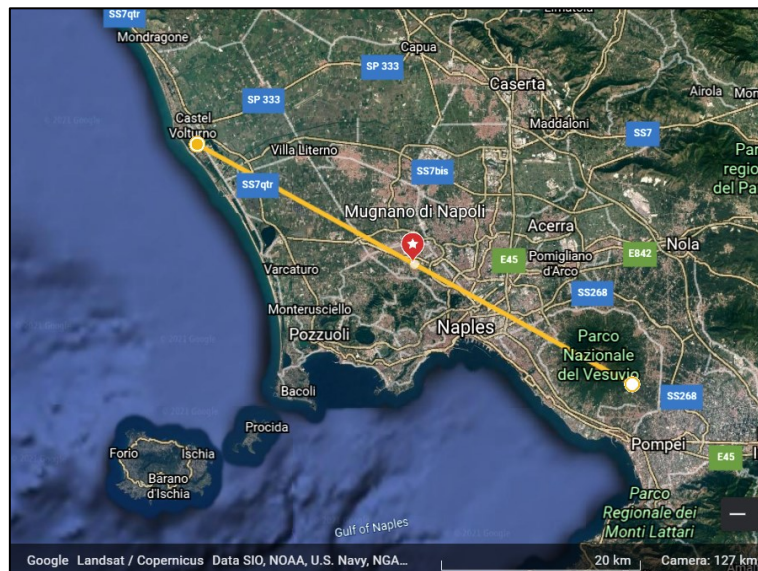


Figure 4. 17: 50km diameter with Mugnano (Napoli) as a centre [11]

The objective is to do an analysis of 144 MWh of electrical energy delivered to the user. This requires almost 200 tons of biomass.

The evaluation of the biomass to energy chain's impact needs the evaluation of each individual contribution, which came after the identification and quantification of the system's inputs and outputs (Figure 4. 18). Due to the material's sustainability, using biomass as a fuel in a reciprocating engine for energy purposes is considered CO₂ neutral; however, the same cannot be said for the amount of energy required to cut and transport the material, especially if fossil fuels are employed.

Cutting and chipping in the field of twigs and trunks is the best solution among those considered, thus the agricultural company should require a tractor with a tow chipper.

Thanks to the high availability of biomass that far exceeds the energy needs of the micro-CHP unit, a small number of trips and hours of work dedicated to logging and chipping are expected, thus making local supply of wood chips feasible.

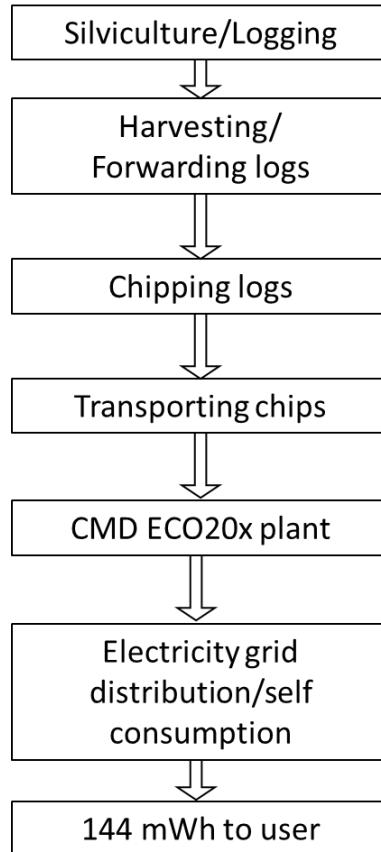


Figure 4. 18: Foreground system flow diagram

The cutting phase takes place considering the felling with a chainsaw. The logs are collected from the felling point and transported to a clearing in the woods. Here the dimensions of the logs are reduced. Chipper could also be used to scale the entire log into coarse flakes. Then, the wood is loaded onto the tractor to the forest edge, where it is transported by truck to the CMD ECO20x.

It is possible to calculate the contribution to CO₂ equivalent emissions by examining each phase in detail. When it comes to logging, a gasoline-powered chainsaw has been considered. More efficient options, such as disc or shear blast chillers, which chop trees randomly, have been rejected, since indiscriminately logging is in contrast with the idea of a sustainable wood management.

A consumption of 0.55 l/h of gasoline is considered, with a productivity of 0.7 t/h, corresponding to about 10 minutes/tree [12]. With these data, the contribution to CO₂ equivalent emission, compared to the 144 MWh of electricity produced downstream of the process, is calculated using the equation (4.4) [13]:

$$\varepsilon_{CO_2cutting} = \dot{m}_{biomass} * \frac{(\varepsilon_{CO_2fuel} * \dot{m}_{fuel})}{P_{oper}} * kg_{CO_2} \quad (4.4)$$

Where:

- $\dot{m}_{biomass}$: the amount of wood to be cut;
- ε_{CO_2fuel} : the quantity of CO₂ produced;
- \dot{m}_{fuel} : the amount of fossil fuel needed;
- P_{oper} : the average productivity of a worker for the specific phase.

For chipping, this phase is carried out on site by bringing the chipper from the company warehouse to this area. In this case, an average consumption of 40 l/h of gasoline is considered with an average productivity of 2.2 ton/h of wood chips. It is possible to use the same equation (4.1).

Two contributions are evaluated for transportation: the first concerns the movement of logs within the forest by tractor trips, and the second one involves the moving of logs from the forest edge to the delivery location by truck. This is the most conservative situation possible, because when the cutting location is close to the delivery site, transportation is frequently done directly only with tractor, saving time and money.

The tractor transport consists of 5 km at an average speed of 15 km/h. A consumption of the tractor of 15 l/h of diesel is considered. The maximum load considered is 6 tons, the limit set by the legislation for single-axle tractor trailers [14].

For truck transportation, 25 km covered at an average speed of 20 km/h and a consumption of 6 l/h of diesel are considered.

The contribution to CO₂ emissions can be evaluated as equation (4.5):

$$\varepsilon_{CO_2transportation} = \frac{\dot{m}_{biomass} * l}{t * v_m} * (\varepsilon_{CO_2fuel} * \dot{m}_{fuel}) * kg_{CO_2} \quad (4.5)$$

Where:

- $\dot{m}_{biomass}$: the amount of transported chips;
- l : distance covered;
- ε_{CO_2fuel} : the quantity of CO₂ produced;
- \dot{m}_{fuel} : the amount of fossil fuel needed;
- t : transporter load;
- v_m : average velocity.

The sum of the contributions related to cutting, chipping, and transportation represents the non-renewable quote of energy and can be compared to CO₂ equivalent emissions of a diesel genset [15], as shown in. Table 4. 6.

	Cutting (ton CO_{2eq})	Chipping (ton CO_{2eq})	Transport – Tractor (ton CO_{2eq})	Transport- Truck (ton CO_{2eq})	Total (ton CO_{2eq})
<i>CMD ECO20x</i>	0.46	1.07	0.48	0.88	2.89
<i>Diesel generator</i>	-	-	-	-	43.93
Δ	-93.4%				

Table 4. 6: LCA analysis of CMD ECO20x in comparison with a diesel generator to deliver 144 MWh to the user

CO₂ emissions for CMD ECO20x are 15 times lower than a diesel generator producing the same energy to the user, which is in accordance with the goal of decreasing the impact of human activity on the climate.

4.4 Economic analysis

Two possible scenarios were considered for the economic analysis:

1. the produced electricity is fed into the national grid;
2. the produced electricity is self-consumed at the installation site of the ECO20x.

In the first case, the user needs to have a special contract the under the *dedicated withdrawal*, pursuant to the Authority for Electricity and Gas (GSE) [16]. Table 4. 7 reports the mean prices for each month of 2021 for the 3 sections. For an installation in the municipality of Mugnano, Naples, the prices related to “Centro-Sud” is referred.

F1												
	gen.	feb.	mar.	apr.	mag.	giu.	lug.	ago.	set.	ott.	nov.	dic.
Centro Nord	75,30	60,78	60,53	70,41	74,40	88,61	108,72	113,63	162,70	230,79	260,47	
Centro Sud	68,84	59,29	59,74	68,44	70,41	88,70	109,03	117,21	162,41	226,21	251,35	
Nord	75,83	65,03	60,62	71,07	74,20	88,84	108,93	112,56	162,69	234,22	262,48	
Sardegna	66,33	58,98	58,91	62,81	57,70	89,29	109,55	98,28	145,57	228,39	252,03	
Sicilia	63,77	60,35	56,10	72,51	69,81	94,20	116,12	132,14	162,26	198,43	247,22	
Sud	61,70	58,43	56,45	63,73	70,14	88,41	109,28	117,09	159,95	213,20	246,59	
Calabria	60,23	59,34	56,39	63,76	70,48	88,79	109,37	117,33	159,21	193,79	246,45	
F2												
	gen.	feb.	mar.	apr.	mag.	giu.	lug.	ago.	set.	ott.	nov.	dic.
Centro Nord	61,36	57,63	62,69	67,80	68,80	78,89	99,27	103,12	149,86	206,17	217,75	
Centro Sud	60,33	57,42	63,01	66,74	69,05	82,48	104,21	115,75	151,42	211,20	220,35	
Nord	62,23	57,47	62,86	68,39	70,76	81,04	100,28	103,54	152,87	215,64	221,44	
Sardegna	52,16	56,86	63,42	68,08	66,64	89,58	108,37	108,14	158,02	222,40	209,80	
Sicilia	59,40	59,02	65,63	69,75	69,23	103,77	109,78	119,91	153,97	221,26	222,46	
Sud	56,57	56,51	62,19	65,81	69,93	80,60	103,48	114,88	153,62	207,07	222,38	
Calabria	58,45	59,42	64,17	70,07	71,33	85,94	104,42	117,09	155,55	213,07	223,93	
F3												
	gen.	feb.	mar.	apr.	mag.	giu.	lug.	ago.	set.	ott.	nov.	dic.
Centro Nord	52,02	40,85	53,35	55,64	56,36	70,35	85,31	92,72	134,58	181,99	194,33	
Centro Sud	51,25	39,95	53,09	55,09	57,60	73,58	89,91	99,21	137,61	183,12	194,35	
Nord	51,97	44,43	52,38	57,04	57,60	71,07	86,78	91,59	136,05	183,67	192,94	
Sardegna	46,96	39,50	54,29	57,20	54,37	75,65	92,52	101,53	138,04	182,74	191,72	
Sicilia	50,85	39,49	51,92	57,35	56,04	86,27	92,79	117,92	139,60	197,67	208,14	
Sud	50,12	38,92	51,78	55,28	56,29	72,27	89,46	98,79	142,45	181,71	195,17	
Calabria	49,72	41,06	53,31	58,20	58,26	77,48	92,06	110,27	140,42	190,10	191,69	

Table 4. 7: Prices (€/MWh) for dedicated withdrawal in Italy in 2021[16]

If the CMD ECO20x works for 7200h, it is possible to assume a weighted average price for the produced electricity of 104.5 €/MWh. In the second scenario the total avoided energy price for 2021 is 190 €/MWh. This last value is conservative due to the increase in the electricity prices over the last months of 2021 [17].

Table 4. 8 presents the data used for the evaluation of costs and revenues.

The electricity supply for briquetting and the thermal energy required from biomass drying can take place directly from the CMD ECO20x plant, so the costs can be considered null. The not-sale is, however, considered.

For the benefits deriving from the avoided cost associated with the purchase of the fuel (natural gases) used in the boiler to produce thermal energy, an efficiency of 90% was assumed for the calculation of the fuel consumption necessary to cover the thermal energy supplied by the ECO20x system.

Annual biomass consumption (ton)	200
Price of Green biomass (€/ton) [12]	60
Transport cost (€/ton) [12]	20
Biomass cost (€/MWh) [12]	111
Electric power for briquetting (MWh)	4.32
Cost of electricity (€/MWh) [18]	190
Total produced electricity (MWh)	144
Price of selling electricity (€/MWh)	104.5
Total thermal energy recovered (MWh)	252
Thermal energy for biomass drying (MWh)	52.2
Price of natural gas (€/MWh) [19], [20]	110
Initial Investment (k€)	180
Maintenance cost (k€)	5
Disposal cost (k€)	8

Table 4. 8: Data for the calculation of costs and revenues

Main economic indexes are reported in the following equations. The total cost to produce 144 MWh with the CMD ECO20x could be calculated through equation (4.6); the revenues from selling electricity is calculated in equation (4.7); ΔCE is the annual savings (4.10) while the SPB is the Simple payback period, calculated through the equation (4.11). VAN is calculated through equation (4.13). A value greater than zero indicates that the investment is profitable. The Gross Profit %age ratio (IP) is calculated through equation (4.14).

$$C_{CMDECO20x} = c_{biom,kWhe} * P_{el} + M + D \quad (4.6)$$

$$R_{el} = (P_{el} - P_{briqu}) * r_{el,kWh} \quad (4.7)$$

$$C_{el,ref} = c_{el} * (P_{el} - P_{el,briqu}) \quad (4.8)$$

$$C_{th,ref} = c_{methane} * \frac{(P_{th} - P_{th,drying})}{\eta_{boiler}} \quad (4.9)$$

$$\Delta CE_{scenario1} = R_{el} + C_{th,ref} - C_{CMDECO20x} \quad (4.10)$$

$$\Delta CE_{scenario2} = C_{el,ref} + C_{th,ref} - C_{CMDECO20x}$$

$$SPB = \frac{ICC}{\Delta CE} \quad (4.11)$$

$$FA = \left(\frac{1}{a} * \left(1 - \frac{1}{(a+1)^n} \right) \right) \quad (4.12)$$

$$VAN = \Delta CE * FA - ICC \quad (4.13)$$

$$IP = \frac{VAN}{ICC}. \quad (4.14)$$

Where:

- $C_{CMDECO20x}$ is the annual cost of the CMD ECO20x;
- $c_{biom,kWhe}$ is the biomass cost per kWh;
- P_{el} is the total produced electrical power;
- M is the annual maintenance costs;
- D is the annual disposal costs;
- R_{el} is the annual revenues due to the electricity selling to the dedicated withdrawal;
- P_{briqu} is the electricity energy required for briquetting;
- $r_{el,kWh}$ is the price to sell 1 kWh of electricity;
- $C_{el,ref}$ is the cost to produce the same electrical power of CMD ECO20x with the reference system (National Grid);
- c_{el} is the unitary cost to buy electrical power from National Grid;
- $C_{th,ref}$ is the cost to produce the same thermal power of CMD ECO20x with the reference system (natural gas boiler);
- $c_{methane}$ is the combustible cost for the boiler;
- $P_{th,drying}$ is the thermal power required for biomass drying;
- η_{boiler} = thermal efficiency of a boiler equal to 0.9;
- a is the discount rate equal to 4%;
- n is supposed to be 20 years;
- ICC is the initial investment cost.

The calculated revenues are summarized in Table 4. 9 for both scenarios.

The investment is profitable both for scenario 1 and 2, even though scenario 2 is more advantageous, with a payback time of less than 6 years and a gross profit %age ratio greater than 1.

However, with the new growth of prices for both natural gases and electricity [21] of 2022, both scenario 1 and 2 will be more profitable in the future.

Indeed, an increase of +41.8 % in natural gas price and an increase of 50% in electricity price is expected in the first semester of 2022 [17].

$C_{CMDECO20x}$	28 k€/year
R_{el}	13 k€/year
$C_{el,ref}$	23 k€/year
$C_{th,ref}$	23.11 k€/year
FA (20 years)	13.75 years
Scenario 1	
ΔCE	21 k€/year
VAN	108 k€
Payback time	8.6 years
IP	0.6
Scenario 2	
ΔCE	31 k€/year
VAN	247 k€
Payback time	5.8 years
IP	1.3

Table 4. 9: Annual Savings, VAN, Gross %age profit and payback time obtained from the operation of the plant.

If biomass is self-produced, due to the availability of ligneous production scrap in the waste management and storage plant, SPB can be reduced drastically in both scenarios.

References of Chapter 4

- [1] N. Shrivastava, S. N. Varma, and M. Pandey, “Experimental Study on the Production of Karanja Oil Methyl Ester and Its Effect on Diesel Engine,” *Int. J. Renew. Energy Dev.*, vol. 1, no. 3, pp. 115–122, Oct. 2012, doi: 10.14710/ijred.1.3.115-122.
- [2] D.lgs., “D.lgs. n. 183, 15 novembre 2017 - Normattiva,” 2017. <https://www.normattiva.it/uri-res/N2Ls?urn:nir:stato:decreto.legislativo:2017-11-15;183> (accessed Nov. 12, 2021).
- [3] J. B. Heywood, *Internal Combustion Engine Fundamentals*. McGraw-Hill Education, 2018.
- [4] C. Caputo, D. Cirillo, M., Costa, G. Di Blasio and D. Piazzullo, “Multi-Level Modeling of Real Syngas Combustion in a Spark Ignition Engine and Experimental Validation,” SAE International, Warrendale, PA, *SAE Technical Paper 2019-24-0012*, Sep. 2019. doi: 10.4271/2019-24-0012.
- [5] M. Costa, G.Di Blasio, M.V.Prati, M.A.Costagliola, D.Cirillo, M.La Villetta, C.Caputo and G.Martoriello, “Multi-objective optimization of a syngas powered

- reciprocating engine equipping a combined heat and power unit,” *Appl. Energy*, vol. 275, p. 115418, Oct. 2020, doi: 10.1016/j.apenergy.2020.115418.
- [6] R. Bates and K. Dölle, “Syngas Use in Internal Combustion Engines - A Review,” *Adv. Res.*, vol. 10, no. 1, pp. 1–8, Jan. 2017, doi: 10.9734/AIR/2017/32896.
- [7] “ETL One | Unitec s.r.l.” <http://www.unitec-srl.com/site/products/etlone/> (accessed Jan. 09, 2022).
- [8] “DECRETO LEGISLATIVO 13 agosto 2010, n. 155 - Normattiva,” 2010. <https://www.normattiva.it/uri-res/N2Ls?urn:nir:stato:decreto.legislativo:2010;155> (accessed Jan. 09, 2022).
- [9] J. B. Guinée and E. Lindeijer, Handbook on life cycle assessment: operational guide to the ISO standards, vol. 7. *Springer Science & Business Media*, 2002.
- [10] G. Guest, R. M. Bright, F. Cherubini, O. Michelsen, and A. H. Strømman, “Life Cycle Assessment of Biomass-based Combined Heat and Power Plants: Centralized Versus Decentralized Deployment Strategies,” *J. Ind. Ecol.*, vol. 15, no. 6, pp. 908–921, 2011.
- [11] Google Earth, “Panoramica,” *Google Earth*. <https://www.google.com/intl/it/earth/> (accessed Jan. 07, 2022).
- [12] C. Caputo, Modelling approach and technical solutions for characterization and performance improvement of real biomass powered m-CHP system, *PhD Thesis. University of Rome “Tor Vergata,”* 2020.
- [13] M. Costa *et al.*, “The ‘INNOVARE’ Project: Innovative Plants for Distributed Poly-Generation by Residual Biomass,” *Energies*, vol. 13, no. 15, p. 4020, 2020.
- [14] “Bosetti & Gatti - D.lgs. n. 285 del 1992 (codice della strada).” https://www.bosettiegatti.eu/info/norme/statali/1992_0285.htm (accessed Jan. 07, 2022).
- [15] EC. Europa, “Life Cycle Assessment - IPP - Environment - European Commission.” <https://ec.europa.eu/environment/ipp/lca.htm> (accessed Jan. 07, 2022).
- [16] GSE, “Rinnovabili elettriche.” <https://www.gse.it/servizi-per-te/fonti-rinnovabili> (accessed Jan. 10, 2022).
- [17] J. Giliberto, “Bollette, la nuova stangata di gennaio supera il 60%,” *Il Sole 24 ORE*, Dec. 19, 2021. <https://www.ilssole24ore.com/art/bollette-nuova-stangata-gennaio-supera-60%-AEFEDT3> (accessed Jan. 11, 2022).
- [18] Facile.it, “Quanto costa un kWh di energia elettrica? | Facile.it.” <https://www.facile.it/energia-luce-gas/tag/costo-kwh.html> (accessed Jan. 11, 2022).
- [19] Facile.it, “Costo metano: quanto costa un metro cubo di gas nel 2021? | Facile.it.” <https://www.facile.it/energia-luce-gas/tag/costo-metro-cubo-gas.html> (accessed Jan. 10, 2022).
- [20] Consulente energia, “Quanto costa un kWh termico: prezzo di un kWh termico con gas metano, costo a kWh con pompa di calore, kWh termici da pellet, quanto vale kWh termico gasolio, kWh termici industriali e domestici”, <http://www.consulente-energia.com/sm-quanto-costa-kwh-termico-prodotto-con-gas-metano-prezzo-kwh-termico-con-gasolio-pellet-pompa-di-calore-kwh-industriali-domestici.html> (accessed Jan. 11, 2022).
- [21] ARERA, “ARERA - Home page.” <https://www.arera.it/it/index.htm> (accessed Jan. 10, 2022).

CHAPTER 5

Biomass-powered micro-cogeneration plants as renewable systems in micro-grids

In recent years, micro-grid, i.e. an independent energy system that serves a specific local area, have become appealing especially if a biomass-to-energy system is involved, as demonstrated by the numerous scientific papers [1]–[3] and worldwide projects [4]–[6] found. In Chapter 4, it was demonstrated that the CMD ECO20x biomass-based micro-cogeneration plant could be a viable alternative to traditional power generation systems. Indeed, biomass energy plants, in contrast to solar and wind energy systems, are dispatchable, meaning they can be easily turned on or off, making bioenergy a feasible and promising solution in smart grids.

Electric reliability has gotten the most attention since 2012 when Superstorm Sandy knocked out power to about eight million people in 15 USA states and the District of Columbia [4]. Moreover, during the Covid-19 pandemic, as explained in Chapter 1, power outages and grid instability have become worldwide issues, making micro-grids more and more advantageous to reduce faults. Compared to the problems identified in the current electrical system, a renewable microgrid allows to achieve the following benefits:

- *Reduction of transmission losses:* the modular structure and no more centralized network allows the generation nodes to be brought closer to the points of consumption, significantly reducing the losses due to the Joule effect [7].
- *Better power management system:* the introduction of an "intelligent" control system able to vary their own absorption according to the contingent needs of the system, allows for a “peak shaving” or “power leveling”, with great advantages in terms of reducing the cost of energy during peak hours, and therefore of energy costs for end-users [8].
- *Sustainable and environmentally friendly solution:* biomass-to-energy system could replace the diesel generator as a dispatchable and modifiable unit, in a CO₂ neutral solution that can be easily implemented.

Aziz et al. [9] carried out a feasibility study of a grid connected and stand-alone micro-grid in Iraq. Island configuration distributed generation system are essential in a country that suffers from daily electricity shortages as PV with battery system can feed the load during electricity absences.

Switching from grid-connected mode to island-mode is a desirable feature for a micro-grid, but it is also a problematic node due to the fact that, when the microgrid is connected to the National grid, or it is in an on-grid mode, the grid itself imposes voltage; on the other hand, when the micro-grid works in island mode, disconnected from the National grid, it is necessary to identify a *master*, an energy system that impose voltage and frequency for any other generation and/or storage system. A control system for a micro-grid is generally made up of a system that develops functions at a centralized level and other distributed systems to which sensors and actuators are associated at the field level, as shown in Figure 5. 1. The displayed control system, called hierarchical, has a tree structure with a general controller (GC), sub-controllers or mains (M) which are responsible for the control of a certain portion of the network or of a specific function, and several sensors and actuators (S) [10].

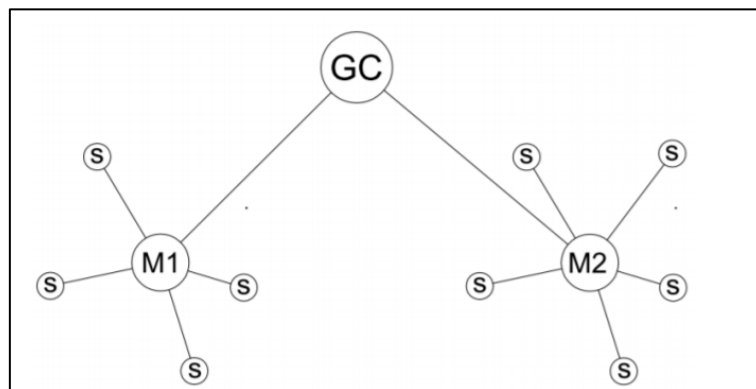


Figure 5. 1: Hierarchical architecture of a micro-grid [10]

A control system of the frequency drop of the micro-grid (frequency drop control) is an indispensable element: the regulation of voltage and frequency must be carried out by adequately controlling the place and the time of each energy generation, in order to allow the tracking of the load and of the production from renewable sources, both elements that present a high degree of uncertainty [11].

A bidirectional inverter that connects the battery to the alternative current (AC) bus is necessary to make it possible to charge and discharge the battery according to the energy

balance between the power generation systems and the connected loads. In off-grid applications, both single-phase and three-phase inverters are normally used [10], [12].

The control system is an essential component for the transition to an off-grid mode. It must necessarily include:

- a telecommunication system to connect all the devices (usually by Wi-Fi or by Virtual Local Area Network);
- a decision support and human interface;
- sensing, measurement and metering of the energy injected or withdrawn from the network by each energy generation and/or storage system.

For the design of a hybrid micro-grid, in which photovoltaic (PV) panels and energy storage system (ESS) will be added to the CMD ECO20x plant, a possible layout has to be defined by identifying all generation and storage systems sizing and all electrical components necessary to make the hybrid system to work both in on-grid and off-grid.

Regarding the ESS, an adequate storage system should store energy during the periods in which the generation exceeds the demand, which can then be used to cover the periods in which the load is greater than the generated power [13]. An ESS for stationary applications in stand-alone micro-grid must satisfy the following requirements:

1. *Reduced cost* during both maintenance and installation operations.
2. *High reliability*. A failure of the EES system can result in total isolation of the micro-grid.
3. *High specific energy*, i.e., electrical energy stored per unit of volume (Wh/l) or per unit of weight (Wh/kg). This requirement involves extending the entire electrical autonomy of the system, while at the same time reducing the number of charge/discharge cycles of the battery pack.
4. *High specific power*, that is the electrical power stored per unit of volume (W/l) or per unit of weight (W/kg). The use of ESS with high specific power allows to reduce the recharge time without loss.
5. *High life cycle*. The life cycle represents the service time which ends when the system performance degrades below acceptable operating limits.

Finally, also the environmental aspects, which are mainly related to the use of toxic materials, must be adequately taken into consideration in the choice of the ESS.

The energy balancing problem, indeed, is one of the main challenges for the effective application of micro-grids of different renewable energy generation systems. A correct energy management is advisable for the minimization of the total operation cost and to ensure a durable energy storage system. The electric system, especially for electrochemical storage, should be sized perfectly to ensure less fluctuations and a stronger ability of peak shaving, along with better economic return [14]. The battery energy storage sizing was analysed by Zhang et al. [15], that carried out a techno-economic analysis under different electricity tariffs of a micro-grid system involving a PV system and a battery connected to the national grid.

The design of a micro-grid involving a biomass powered CHP system was performed by Zheng et al. [16] through a deterministic constrained optimization. A correct modelling of the micro-grid, indeed, was useful to determine major risk factors of different system design.

As shown in Figure 5. 2, the choice of storage systems ranges from capacitors that can store as little as 1Wh of energy for a few seconds to chemical compounds that can be used to store several TWh of energy for years. In the proposed application, two energy storage system were proposed, based on a different time and size scale: the first one is supposed to be a seasonal storage, so a chemical storage system that involves a chemical compound as energy carrier is chosen; the other one, for daily storage, is a common battery or electrochemical storage system.

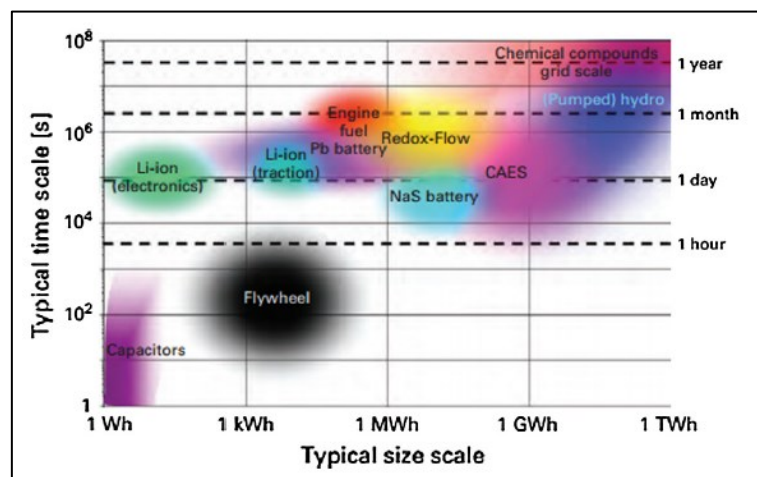


Figure 5. 2 Typical time scale and size of energy storage systems [17].

Among the first category, hydrogen energy storage is one of the most popular [17]. Hydrogen is a storable, transportable, highly versatile, efficient and clean energy carrier

with a high energy density. Off-peak electricity can be used to electrolyze water and produce hydrogen; then, stored hydrogen can be used in fuel cells or burned directly in a gas turbine or in an internal combustion engine to produce electricity during electricity demand peaks.

One of the main disadvantages of using hydrogen for electricity storage is the significant energy losses during a single cycle. For example, electrolysis currently has 60% efficiency, transport and compression can lead to an additional 10% efficiency loss (although this may be less) while electricity reconversion has an efficiency of about 50% for the application of fuel cells (higher efficiency is expected for combustion-based energy generation if cogeneration of heat is integrated). Therefore, the overall efficiency can be around 30%. However, this is compensated by the high storage density.

As regard the second proposed energy storage system, the battery, it is the most widespread technology for the energy storage. In these devices, electrical energy is stored in an electrochemical form by means of reversible conversion reactions. When a battery is discharged, the positive electrode (cathode) is reduced, acquiring electrons and the negative electrode (anode) releases electrons and oxidizes. Inside the electrolyte, positive ions move towards the cathode and negative ions towards the anode by means of a diffusion process. During the charging process, instead, the ions motion reverses and the electrodes gradually recover their initial state. The material used to make the electrodes and the type of electrolyte identify the electrochemical pair with which an accumulator is normally called. There are different types of batteries, identified by several electrochemical pair.

One of the most promising electrochemical storage technologies, which has had a very rapid development in recent years, involves lithium technology. The reasons that have promoted the research and development of these accumulators are largely to be found in the possibility of use for the power supply of electric vehicles and widely used portable devices.

The most widespread and technically mature are lithium-ion batteries with liquid electrolyte (also called “lithium-ion” batteries). Small lithium-ion batteries are commonly available on the market (from fractions of Ah up to ten Ah) which have become the standard for powering small portable appliances (mobile phones, cordless phones,

laptops, etc. ...), while cells of larger sizes are produced on a limited basis and for specific applications [18].

Figure 5. 3 shows the main lithium batteries [19] that could be used as storage systems for micro-grid systems, compared through spider graphs that show: specific energy (or capacity), power, safety, efficiency, useful life and cost. LiCoO₂ batteries have the highest capacity but lower specific power, while the cheapest are lithium-titanium-oxide (LTO) cells, which have the highest efficiency and useful life. Lithium Manganese Cobalt Oxide (NMC) batteries represent the best compromise right now on the market.

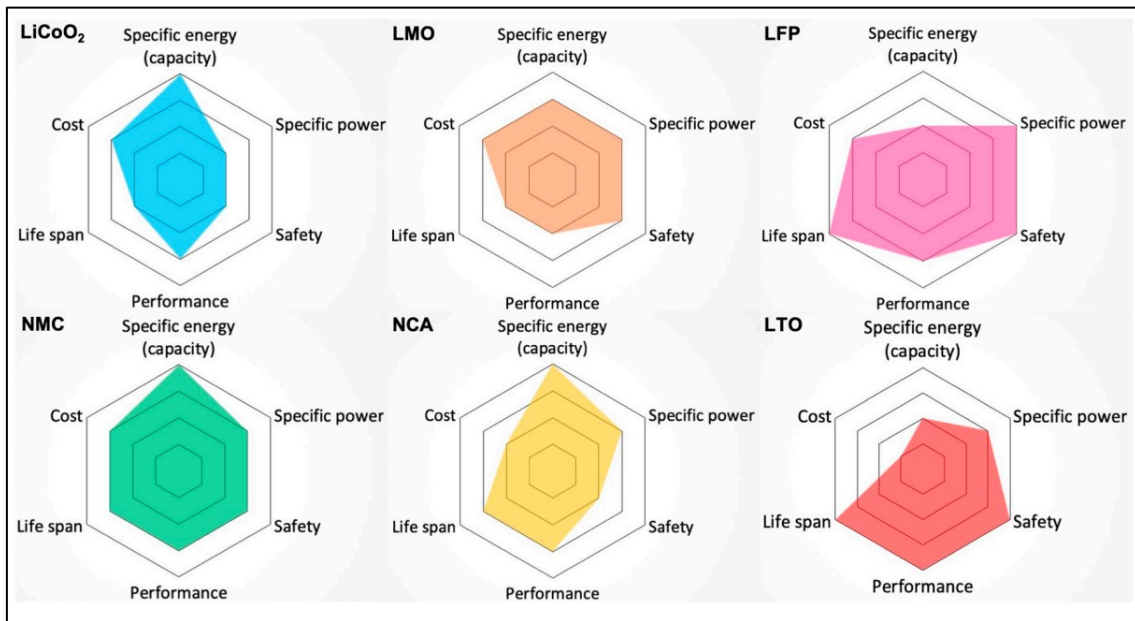


Figure 5. 3: Comparison between different Li-Ion technologies [20].

Next paragraphs describe the work carried out with the Mälardalens University of Sweden, in which a numerical model of a renewable micro-grid was developed, and a simulation was performed to achieve the micro-grid correct sizing as it serves a charging station for electric vehicles. Two cases are considered: the micro-grid is supposed to be located either in Cilento, in the South of Italy or in Västerås, Sweden. The aforementioned locations are proposed as biomass availability is high, due to the fact that both places are close to National Parks but are obviously characterized by different climate data. Västerås, even though milder than the rest of Sweden, presents a rigid winter, with low solar production. On the other hand, Cilento is located in a sunny position, characterized by a mild climate.

Three scenarios were considered:

1. PV + micro-CHP+ Li-Ion battery;

2. PV + Li-Ion battery + hydrogen storage;
3. PV + micro-CHP+ Li-Ion battery + hydrogen storage.

Two different energy dispatch strategies were explored, based on ref [21]:

- a) Cycle-charging strategy (CCOS): CMD ECO20x always runs at full-load.
- b) Load-following (LFOS): CMD ECO20x produces just enough power to meet the electrical load requirement.

Each component sizing is found through an optimization based on a genetic algorithm (GA) to meet the highest number of operative hours and the lowest total life cycle cost.

5.1 Micro-grid model development

The model is an open-source code [22] for simulation, optimization, and design of hybrid power systems for off-grid and, if desired, on-grid applications, written in Matlab® language, and uses GA to find the best power sources and storage system to minimize life cycle cost (LCC) and maximize renewable power system reliability. Indeed, the in-house modelling method allows better flexibility when dealing with gasification process, in contrast with other commercial software, such as HOMER [23], [24] or Trnsys [25]. The proposed micro-grid is shown in Figure 5. 4. Next paragraphs show in detail each component model.

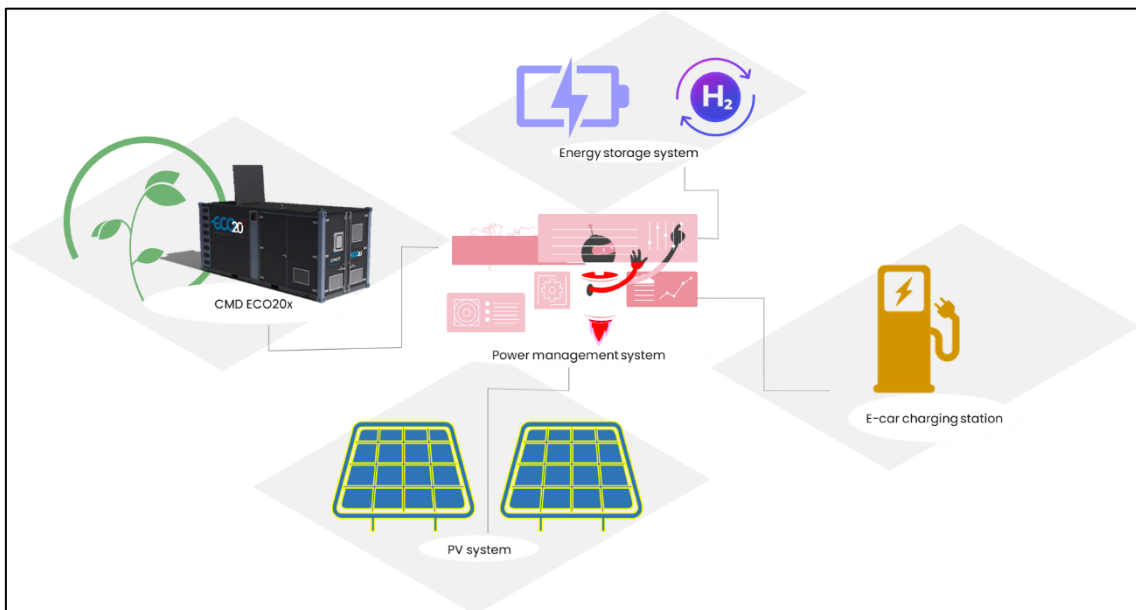


Figure 5. 4: Schematic diagram of the proposed microgrid

5.1.1 PV system model

Both Italian and Sweden climates are favourable in the employment of PV systems, as summers in both countries are characterized by lots of hours of sunshine and daylight.

The hourly simulation of the photovoltaic system is carried out following the Duffie and Beckman [26] equation (5.1):

$$P_{PV} = \eta_{PV,STC} \left[\begin{array}{c} 1 + \frac{\mu}{\eta_{PV,STC}} (T_a - T_{STC}) + \dots \\ \dots + \frac{\mu}{\eta_{PV,STC}} \frac{9.5}{5.7 + 3.8v} \frac{NOCT - 20}{800} (1 - \eta_{PV,STC}) G_{g,t} \end{array} \right] A_{PV} G_{g,t} \quad (5.1)$$

Where:

- P_{PV} is the hourly power output from the PV system (W);
- $\eta_{PV,STC}$ is the efficiency of the PV module at standard test conditions (STC) (%);
- μ is the temperature coefficient of the output power (%/°C);
- T_a is the ambient temperature (°C);
- T_{STC} is the standard test conditions temperature (25°C);
- v is the wind speed (m/s);
- $NOCT$ is the nominal operating cell temperature (°C);
- A_{PV} is the PV array area (m²) related to the array power peak;
- $G_{g,t}$ is the global solar radiation on the tilted surface (W/m²).

The total solar radiation $G_{g,t}$ (W/m²) depends on the horizontal radiation, surface orientation and it is given by three different contributions: beam radiation $G_{b,t}$ (W/m²), diffuse radiation $G_{d,t}$ (W/m²) and reflected radiation $G_{r,t}$ (W/m²), whose are related to the angle of incidence, function of the tilt and azimuth angles and the latitude of the installation site.

5.1.2 CMD ECO20x model

The results deriving from the simulation of the engine model, explained in Chapter 3, were used to develop a map-based engine (MBE) to simplify the process of simulation and allow the employment in the Matlab® environment. The MBE handles maps and characteristics to be interpolated in order to capture the physical behaviour of the ICE.

The MBE performance is here parametrized by introducing the fuel consumption map (Figure 5. 5), a 2-D characteristic map in which the mass flow fuel consumption rate is related to the correspondent engine speed and torque [27]. The supposed syngas composition is derived from the gasification of Biomass A1+, whose analysis was reported in Chapter 2 and whose lower heating value is of nearly 18 MJ/kg.

The micro-cogeneration system considers the user's data of biomass availability along the simulation time.

If biomass is available, the model calculates how many hours the micro-CHP can operate with such quantity, based on a mean biomass hourly consumption of the system that is 24 kg/hr. Then, it calculated, for each operative hour, the relative micro-CHP power.

In the CC strategy, the $P_{mchp,MBE}$ is the power at maximum load and 1500 rpm, which is equivalent to 20 kW. In the LF strategy, the load is calculated to meet the required load from the e-car charging station that is not covered by solar PV.

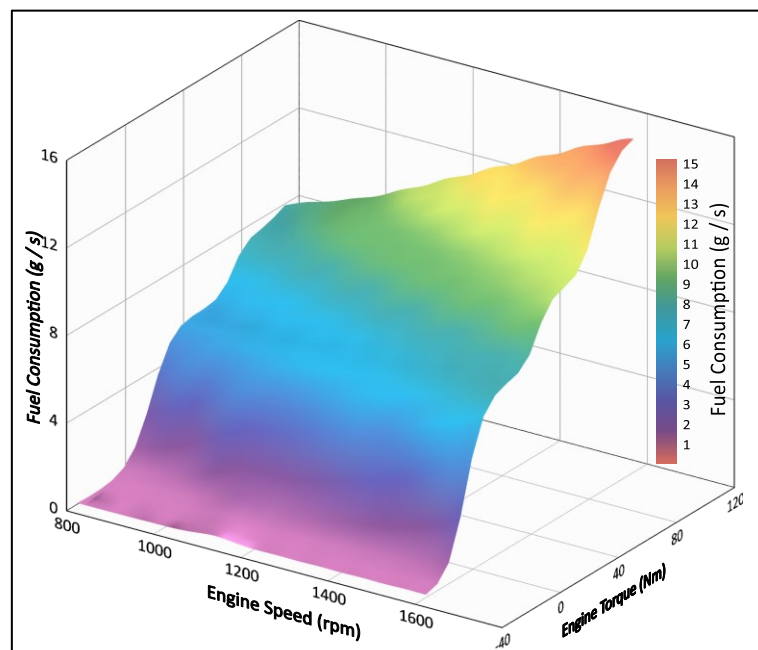


Figure 5. 5: Fuel consumption map (g/s) vs speed (rpm) and torque (Nm) [27].

The model power calculation could be resumed by the following condition (5.2):

$$P_{mchp} = \begin{cases} P_{mchp,MBE} = \frac{Nm_{max} * load * 2\pi * rpm}{60} & A_{biom} > 0 \\ 0 & A_{biom} = 0 \end{cases} \quad (5.2)$$

Where: Nm_{max} is the engine torque at full load, rpm is the engine speed, LHV_{ref} is the reference lower heating value, LHV_{biom} is the lower heating value of the proposed biomass, A_{biom} is the biomass availability. The approximation of the lower heating value is to take into consideration the system de-powering when treating with a more humid biomass or a different kind that is characterized by a lower calorific value. However, this approximation in a short-scale time, will be considered to be an error, as it does not take into account the syngas composition variability that can affect drastically the micro-CHP system performance. However, in a long-scale time, this approximation could well reflect the real-operation of the micro-CHP, since an average syngas composition can be considered.

5.1.3 Battery system model

The battery model reads the battery and inverted efficiency, the defined minimum state of charge (SOC), usually 0.2, and the hourly self-discharge rate and calculates the state of charge following the two equations (5.3) and (5.4) for charging and discharging, respectively:

$$SOC_{batt}(t) = SOC_{batt}(t-1)(1 - \sigma_{sd}(t)) + \left[P_{Ren} - \frac{P_{load}}{\eta_{inv}} \right] \eta(charging) \quad (5.3)$$

$$SOC_{batt}(t) = SOC_{batt}(t-1)(1 - \sigma_{sd}(t)) + \left[\frac{P_{load}}{\eta_{inv}} - P_{Ren} \right] \eta(discharging) \quad (5.4)$$

where, t indicates the time step at which the parameter is calculated (hours), σ_{sd} is the hourly self-discharge rate, P_{ren} is the power produced by PV and micro-CHP systems, P_{load} is the power consumption (W), η_{inv} is the inverter efficiency (%), and η is the battery bank efficiency (%).

5.1.4 H2 system model

If battery state of charge is maximum, and there is still some excess power that will go to dissipation, another chemical storage system can be considered. An electrolyser (EL) is used to store hydrogen into tank, modelled by following the datasheet efficiency and

power consumption based on its operative load. The load is calculated by dividing the excess power by the electrolyser maximum power consumption, correspondent at 100% load, and based on the real operative load, efficiency of the electrolyser is calculated by interpolation. More accurate is the characterization of the EL, more precise will be the definition of the efficiency.

Vice versa, if the battery state of charge is minimum and the requested power from the load is more than 0, hydrogen can be used in a fuel cell (FC). FC efficiency, contrary to EL, is not much influenced by the operative load; so, an interpolation such as the one made for the electrolyser is not required.

The production rate of the EL is chosen from the data sheets available online [28], while and the FC is supposed to be the 25% of the EL.

The hydrogen quantity at time t is calculated by following the equation (5.5) for charging and discharging, respectively:

$$\begin{aligned} H_2(t) &= H_2(t - 1) + (H_{2_{production\ rate,EL}} * load * \eta_{EL,load}); \\ H_2(t) &= H_2(t - 1) - (H_{2_{consumption\ rate,FC}} * load * \eta_{FC}); \end{aligned} \tag{5.5}$$

where, t indicates the time step at which the parameter is calculated (hours), load is the requested power divided by the electrolyser or fuel cell power consumption at 100% load (-), $\eta_{EL, load}$ is the interpolated electrolyser efficiency, η_{FC} is the FC efficiency.

5.1.5 Operational strategy and optimization module

As aforementioned, two operation strategies are here implemented for the proposed scenarios: cycle-charging (CC) operational strategy and load-following (LF) operational strategy. For both dispatch strategies, as shown in Figure 5. 6, at time t, the renewable power production from the PV panels and the micro-CHP system is compared with the load. If there is excess of electricity production, the battery is charged. If there is still some excess of electricity, it is stored into hydrogen production through an electrolyser. If the renewable electricity production is lower than the load, the battery is discharged and, if the load is not met yet, the stored hydrogen is used in a fuel cell.

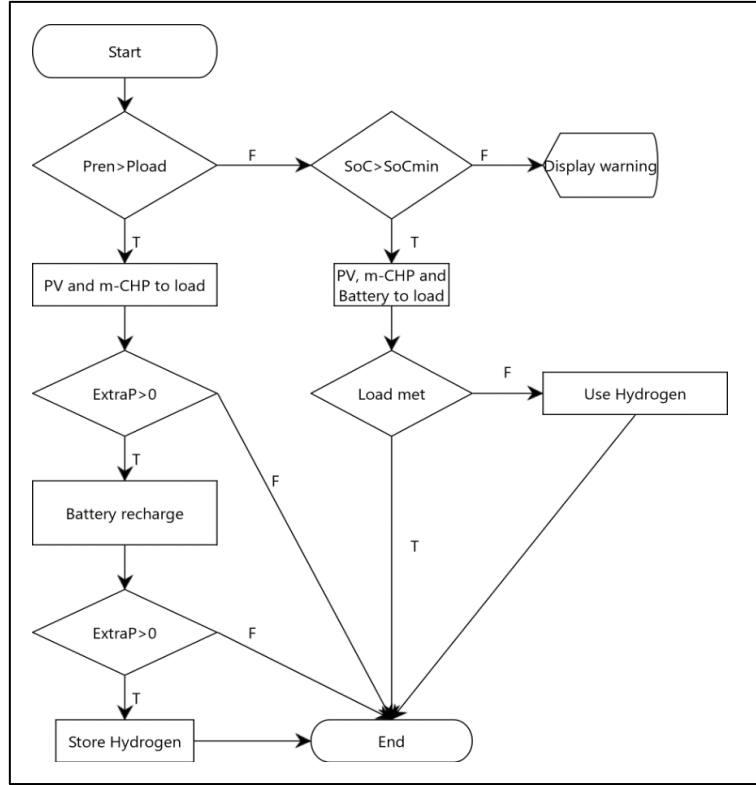


Figure 5. 6: Operational strategy flowchart for the micro-grid.

However, when the dispatch is in the LF mode, the micro-CHP system produces just enough power to meet the instantaneous load per time step, unless it reaches a minimum defined power, usually referred to an 0.2 operative load where it shuts down. In CC, on the other hand, the micro-CHP plant runs at full rated capacity and will continue to operate to charge the storage system.

For the proposed optimization problem, a GA algorithm was implemented in Matlab® environment to find the trade-off solution set. The first objective in the optimization process is to minimize the life cycle cost (LCC), calculated through equation (5.6).

$$LCC = C_0 - \sum_{t=1}^T \frac{OC_t}{(1+i)^t} + \sum_{t=1}^T \frac{MC_t}{(1+i)^t} + \sum_{t=1}^T \frac{RC_t}{(1+i)^t} - \sum_{t=1}^T \frac{SV_t}{(1+i)^t} \quad (5.6)$$

where C_0 is the initial investment cost at time 0 (therefore not requiring discounting), OC is the operating cost for each period t , MC is the maintenance cost, RC is the replacement cost, and SV is the salvage value.

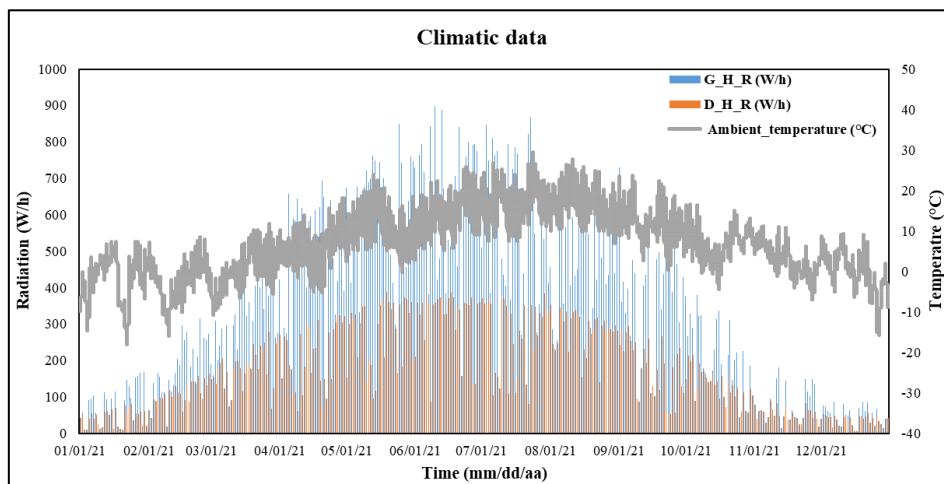
The period of the analysis is denoted by T and the rate used to discount future values is i . The depreciation is assumed as a straight-line and salvage value equal to 10% of the ICC.

The second objective is the reliability that is the total hours in which the load is met by renewable energy sources.

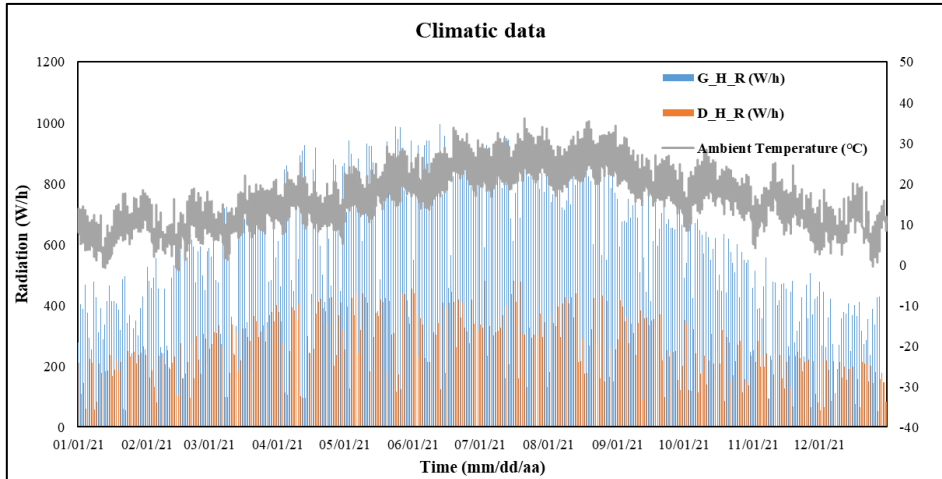
5.1.6 Initialization for both scenarios

For the considered case study, the simulations of one year in Västerås, Sweden and in Cilento, Italy are performed. The start of the analysed period coincided with the 00:00 hour of the 1st of January 2021 and ended on the 31st of December 2021 at 23:59.

Figure 4 reports the main climatic data of interest, global horizontal radiation (G_H_R) (W/m^2), the diffuse horizontal radiation, D_H_R (W/m^2) and ambient temperature ($^{\circ}\text{C}$). Västerås is situated in the southern region of Sweden and compared to the severe and rigid climate of the arctic region, in southern Sweden, winters are short and quite cold, while summer temperatures are similar to those in southern England with a lot more hours of sunshine and daylight. Västerås is characterized by a high radiation in summer, where the global horizontal radiation reaches values of 900 W/m^2 , while in winter the maximum daily solar radiation can reach 200 W/m^2 . External temperature ranges between -10°C and 10°C . Cilento has a mild climate, with similar radiation in summer and winter radiation that reaches values close to 500 W/m^2 . External temperature ranges between 5° in winter to 35°C in summer.



a)



b)

Figure 5. 7: Climatic data of Västerås, Sweden (a) and Cilento (b)

The biomass availability is defined as 220 tons distributed through the year so that 100 tons are delivered the first of January and March as micro-CHP should cover the low solar production; 10 tons are assumed as delivered the 15th of July and 15th of October, as some pruning could be collected to reduce the risk of fire settings or for city green maintenance.

Tilt angle	5	Degree
Azimuth angle	0	Degree
Power rated PV	20000	W
Battery capacity	100000	Wh
Power rated micro-CHP	20000	W
EL H₂ production rate (pr)	30	Nm ³ /h
FC H₂ consumption rate (cr)	8	Nm ³ /h

Table 5. 1: Main parameters of the micro-grid (pre-optimization).

Table 5. 1 reports the main supposed parameters of the proposed micro-grid for the simulation of the whole year. Battery capacity size was considered to be at least 2.5 times the sum of the rated power of PV and micro-CHP systems, whose both rated power are considered 20 kW [27]. The production rate of the electrolyzer (EL) is chosen from the data sheets available online[29], while and the fuel cell (FC)is supposed to be the 25% of

the EL. For the simulation in Cilento the conversion tax is supposed to be equal to 1 SEK = 0,096 euro. If the load is not met, energy is supposed to be provided by a diesel generator. Biomass is supposed to be freely available in the installation site.

Specific cost PV	27	SEK/W
Specific cost battery	3.78	SEK/Wh
Specific cost inverter	2.2	SEK/W
Specific cost diesel generator	11	SEK/W
Specific cost diesel	13.74	SEK/l
Specific cost micro-CHP	55	SEK/W
Specific cost biomass	2.46	SEK/kg
Specific cost H2*	8.41	SEK/W
Project lifetime	25	year
PV system lifetime	25	year
Battery lifetime	15	year
Inverter lifetime	15	year
Diesel generator lifetime	8	year
micro-CHP lifetime	20	year
H2 lifetime	15	year
Tax rate	0.07	
Interest rate	0.03	
Maintenance rate photovoltaic	0.06	
Maintenance rate battery	0.08	
Maintenance rate diesel	0.08	
Maintenance rate micro-CHP	0.08	
Maintenance rate H2	0.05	

*both for the electrolyzed and fuel cell

Table 5. 2: Main supposed economic data [29]

The assumed load profile, reported in Figure 5. 8, is the result of an experimental yearly demand of an electric car recharge station situated in the city of Västerås with an average of 5780 Wh and a high standard deviation of 26850. Indeed, as the emissions of greenhouse gases of passenger cars should be reduced by 80% in the period 2005-2050 [30], an increase of e-car circulation has been seen in recent year. Despite the extensive

study for the characterization of e-car, their charging infrastructure design are still limited and under development [31] and usually entail electricity taken from national grid, which is not entirely produced by RES, or in remote areas, from diesel generator. For these reasons, the e-car charging station is an extremely interesting case study for the simulation of a renewable micro-grid.

Battery is supposed to be fully charged at the start of the simulation. The proposed e-car recharge station is characterized by a quasi-zero demand during night-time and maximum demand is usually situated at 8:00 am and pm, when people start and end their worktime.

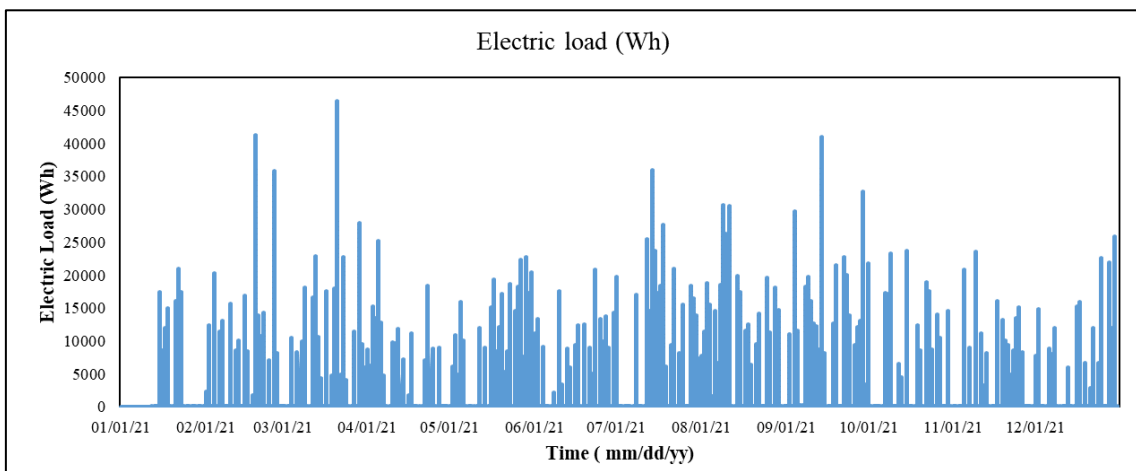


Figure 5. 8: Proposed electric load (1 electric car recharge station).

Before starting the simulation, some boundaries regarding the EES should be made. Indeed, as the proposed micro-grid is not connected to the National grid, the battery capacity should always be able to switch on the CMD ECO20x.

To define this lower limit, a parametric analysis was made by varying the number of strings of a Li-ion battery, that can guarantee a nominal voltage of 48V, as each single cell has a nominal voltage of 3.8 V [27] and a variable number of strings in parallel, where the capacity of a single string is assumed to be 5 Ah (typical value) [27]. To model the power demand required by the CMD ECO20x system to switch on, the absorbed power of the valve motors, of the thermal resistance that keeps the cooling water of the engine at temperature, and of the auxiliaries active during a typical loading has been calculated.

In particular, the following rated required powers were considered, summarized in Table 5. 3.

Component	M1	M2+M5	M3	M6	M8	Pre-heating	Other (PLC,etc)
Max required power (kW)	0.5	0.5	0.75	1.1	1.2	1	1

Table 5. 3: Max required power from each component of CMD ECO20x to switch on

The required power has peaks of 4.5 kW and a minimum power of 1 kW for a total duration of 60 min, the standard time for the system to be switched on. Figure 5. 9 shows the required power over time.

Figure 5. 10 shows the state of charge as time varies for all the simulations under consideration. The minimum battery capacity is 30Ah, which corresponds to 6 parallels of 5Ah, since the 25Ah battery SoC drops below 20%, which if repeated many times drastically reduces the useful life of the battery.

This capacity should be increased by a safety factor of 2, thus reaching a minimum required capacity of 3.12 kWh (i.e., 65 Ah minimum).

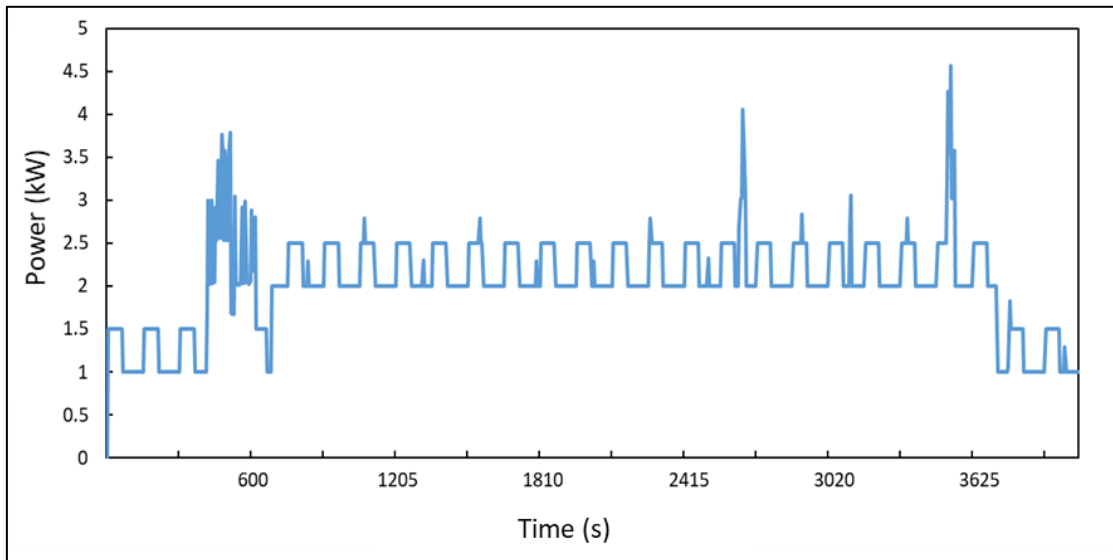


Figure 5. 9: Required power to switch on CMD ECO20x

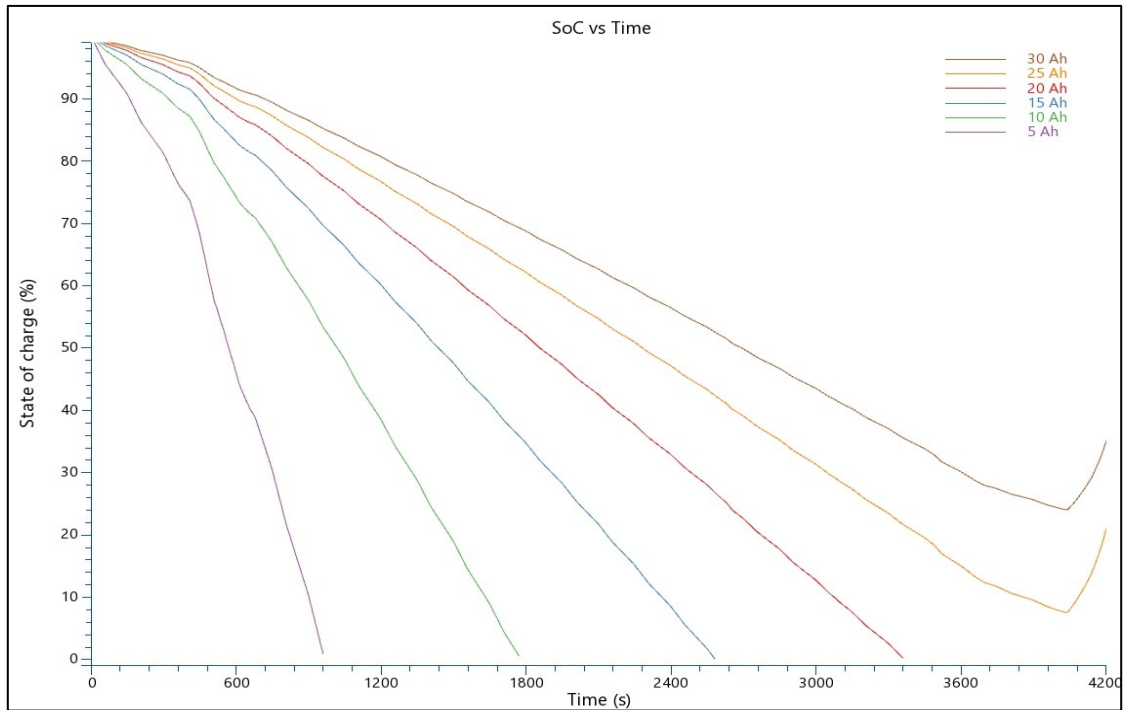


Figure 5. 10: Parametric analysis by varying the number of strings in a Li-Ion battery

Table 5. 4 reports the proposed ranges of D.O.E for the analysed cases and a summary of the proposed optimization.

Input		
Tilt angle	0-90	Degree
Azimuth angle	0-90	Degree
Power rated PV	0-100000	W
Battery capacity	312-100000	Wh
Power rated micro-CHP	0-100000	W
EL H₂ production rate (pr)	0-90	Nm ³ /h
FC H₂ consumption rate (cr)	0-90	Nm ³ /h
Output		
LCC		Minimize
Reliability		Maximize

Table 5. 4: Range of variation for the proposed simulation and summary optimization of the micro-grid.

5.2 Västerås case study

Figure 5. 11 depicts the load meeting of renewable source for the CC operational strategy (CCOS) in two selected months: January and July in which, respectively, the mean base load is minimum and maximum for the three assumed cases and for both dispatch strategies.

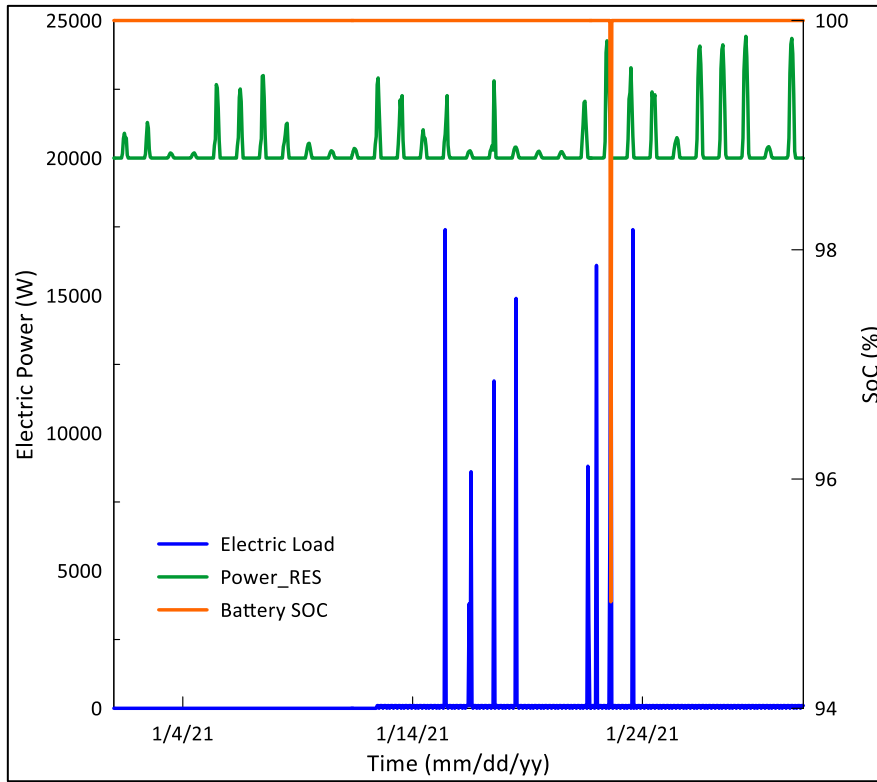
Hydrogen power is assumed positive if energy is stored in the electrolyser; on the contrary, it is negative if energy is used in the fuel cell.

As it can be seen, the load is met in January and July if biomass micro-CHP system is involved, and so case a) and case c); for case b), which is PV+Hydrogen micro-grid, the load is not met in January as PV power is low. This results in a total reliability lower than 8760, which means that for 481 hours the recharge car station load is met by diesel generator or, if connected, by Sweden national grid.

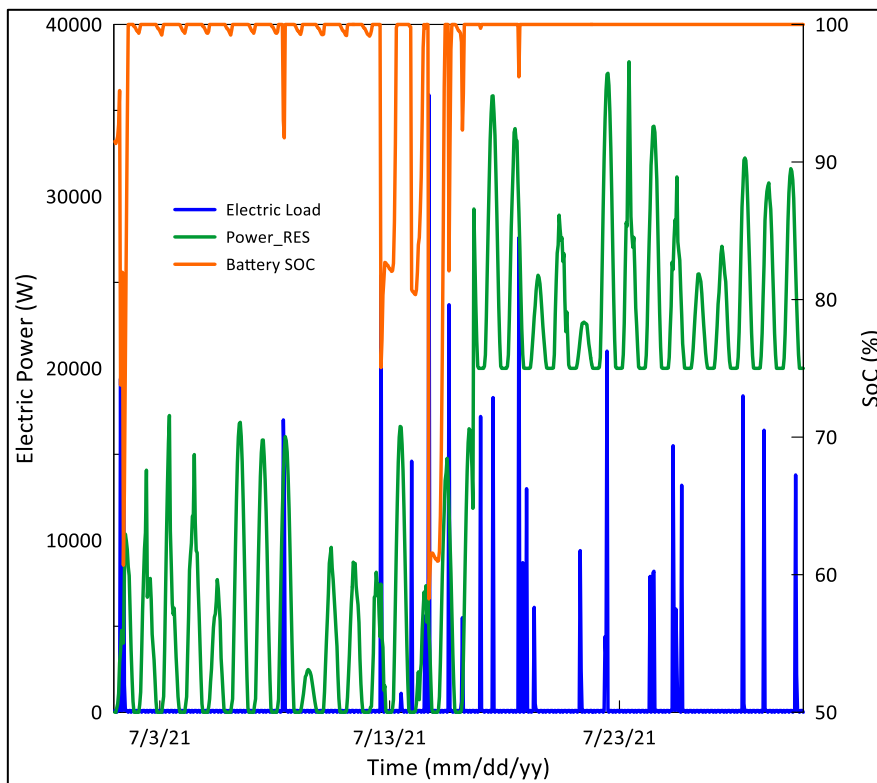
In July, micro-CHP unit power is not thoroughly the month as biomass availability was only 10 tons, so it covers 400 hours, while in January the micro-CHP system functions no-stop, due to high availability of biomass and low solar energy source due to the Swedish rigid climate.

Figure 5. 12 shows the results of the simulation with LF operational strategy (LFOS) for case a), b) and c) in January and July.

In LF, battery is more stressed than CC, in which battery SoC standard deviation is very low. Case b) is shown to stress battery the most, with a high standard deviation of battery SoC that could highly impact the battery life. LF shows how the micro-CHP system is almost redundant in July, as the produced energy power is mainly from solar PV, while in January micro-CHP is necessary to produce electricity during peaks. Table 5. 5 reports the total LCC and reliability for each proposed case. There is no difference between case b) with CCOS and LFOS, as there is no dispatchable unit that can meet the load. The solution of micro-CHP and solar PV with a LFOS happens to be the cheapest and with the maximum RES penetration, while case c) is the most expensive one. The transition from CC to LF strategy allows for both cases a) and c) a reduction of overall LCC of more than 50%.

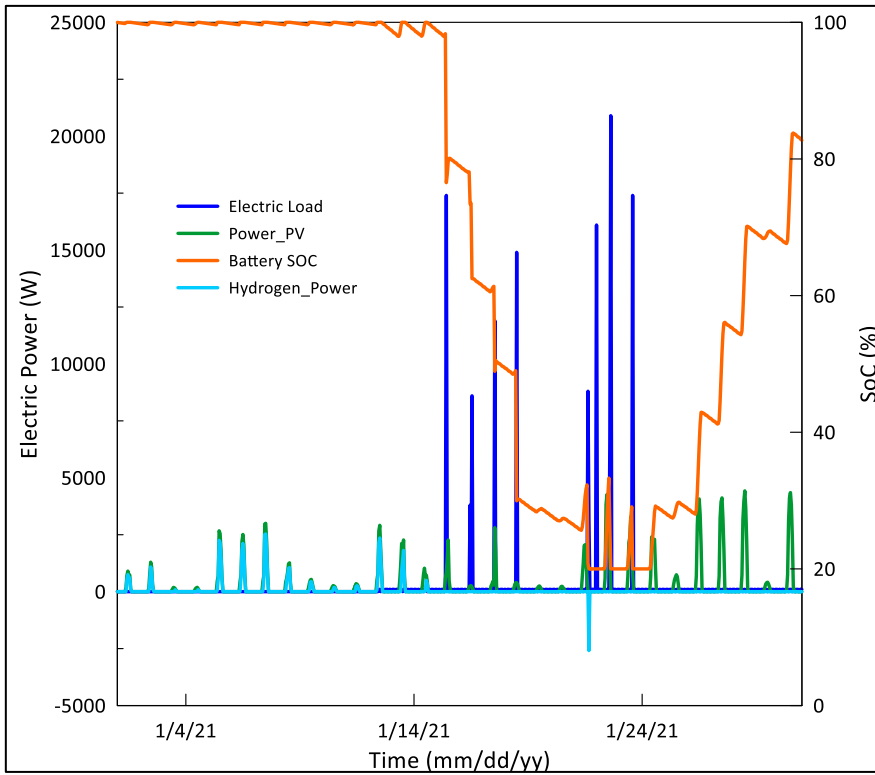


January

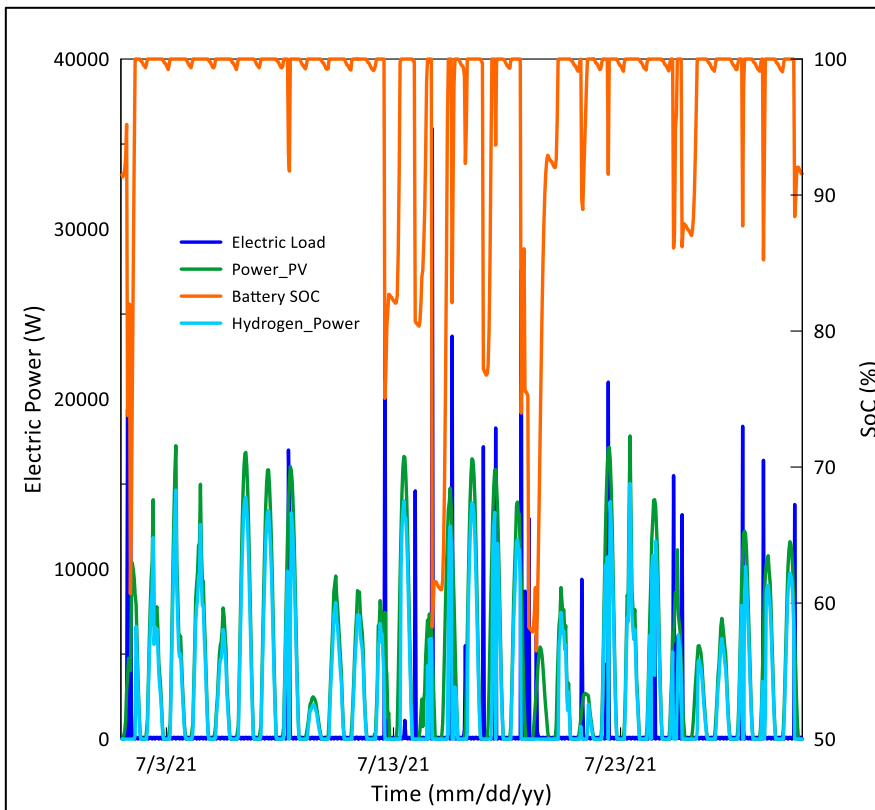


July

a)

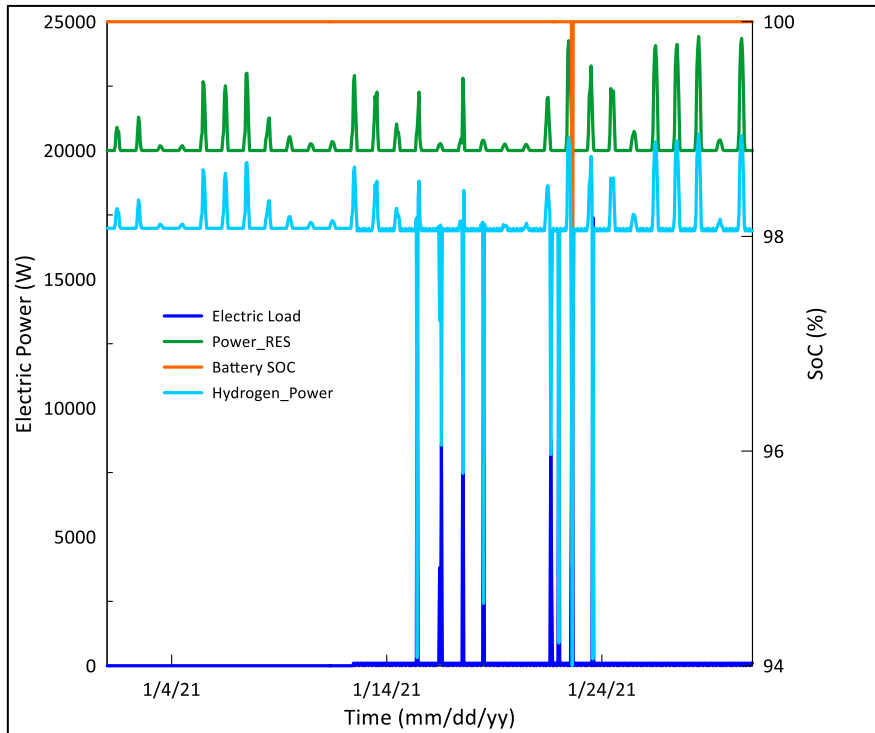


January

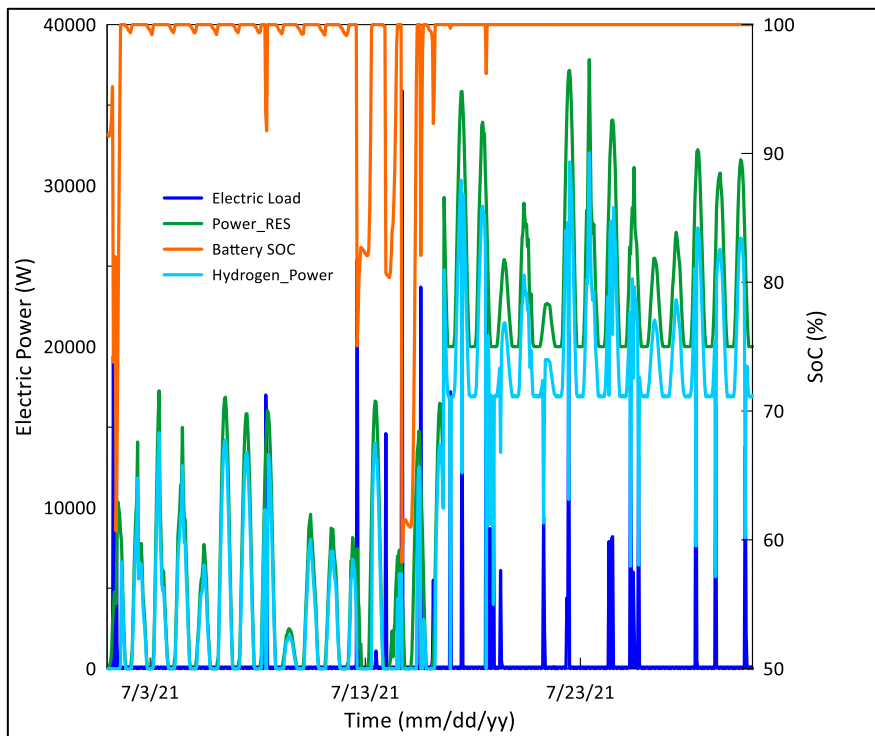


July

b)



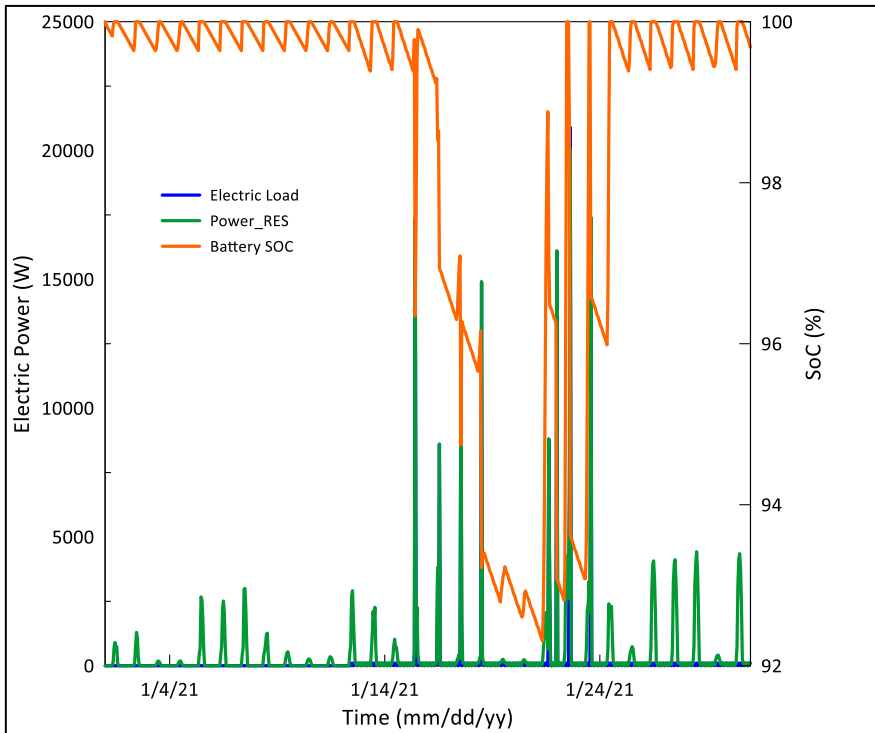
January



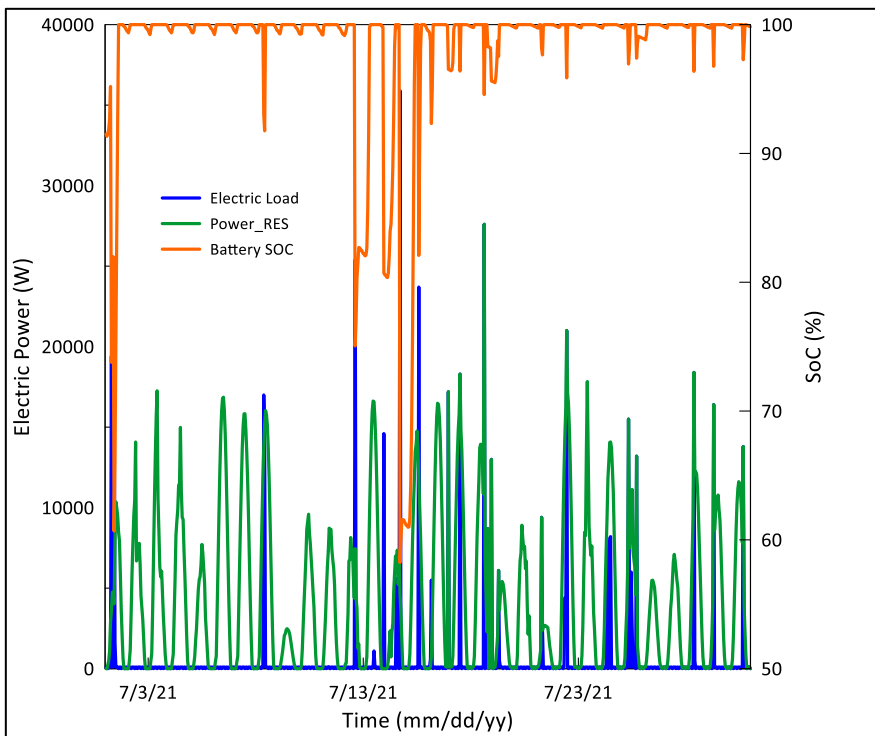
July

c)

Figure 5. 11: Simulation results for 2 selected months: January (up) and July (down) for the case a), b) and c) with CC operational strategy (Västerås case study).

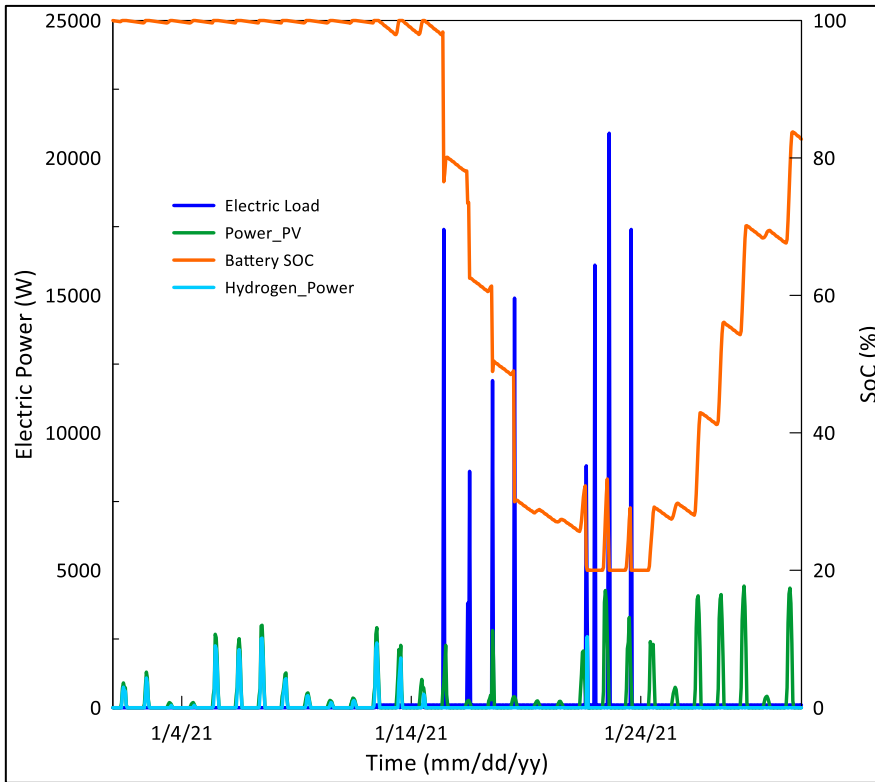


January

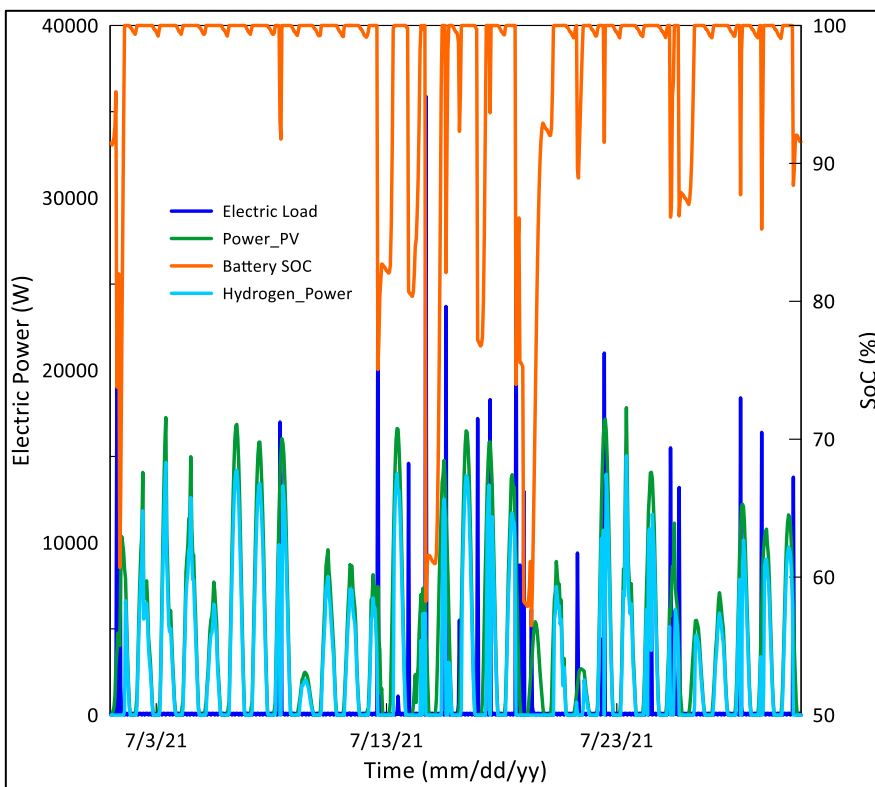


July

a)

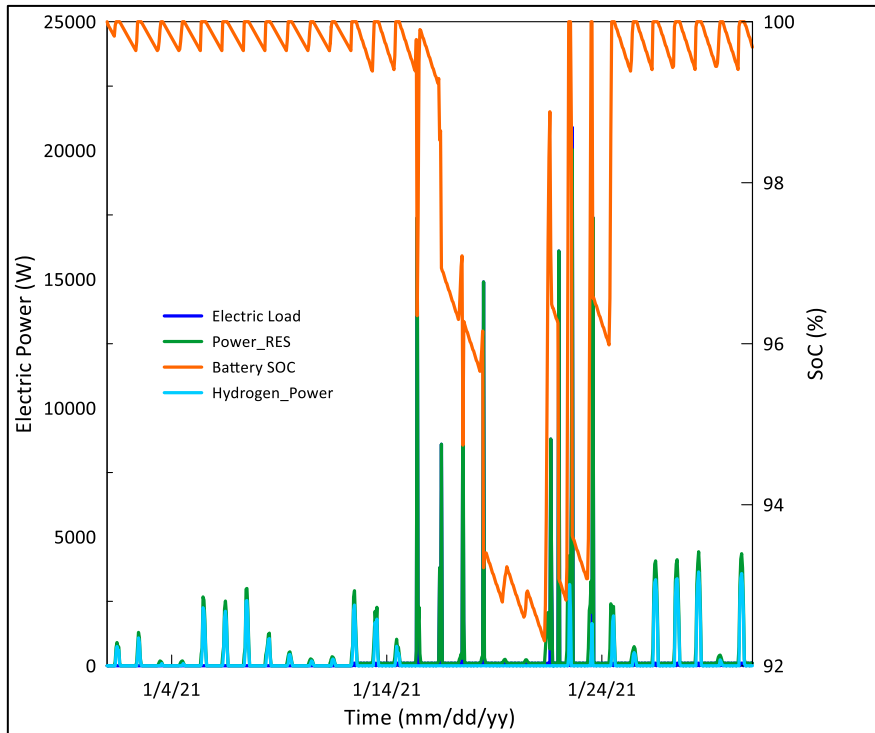


January

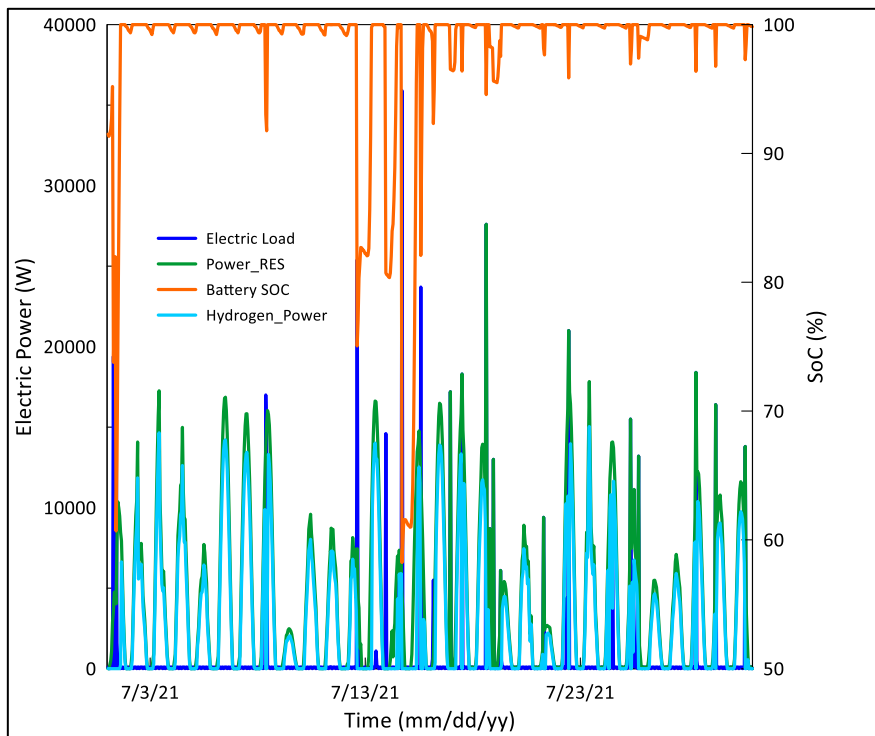


July

b)



January



July

c)

Figure 5. 12: Simulation results for 2 selected months: January (up) and July (down) for the case a), b) and c) of LF operational strategy (Västerås case study).

Reliability for each cases shows that an almost 100% renewable energy conversion mix is possible for renewable e-car charging station and could replace any existing technology.

	Case a)		Case b)		Case c)	
	CC	LF	CC	LF	CC	LF
Reliability (hours)	8760	8760	8279	8279	8760	8760
LCC (SEK)	1.85E+07	8.35E+06	1.29E+07	1.29E+07	2.79E+08	1.83E+07
Δ LCC		-54.8		0		-93.4

Table 5. 5: Total LCC and reliability for each proposed case for Västerås case study

The LF is the most appropriate operational strategy for the proposed application for the three possible microgrid configuration. In case a) and c) with LFOS, diesel generator does not run at all, without penalizing the overall cost, with a positive impact of the environment.

Figure 5. 13 shows the hydrogen quantity stored in case b) and case c) for both strategies along the simulated year. During winter, as solar PV produces very low electrical energy, there is very low hydrogen stocking (case b)), while during summer the abundance of solar energy allows a relatively high hydrogen storage (up to 120 Nm³). For case b), the hydrogen is fully consumed by the end of November, resulting in a lower total reliability (8279 h in a year), while for case c) hydrogen never gets used in both operational strategies. Case b) should probably require a higher H₂ production rate.

In case c) with CCOS, hydrogen quantity rose to over 4000 Nm³, a significant quantity that is, however, unhelpful for the proposed study if not used by the micro-grid; however, also for case c) LFOS the hydrogen is almost never used so the stored quantity (160 Nm³) is useless for the study.

The micro grid is, however, shown to be oversized for case a) and c) and the energy balancing problem is not resolved for case b). An optimization is required to avoid any redundancies between technologies and the hydrogen over-stocking.

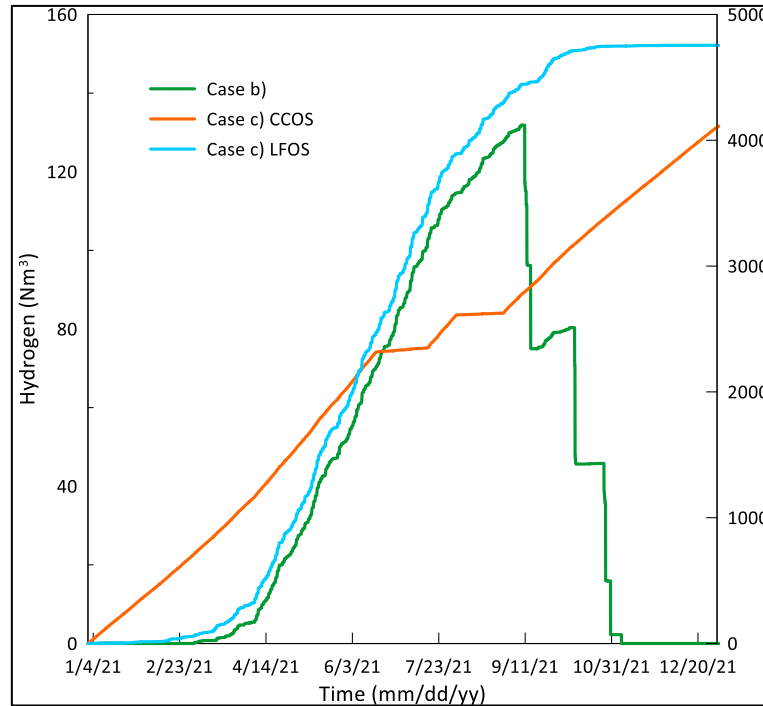


Figure 5. 13: Hydrogen quantity over time for case b) and case c) for Västerås case study.

5.2.1 Genetic algorithm optimization for Västerås case study

A GA optimization is performed for each proposed case, jumping to convergence after 30 minutes, almost 5 minutes per case. Matlab® workflow only saves last generation of scores, whom is the Pareto front, and population, i.e., the optimal setting parameters. The Matlab® workflow saves in an Excel worksheet 100 solution.

As a result of the overall analysis, Figure 5. 14 shows the Pareto fronts of the proposed simulation for each case and operational strategy. CC strategy presents solutions with high LCC. LFOS case 1 and case 3 overlap one to each other and present solution with high reliability and average LCC. Case 2 presents the cheapest solutions but low reliability. Table 5. 6 reports some optimized point of LFOS Case 3. The Pareto front points highlight the need of reducing the rated power of renewable systems and electrical storage to achieve a lower LCC while maintaining high reliability.

A lower tilt angle and high azimuth angle are also required to increase the solar maximum productivity. An azimuth angle close to 0° is in agreement with ref. [32]. The optimum value of tilt angle for annual maximized production is close to 40°, according to refs. [33],

[34]. Considering the interaction between seven different input variables, this value of tilt angle can be considered acceptable. Each energy conversion system rated power is supposed to be approximated to the nearest integer.

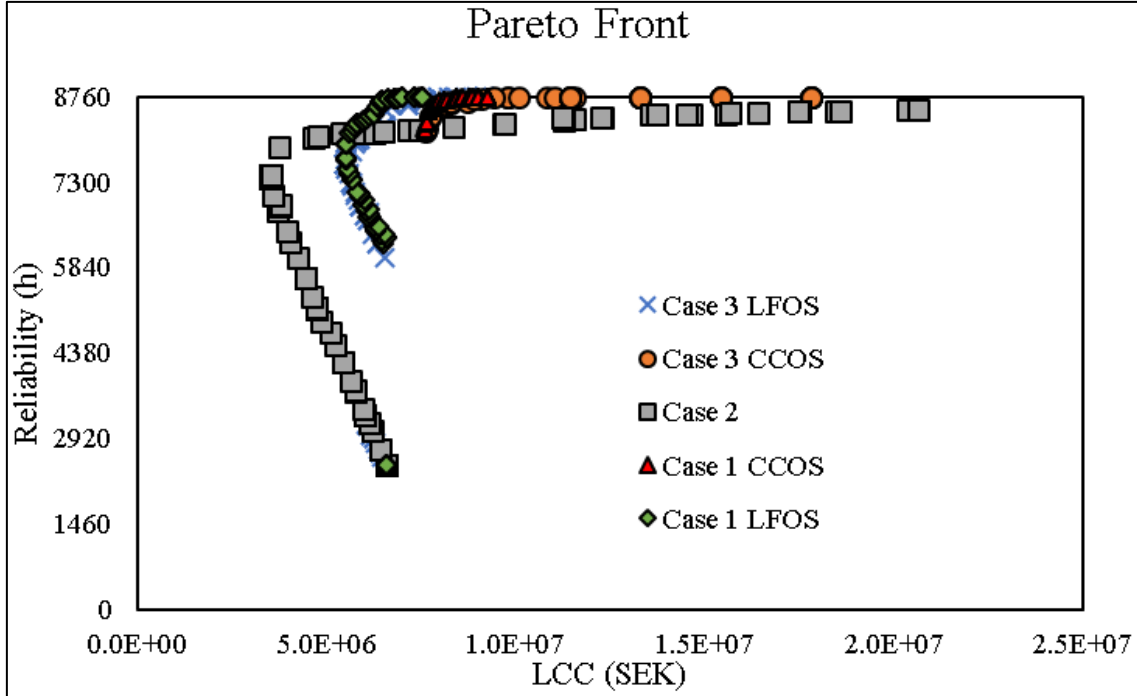


Figure 5. 14: Pareto front of the micro-grid located in Västerås

The proposed optimal microgrid size is chosen to achieve the 100% RES. The optimized micro-grid presents 15 kW PV panels (-25%), a 18.5 kW (-7.5%) microCHP, a 70kWh (-30%) Li-Ion Battery, a 90 Nm³/h (+50%) electrolyser hydrogen production rate and 8 Nm³/h (+11.1%) fuel cell hydrogen consumption rate with an operational strategy of load following type – in which biomass micro-CHP follows the proposed load if load is not met by renewables plus storage system. This optimized system allows maximum reliability (8760 h) and a 30% reduction of the total LCC as compared with the initially proposed hybrid system.

Tilt (°deg)	Azimuth (°deg)	Power _{PV} (W)	Power _{ECO20x} (W)	Capacity _B (Wh)	EL _{pr} (Nm ³ /h)	FC _{cr} (Nm ³ /h)	LCC (SEK)	Reliability (hours)
2	1	1	0	1	2	1	6.57E+06	2469
2	3	2	0	1	2	2	6.46E+06	2612

Tilt (°deg)	Azimuth (°deg)	Power_{PV} (W)	Power_{ECO20x} (W)	Capacity_B (Wh)	EL_{pr} (Nm³/h)	FC_{cr} (Nm³/h)	LCC (SEK)	Reliability (hours)
2	2	2	0	1	3	1	6.37E+06	2734
2	2	2	0	1	3	2	6.29E+06	2841
2	2	2	0	0	3	2	6.23E+06	2917
2	1	2	0	0	4	2	6.18E+06	2987
3	3	2	0	0	3	1	6.08E+06	3128
3	3	3	0	0	3	1	6.06E+06	3153
6	2	4073	328	108	21	12	6.52E+06	6001
6	3	4888	393	129	24	15	6.35E+06	6260
8	4	4315	13	978	33	12	6.23E+06	6407
6	2	3967	274	219	22	12	6.07E+06	6637
9	4	5350	15	1213	41	15	6.00E+06	6732
4	3	1920	142	4188	19	4	6.14E+06	6789
8	2	4760	329	263	25	12	5.90E+06	6898
7	2	5100	353	282	27	13	5.83E+06	6997
9	2	5461	378	302	29	14	5.77E+06	7082
9	2	5712	396	315	30	14	5.75E+06	7115
7	2	3707	181	3409	32	10	5.67E+06	7245
5	3	3871	259	7861	36	9	5.69E+06	7292
7	4	5261	290	8772	45	12	5.58E+06	7452
10	2	6260	306	5759	53	16	5.51E+06	7513
3	5	8537	111	7363	90	0	5.48E+06	7606
9	5	7395	408	12332	62	16	5.50E+06	7687
2	5	10031	1953	12969	89	0	5.65E+06	7828
2	5	9909	3402	17686	88	4	5.77E+06	7954
4	5	10004	3801	19093	89	5	5.80E+06	8001

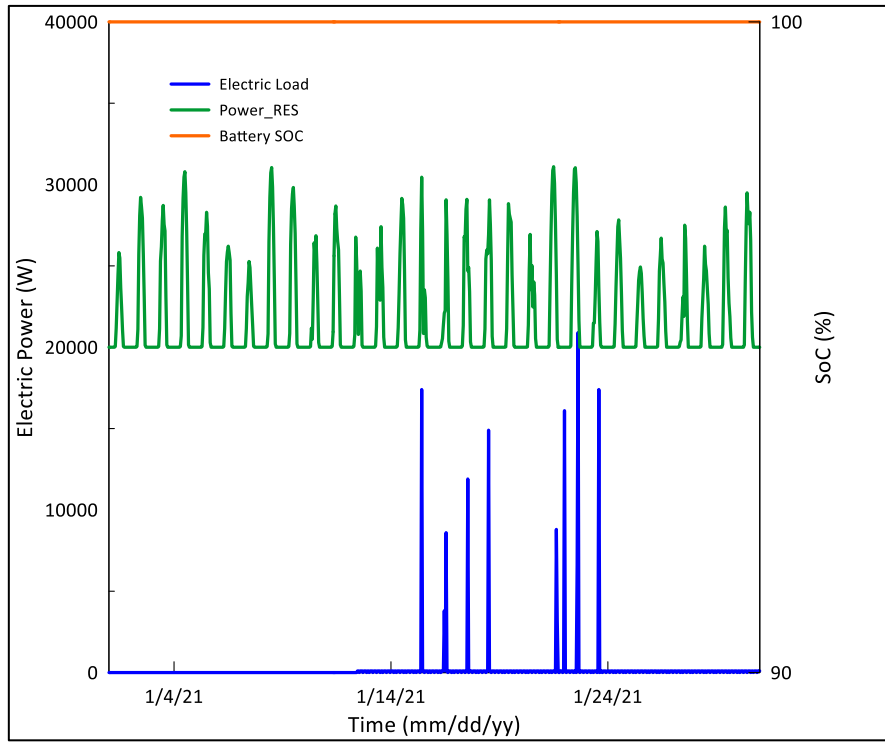
Tilt (°deg)	Azimuth (°deg)	Power_{PV} (W)	Power_{ECO20x} (W)	Capacity_B (Wh)	EL_{pr} (Nm³/h)	FC_{cr} (Nm³/h)	LCC (SEK)	Reliability (hours)
2	5	10671	5884	26321	88	5	6.20E+06	8167
2	5	10508	6247	28377	89	3	6.38E+06	8180
3	5	10942	7467	32504	89	4	6.55E+06	8268
3	4	11704	7248	31035	89	0	6.56E+06	8511
3	5	12059	8048	33689	89	0	6.72E+06	8603
3	5	12059	8048	33689	89	0	6.71E+06	8613
7	5	9863	13038	49703	85	25	7.15E+06	8616
4	5	13111	13570	53145	90	7	7.60E+06	8696
4	4	13635	15039	58097	89	7	7.94E+06	8741
4	5	13856	15782	60674	90	8	8.20E+06	8743
3	5	13899	16062	61787	89	6	8.43E+06	8745
3	5	14205	17450	66615	90	7	8.97E+06	8746
3	5	14481	18291	69492	90	8	9.17E+06	8760

Table 5. 6: Main parameters of the pareto front points (case 3 LF - Västerås)

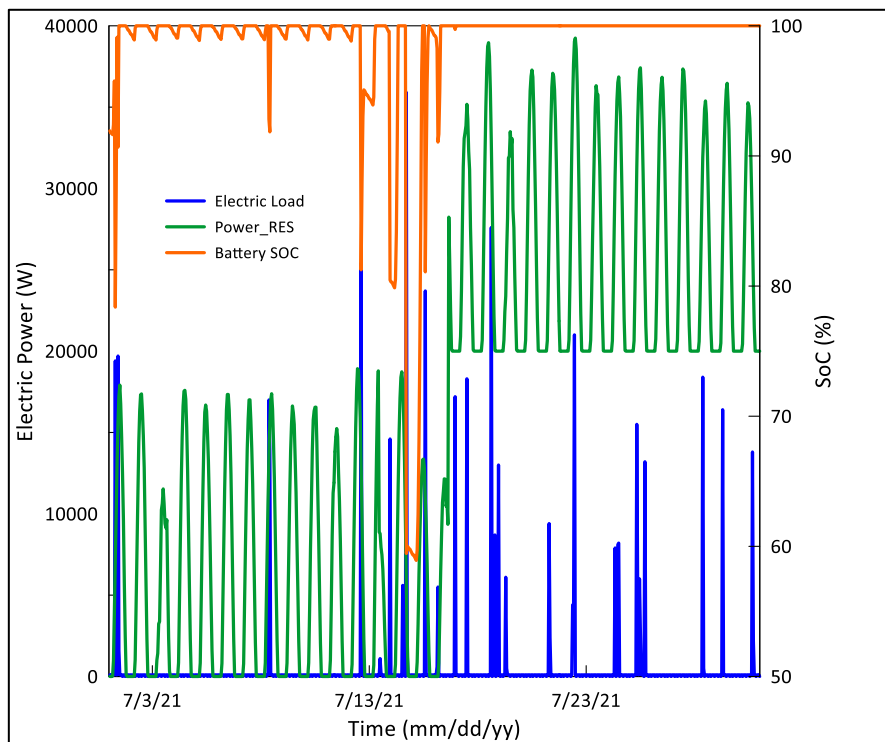
5.3 Cilento case study

Figure 5. 15 depicts the load meeting of renewable source for the CC operational strategy in two selected months: January and July for the three assumed cases and for both dispatch strategies when the micro-grid is installed in Cilento, Italy. Cilento is located, as aforementioned, near Salerno in the Campania region.

Compared to the Västerås case study, PV production reaches 11 kW in winter; in Sweden PV production did not exceed 5 kW. Like the Västerås case study, in the CCOS, micro-CHP system is almost redundant, except in January, in which the load is met only if biomass micro-CHP system is involved, which are case a) and case c).

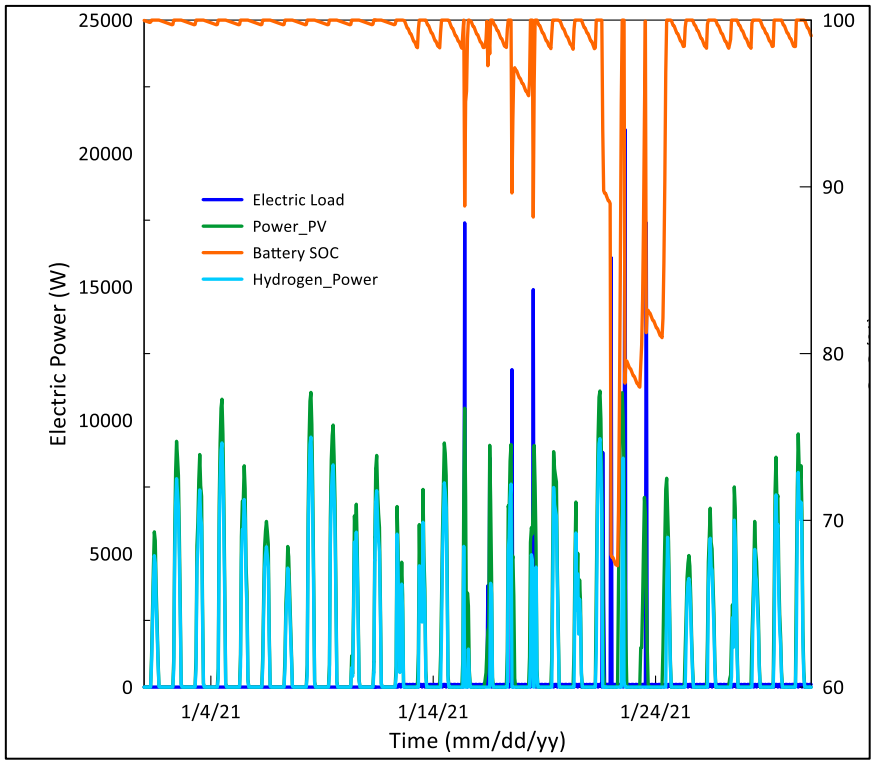


January

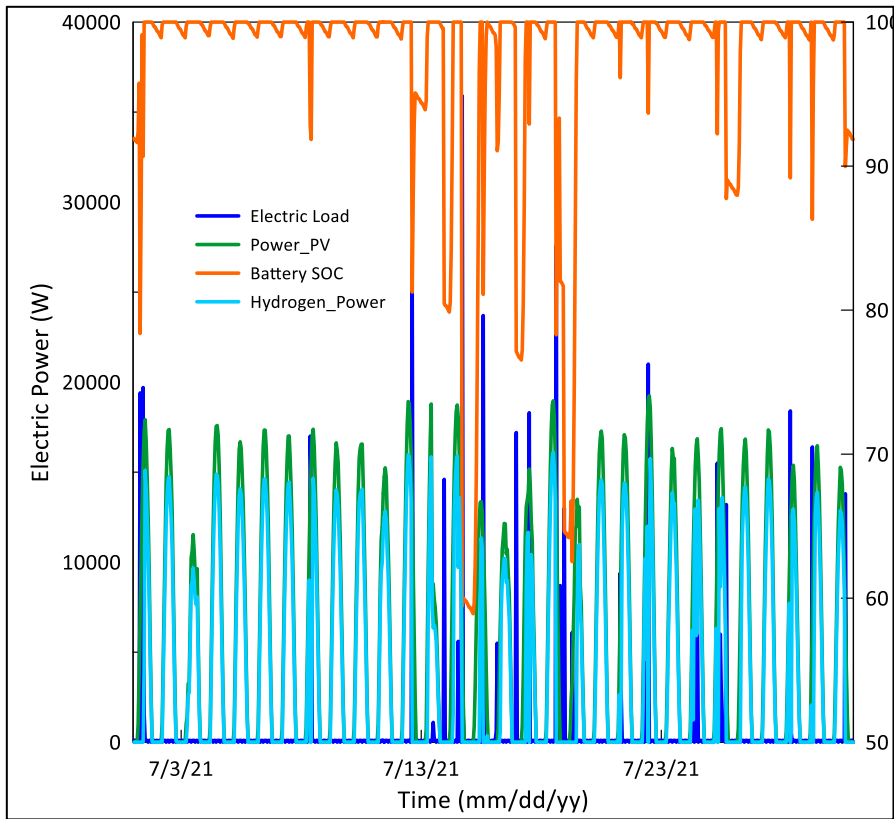


July

a)

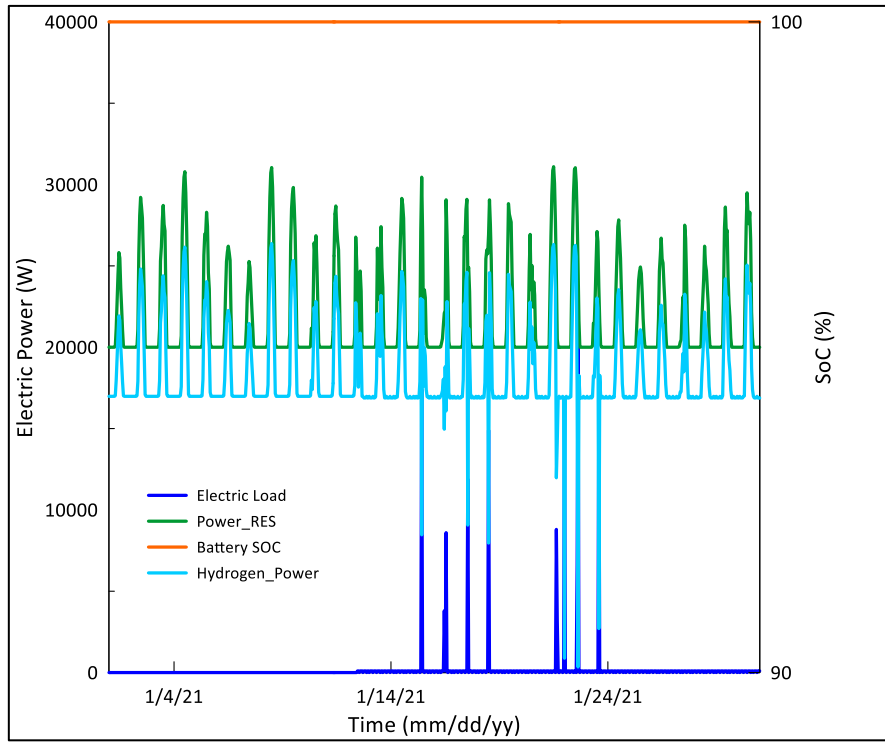


January

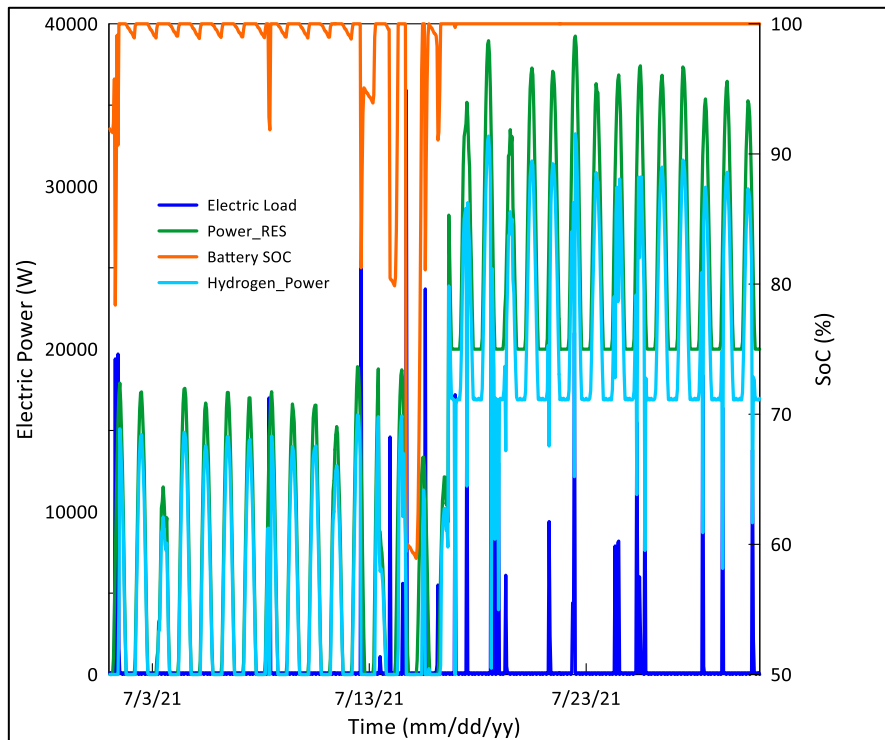


July

b)



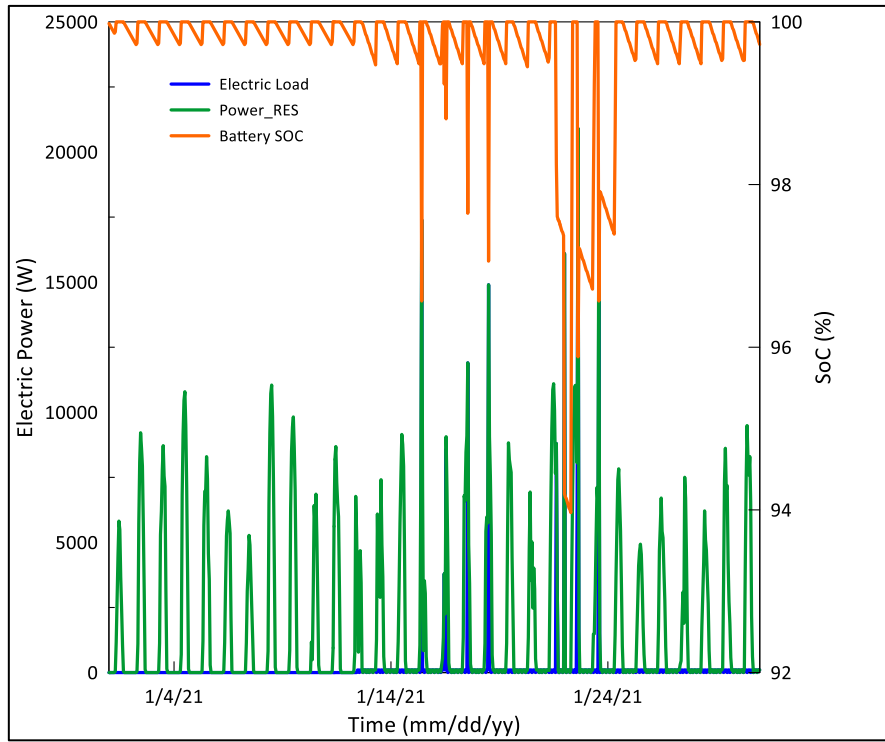
January



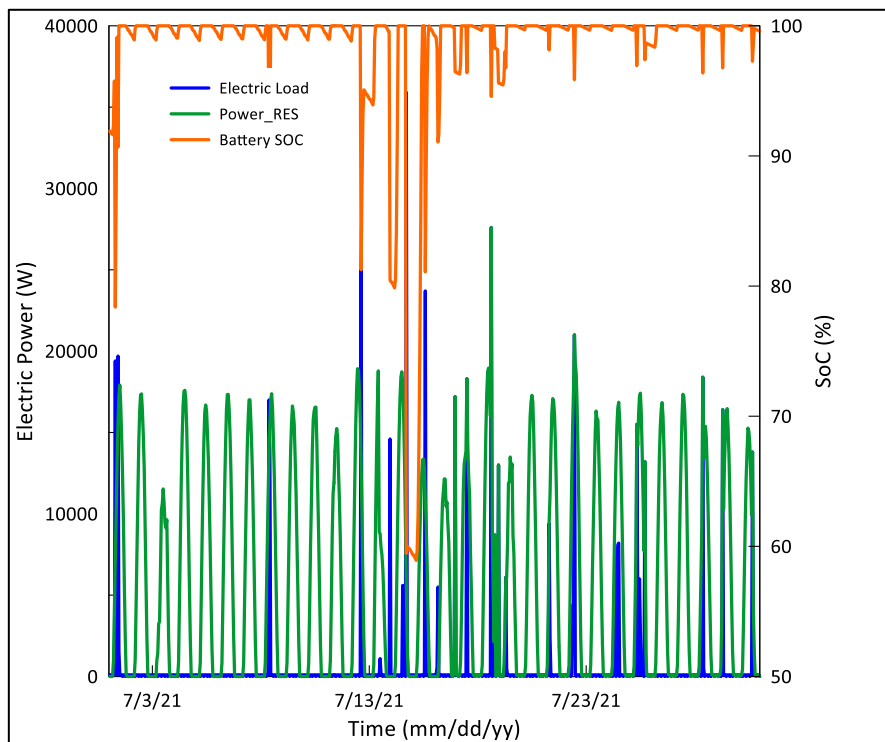
July

c)

Figure 5. 15: Simulation results for 2 selected months: January (up) and July (down) for the case a), b) and c) with CC operational strategy (Cilento case study).

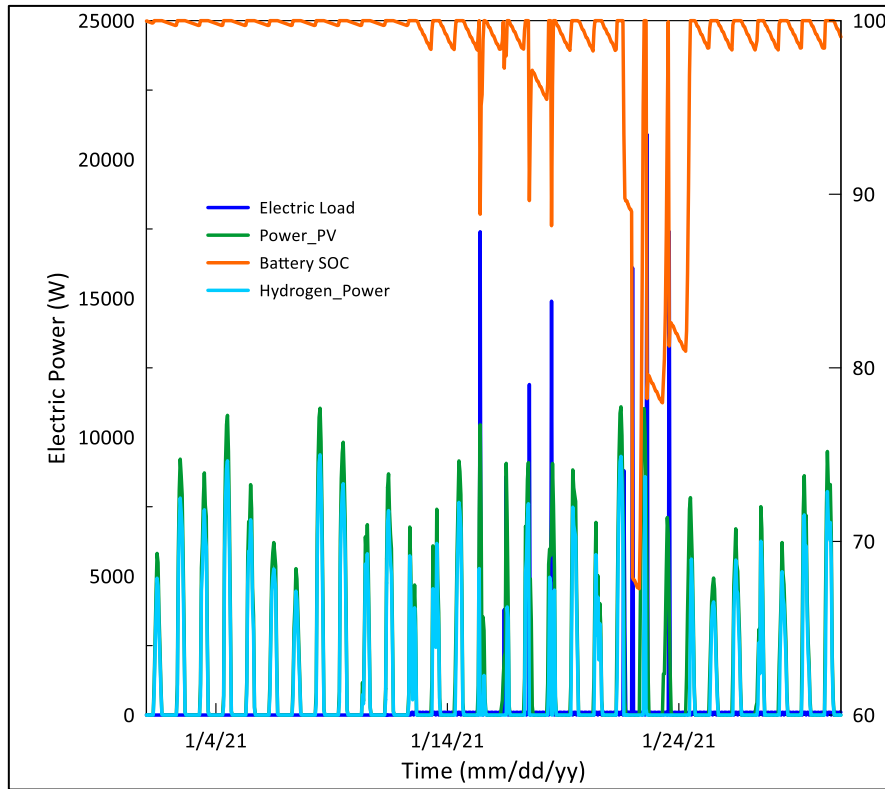


January

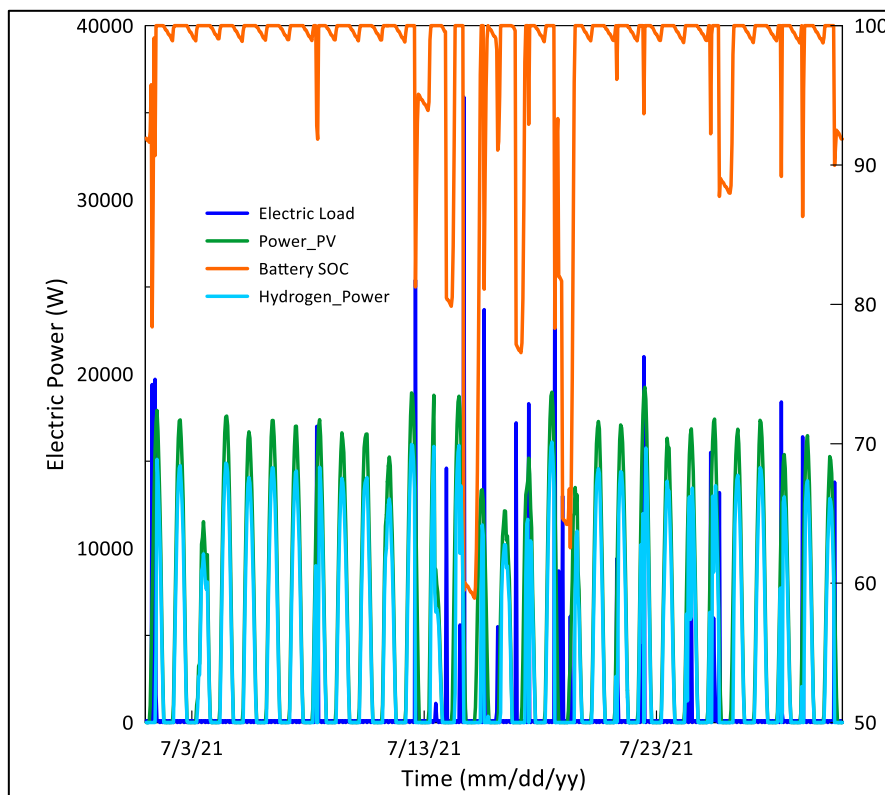


July

a)

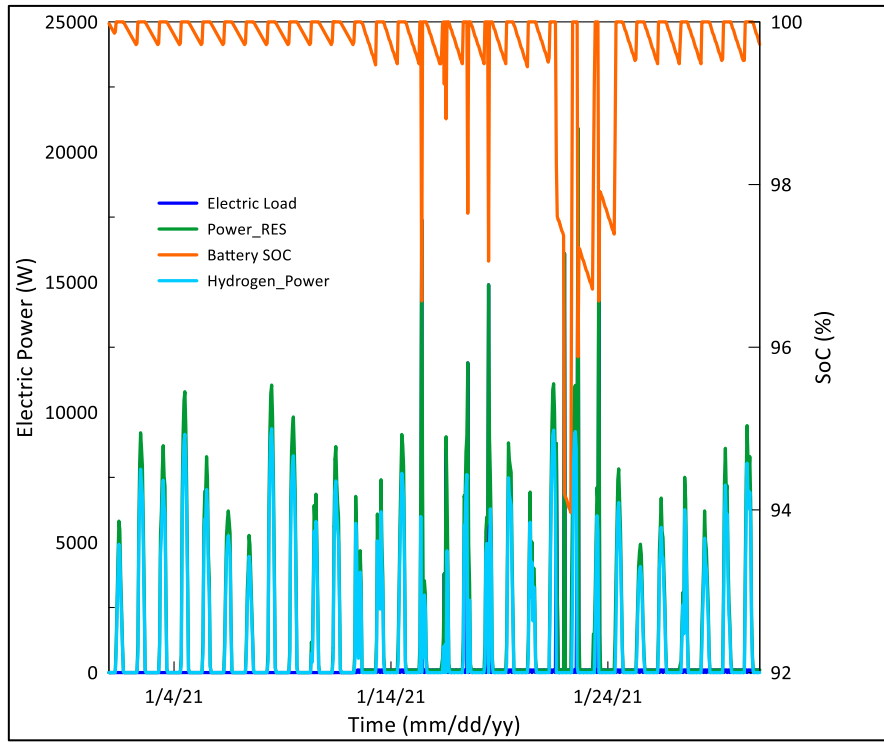


January

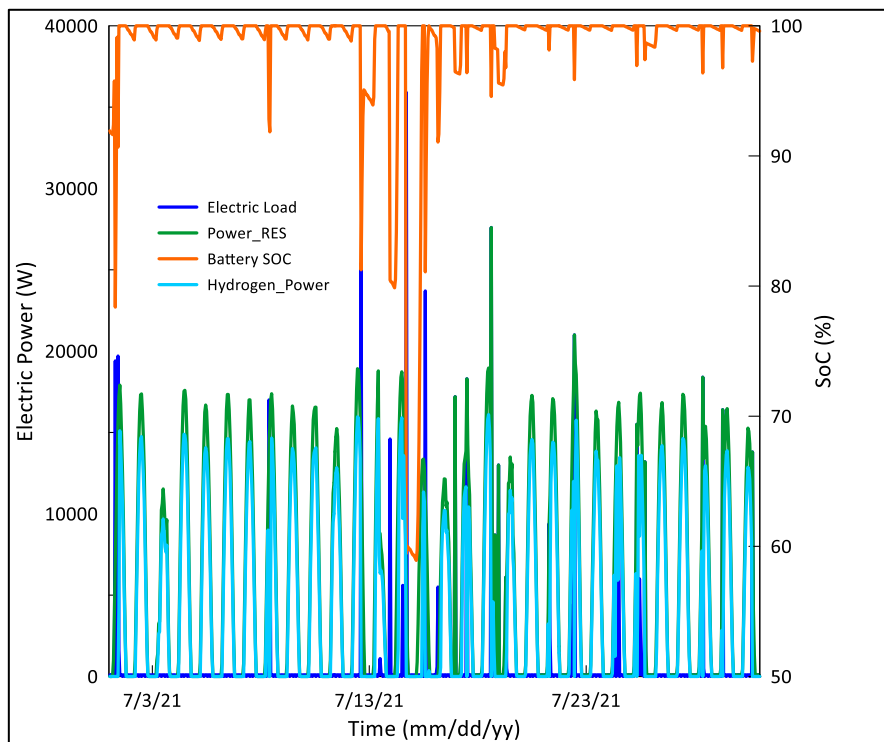


July

b)



January



July

c)

Figure 5. 16: Simulation results for 2 selected months: January (up) and July (down) for the case a), b) and c) of LF operational strategy (Cilento case study).

Hydrogen power is almost always positive, making hydrogen a useful way to storage electricity, but only if the hydrogen is sold to third part, as it is almost never used in the Cilento scenario. This is expected, as the PV production is higher during winter than Swedish scenario.

Figure 5. 16 shows the results of the simulation with LFOS for case a), b) and c) in January and July in the Cilento scenario. In LF, battery is more stressed out and used than CC, in which battery SoC standard deviation is very low. Similar to the Västerås case study, case b) is shown to stress battery the most, with a high standard deviation of battery SoC that could reduce battery life.

For Cilento case study, LF shows how the micro-CHP system is almost never used in January and in July, as the produced energy power is mainly from solar PV. This shows how the micro-grid is probably oversized for the proposed application and solar panel could meet alone the required electrical load. However, since solar production is instable and derived from climatic data, a micro-grid composed by only solar PV is not desirable but should be coupled with a dispatchable unit, such as biomass micro-CHP or diesel generator, with the first one being more environmental-friendly. Table 5. 7 reports the total LCC and reliability for each proposed case in the Cilento scenario.

Similar to Västerås case study, LF solutions are the cheapest and with the maximum RES penetration, allowing for both cases a) and c) a reduction of overall LCC of, respectively, 25% and 90%. Reliability shows that an almost 100% renewable energy conversion mix is possible for renewable e-car charging station for all cases, if the micro-grid is located in Cilento, Italy, as compared to the Västerås, Sweden. Indeed, in case b) diesel generator runs for 14h, as compared to the 241 in the Västerås case study.

	Case a)		Case b)		Case c)	
	CCOS	LFOS	CCOS	LFOS	CCOS	LFOS
Reliability (hours)	8760	8760	8746	8746	8760	8760
LCC (€)	1.18E+06	8.83E+05	2.96E+06	2.96E+06	3.87E+07	3.65E+06
Δ LCC		-25%		0		-90%

Table 5. 7: Total LCC and reliability for each proposed case for Cilento case study

Figure 5. 13 shows the hydrogen quantity stored in case b) and case c) for both strategies along the simulated year. Compared to the Swedish case study, hydrogen production is higher, reaching value up to 350 Nm³ for case b) and case c) with LF strategy and a value almost equal to 5000 Nm³ for case c) with CC strategy. The growth rate is almost exponential, with relative low period in which hydrogen is consumed.

An optimization is required also for the Cilento case scenario to avoid any redundancies between technologies and the hydrogen over-stocking.

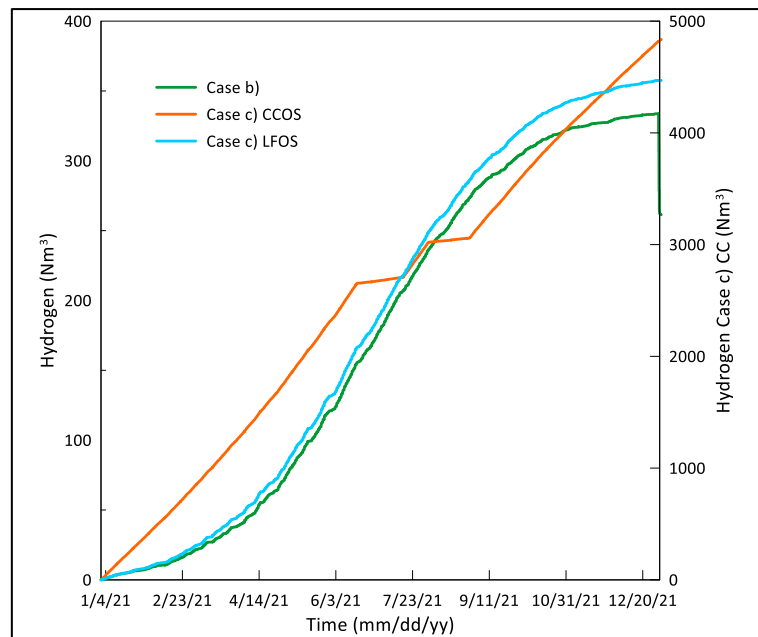


Figure 5. 17: Hydrogen quantity over time for case b) and case c) for Cilento case study.

5.2.1 Genetic algorithm optimization for Cilento case study

A GA optimization was performed also for Cilento case study in the Matlab® environment. As shown in Figure 5. 18, the 100 Pareto fronts points propose cheaper solutions for case b), without the micro-CHP, and more reliable solutions if CMD ECO20x is involved. However, compared to the GA analysis of Swedish case scenario, in which no points of the Pareto front in case b) reaches the 100% reliability, in Cilento case scenario more than 1 solution of case b) propose a reliability of 8760h. This is expectable as PV production in winter is higher than South of Sweden.

LF case 1 and case 3 overlap one to each other and present solution with high reliability and average LCC. Table 5. 8 reports some optimized point of LF Case 3.

Similar to the Västerås case study, the Pareto front points highlight the need of reducing the rated power of renewable systems and electrical storage to achieve a lower LCC while maintaining high reliability.

A higher tilt angle than the Swedish scenario is desirable and in agreement with refs. [33], [34], which proposed a value close to 40° to achieve maximum PV production. Tilt angle, instead, shows value between 20° and 50°, as compared to the 0° deg of the Västerås case study.

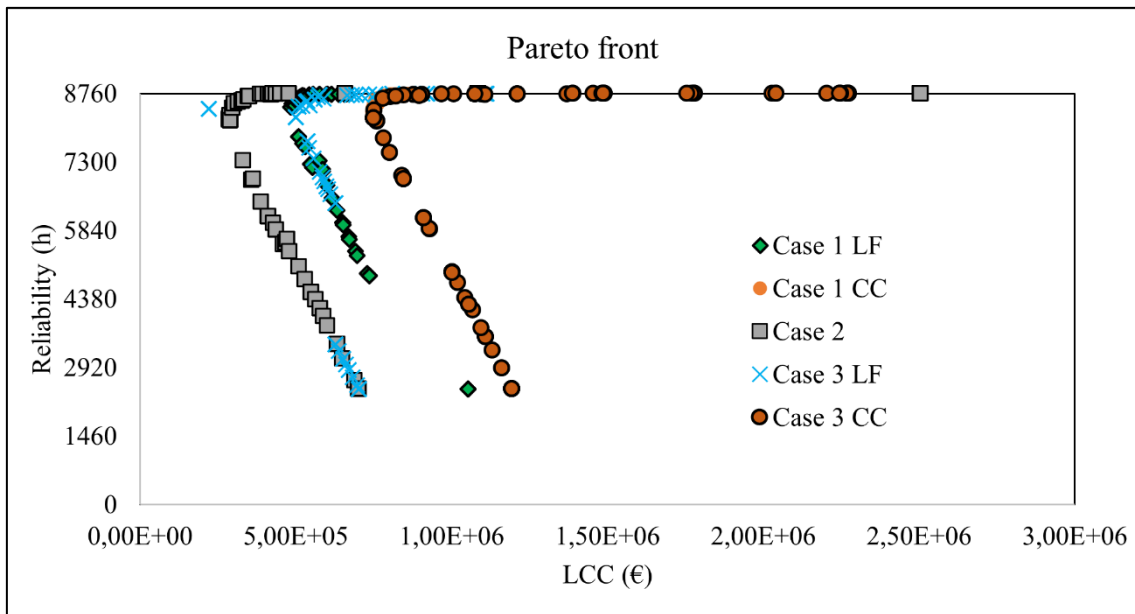


Figure 5. 18: Pareto front of the micro-grid located in Cilento

The proposed optimal microgrid size is chosen to achieve the 100% RES. Compared to the Västerås case scenario, the optimized micro-grid is quite smaller, with a micro-CHP of 14.5 kW (-16%) and PV system with peak power close to 13.5 kW (-11%), a 50kWh (-28%) Li-Ion Battery, a 40 Nm³/h (-55%) electrolyser hydrogen production rate and 20 Nm³/h (+50%) fuel cell hydrogen consumption rate with an operational strategy of load following type – in which biomass micro-CHP follows the proposed load if load is not met by renewables plus storage system. This optimized system allows maximum reliability (8760 h) and a 70% reduction of the total LCC as compared with the initially

proposed hybrid system with LF strategy. However, all proposed solutions are equivalent and implementable, according to user preferences.

Tilt (°deg)	Azimuth (°deg)	Power _{PV} (W)	Power _{ECO20x} (W)	Capacity _B (Wh)	EL _{pr} (Nm ³ /h)	FC _{cr} (Nm ³ /h)	LCC (€)	Reliability (hours)
57.9	53.0	13409.4	14445.0	53929.4	40.2	20.8	1.11E+06	8760
57.7	50.6	12405.4	13588.2	56191.8	43.0	27.1	9.05E+05	8758
56.1	53.7	12214.3	13724.3	56859.2	45.3	32.5	9.21E+05	8758
56.1	53.7	12214.3	13724.3	56859.2	45.3	32.5	9.21E+05	8758
56.1	53.7	12214.3	13724.3	56859.2	45.3	32.5	9.21E+05	8758
56.1	53.7	12214.3	13724.3	56859.2	45.3	32.5	9.21E+05	8758
57.5	51.1	12373.5	13610.9	56303.0	43.4	28.0	9.06E+05	8757
57.4	51.1	12373.5	13610.9	56303.0	43.4	28.0	9.06E+05	8757
35.1	44.7	9033.8	11343.3	61350.5	49.2	70.5	8.10E+05	8752
35.1	44.7	9033.8	11343.3	61350.5	49.2	70.5	8.10E+05	8752
35.1	44.7	9033.8	11343.3	61350.5	49.2	70.5	8.10E+05	8752
35.1	44.6	9033.8	11343.3	61350.4	49.2	70.5	8.10E+05	8752
59.9	25.9	6686.9	10126.8	81501.3	54.8	61.2	7.56E+05	8751
59.9	25.9	6686.9	10126.8	81501.3	54.8	61.2	7.56E+05	8751
59.9	25.9	6686.9	10126.8	81501.3	54.8	61.2	7.56E+05	8751
59.9	25.9	6686.9	10126.8	81501.3	54.8	61.2	7.56E+05	8751
64.8	22.1	6217.5	9883.5	85531.5	55.9	59.3	7.35E+05	8748
52.9	46.2	6840.7	9529.5	68996.5	62.9	72.2	7.10E+05	8739
56.6	46.5	6386.6	9113.0	70360.7	65.6	72.3	6.93E+05	8737
56.6	46.5	6386.6	9113.0	70360.7	65.6	72.3	6.93E+05	8737
56.6	46.5	6386.6	9113.0	70360.7	65.6	72.3	6.93E+05	8737
65.9	19.5	7637.5	846.2	54504.7	40.3	0.2	5.74E+05	8735
65.9	19.5	7637.5	846.2	54504.7	40.3	0.2	5.76E+05	8735
52.3	44.7	5766.0	8690.6	71423.9	66.4	80.1	6.80E+05	8735
56.7	45.0	5221.1	8190.8	73061.0	69.7	80.2	6.65E+05	8722

Tilt (°deg)	Azimuth (°deg)	Power _{PV} (W)	Power _{ECO20x} (W)	Capacity _B (Wh)	EL _{pr} (Nm ³ /h)	FC _{cr} (Nm ³ /h)	LCC (€)	Reliability (hours)
63.5	26.6	7137.2	2948.5	59165.9	47.7	20.7	5.72E+05	8680
65.3	29.9	7858.5	3577.8	45965.8	43.6	16.6	5.89E+05	8648
64.4	23.8	7234.8	2070.3	57597.4	45.2	13.5	5.60E+05	8638
65.9	23.8	7258.3	2556.2	51546.2	43.3	14.2	5.61E+05	8627
66.6	21.7	7730.2	1136.5	53915.6	41.5	1.6	5.38E+05	8603
66.8	21.2	7655.4	935.7	53877.2	41.5	1.2	5.34E+05	8593
66.9	21.5	7556.5	891.7	52425.8	41.6	2.2	5.32E+05	8574
64.0	32.9	6141.4	3096.6	40232.6	49.6	36.8	5.44E+05	8509
67.3	24.6	6730.6	1071.3	43383.3	43.6	13.8	5.21E+05	8498
69.4	22.9	7162.9	506.0	37764.8	39.3	2.7	5.08E+05	8483
69.4	22.9	7162.9	506.0	37764.8	39.3	2.7	5.08E+05	8483
69.4	22.9	7162.9	506.0	37764.8	39.3	2.7	5.08E+05	8483
1.2	2.5	0.8	0.1	0.3	3.0	0.0	2.21E+05	8435
1.2	2.5	0.8	0.1	0.3	3.0	0.0	2.21E+05	8435

Table 5. 8: Main parameters of the pareto front points (case 3 LF - Cilento)

For both micro-grid locations, a 100% RES system is shown to be possible in an area with an abundance of solar energy and biomass availability.

Cilento and Västerås, even if presenting different climate, are joined by the possibility of achieving an e-car charging station, connected to a highly environmental-friendly energy grid.

References of Chapter 5

- [1] C. Ghenai and I. Janajreh, "Design of Solar-Biomass Hybrid Microgrid System in Sharjah," *Energy Procedia*, vol. 103, pp. 357–362, Dec. 2016, doi: 10.1016/j.egypro.2016.11.299.
- [2] M. Løtveit, J. A. Suul, E. Tedeschi, and M. Molinas, "A study of biomass in a hybrid stand-alone Micro-Grid for the rural village of Wawashang, Nicaragua," 2014, pp. 1–7.

- [3] M. Gliński, C. Bojesen, W. Rybiński, and S. Bykuć, “Modelling of the biomass mCHP unit for power peak shaving in the local electrical grid,” *Energies*, vol. 12, no. 3, p. 458, 2019.
- [4] “Microgrid Benefits: Eight Ways a Microgrid Will Improve Your Operation,” *Microgrid Knowledge*, Apr. 10, 2018. <https://microgridknowledge.com/microgrid-benefits-eight/> (accessed Jan. 18, 2022).
- [5] V. Voices, “Bioenergy Microgrids - Making Energy Secure with Biomass,” *VECKTA*, Mar. 25, 2021. <https://www.veckta.com/2021/03/25/bioenergy-microgrids/> (accessed Jan. 19, 2022).
- [6] A. López-González, B. Domenech, D. Gómez-Hernández, and L. Ferrer-Martí, “Renewable microgrid projects for autonomous small-scale electrification in Andean countries,” *Renewable and Sustainable Energy Reviews*, vol. 79, pp. 1255–1265, Nov. 2017, doi: 10.1016/j.rser.2017.05.203.
- [7] J. Li *et al.*, “Analysis of a new design of the hybrid energy storage system used in the residential m-CHP systems,” *Applied Energy*, vol. 187, pp. 169–179, 2017.
- [8] D. I. G. Ferruzzi, “La gestione di una microgrid nel mercato liberalizzato dell’energia elettrica,” 2013.
- [9] A. S. Aziz, M. F. N. Tajuddin, M. R. Adzman, M. F. Mohammed, and M. A. Ramli, “Feasibility analysis of grid-connected and islanded operation of a solar PV microgrid system: A case study of Iraq,” *Energy*, vol. 191, p. 116591, 2020.
- [10] I. Bertini, M. Di Silvestre, G. Graditi, M. Ippolito, E. Riva Sanseverino, and G. Zizzo, “Architetture e logiche di controllo ottimale di microreti per la razionalizzazione energetica Report 1–Identificazione ed analisi di architetture e logiche di controllo ottimale di microreti per la razionalizzazione energetica,” 2011.
- [11] D. Milan, “Modello di microgrid per l’analisi delle strategie di gestione dello scambio di potenza attiva/reattiva con la rete,” 2015.
- [12] F. Benedetti, “Micro-reti di distribuzione: controllo e modelli delle sorgenti,” 2011.
- [13] H. Chen, T. N. Cong, W. Yang, C. Tan, Y. Li, and Y. Ding, “Progress in electrical energy storage system: A critical review,” *Progress in natural science*, vol. 19, no. 3, pp. 291–312, 2009.
- [14] C. Wang, Y. Liu, X. Li, L. Guo, L. Qiao, and H. Lu, “Energy management system for stand-alone diesel-wind-biomass microgrid with energy storage system,” *Energy*, vol. 97, pp. 90–104, 2016.
- [15] Y. Zhang, T. Ma, P. E. Campana, Y. Yamaguchi, and Y. Dai, “A techno-economic sizing method for grid-connected household photovoltaic battery systems,” *Applied Energy*, vol. 269, p. 115106, 2020.
- [16] Y. Zheng, B. M. Jenkins, K. Kornbluth, and C. Træholt, “Optimization under uncertainty of a biomass-integrated renewable energy microgrid with energy storage,” *Renewable energy*, vol. 123, pp. 204–217, 2018.
- [17] M. Aneke and M. Wang, “Energy storage technologies and real life applications—A state of the art review,” *Applied Energy*, vol. 179, pp. 350–377, 2016.
- [18] “Lithium battery,” *Wikipedia*. Nov. 22, 2021. Accessed: Jan. 23, 2022. [Online]. Available: https://en.wikipedia.org/w/index.php?title=Lithium_battery&oldid=1056497818
- [19] Y. Miao, P. Hynan, A. Von Jouanne, and A. Yokochi, “Current Li-ion battery technologies in electric vehicles and opportunities for advancements,” *Energies*, vol. 12, no. 6, p. 1074, 2019.

- [20] R. Collin, Y. Miao, A. Yokochi, P. Enjeti, and A. Von Jouanne, “Advanced electric vehicle fast-charging technologies,” *Energies*, vol. 12, no. 10, p. 1839, 2019.
- [21] M. R. Quitoras, P. E. Campana, and C. Crawford, “Exploring electricity generation alternatives for Canadian Arctic communities using a multi-objective genetic algorithm approach,” *Energy Conversion and Management*, vol. 210, p. 112471, 2020.
- [22] “optice.net.” <https://optice.net/> (accessed Oct. 21, 2021).
- [23] I. Kim, J.-A. James, and J. Crittenden, “The case study of combined cooling heat and power and photovoltaic systems for building customers using HOMER software,” *Electric power systems Research*, vol. 143, pp. 490–502, 2017.
- [24] R. Sen and S. C. Bhattacharyya, “Off-grid electricity generation with renewable energy technologies in India: An application of HOMER,” *Renewable Energy*, vol. 62, pp. 388–398, 2014.
- [25] F. Calise, F. L. Cappiello, A. Carteni, M. D. d’Accadia, and M. Vicidomini, “A novel paradigm for a sustainable mobility based on electric vehicles, photovoltaic panels and electric energy storage systems: Case studies for Naples and Salerno (Italy),” *Renewable and Sustainable Energy Reviews*, vol. 111, pp. 97–114, 2019.
- [26] J. A. Duffie and W. A. Beckman, *Solar engineering of thermal processes*. John Wiley & Sons, 2013.
- [27] M. Costa, G. Martoriello, and R. Tuccillo, “Modelling of an innovative and autonomous micro-grid based on a biomass-solar PV hybrid power system”, *Proceedings of ICAE 2020*, vol. 238, p. 02003.
- [28] “PEM Electrolyser,” *Nel Hydrogen*, May 28, 2018. <https://nelhydrogen.com/product/c10-c20-c30/> (accessed Oct. 21, 2021).
- [29] J. Nömm, S. K. Rönnberg, and M. H. Bollen, “Techno-economic analysis with energy flow modeling for investigating the investment risks related to consumption changes within a standalone microgrid in Sweden,” *Energy*, vol. 225, p. 120156, 2021.
- [30] C. Stryja, H. Fromm, S. Ried, P. Jochem, and W. Fichtner, “On the necessity and nature of E-mobility services—towards a service description framework,” 2015, pp. 109–122.
- [31] W. Jing, Y. Yan, I. Kim, and M. Sarvi, “Electric vehicles: A review of network modelling and future research needs,” *Advances in Mechanical Engineering*, vol. 8, no. 1, p. 1687814015627981, 2016.
- [32] S. Killinger *et al.*, “On the search for representative characteristics of PV systems: Data collection and analysis of PV system azimuth, tilt, capacity, yield and shading,” *Solar Energy*, vol. 173, pp. 1087–1106, 2018.
- [33] M. Z. Jacobson and V. Jadhav, “World estimates of PV optimal tilt angles and ratios of sunlight incident upon tilted and tracked PV panels relative to horizontal panels,” *Solar Energy*, vol. 169, pp. 55–66, 2018.
- [34] Y. Yang, P. E. Campana, B. Stridh, and J. Yan, “Potential analysis of roof-mounted solar photovoltaics in Sweden,” *Applied Energy*, vol. 279, p. 115786, 2020.

Conclusions

The present Ph.D. work, funded within the Bilateral Agreement Confindustria-National Research Council, and carried at the University of Naples “Federico II”, the National Research Council – Istituto di Scienze e Tecnologie per l'Energia e la Mobilità Sostenibili (CNR-STEMS) and the company Costruzioni Motori Diesel (CMD) SpA, focused on the optimization of micro-cogeneration systems based on biomass gasification and internal combustion engine coupling, with the intention of giving a tangible contribution to support the development of biomass-to-energy conversion systems.

After an initial phase of literature review, in which the importance of bioenergy and biomass powered micro-CHP system was discovered in the current energy scenario, the micro-CHP system manufactured by CMD, the CMD ECO20x unit, was analysed into great detail.

A fully experimental analysis of the CMD ECO20x system was carried out to highlight any possible inefficiency in each of its components. The performed experimental activity includes the evaluation of syngas composition, the in-cylinder pressure cycle and the main energy output measurements at the ICE, as well as the characterisation of the exhausts. The analysis was executed under different feedstocks. The micro-CHP system was found to struggle with high ash %age feedstocks. Preliminary investigations were required to propose optimizations to be performed, both on the gasification process and for the improvement of combustion within the engine cylinders.

The numerical simulation and the multi-objective optimization, described in Chapter 3, provided useful information to upgrade the m-CHP design and control. The optimization results allowed the engine to be calibrated ad hoc for syngas operation, since it was originally built for natural gas combustion, so to account for the variable composition of the gaseous fuel resulting from the biomass conversion into the gasifier. The numerical and empirical findings also revealed significant inefficiencies in the heat recovery system, and various solutions were analysed to gain some more thermal power.

Finally, the changes made on the ECO20x unit allowed not only to improve its overall efficiency and reliability, but also to build the groundwork for the plant development by the Company, with a new omnivorous configuration of the gasifier capable of converting a variety of ligneous biomasses into useful energy.

The demonstration of the operation of the mCHP plant in the Municipality of Mugnano, Naples, and the assessment of its environmental impact and its sustainability were very encouraging and are indeed a stimulus for the diffusion of this type of plant to be a green substitute in a waste management and storage plant.

Finally, thanks to a collaboration with the Mälardalen University (Sweden), a numerical study on the micro-CHP integration with photovoltaic (PV) solar energy, hydrogen, and battery energy storage systems was made in order to understand the possibility of providing energy to charging stations for electric vehicles while adhering to the constraints of compactness, high quality service, and ultra-low environmental impact.

These findings are critical for the ongoing project "Borgo 4.0 – E-mobility" (2020-ongoing), which is being sponsored by POR CAMPANIA FESR 2014-2020 – Asse prioritario 1 “Ricerca e Innovazione” and aims to develop a completely new and renewable charging infrastructure.

The principal conclusions of the work can be synthetically drawn as following:

- A complete characterization of the CMD ECO20x plant led to the conclusions that the engine needed a recalibration of its working parameters, regarding the spark advance ($^{\circ}\text{CAD}$) and the mixture lambda - i.e. the air-to-fuel ratio against the stoichiometric air-to-fuel ratio. A more delayed start of spark and a leaner mixture than the original parameters, allowed to improve the electrical output and reduce noxious emissions. Also, a revision of the heat recovery layout was necessary to improve the thermal output of the system. The use of exhaust gases for the preliminary drying of the biomass was analysed and will be implemented in the future.
- A numerical model of the whole system was realised through the combined use of ThermoFlow™ and GT-Suite® environments, which resulted in a highly integrated digital twin of the ECO20x unit, validated on the ground of experimental data. Optimizations, both single and multi-objective, were carried out numerically in order to show some important engine operating conditions able to keep polluting substances below the limit established by the Italian regulation, namely Dlg183/17. Adapting this new value of parameters in the real plant configuration was industrially relevant to turn the CMD ECO20x system into a more efficient plant without changing components. NO_x formations were found

to be highly affected by spark timing, which is also the main responsible for the improvement of the ICE brake power. By implementing a right synchronisation of ignition in the real system, as derived from the numerical optimization, an important reduction up to 60% was achieved without any losses on the brake power. CO emissions were influenced by the air-to-fuel mixture with high reduction achieved by lowering the fuel amount in the mixture and through a catalytic converter.

- The need to manage the start of combustion for each feedstock and, therefore, to achieve a smart control of the combustion phase in the engine was needed. For this purpose, an ECU from automotive derivation was adapted to the scope, and the signal deriving from the analysis of the ion current was used as feedback to control the position of the pressure peak. The signal of the ion current was also used to evaluate the state of the spark plug, with information about its cleaning. In this way, by using appropriate control logics, it was possible to automatically clean the spark plug that started to get dirty and to report the anomaly to the operator, allowing easy recognition of the phenomenon and avoiding missed engine start-ups or unwanted misfiring. Changing or cleaning the spark plug in time can in fact prevent the engine from running unbalanced, with potential damage to the supports and intake and exhaust manifolds if the condition continued over time.
- The demonstration of sustainability of the system CMD ECO20x during the installation period which lasted 6 months in the Municipality of Mugnano, Naples, represented a fundamental proof for the diffusion of this type of plant in substitution of traditional gensets, according to the concept of distributed energy produced through local resources. The sustainability analysis of the plant was carried out both by analysing the quality of the air in the installation area and evaluating the environmental impact of the whole biomass-energy supply chain through a simple LCA. The biomass supply chain was assessed due to the need to use fossil fuels for some operations such as cutting with a chainsaw or transporting woodchips, confirming a global contribution to greenhouse gas emissions lower than an equivalent diesel-fuelled genset, a very widespread technology especially in rural areas.

- Thanks to a collaboration with the Mälardalen University (Sweden), the optimization of the micro-CHP integration with photovoltaic (PV) solar energy, hydrogen and battery storage was carried out numerically, through a properly developed model of the whole micro-grid in dynamic regime. The micro-grid was considered as installed either in Cilento or in Västerås, Sweden, so to account for the different weather conditions and to highlight the main differences between the two locations and climates. The Pareto front was found for both solutions. The micro-grid in Västerås presented a longer involvement of the micro-CHP system than in Cilento, as PV production during winter is lower.

These results are used as important information for the on-going Project “BORGGO 4.0”, funded by POR CAMPANIA FESR 2014-2020, in the creation of a totally innovative and 100% renewable electric vehicle charging infrastructure. Next steps are the implementation and validation of the proposed micro-grid modeling.

Acknowledgments

Here comes the hardest part: the acknowledgments. Three years is a long time, and I would like to take a moment to thank everyone for their fundamental contribution in achieving this important goal.

First of all, I gratefully acknowledge Dott. Ing. Michela Costa (CNR-STEMS) for her unceasing and hectic support in research activities, and Prof. Ing. Tuccillo (University of Naples “Federico II”) for being a wonderful guide in these academic years. Both have contributed in such an important way to my professional and human formation.

I would like to thank Costruzioni Motori Diesel - Energy Department and Ing. Domenico Cirillo, technical manager, for their “industrial point of view”. Domenico’s scientific curiosity and desire for discovery is contagious and has helped me to find joy in the things I do. Greetings to all the R&D group of the CMD-Energy Department, in particular Dr. Ing. Maurizio La Villetta and Arch. Stefano Esposito for their helpful and welcoming guide during my internship months in CMD.

I want to express my gratitude to the researchers of CNR-STEMS, for their essential contribution in the experimental activities and their generous guidance in these three years: Dr. Ing. Maria Vittoria Prati, Dr. Ing. Maria Antonietta Costagliola, Dr. Ing. Gabriele di Blasio, Dr. Ing. Roberto Ianniello, Dr. Ing. Giovanna Ruoppolo and Dr. Ing. Urciuolo. It was a pleasure to work closely to them. A special acknowledge goes to Dr. Ing. Daniele Piazzullo and Dr. Ing. Carmine Caputo, my partners in crime, and Ing. Davide Adinolfi, a caring resource to the team.

In addition, I would like to thank my dad and my mom, as they are the rocks upon which I stand, my brother Giuseppe, for being present in all my important moment even if he is 20-hours flight away from me, and my grandparents Licia, Pino and Frasia, who guide me from above.

Greetings to all my friends, those who are here and those who are away: Roberto, Francesca, Maura, Giuliano, Mel, Imma, Federica, Silvia, Jacopo, Fabrizio and Dok. Each one of you has supported me in some way during these three years and I thank you for that.

Last but not least, I wish to dedicate special words of gratitude and love to my boyfriend Dario. I don't know where to begin to thank you: you know when I need your patience, kindness, silliness or just an "undesired" hug.

Yours truly,
Gaia Martoriello